Final Report for
Contract DE-FG36-08GO18192
Stanford Geothermal Program
September 2008 – June 2012

Fracture Characterization in Enhanced Geothermal Systems by Wellbore and Reservoir Analysis

PI: Roland N. Horne
Department of Energy Resources Engineering
Stanford University
Stanford, CA

Table of Contents

1. FRACTURE CHARACTERIZATION USING PRODUCTION DATA 1

1.1 SUMMARY 1

1.2 INTRODUCTION 1

1.3 CHARACTERIZATION BASED ON FLOW-RATE AND TRACER DATA 3

1.4 OPTIMIZATION OF INJECTION SCHEDULING 33

1.5 CONCLUSION 45

2. FRACTURE CHARACTERIZATION USING NANOPARTICLES 49

2.1 SUMMARY 49

2.2 INTRODUCTION 50

2.3 MATERIALS AND METHODS 55

2.4 RESULTS 65

2.5 CONCLUSION 104

3. FRACTURE CHARACTERIZATION USING RESISTIVITY 107

3.1 SUMMARY 107

3.2 INTRODUCTION 107

3.3 RESISTIVITY MODEL 109

3.4 THE ELECTRIC FIELD SOLVED USING TOUGH2 113

3.5 DISCRETE-FRACTURE NETWORKS 121

3.6 INVERSE ANALYSIS 132

3.7 FUTURE WORK 141

4. FRACTURE CHARACTERIZATION USING THERMAL AND TRACER DATA143

4.1 SUMMARY 143

4.2 INTRODUCTION 144

4.3 COMBINED TRACER AND TEMPERATURE ANALYTICAL MODELS 146

4.4 RESULTS FROM COMBINED TRACER AND TEMPERATURE ANALYSIS 150

4.5 SCALING CORRELATIONS AND GEOMECHANICS CONCEPTS **168**

4.6 CORRELATION OF FRACTURE PROPERTIES AND LITHOLOGY TO PERMEABLE ZONE LOCATIONS **174**

4.7 FUTURE WORK **180**

5. REFERENCES **181**

1. FRACTURE CHARACTERIZATION USING PRODUCTION DATA

This research project was conducted by Research Assistant Egill Juliusson, Senior Research Engineer Kewen Li and Professor Roland Horne. The objective of this project was to investigate ways to characterize fractured geothermal reservoirs using production data.

1.1 SUMMARY

This report highlights the work that was done to characterize fractured geothermal reservoirs using production data. That includes methods that were developed to infer characteristic functions from production data and models that were designed to optimize reinjection scheduling into geothermal reservoirs, based on these characteristic functions.

The characterization method provides a robust way of interpreting tracer and flow rate data from fractured reservoirs. The flow-rate data are used to infer the interwell connectivity, which describes how injected fluids are divided between producers in the reservoir. The tracer data are used to find the tracer kernel for each injector-producer connection. The tracer kernel describes the volume and dispersive properties of the interwell flow path. A combination of parametric and nonparametric regression methods were developed to estimate the tracer kernels for situations where data is collected at variable flow-rate or variable injected concentration conditions.

The characteristic functions can be used to calibrate thermal transport models, which can in turn be used to predict the productivity of geothermal systems. This predictive model can be used to optimize injection scheduling in a geothermal reservoir, as is illustrated in this report.

1.2 INTRODUCTION

Robust methods to characterize fractured reservoirs are crucial for successful development of geothermal fields, both conventional and EGS. Large faults and fractures can sometimes be mapped with seismic surveys but in severely fractured systems it becomes increasingly difficult to interpret the seismic data. This fact elevates the importance of utilizing well production data to characterize these systems to the furthest possible extent.

Well-to-well connections in fractured fields are famously hard to predict as illustrated in the classic Wairakei tracer tests reported by McCabe et al. (1983). Figure 1.1 shows that the distances between wells were in no way indicative of tracer-determined well connectivity, nor could the surface fault traces be used to determine which wells were best connected. The importance of understanding how fracture networks govern the flow in a geothermal system was demonstrated clearly by Yahara and Tokita (2010), as they reported on problems with the expansion of the Hatchobaru geothermal field in Japan. In that case it took about five years to understand the subsurface flow mechanisms and make the relevant modifications to bring the power production up to full capacity.

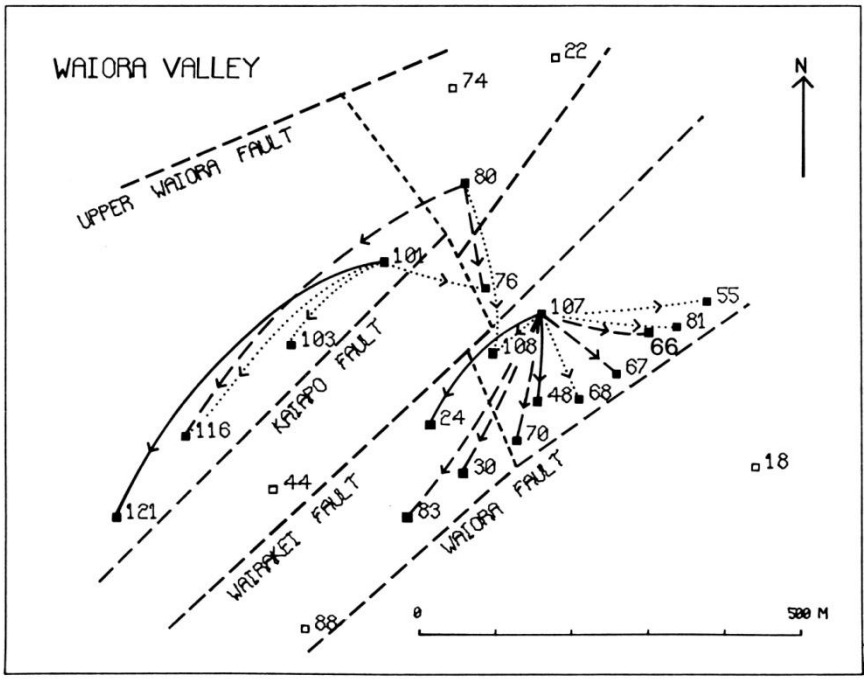

Figure 1.1: Graphical summary of tracer returns in the Wairakei geothermal field. Continuous arrowed lines indicate tracer returns of more than 1%; dashed lines indicate 0.1% to 1% returns; dotted lines indicate returns of less than 0.1% (from McCabe et al., 1983).

Full-physics flow simulation models are often used to characterize the subsurface, in geothermal, groundwater and oil and gas applications. Characterizing fractures with such models has proven difficult because; a) simulating fractures is very inefficient computationally, and; b) the stochastic nature of fractured reservoirs makes history matching subject to very high uncertainty.

An important aspect of developing a geothermal field is the design of an efficient injection schedule. A forward model that can estimate the field performance at various injection schedules is required to solve this design problem properly. The forward model must be run multiple times to find the optimal schedule and therefore it is desirable that the model can run fast and be robust computationally. This is seldom the case when full-physics flow simulation models are used to characterize a geothermal system.

In this work a systems analysis approach was used to characterize fractured reservoirs. The approach was designed to be data-driven with an emphasis on efficiency and capturing the effects of fractures. Part of the challenge was to find which data would be best suited for the task, and how multiple data sources could be interpreted jointly to yield an informative characterization of the reservoir.

The characterization method was used to calibrate a well-to-well thermal transport model. The thermal and flow rate transport models were used jointly to predict the performance of the resource at a given injection schedule. A formulation for the optimal injection scheduling problem was designed and solved in a robust and efficient manner, as illustrated in this report.

1.3 CHARACTERIZATION BASED ON FLOW-RATE AND TRACER DATA

At the conclusion of this study it was found that flow-rate (or bottomhole-pressure) data and tracer data could be used very efficiently to characterize fractured reservoirs. The flow-rate data were essential for defining the fractional amount of injected water that goes towards each producer. The tracer data were used to describe the transport properties of each injector-producer flow path in more detail by a function referred to as the tracer kernel.

This section describes the details of how flow-rate and tracer data were used to characterize the reservoir. The handling of flow-rate data follows the method of Lee (2010). A new model that relies on a combination of injected flow-rate and tracer concentration was developed to describe variations in produced tracer concentration. Central to this model is the definition of the tracer kernel, which was derived with reference to the advection-dispersion equation.

1.3.1 Flow-Rate Models

Interwell connectivity (IWC) models have been discussed by several researchers over the past decade (Albertoni and Lake, 2002; Dinh, 2009; Juliusson, 2012; Lee, 2010; Yousef et al., 2005). These models are applicable in reservoirs with low compressibility when production wells run at constant bottomhole pressure conditions (the Interwell Transmissibility Model (Juliusson, 2012) is an exception). The IWC's are particularly useful for mapping highly conductive flow paths between wells. The method outlined by Dinh (2009) relies on bottomhole pressure data, the Interwell Transmissibility method presented in the Quarterly Report from Spring 2012 requires both bottomhole pressure and flow-rate data, but the methods developed by Albertoni and Lake (2002), Yousef et al. (2005), and Lee (2010) depend only on flow-rate data. A recent flow-rate based method, referred to as the M-ARX method Lee (2010), was used to compute IWC in this work. The M-ARX method will be described briefly in this section to introduce the nomenclature and lay the foundation for the tracer kernel method described in the next section.

The M-ARX interwell connectivity method is derived from a set of volume balances:

$$\frac{dq_{Pj}(t)}{dt} + \sum_{k=1}^{N_P} \frac{\alpha_{jk}}{\gamma_j} q_{Pk}(t) = \sum_{i=1}^{N_I} \frac{\beta_{ji}}{\gamma_j} q_{Ii}(t) \tag{2.1}$$

where t denotes time, q_I and q_P are the injection and production rates, respectively, N_I and N_P are the number of injection and production wells, respectively, α and β are proportionality coefficients and γ is a constant that governs the time lag of the response in the producers.

The set of volume balances defined by Equation (2.1) can be represented in matrix form as:

$$\frac{d\boldsymbol{q_P}(t)}{dt} + \boldsymbol{A_c q_P}(t) = \boldsymbol{B_c q_I}(t) \tag{2.2}$$

where:

$$\boldsymbol{A_c} = \begin{bmatrix} \gamma_1 & \cdots & 0 \\ \vdots & \ddots & \vdots \\ 0 & \cdots & \gamma_{N_P} \end{bmatrix}^{-1} \begin{bmatrix} \alpha_{11} & \cdots & \alpha_{1N_P} \\ \vdots & \ddots & \vdots \\ \alpha_{N_P1} & \cdots & \alpha_{N_PN_P} \end{bmatrix} \tag{2.3}$$

and:

$$\boldsymbol{B_c} = \begin{bmatrix} \gamma_1 & \cdots & 0 \\ \vdots & \ddots & \vdots \\ 0 & \cdots & \gamma_{N_P} \end{bmatrix}^{-1} \begin{bmatrix} \beta_{11} & \cdots & \beta_{1N_P} \\ \vdots & \ddots & \vdots \\ \beta_{N_I1} & \cdots & \beta_{N_IN_P} \end{bmatrix} \tag{2.4}$$

The following analytical solution exists for Equation (2.2):

$$\boldsymbol{q_P}(t) = \boldsymbol{q_P}(0)e^{-A_c t} + \int_0^t \boldsymbol{q_I}(t-\tau)B_c e^{-A_c \tau} d\tau \tag{2.5}$$

The main advantage that the M-ARX model has over those derived by Albertoni and Lake (2002) and Yousef et al. (2005) is that the producer-producer interactions are taken into account, in addition to the injector-producer interactions. For practical applications it is more convenient to deal with the discrete form of Equation (2.2):

$$\boldsymbol{q_P}(n+1) = -\boldsymbol{A}\boldsymbol{q_P}(n) + \boldsymbol{B}\boldsymbol{q_I}(n) \tag{2.6}$$

where ν is a time-like discrete variable, and $\boldsymbol{A}$ and $\boldsymbol{B}$ are the discrete counterparts of $\boldsymbol{A_c}$ and $\boldsymbol{B_c}$, respectively. Equation (2.6) defines a Multivariate AutoRegressive model for determining $\boldsymbol{q_P}$ with eXogenous inputs, $\boldsymbol{q_I}$ (hence the abbreviation M-ARX). A set of $n+1$ measurements yields n equations which can be solved together to find the elements of $\boldsymbol{A}$ and $\boldsymbol{B}$:

$$[\boldsymbol{q_P}(2) \ldots \boldsymbol{q_P}(N+1)] = [-\boldsymbol{A} + \boldsymbol{B}] \begin{bmatrix} \boldsymbol{q_P}(1) & \ldots & \boldsymbol{q_P}(N) \\ \boldsymbol{q_I}(1) & \ldots & \boldsymbol{q_I}(N) \end{bmatrix} \tag{2.7}$$

The solution to Equation (2.6) is stable, as long as $\boldsymbol{0} \preccurlyeq (\boldsymbol{I} + \boldsymbol{A})^{-1}\boldsymbol{B} \preccurlyeq \boldsymbol{1}$ (elementwise). It can be shown via the Z-transform (discrete analog of Laplace transform) that if the injection rates are kept constant, the production rates will stabilize at:

$$\boldsymbol{q_P} = (\boldsymbol{I} + \boldsymbol{A})^{-1}\boldsymbol{B}\boldsymbol{q_I} = \boldsymbol{F}\boldsymbol{q_I} \tag{2.8}$$

The elements of the matrix $\boldsymbol{F} = (\boldsymbol{I} + \boldsymbol{A})^{-1}\boldsymbol{B}$ then define the interwell connectivity for each of the injector-producer pairs in terms of flow-rate. With this definition of $\boldsymbol{F}$ the portion of flow leaving injector i arriving at producer j will be:

$$q_{IiPj} = F_{IiPj} q_{Ii} \tag{2.9}$$

If the total compressibility is small, the flow-rates stabilize relatively quickly, i.e., within a few hours. This would be the case for production from most liquid-dominated systems, and thus the M-ARX model would be suitable, e.g., for optimizing injection scheduling (Juliusson, 2012; Liang et al., 2007; Sayarpour et al., 2006).

M-ARX is a very useful and robust method that can be applied easily to large amounts of flow-rate data from liquid-dominated reservoirs. By inspection of the IWCs computed by the M-ARX model one can already gain much insight into the layout of flow paths in the reservoir. A slight drawback to the M-ARX model is that it is based on the assumption that the bottomhole pressure at the producers will remain constant over time. Thus, it is not suited for cases where both injection and production rates are controlled directly. A transmissibility based model that is designed to handle controlled flow-rates at both the injectors and the producers was presented in the Quarterly Report from Spring 2011.

1.3.2 Tracer Models

A myriad of tracer transport models can be found in the literature. Many different models have been developed because a large number of assumptions must be made about the nature of the tracer, the medium through which it flows and the fluid flow pattern. Most of these models are based on some form of the Advection-Dispersion Equation (ADE). One of the main goals of this work was to develop a tracer transport model that could be applied at variable flow rate conditions. This led to the consideration of the ADE with time varying coefficients:

$$\frac{\partial c}{\partial t} + u(t)\frac{\partial c}{\partial x} - D(t)\frac{\partial^2 c}{\partial t^2} + \lambda(t)c = 0 \tag{2.10}$$

where x is distance along the flow path, c is tracer concentration, R is the retardation factor, $u(t)$ is the (interstitial) flow velocity, $D(t)$ is the diffusion coefficient and $\lambda(t)$ is the decay factor. By assuming a linear dispersion model, $D(t) = a\,u(t)$, which is commonly used in hydrological studies (Bear, 1972), the following change of variables can be made:

$$Q(t) = A\phi \int_0^t u(\tau)d\tau \tag{2.11}$$

$$V_x = RA\phi x \tag{2.12}$$

$$V_d = RA\phi a \tag{2.13}$$

$$\lambda_R = \lambda/R \tag{2.14}$$

where A is the cross-sectional area of the flow path perpendicular to the x-direction, and ϕ is the porosity of the flow path. With these variables, the ADE can be rewritten as:

$$\frac{\partial c}{\partial Q} + \frac{\partial c}{\partial V_x} - V_\alpha \frac{\partial^2 c}{\partial V_x^2} + \lambda_R(Q)c = 0 \tag{2.15}$$

This form of the ADE has all coefficients constant other than the decay factor. The solutions to Equation (2.15) for a unit impulse injection are presented in Table 1.1 for the various combinations flux and resident fluid boundary conditions. A similar table and the meaning of the boundary conditions are discussed in more detail in Kreft and Zuber (1978). The solutions are denoted by κ to emphasize that they are specific to a unit impulse injection and depend on the cumulative flow, Q. These solutions are referred to as tracer kernels.

Table 1.1: Tracer kernels for various boundary conditions.

Description	**Initial and boundary conditions**	**Tracer kernel**
Infinite bed, injection and detection in resident fluid	$c_R(V_x, 0) = \delta(V_x)$ $\lim_{V_x \to \pm\infty} c_R(V_x, Q) = 0$	$\kappa_{RR} = \frac{1}{\sqrt{4\pi V_d Q}} e^{-\frac{(V_x - Q)^2}{4V_d Q}} e^{-\int_0^Q \lambda_R(\tilde{Q}) d\tilde{Q}}$
Infinite bed, injection in resident fluid and detection in flux	$c_F(V_x, 0) = \left(1 + \frac{V_d}{V_x}\right)\delta(V_x)$ $\lim_{V_x \to \pm\infty} c_F(V_x, Q) = 0$	$\kappa_{RF} = \frac{V_x + Q}{2\sqrt{4\pi V_d Q^3}} e^{-\frac{(V_x - Q)^2}{4V_d Q}} e^{-\int_0^Q \lambda_R(\tilde{Q}) d\tilde{Q}}$
Semi-infinite bed, injection in flux and detection in resident fluid	$c_R(0, Q) - V_d \frac{\partial c_R(V_x, Q)}{\partial V_x}\Big\|_{V_x \to 0^+} = \delta(Q)$ $c_R(V_x, 0) = 0 \quad for \quad V_x > 0$ $\lim_{V_x \to \infty} c_R(V_x, Q) = 0$	$\kappa_{FR} = \left[\frac{2}{\sqrt{4\pi V_d Q}} e^{-\frac{(V_x - Q)^2}{4V_d Q}} - \frac{1}{2V_d} e^{\frac{V_x}{V_d}} erfc\left(\frac{V_x + Q}{\sqrt{4V_d Q}}\right)\right] e^{-\int_0^Q \lambda_R(\tilde{Q}) d\tilde{Q}}$
Semi-infinite bed, injection and detection in flux	$c_F(0, Q) = \delta(Q)$ $c_F(V_x, 0) = 0 \quad for \quad V_x > 0$ $\lim_{V_x \to \infty} c_F(V_x, Q) = 0$	$\kappa_{FF} = \frac{V_x}{\sqrt{4\pi V_d Q^3}} e^{-\frac{(V_x - Q)^2}{4V_d Q}} e^{-\int_0^Q \lambda_R(\tilde{Q}) d\tilde{Q}}$

The tracer kernels can be used as basis functions to compute the tracer response at variable flow-rate and variable injected tracer concentration conditions. Having an analytical model of this type is useful both for prediction and inference based on data that has been collected at variable flow-rate and concentration conditions. In interwell tracer testing the tracer concentration is usually measured in flux, both at the injection well and production well. Therefore the flux-flux (FF) tracer kernel from Table 1.1 can be used to compute the response in the production well as:

$$c_P(Q(t); c_I, \kappa_{FF}) = \int_0^{Q(t)} c_I\big(Q(t) - \tilde{Q}\big)\kappa_{FF}\big(\tilde{Q}\big)d\tilde{Q} \tag{2.16}$$

where c_I and c_P are the injected and produced tracer concentration, respectively.

The representation given by Equation (2.16) was expanded to multiwell systems by accounting for the mixing of the various injection streams at each producer with the mixing weight:

$$w_{IiPj}(t) = \int_0^t \frac{q_{IiPj}(\tau)}{q_{Pj}(\tau)} \frac{e^{-\frac{t-\tau}{\varsigma}}}{\varsigma} d\tau \tag{2.17}$$

where q_{IiPj} is the IWC-dependent flow-rate shown in Equation (2.9), and ς is a factor that accounts for the mixing time of the two fluids.

With this, the produced concentration in well j can be computed as:

$$c_{Pj}(t) = \sum_{i=1}^{N_I} w_{ij}(t)\, c_{ij}\left(Q_{ij}(t); c_{Ii}, \kappa_{ij}\right) \tag{2.18}$$

where c_{ij} denotes the convolution given by Equation (2.16) and $Q_{ij}(t) = \int_0^t q_{ij}(\tau)d\tau$. To simplify the notation, the subscript $IiPj$ was reduced to ij and the subscript FF for the tracer kernel was left out, but implied.

1.3.3 Tracer Kernel Estimation

In order to apply Equation (2.18), the tracer kernels, κ_{ij}, need to be estimated from tracer return data. Given impulse tracer test data, the tracer kernel can be estimated from:

$$\kappa_{ij}(Q_{ij}) = \frac{c_{ij}^{impulse}(Q_{ij})}{m_{ij}w_{ij}} \tag{2.19}$$

where m_{ij} denotes the tracer from injector i that is recovered in producer j. Ideally, the integral of Equation (2.19) should equal one, but this would not always be the case in practice and therefore the kernel integral is defined as the dimensionless factor that accounts for the difference between the IWC and the fractional tracer returns:

$$f_{ij} = \int_0^\infty \kappa_{ij}(Q)dQ \tag{2.20}$$

A traditional multiwell tracer test will have different types of tracer going into each injection well, so as not to create any confusion about the origins of each tracer. However, there are situations where the same tracer, e.g. a recirculating chemical compound (CO_2, Cl^-), could be going into all of the injection wells at once. In such cases both the injection rates and injected concentrations will often vary and inferring the underlying tracer kernels involves solving a multiple input deconvolution problem, i.e. a highly under-determined inverse problem. Methods for solving this problem with both parametric and nonparametric tracer kernel models were developed as part of this work.

1.3.3.1 Parametric Deconvolution

A parametric model for the multiwell flux-flux (FF) tracer kernel could be defined as:

$$\kappa_{ij}(Q_{ij}) = f_{ij}\sqrt{\frac{Pe_{ij}V_{x,ij}}{4\pi Q_{ij}^3}}\, e^{-\frac{Pe_{ij}\left(V_{x,ij}-Q_{ij}\right)^2}{4V_{x,ij}Q_{ij}}} \tag{2.21}$$

where the three unknown parameters are $V_{x,ij}$, $Pe_{ij} = V_{x,ij}/V_{d,ij}$, and f_{ij}. Note that the correction factor, f, has been added to the definition of the tracer kernel to allow more flexibility in the model. The unknown parameters are grouped into the vector $\boldsymbol{\chi_{ij}} = \left[V_{x,ij}, Pe_{ij}, f_{ij}\right]$, for notational convenience.

Nonlinear regression methods were used find those parameters which provide the best match between the observed data and the model. This was achieved based on the following constrained least-squares problem:

$$\min_{\chi_j} \quad O(\boldsymbol{\chi_j}) = \left(\mathbf{c_{Pj}} - \mathbf{H_j}\,\boldsymbol{\kappa_j}(\boldsymbol{\chi_j})\right)^{\mathrm{T}}\left(\mathbf{c_{Pj}} - \mathbf{H_j}\,\boldsymbol{\kappa_j}(\boldsymbol{\chi_j})\right) \tag{2.22}$$

$$s.t. \quad \boldsymbol{\chi_j} \geq \boldsymbol{lb} \tag{2.23}$$

$$\boldsymbol{\chi_j} \leq \boldsymbol{ub} \tag{2.24}$$

Several of the variables appearing in this problem need further definition. The matrix $\boldsymbol{H_j}$ represents an approximation of the sum and integration of the kernels in Equation (2.18), i.e.:

$$\boldsymbol{c_{Pj}}(\boldsymbol{t}) \approx \boldsymbol{H_j}\boldsymbol{\kappa_j}(\boldsymbol{\chi_j}) \tag{2.25}$$

where:

$$\boldsymbol{\kappa_j}(\boldsymbol{\chi_j}) = \begin{bmatrix} \boldsymbol{\kappa_{1j}}(\boldsymbol{\chi_{1j}}) \\ \vdots \\ \boldsymbol{\kappa_{N_1 j}}(\boldsymbol{\chi_{N_1 j}}) \end{bmatrix} \tag{2.26}$$

and each vector $\boldsymbol{\kappa_{ij}}(\boldsymbol{\chi_{ij}})$ represents a vector of kernel values at each point chosen for the discretization of the kernel. Similarly, the matrix $\boldsymbol{H_j}$ is a matrix of matrices, i.e.:

$$\mathbf{H_j} = \left[\mathbf{H_{1j}} \cdots \mathbf{H_{N_1 j}}\right] \tag{2.27}$$

Each submatrix, $\boldsymbol{H_{ij}}$, represents the convolution integral which computes the response at each of the measurement times defined in $\boldsymbol{t}$. If there are n time measurements m discretization points for each kernel, then the size of H_{ij} is $n \times m$. The structure of $\boldsymbol{H_{ij}}$ depends on which discretization rule is used for the integration. A detailed description of the structure of $\boldsymbol{H_{ij}}$ for a trapezoidal discretization rule is given in Juliusson (2012).

The nonlinear least-squares problem (2.22) can be solved more efficiently by supplying the analytical formulation for the gradient and the Hessian matrix to the numerical solver. Therefore, the gradient was derived and computed as:

$$\frac{\partial O(\boldsymbol{\chi_j})}{\partial \boldsymbol{\chi_j}} = \begin{bmatrix} \left(\boldsymbol{H_{1j}} \frac{\partial \kappa_{1j}}{\partial \chi_{1j,1}}\right)^T \\ \left(\boldsymbol{H_{1j}} \frac{\partial \kappa_{1j}}{\partial \chi_{1j,2}}\right)^T \\ \vdots \\ \left(\boldsymbol{H_{N_I j}} \frac{\partial \kappa_{N_I j}}{\partial \chi_{N_I j,3}}\right)^T \end{bmatrix} \left(\mathbf{c_{Pj}} - \mathbf{H_j}\, \boldsymbol{\kappa_j}(\boldsymbol{\chi_j})\right) = \boldsymbol{J_j^T \Delta r_j} \tag{2.28}$$

The Hessian was approximated using only the first derivative terms. Thus, it could be computed from the Jacobian as:

$$\frac{\partial^2 O(\boldsymbol{\chi_j})}{\partial \boldsymbol{\chi_j^2}} = \boldsymbol{J_j^2 J_j} \tag{2.29}$$

The full structure of the Hessian, i.e. with the second derivative terms included, is given in the Quarterly Report from Spring 2010. However, the second derivative terms are often left out (Gauss-Newton method), and that proved computationally efficient in this case.

The analytical equations for the derivatives of the kernel functions with respect to V_x, Pe and f, were computed automatically using the Symbolic Toolbox in MATLAB, and will not be recounted here. The MATLAB function fmincon was then used to solve problem (2.22), using the trust-region-reflective algorithm. The objective function had a number of local minima and therefore it was often necessary to try a few different initial guesses to achieve convergence to the "true" solution. A Genetic Algorithm was applied to provide a structured approach to finding a good initial guess for $\boldsymbol{\chi_j}$.

In practice, tracer breakthrough usually occurs only in some of the production wells. Solving the multiwell tracer deconvolution problem when this is the case becomes a bit more challenging because in the model it is assumed that all injectors influence each producer. But by looking at the sensitivity of the production data to the injection data it was often possible to find out which kernels were reproduced with strong dependence on the data and which ones were highly susceptible to random noise. Obtaining this information was valuable because it provided further understanding of which injector-producer pairs had a significant connection. Rigorous methods to test hypotheses of whether or not a parameter is significant are well known for unconstrained linear regression models. Problem (2.22), however, is nonlinear and constrained. Therefore a heuristic method was devised to determine which kernel estimates were the most significant,

although the method was based on principles similar to those used in hypothesis testing with linear regression models.

The test statistic used to determine the influence of each kernel was based on parameter uncertainties. These were based on the values of the Hessian matrix at the final solution. The covariance matrix for the kernel parameters, $\boldsymbol{\chi_j}$ was computed as:

$$\hat{\boldsymbol{\Sigma}}_{\mathbf{j}}^{\mathbf{2}} = \hat{\sigma}_{\mathrm{r_j}}^2 \left(\hat{\mathbf{J}}_{\mathbf{j}}^{\mathbf{T}} \hat{\mathbf{J}}_{\mathbf{j}}\right)^{-1} \tag{2.30}$$

where $\hat{\sigma}_r^2$ denotes the sample variance of the residuals:

$$\hat{\sigma}_{\mathrm{r_j}}^2 = \left(\mathbf{c_{Pj}} - \hat{\mathbf{c}}_{\mathbf{Pj}}\right)^{\mathrm{T}} \left(\mathbf{c_{Pj}} - \hat{\mathbf{c}}_{\mathbf{Pj}}\right) / (\mathrm{n} - 3\mathrm{N_I}) \tag{2.31}$$

and the $\widehat{\ }$ denotes the best estimate.

To test the influence of each kernel on the output it was logical to focus on the multipliers f_{ij}, as they represented a linear scaling of the kernel function. If the influence of a kernel was small, or zero, solutions with small f_{ij} would be favored. Moreover, if there was a poor connection between injector i and producer j, the uncertainty in the corresponding kernel parameters would should be large, because there were few data to constrain that kernel estimate. Finally the IWCs are good indicators of the influence of a particular injector-producer connection. Thus, the following test statistic was computed:

$$\mathrm{S0_{ij}} = \frac{\mathrm{F_{ij} f_{ij}} / \hat{\sigma}_{\mathrm{f_{ij}}}}{\sum_{\mathrm{k=1}}^{\mathrm{N_I}} \mathrm{F_{kj} f_{kj}} / \hat{\sigma}_{\mathrm{f_{kj}}}} \tag{2.32}$$

where $\hat{\sigma}_{f_{ij}}^2$ denotes the variance of f_{ij}. The measure $S0$ ranges between 0 and 1, and those values were used to determine which kernels to include, for example by applying some threshold value or by including a certain number of the most influential connections for each producer.

Example applications of parametric kernel estimation are given in Sections 1.4 and 1.5. The parameter constraints that were used for those examples were $1{,}000 < V_x < 1{,}000{,}000$ [m^3], $1 < Pe < 100$ and $0.5 < f < 2$.

1.3.3.2 Nonparametric Deconvolution

Nonparametric models are preferable to parametric when there is considerable uncertainty in the formulation of the parametric function. The nonparametric kernel function is a set of points which represent the value of the kernel at discrete points of cumulative flow. The tracer kernel is then defined by some interpolation between these points.

In the same way as for the parametric problem, the model relating the input and output concentrations is given by Equation (2.18). For the nonparametric model, this equation was approximated with the trapezoidal discretization rule:

$$\int_0^{Q(t)} c_{Ii}(Q(t)-\tilde{Q})\kappa(\tilde{Q})d\tilde{Q} = \frac{1}{2}\sum_{k=1}^{K}\left[c_{Ii}(Q(t)-\tilde{Q}_{k+1})\kappa(\tilde{Q}_{k+1}) + c_{Ii}(Q(t)-\tilde{Q}_k)\kappa(\tilde{Q}_k)\right](\tilde{Q}_{k+1}-\tilde{Q}_k) + \frac{c_{Ii}(0)\kappa(Q(t)) + c_{Ii}(Q(t)-\tilde{Q}_K)\kappa(\tilde{Q}_K)}{2}(Q(t)-\tilde{Q}_K) \quad (2.33)$$

where K is the number of the largest discretization element which is smaller than $Q(t)$.

Special attention has to be given to $\kappa(Q(t))$ in the last term in Equation (2.33). When $Q(t) \leq \tilde{Q}_m$ the following interpolation was used for the last term:

$$\kappa(\mathrm{Q(t)}) = \kappa(\widetilde{\mathrm{Q}}_{\mathrm{K}})\frac{\widetilde{\mathrm{Q}}_{\mathrm{K+1}} - \mathrm{Q(t)}}{\widetilde{\mathrm{Q}}_{\mathrm{K+1}} - \widetilde{\mathrm{Q}}_{\mathrm{K}}} + \kappa(\widetilde{\mathrm{Q}}_{\mathrm{K+1}})\frac{\mathrm{Q(t)} - \widetilde{\mathrm{Q}}_{\mathrm{K}}}{\widetilde{\mathrm{Q}}_{\mathrm{K+1}} - \widetilde{\mathrm{Q}}_{\mathrm{K}}} \quad (2.34)$$

but for $Q(t) > \tilde{Q}_m$ it was assumed that $\kappa(Q(t)) = 0$.

Each submatrix $\boldsymbol{H_{ij}}$ was based on this discretization rule which lead to the produced tracer concentration which was computed similarly as in Equation (2.25):

$$\mathbf{c_{Pj}(t)} \approx \mathbf{H_j \kappa_j} \quad (2.35)$$

Note that here the vector $\boldsymbol{\kappa_j}$ represents the combination of the nonparametric kernels:

$$\boldsymbol{\kappa_j} = \begin{bmatrix} \boldsymbol{\kappa_{1j}} \\ \vdots \\ \boldsymbol{\kappa_{N_1 j}} \end{bmatrix} \quad (2.36)$$

and each nonparametric kernel is represented by the m discretization points as:

$$\kappa_{\mathrm{ij}} = \begin{bmatrix} \kappa_{\mathrm{ij}}(\mathrm{Q_{ij,1}}) & \cdots & \kappa_{\mathrm{ij}}(\mathrm{Q_{ij,m}}) \end{bmatrix}^{\mathrm{T}} \quad (2.37)$$

The matrix $\boldsymbol{H_j}$ is given by Equation (2.27).

Estimates of nonparametric curves are somewhat susceptible to noise and therefore a regularization term is usually added to nonparametric estimation problems, to enforce a degree of

smoothness on the kernel estimates. This has been done in the following regularized linear least-squares problem which was formulated to determine the value of $\boldsymbol{\kappa_j}$:

$$\min_{\boldsymbol{\kappa_j}} O(\boldsymbol{\kappa_j}) \tag{2.38}$$

$$s.t. \quad \boldsymbol{\kappa_j} \geq \mathbf{0} \tag{2.39}$$

where:

$$Q(\boldsymbol{\kappa_j}) = \frac{1}{2}(\boldsymbol{c_{Pj}} - \boldsymbol{H_j}\boldsymbol{\kappa_j})^T(\boldsymbol{c_{Pj}} - \boldsymbol{H_j}\boldsymbol{\kappa_j}) + \frac{1}{2}(\boldsymbol{\kappa_j} - \boldsymbol{\kappa_{j,prior}})^T(\boldsymbol{\kappa_j} - \boldsymbol{\kappa_{j,prior}}). \tag{2.40}$$

The regularization (or roughness penalty) matrix is a block diagonal matrix:

$$\boldsymbol{R_j} = \begin{bmatrix} \boldsymbol{R_{1j}} & 0 & \cdots & 0 \\ 0 & \boldsymbol{R_{2j}} & \cdots & 0 \\ \vdots & \vdots & \ddots & \vdots \\ 0 & 0 & \cdots & \boldsymbol{R_{N_1 j}} \end{bmatrix} \tag{2.41}$$

and a general formulation that was used for element (p, q) of the block matrices is as follows:

$$\mathrm{R}_{\mathrm{ij}}^{\mathrm{pq,d}} = \theta_{ij} \sum_{k=1}^{m-d} (-1)^{q-k} \binom{d}{q-k} (-1)^{p-k} \binom{d}{p-k} \tag{2.42}$$

where:

$$\binom{i}{j} = 0 \quad if \;\; j < 0 \;\; or \;\; j > i \tag{2.43}$$

The regularization term adds a penalty to the objective function if the kernel estimate deviates from the prior. It does this by adding or subtracting the deviations from one discretization point to the next with a given rule. The span of this smoothing scheme depends on the parameter d. For example, with $d = 2$, the regularization term becomes:

$$\frac{1}{2}(\boldsymbol{\kappa} - \boldsymbol{\kappa_{prior}})^T \boldsymbol{R}(\boldsymbol{\kappa} - \boldsymbol{\kappa_{prior}}) = \frac{\theta}{2} \sum_{k=2}^{m-1} [(\kappa_{k-1} - \kappa_{k-1,prior}) - 2(\kappa_k - \kappa_{k,prior}) + (\kappa_{k+1} - \kappa_{k+1,prior})] \tag{2.44}$$

The regularization weight θ_{ij} usually had to be tuned manually to find an acceptable balance between reproduction of the data and reproduction of the prior kernel estimates. For the examples given in this paper, the parametric kernel estimates were used as priors and the regularization weights ranged between 10^9 and 10^{11}.

The gradient and Hessian for the objective function were used to help the optimization algorithm. The gradient for problem (2.38) is:

$$\frac{\partial O(\boldsymbol{\kappa_j})}{\partial \boldsymbol{\kappa_j}} = -\boldsymbol{H_j^T}\left(\boldsymbol{c_{Pj}} - \boldsymbol{H_j}\boldsymbol{\kappa_j}\right) + \boldsymbol{R_j}\left(\boldsymbol{\kappa_j} - \boldsymbol{\kappa_{j,prior}}\right) \tag{2.45}$$

and the Hessian is:

$$\frac{\partial^2 O(\boldsymbol{\kappa_j})}{\partial \boldsymbol{\kappa_j^2}} = -\boldsymbol{H_j^T}\boldsymbol{H_j} + \boldsymbol{R_j} \tag{2.46}$$

A practical approach was needed for determining the discretization interval for the nonparametric kernels. In an effort to divide the kernels into parts that would contribute evenly to the production signal, a discretization scheme was devised based on the reasoning that follows. The integral of the parametric kernel should equal f. With a trapezoidal integration scheme, with m points, the kernel could be divided into $m-1$ sections, each with area $f/(m-1)$. Therefore a practical set of discretization points could be found by solving (starting from $Q_1 = 0$):

$$\frac{\kappa(\mathrm{Q_{k+1}}) + \kappa(\mathrm{Q_k})}{2}(\mathrm{Q_{k+1}} - \mathrm{Q_k}) = \frac{\mathrm{f}}{\mathrm{m}-1} \tag{2.47}$$

for Q_{k+1}. The solution was found using the MATLAB routine fminbnd which is based on a golden section search and parabolic interpolation. To ensure that $Q_{k+1} > Q_k$, Q_k was used as a lower bound on each search. The upper bound was given by $Q_k + V_x$. Theoretically, the last value in the discretization should tend to infinity. However, as a result of the upper bound estimate required for the initial guess, the last point would have some limited value. An example discretization based on this method is shown in Figure 1.2.

Confidence intervals for the nonparametric kernels were estimated with the parametric bootstrap method. A parametric bootstrap is a simple way of inferring the noise in a set of data from a model fitted to that same set of data. The distribution of errors is estimated by collecting the residuals in a vector:

$$\mathbf{r_j} = \mathbf{c_{Pj}} - \hat{\mathbf{c}}_{\mathbf{Pj}} \tag{2.48}$$

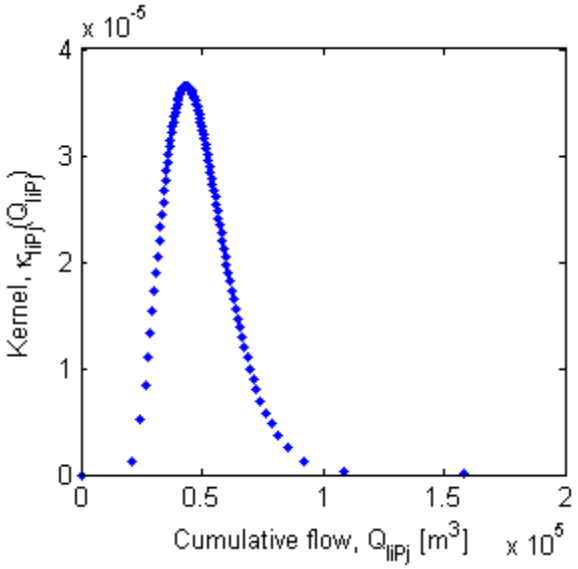

Figure 1.2: Example of a kernel discretization with 100 points found using the equal area rule given by Equation (2.47).

Then a new tracer production signal, $\boldsymbol{c_{Pj}^{sim}}$, could be created by drawing n samples, randomly with replacement, from the residual, $\boldsymbol{r_j}$, and adding them to the modeled response, $\boldsymbol{\hat{c}_{Pj}}$. This was done a large number of times (say 1000 times) and a new fit was found for each new set of simulated production data. The resulting fits were used to infer the median value of the kernel estimates and 95% confindence bounds.

1.3.4 Example I

In this section an example application of the tracer kernel model will be presented with data generated from a relatively simple discrete fracture model, referred to as Reservoir Model I. The main purpose with this example is to illustrate the tracer kernel inference procedure with a simple conceptual model. Synthetic data was generated for this case where both the flow-rates and injected concentrations varied simultaneously.

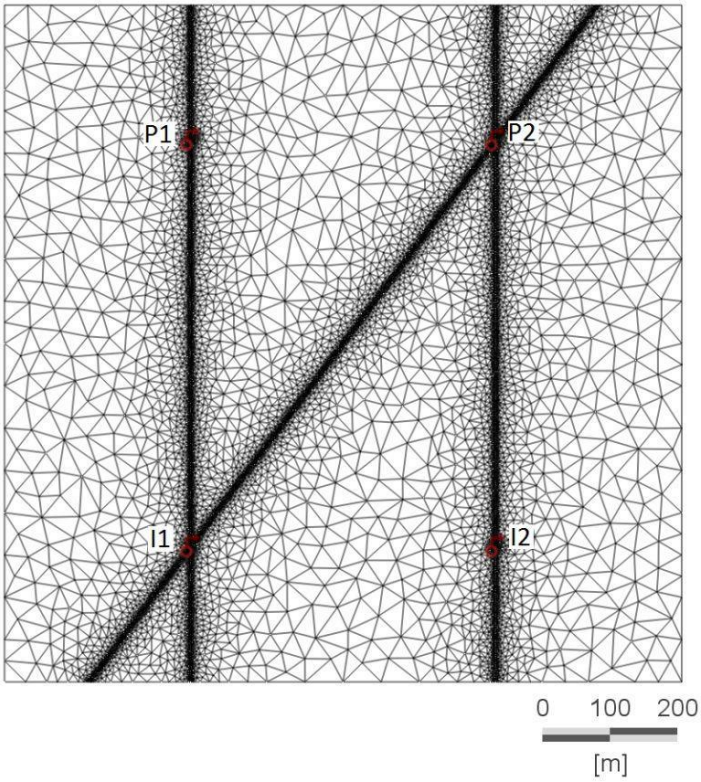

Figure 1.3: Computational grid for Reservoir Model I.

Reservoir Model I, shown in Figure 1.3, was built using the FEFLOW groundwater simulation software FEFLOW (DHI-WASY, 2010) and the computational gridding software Triangle (Shewchuk, 1996). The main properties of the model are summarized in Table 1.2.

Table 1.2: Properties for Reservoir Model I.

General	
Dimensions	1000x1000x500 m^3
Longitudinal dispersivity	50 m
Transverse dispersivity	5 m
Rock heat capacity	2520 $kJ/m^3/C$
Rock heat conductivity	3 J/m/s/C
Fractures	
Number of fractures	3
Discrete fractures	Yes
Porosity	0.05
Hydraulic conductivity	0.01 m/s
Total compressibility	10^{-10} 1/Pa
Matrix	
Porosity	0.001
Hydraulic conductivity	2×10^{-9} m/s
Total compressibility	10^{-11} 1/Pa

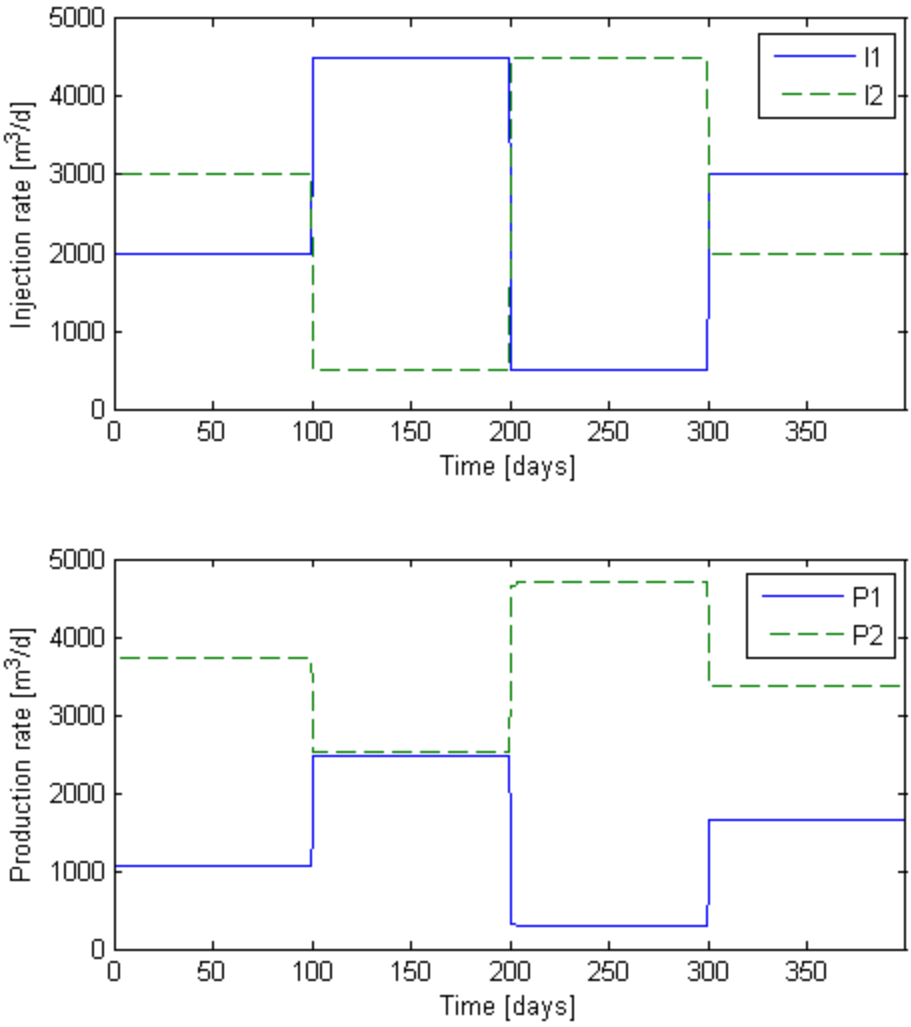

Figure 1.4: Flow-rate history for example I.

The injection- and production-rate data generated with Model I are shown in Figure 1.4 and the tracer concentration data are shown in Figure 1.5. These data were used to infer the IWCs and the tracer kernels.

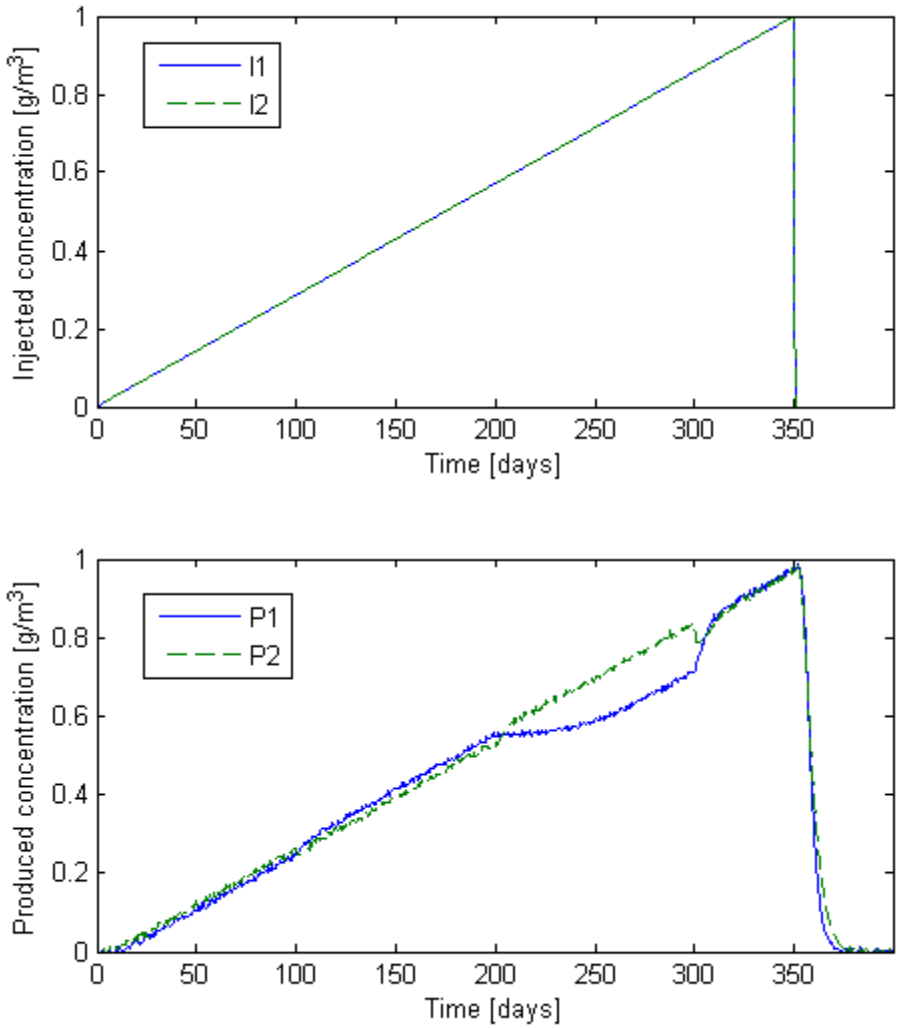

Figure 1.5: Concentration history for example I.

The IWCs were obtained by applying the M-ARX method to the flow-rate data. The resulting IWC parameters are listed in Table 1.3. The tracer kernels were first estimated with a parametric inversion approach, and then a nonparametric approach.

Table 1.3: Interwell connectivity for Reservoir Model I.

F	*P1*	*P2*
I1	0.5477	0.4486
I2	0.0024	0.9871

1.3.4.1 Parametric Kernel Estimate

A parametric kernel estimate was carried out with the data obtained during the first 350 days of production. The solution yielded the fit shown in Figure 1.6. The time factor for the mixing weight (ς in Equation (2.17)) was tuned a bit manually to improve the agreement between the model and the data. Figure 1.6 also shows how the kernel estimates could be used to predict the tracer concentration over the last 50 days.

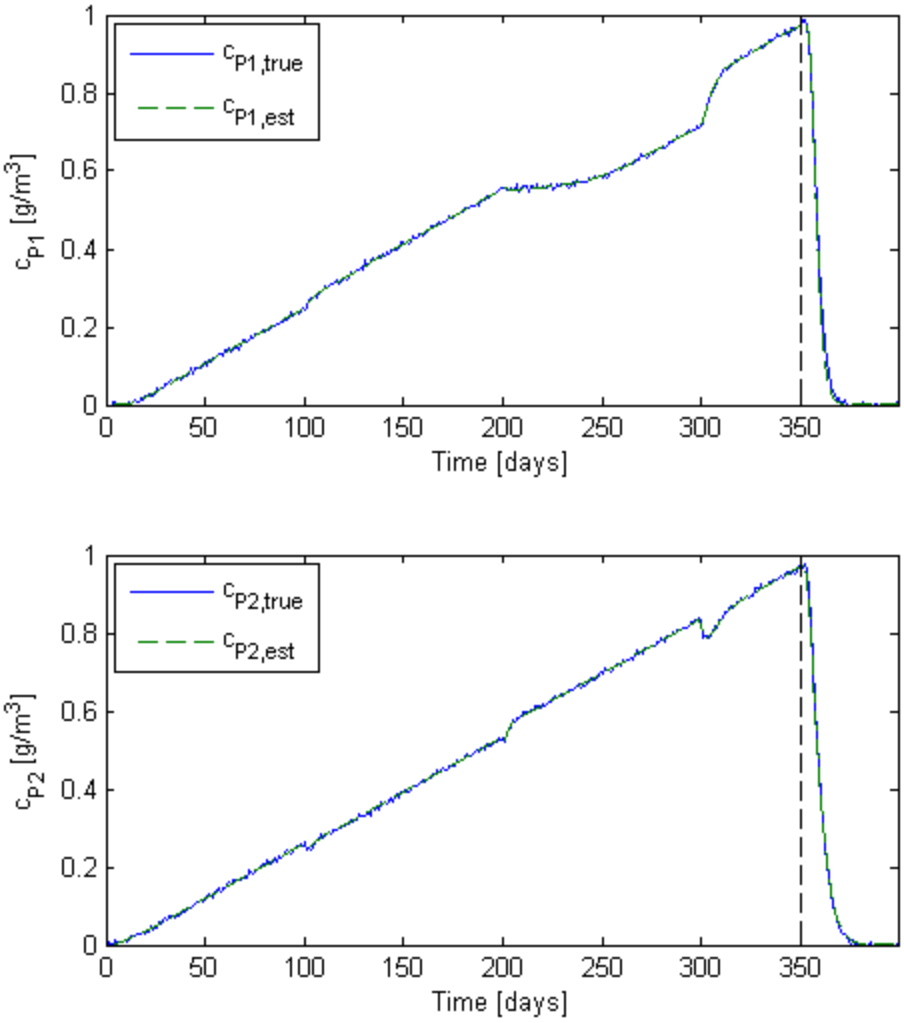

Figure 1.6: Reproduction of the tracer data with parametric kernels for example I. The true data are shown as blue solid lines and the reproduced data are given by green dashed lines. The vertical black dashed line divides the estimation and prediction periods.

The tracer kernel estimates were compared to kernels computed from simulations of impulse injection tracer returns (Equation (2.19)). The comparison is shown in Figure 1.7. The kernel estimate for the three fracture dominated connections were all quite good, but not perfect. One

reason for this was that the transient in the concentration data series was generated by a nonlinear source (i.e. the flow rate). This made the problem harder to solve than it would have been if only the tracer concentration had been varied. In addition to that, the details of the tracer kernel might have varied a bit with the flow configuration. In other words, the "true" kernel may not have been completely representative for all flow configurations. Finally, the inverse of the multiple input tracer kernel model is an under-determined problem, which means that multiple solutions are possible. The space of feasible solutions was certainly restricted by using a parametric model for the kernels and mixing weights, but there seems to have been some room for variation, as is indicated by the exceptionally good fit seen in Figure 1.6.

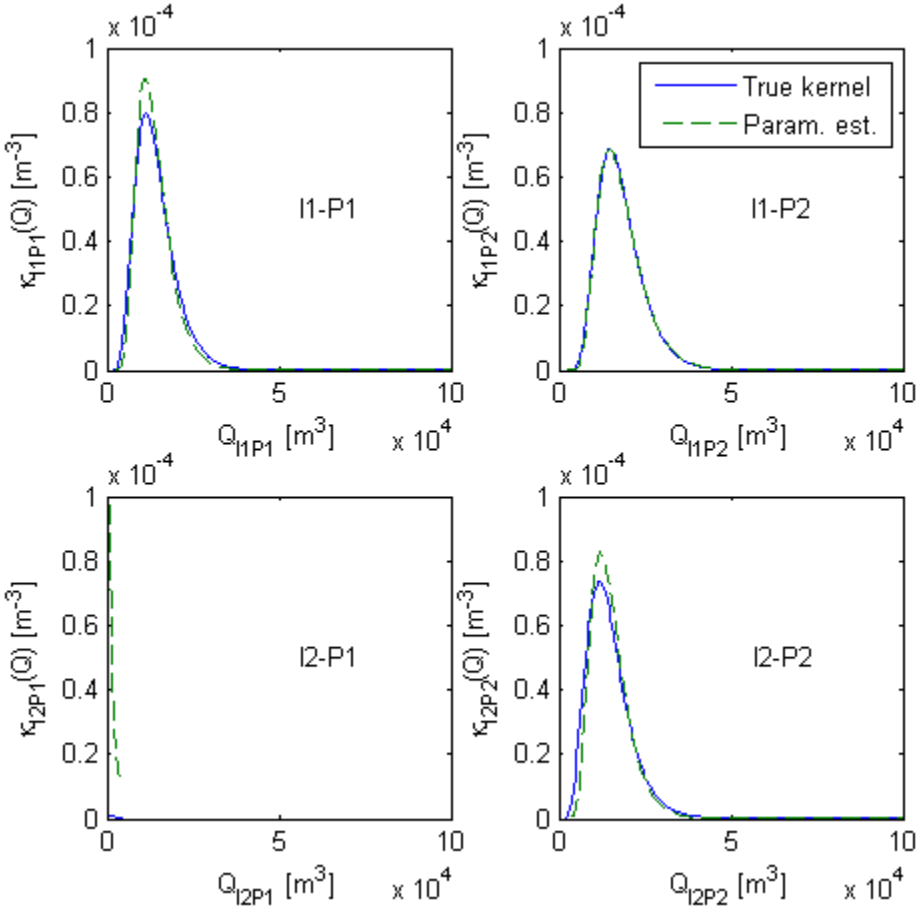

Figure 1.7: Parametric kernel estimates for example I. The "true" kernels, obtained from a constant injection rate (2500 m^3/day) case, are plotted with blue solid lines. Parametric estimates are given by green dashed lines.

The parametric estimates for the tracer kernels are given in Table 1.4. Note that κ_{I2P1} was given the smallest allowable pore volume, V_x, and a large correction factor f. This assignment was somewhat random because the tracer from I2 never broke through in P1. In other words, because this kernel did not impact the signal in P1 in any significant manner, its estimate was more-or-less arbitrary.

Table 1.4: Kernel parameter estimates for example I.

V_x	*P1*	*P2*
I1	14,425	17,598
I2	1,000	14,986
Pe		
I1	22.91	16.75
I2	1.00	19.99
f		
I1	1.001	0.997
I2	1.351	0.999

The test statistic $S0$ indicated that all wells were connected other than I2 and P1 (Table 1.5), given a threshold value of 0.01. This was to be expected as there was no fracture connecting wells I2 and P1.

Table 1.5: Test statistic to determine the influence of each kernel for example I.

$S0$	*P1*	*P2*
I1	0.9974	0.3350
I2	0.0026	0.6650

1.3.4.2 Nonparametric Kernel Estimate

Nonparametric kernel estimates were also obtained for the data shown in Figure 1.4 and Figure 1.5. The statistically valid parametric kernels shown in Figure 1.7 were used as priors and the θ's were tuned to find an acceptable balance between matching the priors and the data.

The time scale for the mixing weights, ς in Equation (2.17), was also tuned manually to improve the fit. Otherwise the problem was solved by a straight forward application of the nonparametric estimation method outlined in Section 1.3.3.2. The resulting data fit is shown in Figure 1.8, where data from the first 350 days were used to calibrate the kernels, and the rest of the data were predicted based on the kernel estimates.

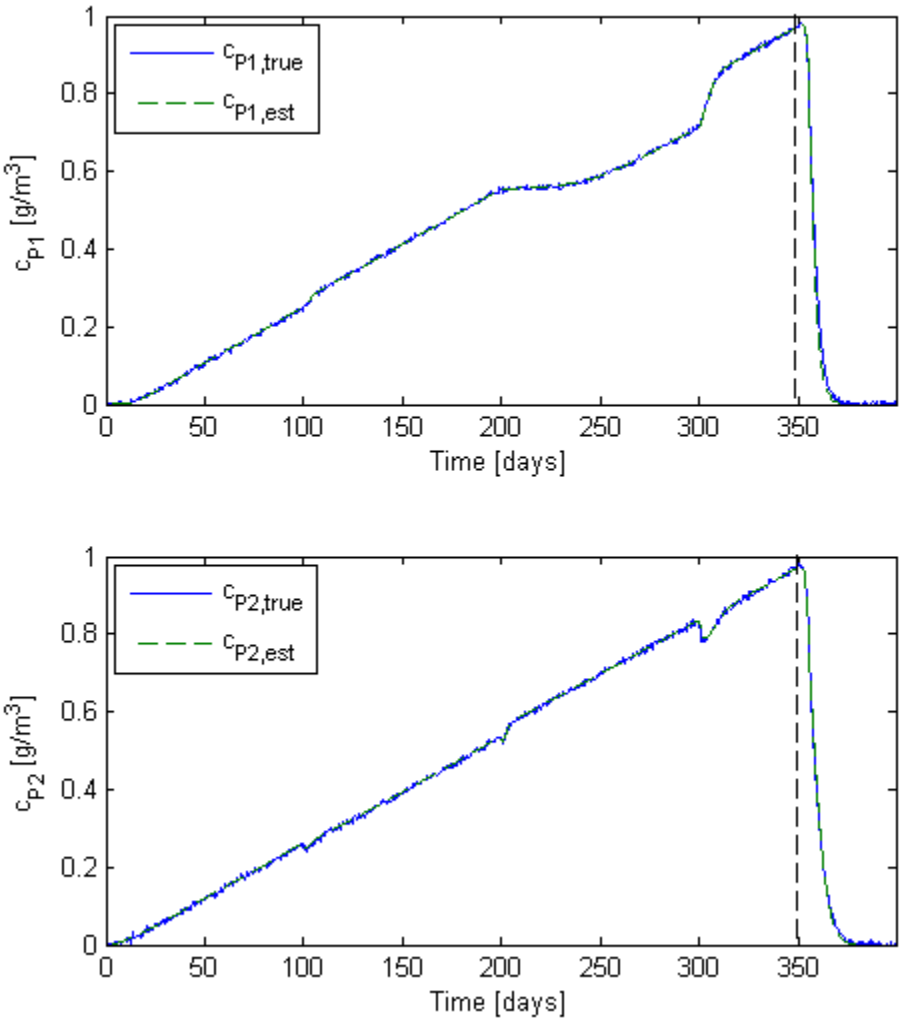

Figure 1.8: Reproduction of the tracer data with nonparametric kernels for example I. The true data are shown as blue solid lines and the reproduced data are given by green dashed lines. The vertical black dashed line divides the estimation and prediction periods.

The estimated kernels with uncertainty bounds obtained from bootstrapping are illustrated in Figure 1.9. The estimated kernel for the I1P1 connection turned out to be a bit less dispersive than the actual kernel. The reason for this was probably that the time scale for the mixing weights was tuned to a relatively large value to improve the fit. The large time scale acted as a smoother on the response, thus incentivizing a slightly less dispersive kernel estimate. Another way to fix this was to reduce the interwell connectivity parameter for I1P2 to a very small number, i.e. 10^{-4} or less. In either case the best estimate for κ_{I1P1}, would not be perfect, most likely because the tracer kernel model did not describe the given scenario perfectly.

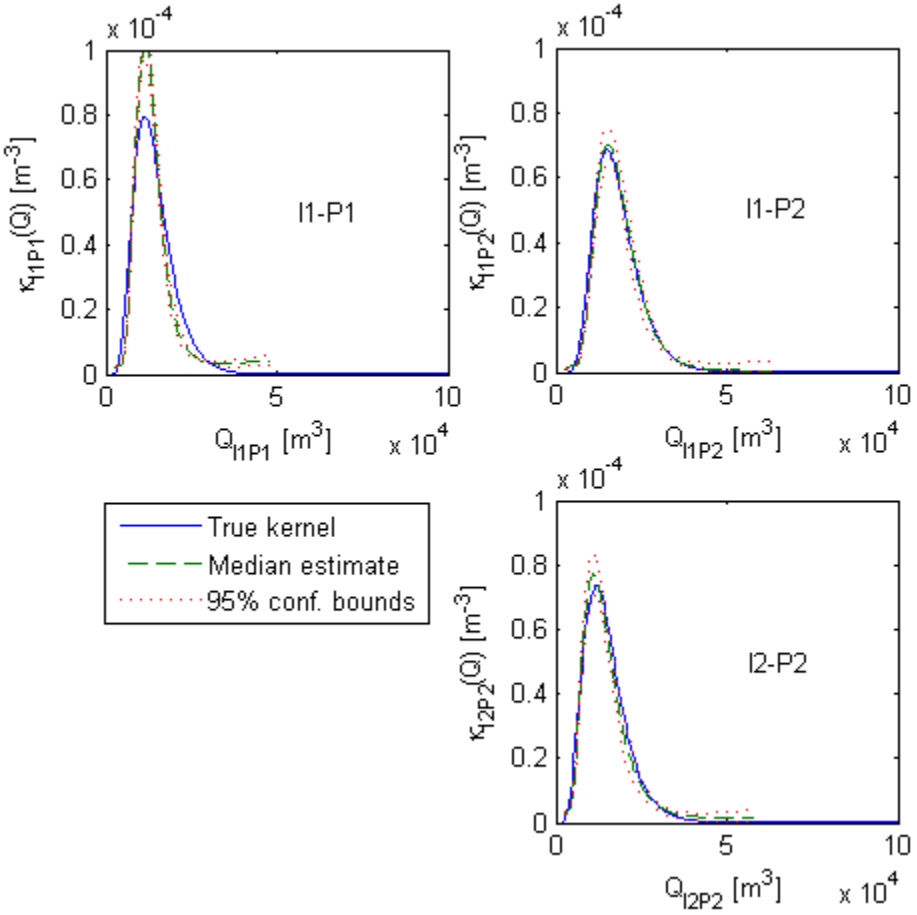

Figure 1.9: Nonparametric kernel estimates and 95% confidence bounds obtained from parametric bootstrapping for those kernels deemed significant for example I.

Estimates of pore volume and correction factor based on the nonparametric kernels are given in Table 1.6.

Table 1.6: Pore volume and correction factor computed from nonparametric kernels for example I.

V_x	*P1*	*P2*
I1	13,492	17,238
I2		14,505
f		
I1	0.996	0.996
I2		0.998

1.3.5 Example II

The reservoir model used for the second example was based partially on the structure of the fractured Soultz-sous-Forets enhanced geothermal system in France. A three-dimensional map of the main fractures was obtained from Place et al. (2011). The fractures were imported into the

discrete fracture generation software FRACMAN. Additional fractures were generated based on data from Massart et al. (2010), and then a two-dimensional slice, 3000x1000 m^2, of fracture traces was extracted from a region of interest. The computational grid for the two-dimensional slice is shown in Figure 1.10 and the main properties of the FEFLOW reservoir model are given in Table 1.7.

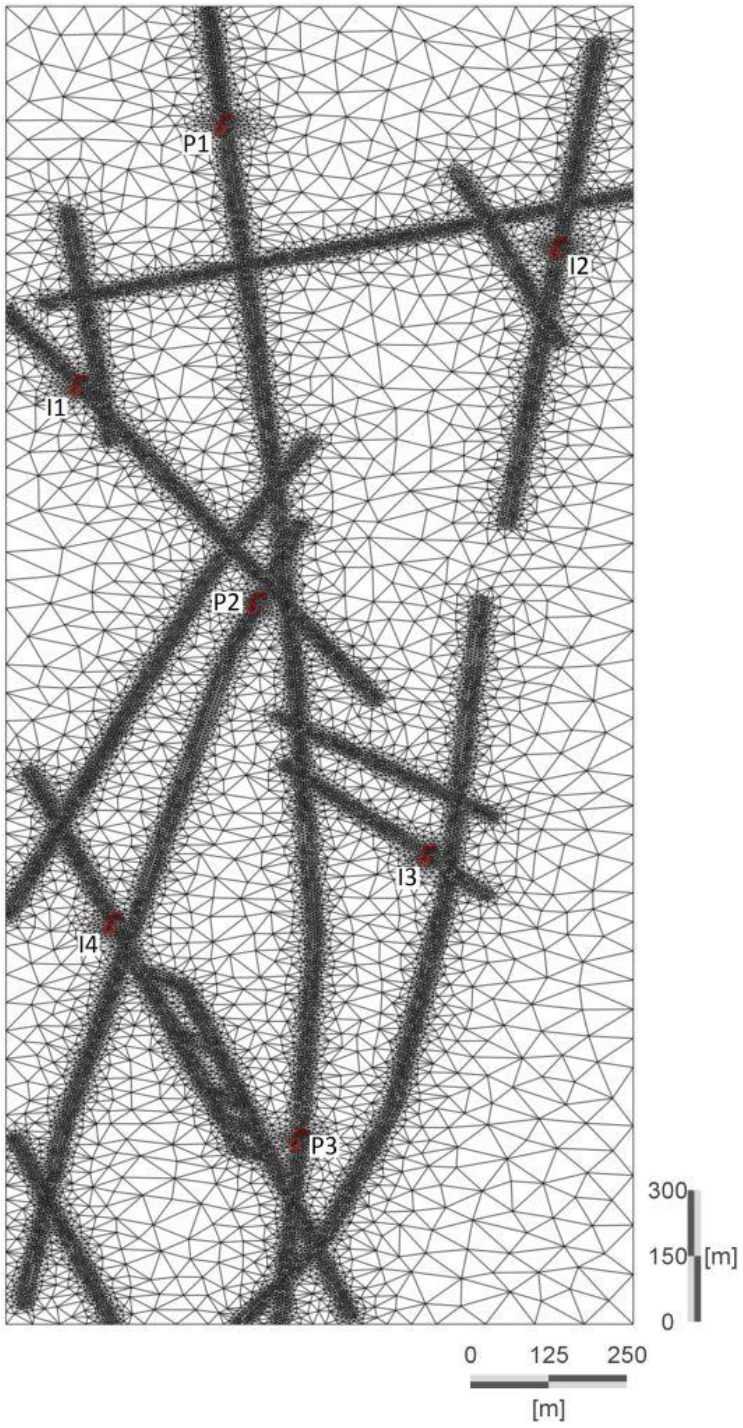

Figure 1.10: Computational grid for Reservoir Model II.

Table 1.7: Summary of properties for Reservoir Model II.

General	
Dimensions	3000x1000x500 m^3
Longitudinal dispersivity	50 m
Transverse dispersivity	5 m
Rock heat capacity	2520 $kJ/m^3/C$
Rock heat conductivity	3 J/m/s/C
Fractures	
Number of fractures	19
Discrete fractures	Yes
Porosity	0.03
Hydraulic conductivity	$\propto L^{1.87}$ m/s
Total compressibility	10^{-10} 1/Pa
Matrix	
Porosity	0.001
Hydraulic conductivity	10^{-10} m/s
Total compressibility	10^{-11} 1/Pa

In this example it was assumed that the flow-rate data to determine the IWCs were collected first and then the injection rates were held constant (at 3000 m^3/day for each well) for a period while the injected concentration was varied. The variable flow-rate data that were used to infer the IWCs are shown in Figure 1.11 and the IWC estimates are given in Table 1.8. The injected and produced concentration histories that were obtained are shown in Figure 1.12.

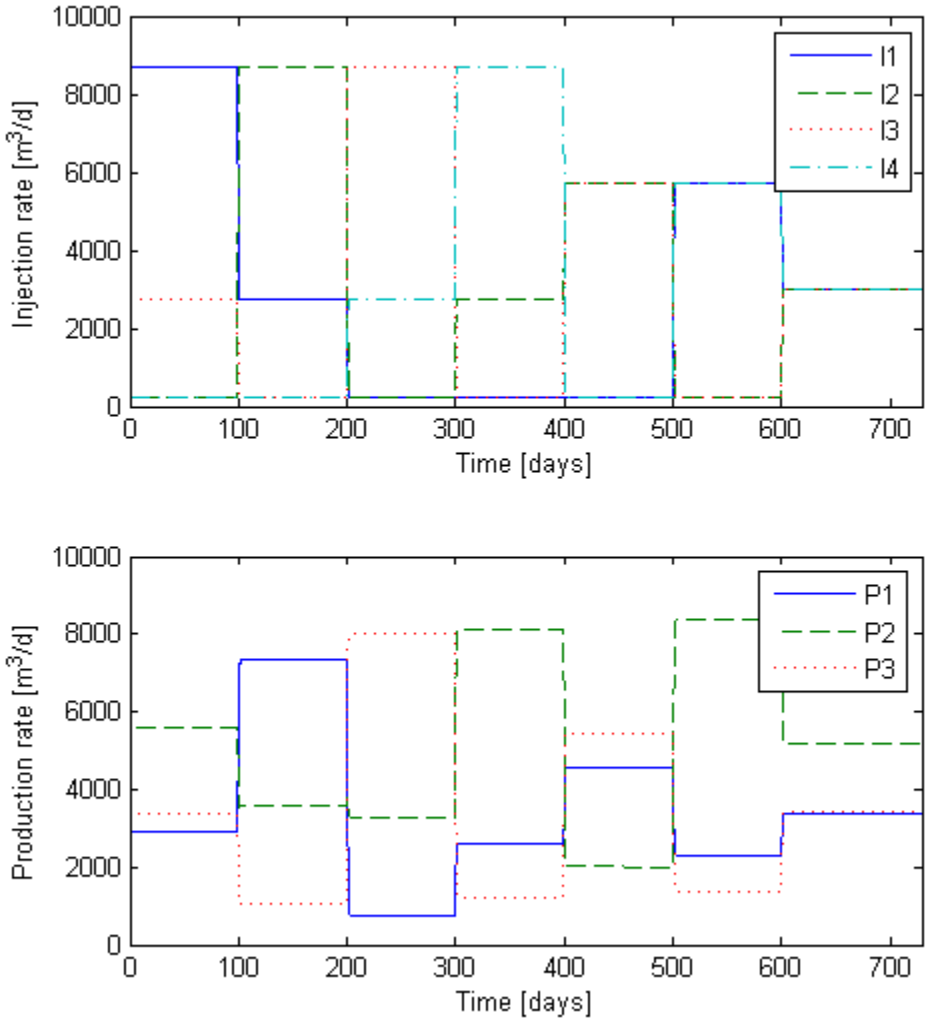

Figure 1.11: Flow-rate history for example II.

Table 1.8: Interwell connectivity for Reservoir Model II.

F	*P1*	*P2*	*P3*
I1	0.3015	0.5846	0.1060
I2	0.7362	0.1967	0.0606
I3	0.0358	0.0900	0.8764
I4	0.0583	0.8497	0.0939

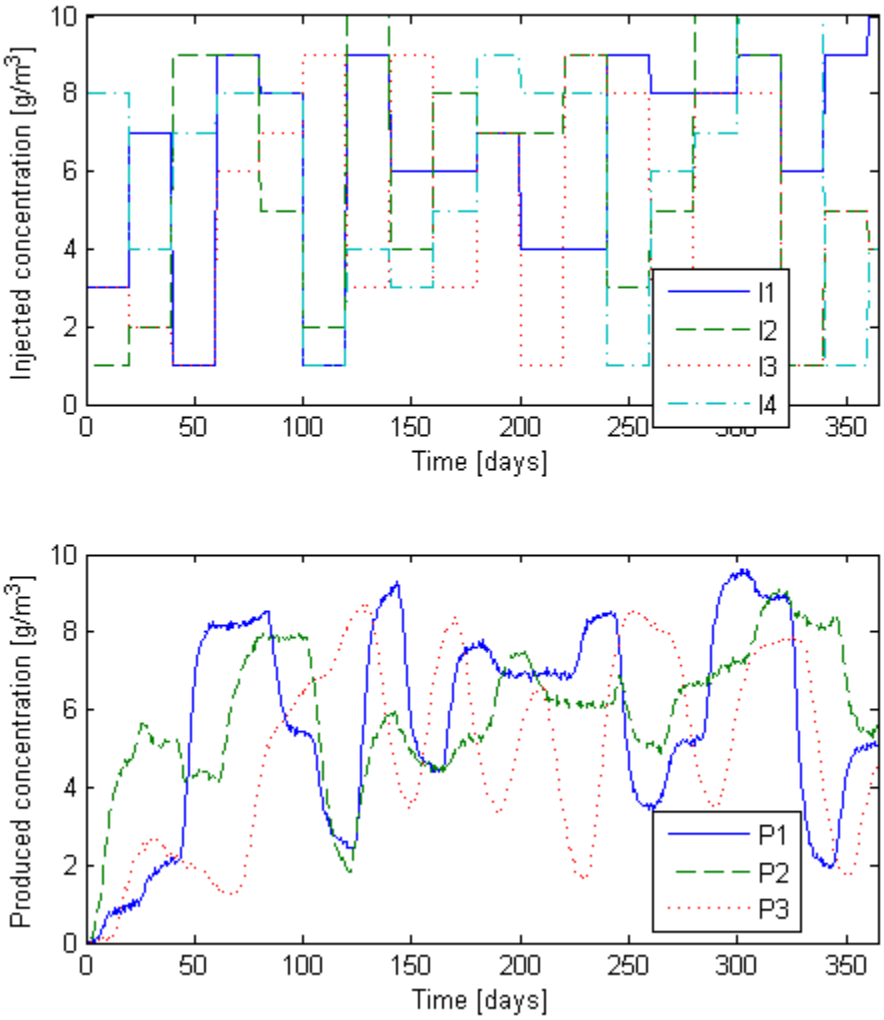

Figure 1.12: Concentration history for example II.

1.3.5.1 Parametric Kernel Estimation

The parametric kernel estimation algorithm usually yielded a result for example II within about half an hour (running on a PC Desktop with 8 GB of RAM and an Intel Core i7 processor), depending on the progress of the genetic algorithm. The fitted data is compared to the actual data set for each producer in Figure 1.13.

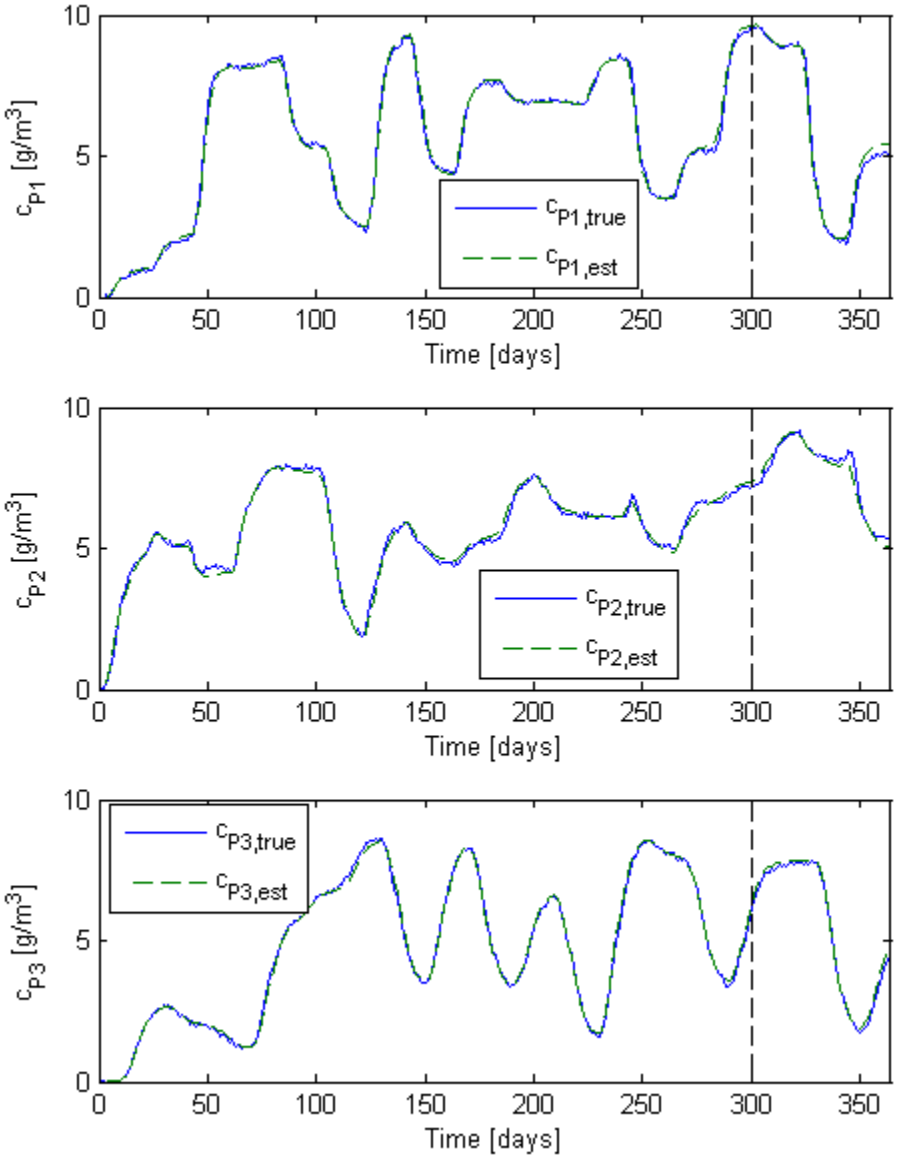

Figure 1.13: Reproduction of the tracer data with parametric kernels for example II. The true data are shown as blue solid lines and the reproduced data are given by green dashed lines. The vertical black dashed line divides the estimation and prediction periods.

The best estimate that the algorithm yielded for each of the 12 kernels is shown in Figure 1.14, along with the "true" kernels which were obtained by simulating a unit step injection test with the same numerical reservoir model. The parameter estimates are given in Table 1.9.

Table 1.9: Kernel parameter estimates for example II.

V_x	*P1*	*P2*	*P3*
I1	32,330	15,759	29,737
I2	18,748	26,487	47,999
I3	79,027	35,261	49,699
I4	22,112	29,847	19,343
Pe			
I1	4.09	2.40	1.00
I2	12.42	1.00	1.00
I3	100.00	1.00	25.52
I4	1.00	6.36	18.35
f			
I1	0.500	1.273	0.500
I2	1.306	0.500	0.500
I3	0.500	0.500	1.165
I4	0.500	0.979	0.500

Figure 1.14 shows that six of the 12 kernels were reproduced quite accurately. These were the kernels that influenced the production signals the most. This result could have been anticipated by looking at the IWCs, perhaps with the exception of the I1P3 kernel which seems to have been poorly captured, as compared to the I4P3 kernel which was captured relatively well. The values of the influence statistic, $S0$, for this case are listed in Table 1.10.

Table 1.10: Test statistic to determine the influence of each kernel in example II.

$S0$	*P1*	*P2*	*P3*
I1	0.0521	0.3391	0.0048
I2	0.9435	0.0067	0.0016
I3	0.0000	0.0016	0.9747
I4	0.0044	0.6526	0.0189

Table 1.11: List of valid injector-producer connections for example II based on the test statistic $S0$.

	P1	*P2*	*P3*
I1	True	True	False
I2	True	False	False
I3	False	False	True
I4	False	True	True

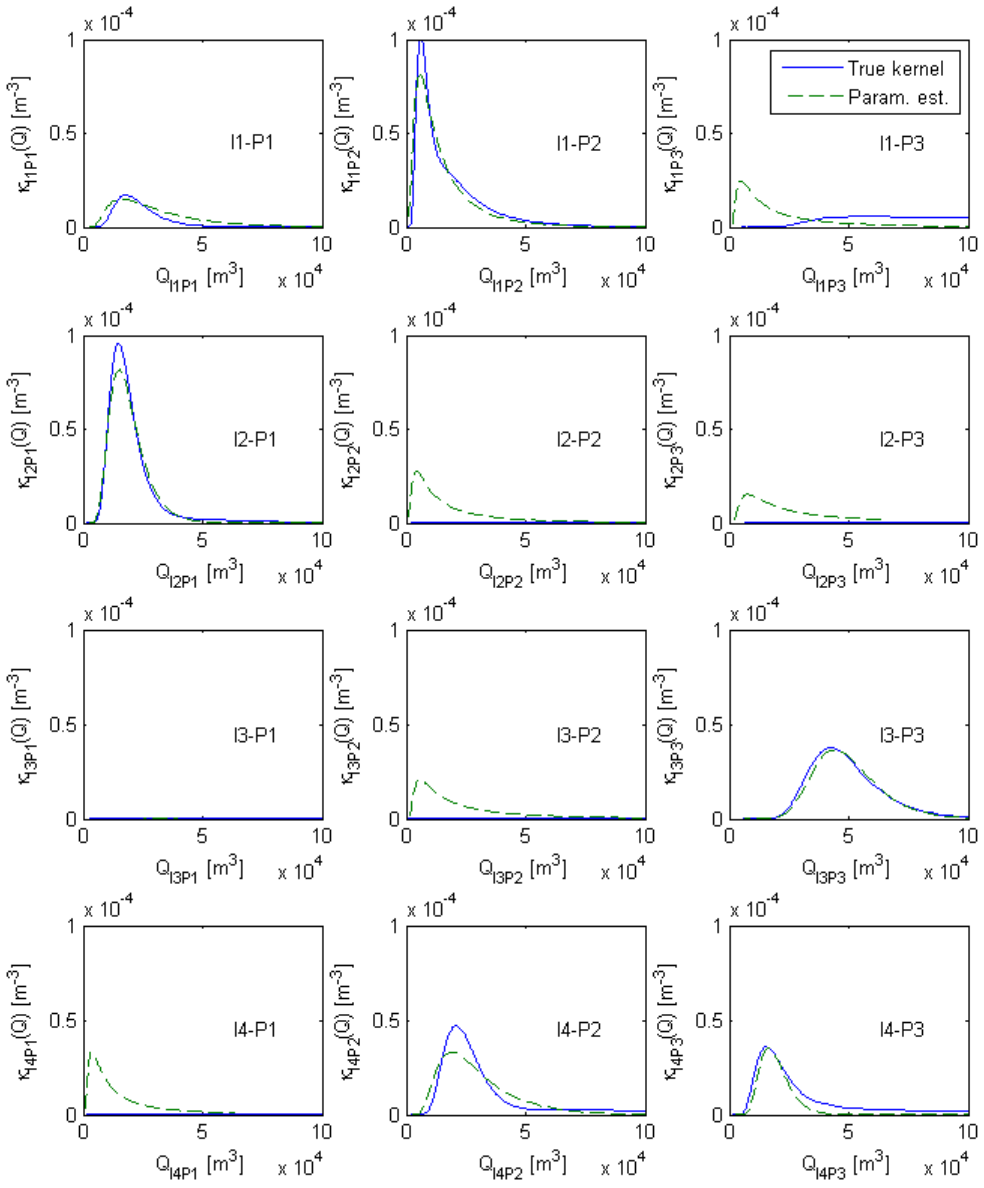

Figure 1.14: Parametric kernel estimates for example II. The "true" kernels, obtained from a tracer impulse simulation with constant injection rates (3000 m^3/day), are plotted with blue solid lines. Parametric estimates are given by green dashed lines.

A 0.01 threshold on $S0$, gave the Boolean matrix shown in Table 1.11 for whether there was a meaningful connection between wells or not.

1.3.5.2 Nonparametric Kernel Estimation

It was clear from the parametric example that the fit for producer P2 could be improved (Figure 1.13). The reason for this was apparent when looking at the kernel estimates for the two best connections for P2. The parametric model could not describe those kernels very well. This problem was solved by using a nonparametric kernel model.

As noted earlier, the parametric kernel estimates were used as priors, κ_{prior}. Given a good prior, it was relatively straight forward to get a good fit to the production data, as shown in Figure 1.15.

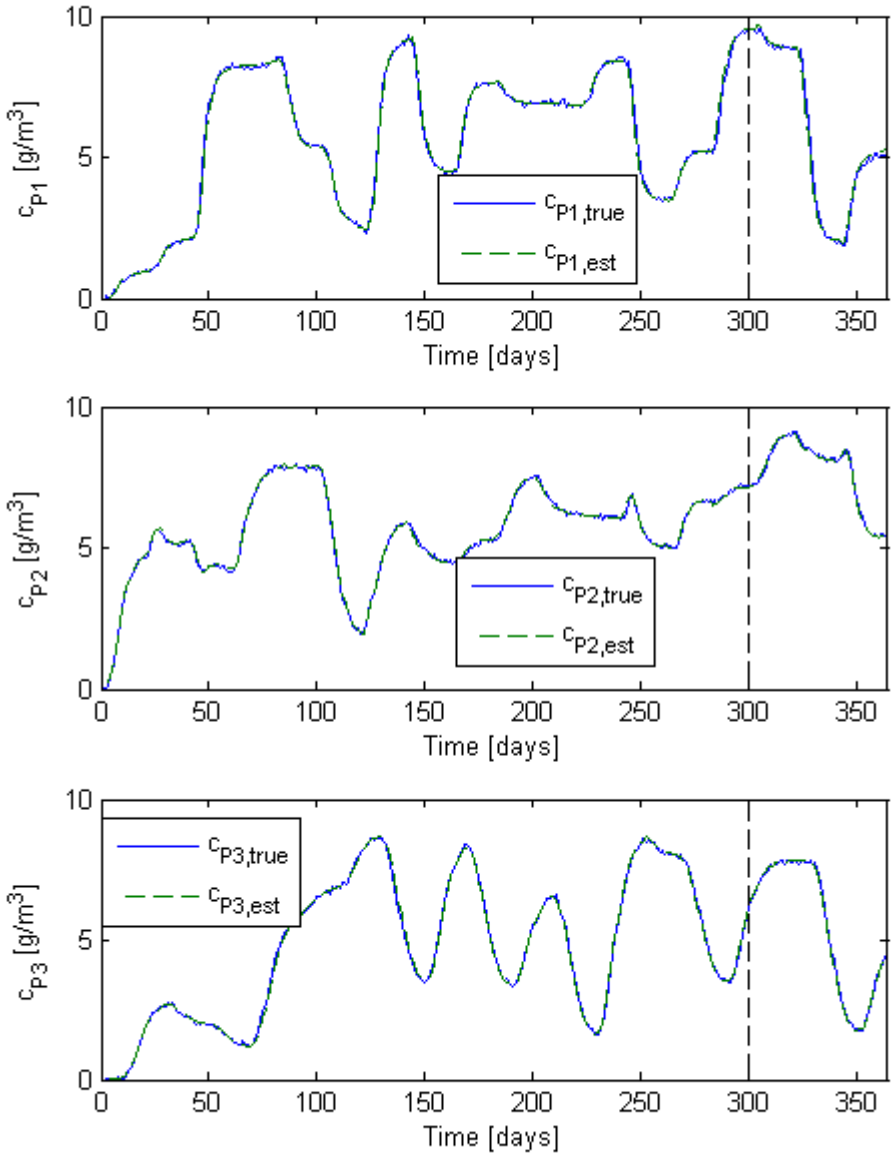

Figure 1.15: Reproduction of the tracer data with nonparametric kernels for example II. The true data are shown as blue solid lines and the reproduced data are given by green dashed lines. The vertical black dashed line divides the estimation and prediction periods.

The MATLAB algorithm fmincon was used to solve the problem, with the trust-region-reflective algorithm. Considerable tightening of the default convergence criteria for fmincon was required to get a good solution, i.e. by allowing more iterations, and lowering tolerances on the minimum step size and function change.

The weighting parameters for the regularization term, θ_{ij}, were also tuned individually to enforce smoothness in the kernel estimates. These estimates were centered around 10^{10} with an order of magnitude higher value for those kernels that had little influence, and vice versa for those that had much influence, on the production signal. The resulting kernel estimates and confidence intervals are shown in Figure 1.16. The 95% confidence intervals were very large for some of the kernels. This occurred mostly near the tail end of the less significant kernels, because the contribution of these parts to the production signal was very small, leaving the tail estimates particularly susceptible to noise.

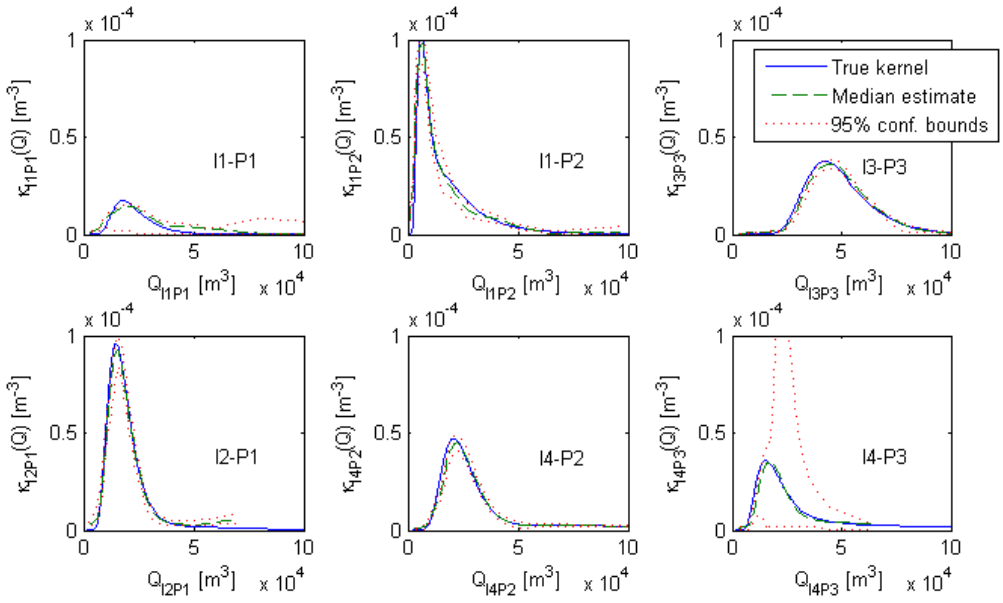

Figure 1.16: Nonparametric kernel estimates and 95% confidence bounds obtained from parametric bootstrapping for those kernels deemed significant for example II.

The pore volume and correction factor based on the kernels in Figure 1.16 are given in Table 1.12.

1.3.6 Discussion

The M-ARX method (Lee, 2010) describes the bulk division of injection streams in the reservoir. The tracer kernel adds information about the breakthrough curve, which is representative of the geometry of the fluid flow path. Combined, these two pieces of information yield an informative field map, as represented in Figure 1.17.

Table 1.12: Pore volume and correction factor computed from nonparametric kernels for example II.

V_x	*P1*	*P2*	*P3*
I1	30,715	16,890	
I2	21,115		
I3			50,123
I4		38,215	24,579
f			
I1	0.454	1.396	
I2	1.399		
I3			1.224
I4		1.078	0.677

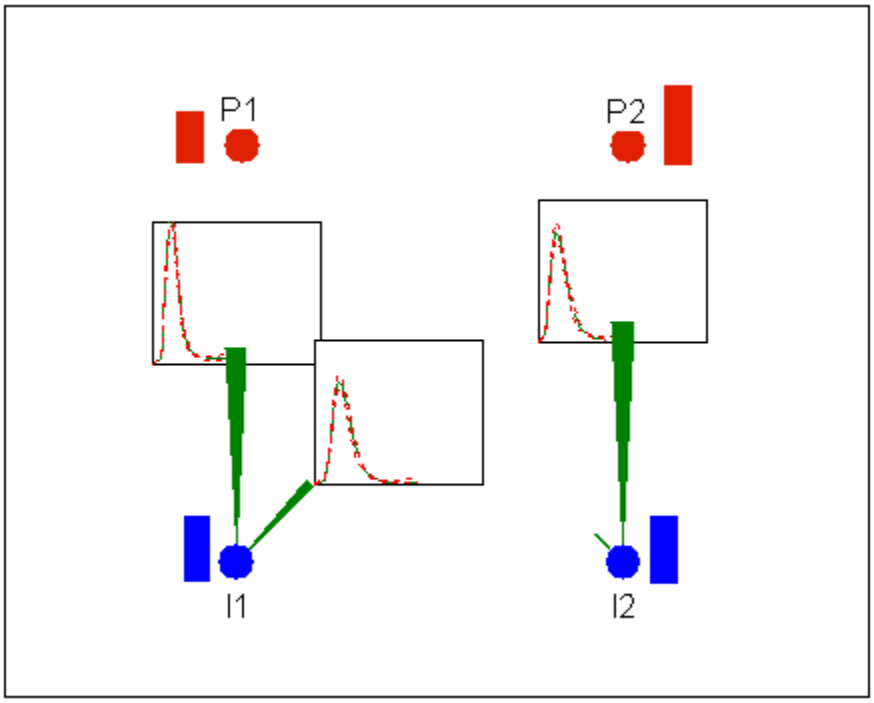

Figure 1.17: A map of the reservoir from example I using only the interwell connectivity (green triangles) and tracer kernels to describe the field. Injection and production rates are illustrated with rectangular columns next the wells.

The tracer kernel method works as well as reported in this work because the streamlines in the model are strongly constrained by the fractures in the reservoir. In other words, the injector-producer flow paths are effectively fixed and are therefore well described by the tracer kernels.

It should be noted that the streamlines can be forced to leave the fractures by controlling both the injection and production rates, and in such cases the tracer kernel method would be much less effective. In practical field applications, however, it would seldom be feasible to force the

injection and production rates such that the streamlines would go through the matrix, because that would cost too much energy for pumping. Thus, the tracer kernel method should be reasonably applicable in many practical scenarios, even when the production rates are being controlled within the extent of feasible bottomhole pressure conditions.

One practical application of interest with the tracer kernel method is to optimize reinjection scheduling in geothermal reservoirs (Juliusson and Horne, 2011). In this case, IWCs can be used in quantify the division of the injection streams, and the tracer kernels can be used to calibrate a thermal transport model for the injector-producer connections. This would be particularly interesting for early stage optimization of injection rates in Enhanced Geothermal Systems or other fractured liquid-dominated geothermal systems. The largest remaining uncertainty with the use of this method lies in efficient quantification of the effective heat transfer area (or effective aperture) of the flow path. A few methods have been proposed to resolve this uncertainty, e.g. by Kocabas (2005) and Williams et al. (2010).

As the description of the inversion process and the example applications indicate, it is necessary to have both flow-rate and concentration (saturation) data recorded quite frequently for proper inversion. For the flow-rate data, it would in most cases be sufficient to have one or two measurements per day. The required measurement interval for the concentration data depends on the travel time of the fluid. A recommended interval for recording the concentrations would be around one fifth of the shortest expected travel time of the peak tracer concentration. Of course this interval may be hard to determine a-priori, but it would likely be smaller than what is considered standard practice in current field applications. Thus, it would probably be best if an automated recording device for measuring concentration were put in place.

1.4 OPTIMIZATION OF INJECTION SCHEDULING

Determining how to allocate water to injection wells in geothermal fields is an important and challenging task. Conceptually, the objective of the injection scheduling problem is to delay thermal breakthrough as long as possible, while maintaining as much pressure support for the production wells as possible. With more advanced models it is possible to aim towards maximizing thermal recovery from the geothermal resource, or the net present value of production from the reservoir. The same requirement applies to both enhanced geothermal systems (EGS) and conventional hydrothermal resources.

Lovekin and Horne (1989) discussed methods for optimizing injection schedules in geothermal reservoirs based on tracer return data. They posed the problem as either, a linear program where only the injection rates were adjusted, or a quadratic program where both injection and production rates were adjusted. The objective functions depended on interwell connectivity (IWC) parameters (or arc costs) that were inferred from tracer test. The IWC parameters were computed in an empirical manner and their value was independent of the injection and production rates.

Whether tracer returns vary much with injection and production rates has been debated. In cases where the flow rates being circulated by the power plant are small in comparison to a large ground water current flowing through the reservoir, it seems reasonable to assume that the tracer returns would be insensitive to the particular injection and production rates. In hot dry rock

systems, on the other hand, the natural ground water current should be negligible and thus the tracer returns would vary more significantly with the injection and production rates. This observation led our research efforts towards defining methods to predict tracer returns under variable flow rate conditions, as discussed in Section 1.3.

One of the key reasons for the success of the tracer kernel method was that the fractures limited the variability in the streamlines between wells as the injection and production rates changed. As a result the well-to-well connections could be described by a small number of parameters that represent each flow path. We take advantage of this fact in solving the injection scheduling problem. An objective function is suggested and the results verified by comparison to results from numerical simulation. Besides presenting a practical method for optimizing field management, working through the problem revealed the challenges involved in solving the problem efficiently. This should help focus further research on ways to overcome those particular challenges.

1.4.1 Objective Function

Utilizing tracer data to optimize injection strategies in geothermal reservoirs was discussed by Lovekin and Horne (1989). Several publications by Shook (2001, 2003, 2004) also discuss the potential application of tracer data to infer reservoir properties that could be used to optimize injection schedules. Other publications with reference to the topic usually take an approach of comparing a small number of preconceived options. For example, Barelli et al. (1995) investigated whether it would be better to produce at constant flow rate or constant reservoir pressure from the Laderello geothermal field in Italy. More recently, Ganefianto et al. (2010) presented a paper on optimizing injection in the Salak geothermal field in Indonesia. Their work entailed a comparison of six injection scenarios, which were based on full numerical reservoir simulations. Some of those scenarios also included alternative locations for reinjection. Juliusson et al. (2011) looked at the broader problem of optimizing how much energy to extract from a geothermal resource over time.

Methods for predicting thermal breakthrough in fractured reservoirs based on information interpretable from tracer tests have also been discussed, e.g., by Lauwerier (1955), Gringarten and Witherspoon (1975), Bodvarsson and Pruess (1984), Kocabas (2005), and Wu et al. (2008). The work of these authors inspired our method for optimizing injection schedules.

The objective function was designed to maximize the net present value of production from the reservoir, which was computed as:

$$O(\bar{q}_I) = \sum_{j=1}^{N_P} \int_0^{t_f} P(t) z_j\left(T_{Pj}(t, \bar{q}_I), T_I, T_{p,min}\right) q_{Pj}(\bar{q}_I) e^{-rt} dt \tag{2.49}$$

where $P(t)$ denotes the unit price of energy and r denotes the discount rate for the investment. An empirical correlation was used to compute the specific power output, z, as a function of the injection and production temperature. The correlation, presented by Bennett and Horne (2011), was based on results presented in the well-known MIT report on the Future of Geothermal

Energy in the United States (Tester et al., 2006). The specific power output, in units of kW/(m^3/day), was:

$$\begin{aligned} z_j'\left(T_{Pj}(t,\bar{q}_I),T_I\right) = {} & 3.854\times10^{-5}\left(T_{Pj}(t,\bar{q}_I)-\zeta\right)^2 \\ & -1.268\times10^{-3}\left(T_{Pj}(t,\bar{q}_I)-\zeta\right) \\ & -2.123\times10^{-2} \end{aligned} \tag{2.50}$$

with:

$$\zeta = 0.563T_I - 14.51 \tag{2.51}$$

and temperatures taken in degrees Celcius. Water density was assumed to be 900 kg/m^3 when converting the correlations to volumetric units.

In practice, power plants are designed to work at a given temperature range. To include this consideration, a minimum temperature threshold was added to the power output correlation. This threshold was modeled by a smooth function to avoid complications in the optimization procedure. Thus, the specific power output was defined as:

$$z_j\left(T_{Pj}(t,\bar{q}_I),T_I,T_{Pmin}\right) = \frac{1}{2}\left(erf\left(T_{Pj}(t,\bar{q}_I)-T_{P,min}\right)+1\right)z_j'\left(T_{Pj}(t,\bar{q}_I),T_I\right) \tag{2.52}$$

where erf denotes the error function and $T_{P,min}$ denotes the minimum design temperature threshold. The specific power output curve is plotted as a function of production and injection temperature, with a design threshold of 120 C, in Figure 1.18.

The production temperature for the multiwell case was computed as:

$$\begin{aligned} T_{Pj}(t,\bar{q}_I) &= \sum_{i=1}^{N_I} w_{ij}T_{ij}(t,q_{Ii}) \\ &= \sum_{i=1}^{N_I} w_{ij}\left(T_0-(T_0-T_I)T_{D,ij}(t,q_{Ii})\right) \end{aligned} \tag{2.53}$$

The parameter w_{ij} denotes the mixing weight given by Equation (2.2). T_0 was the initial temperature in the reservoir and $T_{D,ij}$ represented a function of dimensionless temperature change as reported by most authors that have discussed thermal breakthrough in fractured reservoirs. For example, using Lauwerier's (1955) formulation:

$$T_{D,ij}(t,q_{Ii}) = erfc\left(\frac{\xi_{ij}}{2\sqrt{\theta(\tau_{ij}-\xi_{ij})}}\right)U(\tau_{ij}-\xi_{ij}) \tag{2.54}$$

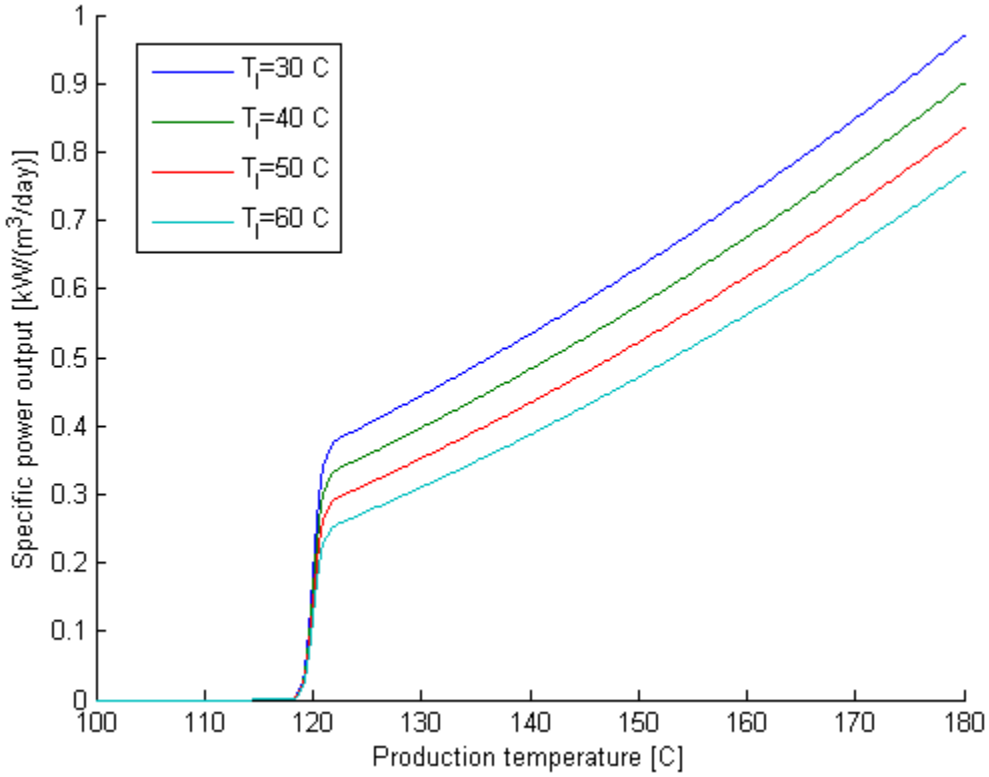

Figure 1.18: Specific power output correlation as a function of injection and production temperature. A minimum design temperature threshold of 120 C was applied in this case.

In this formula *erfc* denotes the complementary error function and U is the unit step function. The dimensionless variables ξ, τ and θ are defined as:

$$\xi_{ij} = \frac{K_r}{b_{ij}^2 \rho_w c_w} \frac{V_{x,ij}}{R \phi_f F_{ij} q_{Ii}} \tag{2.55}$$

$$\tau_{ij} = \frac{K_r}{b_{ij}^2 \rho_{af} C_{af}} t \tag{2.56}$$

$$\theta = \frac{\rho_{af} C_{af}}{\rho_{am} C_{am}} \tag{2.57}$$

where b_{ij} denotes the fracture half aperture, ϕ_f is the fracture porosity, K_r is the thermal conductivity of the rock, $R = 1 + \phi_m(1 - \phi_f)/\phi_f$ is the tracer retardation factor with ϕ_m representing the matrix porosity. The groups

$$\rho_{af} C_{af} = \phi_f \rho_w C_w + (1 - \phi_f) \rho_r C_r \tag{2.58}$$

and

$$\rho_{am}C_{am} = \phi_m\rho_w C_w + (1-\phi_m)\rho_r C_r \tag{2.59}$$

represent the average volumetric heat capacity for the fracture and the surrounding rock matrix, respectively.

The thermodynamic parameters needed in Equation (2.54) can be estimated fairly accurately based on existing knowledge of the petrology and reservoir fluid. The largest uncertainties are usually related to the geometry of the flow paths. The production rates can be estimated based on Equation (2.9) and the pore volume can be estimated by the first moment of the tracer kernels:

$$V_{x,ij} = \frac{\int_0^{Q_{ij}(t_f)} Q'_{ij}\kappa_{ij}(Q'_{ij})dQ'_{ij}}{\int_0^{Q_{ij}(t_f)} \kappa_{ij}(Q'_{ij})dQ'_{ij}} \tag{2.60}$$

or a slug tracer return curve:

$$V_{x,ij} = \frac{\int_0^{Q_{ij}(t_f)} Q'_{ij}c_{ij}^{impulse}(Q'_{ij})dQ'_{ij}}{\int_0^{Q_{ij}(t_f)} c_{ij}^{impulse}(Q'_{ij})dQ'_{ij}} \tag{2.61}$$

Methods to determine ϕ_f, b, or the group $\phi_f b$, which will appear upon simplification of Equation (2.54), have not been well established. Thermally reactive tracer methods like those being proposed by Reimus et al. (2011) may make it possible to determine the effective fracture aperture at an early stage of development, in the near future. It should also be noted that the Lauwerier solution assumes flow through a single fracture surrounded by a matrix of infinite size. Thus, this solution will tend to give optimistic results, especially at late times when thermal interaction between parallel flow paths has become significant.

With these definitions, the optimization problem for injection rate scheduling was presented as:

$$\max_{\boldsymbol{q_I}} \quad O(\bar{q}_I) = \sum_{j=1}^{N_P}\int_0^{t_f} P(t)z_j\big(T_{Pj}(t,\bar{q}_I), T_I, T_{p,min}\big)q_{Pj}(\bar{q}_I)e^{-rt}dt \tag{2.62}$$

$$s.t. \qquad \sum_{i=1}^{N_I} q_{Ii} \le q_{I,tot} \tag{2.63}$$

$$q_{Ii} \le q_{Ii,max}, \qquad i = 1\cdots N_I \tag{2.64}$$

$$q_{Ii} \ge 0, \qquad i = 1\cdots N_I \tag{2.65}$$

Two examples that illustrate the application of this optimization method follow. In each of the examples, the initial temperature was assumed to be 150 C and the injected temperature was 50 C. As an initial guess the flow rates were assumed to be distributed evenly between the injectors, such that the maximum allowable rate, $q_{I,tot}$, was reached. The producers would produce at a constant bottomhole pressure. The porosity was assumed to be known (e.g. determined by core sampling) as well as the thermodynamic properties of the rock and water. The unknown variables, that needed to be determined from production data, were the interwell connectivities, F, the correction factors, f, the fracture pore volumes V_x, and the fracture apertures, b.

The problem was solved with MATLAB's built-in optimization package fmincon. The solution times were minimal, on the order of a few seconds. Nothing conclusive will be stated about the regions of convexity for the problem. However, based on contour plots of the objective function for the cases investigated, the objective function seemed to be nonconvex in general, but convex in the area of interest, i.e., an area of reasonable initial guesses for the solution. This made the problem easy to solve computationally.

1.4.2 Example I

We begin by illustrating the application of the injection scheduling method on the simple reservoir model introduced in Section 1.3.4. The model has two injectors and two producers and the aim is to determine those injection rates that maximize the net present value of production over a 30 year period.

The interwell connectivity parameters and pore volumes given in Table 1.3 and Table 1.6, respectively, were used to calibrate the objective function. It was also assumed that the aperture-porosity, $b\phi_f$, was known. Of course the apertures would not be known in practice, but they were assumed to be known to illustrate the applicability of the optimization method.

In the case illustrated here, the injection rates were constrained to be below 4000 m^3/day for well I1 and 3000 m^3/day for well I2. Moreover, the total injection rate was constrained to be less than or equal to 3000 m^3/day. As an initial guess, it was assumed that 2500 m^3/day were being injected into each well. Solving the problem yielded an optimal allocation rate of 1652 m^3/day (64%) for I1 and 844 m^3/day (36%) for I2. The objective function and constraints are shown in Figure 1.19.

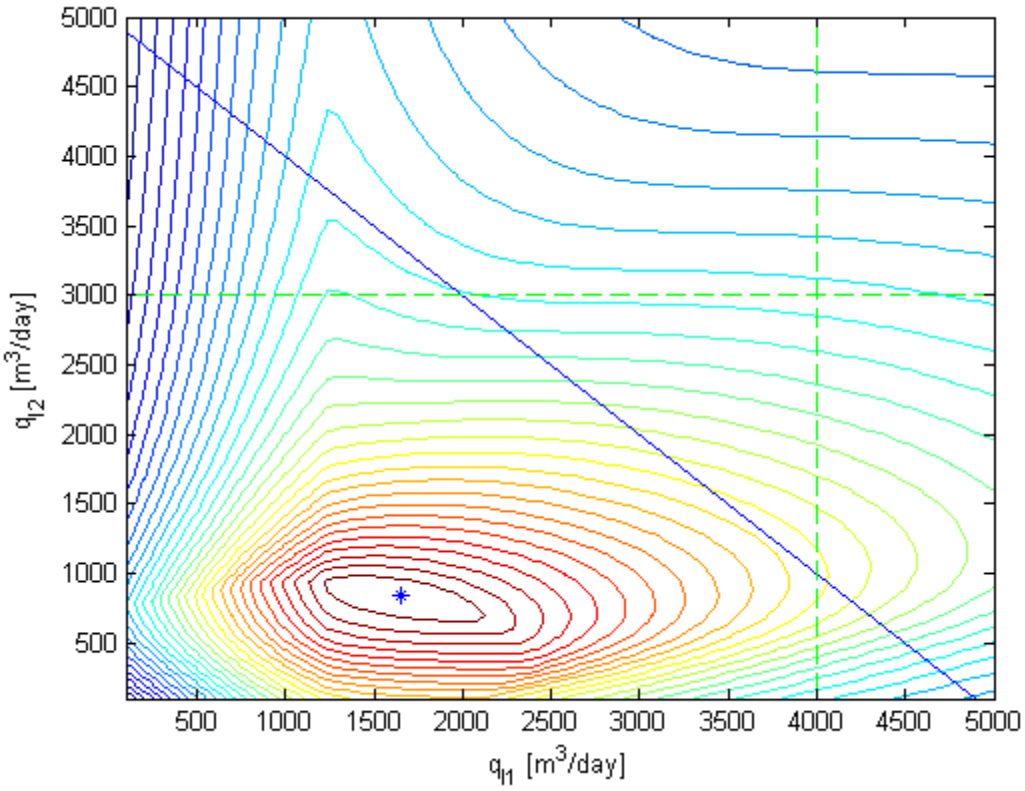

Figure 1.19: A contour plot of the objective function based on net present value of production. A maximum total injection constraint of 5000 m^3/day is illustrated by the blue diagonal line. Maximum injection constraints of 4000 and 3000 m^3/day for injectors I1 and I2, respectively, are shown by the green dashed lines. The optimum feasible point is shown by the blue star.

The success of the optimization method depended on how well the thermal breakthrough could be predicted by the analytical heat transfer equations. To investigate this, the thermal drawdown $T_{Pj}(t, \boldsymbol{q_I})$, predicted by Equation (2.53), was compared to the simulated values. Comparisons were made with equal injection into each injector (Figure 1.20) and at the optimal injection configuration (Figure 1.21). As the figures show, the Lauwerier solution provided a relatively accurate estimate of the thermal breakthrough curve.

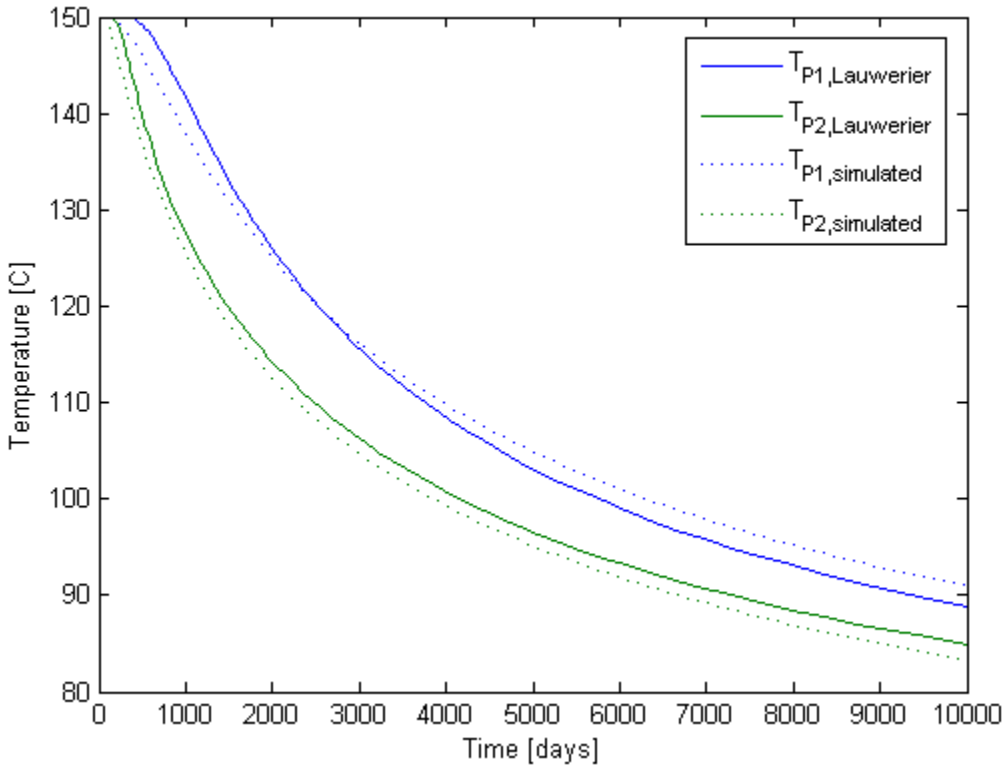

Figure 1.20: Comparison of simulated thermal breakthrough and thermal breakthrough as predicted by the Lauwerier (1955) analytical model. For this case water at 50 C was injected at 2500 m^3day into each of the two injectors.

The optimal solution in this case was well below the maximum allowable injection rate. This was because the power output would drop significantly if the production temperature fell below 120 C. Figure 1.21 shows how the predicted temperature converged to a value close to 120 C near the end of the production period for producer P2. The temperature in producer P1, however, was allowed to fall below the 120 C threshold at an earlier time. This shows that the relative benefit of keeping P2 at a high production rate at the late stages outweighed the benefit of maintaining production in P1 at late stages. Comparison to the simulated thermal returns shows that the actual decline in production would occur earlier than predicted by the analytical model.

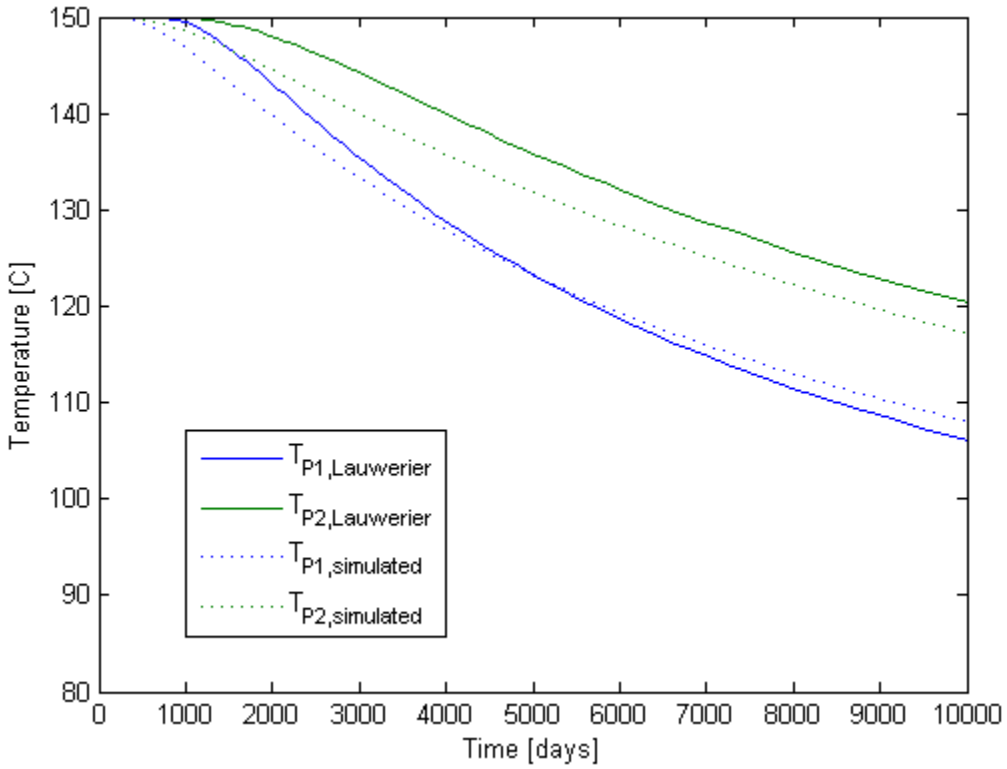

Figure 1.21: Simulated thermal breakthrough and thermal breakthrough as predicted by the Lauwerier (1955) analytical model. For this case water at 50 C was injected at the optimal allocation of 1652 m^3/day into injector I1 and 844 m^3/day into I2.

The increase in the objective function over the initial guess (where all injection rates were equal) was quite significant, or about 91%. This number can be deceiving though because it is given relative to an arbitrary initial guess for the flow rates. The number does not, however, include the savings that could be made by building a smaller power plant, if one knew from the beginning that a smaller total flow rate would actually yield higher returns over a 30 year period. Taking the plant size into consideration in the objective should lead to even smaller optimal flow rates.

1.4.3 Example II

In this section, the application of the injection optimization method to Reservoir Model II is described. The model, which is based on data obtained from the Soultz-sous-Forêts enhanced geothermal system in France, included four injection wells and three production wells. Further description is given in Section 1.3.5.

The required estimates for F, and V_x are presented in Table 1.8 and Table 1.12, respectively.

The upper bound on the injection for individual wells was 4500 m^3/day, and a 12000 m^3/day upper limit was set on the total injection rate. The initial guess for the injection rates was 2500 m^3/day for each injector. The optimal injection rates, based on these parameters, are shown in Table 1.13.

Table 1.13: Optimal injection rates for Example II.

q_{Ii}	*[m^3/day]*	$Ii/\sum Ii$
I1	1375	19%
I2	1574	21%
I3	2617	35%
I4	1821	25%
$\sum Ii$	7380	100%

The objective function could not be plotted in this case, as it was four-dimensional. However, slices of the objective function could be viewed, with two of the decision variables fixed at the optimal values. Figure 1.22 shows a q_{I1}-q_{I2} slice of the objective function with q_{I3} and q_{I4} fixed at the optimal values. These plots were useful to verify that the optimization algorithm had not become trapped in some local maximum.

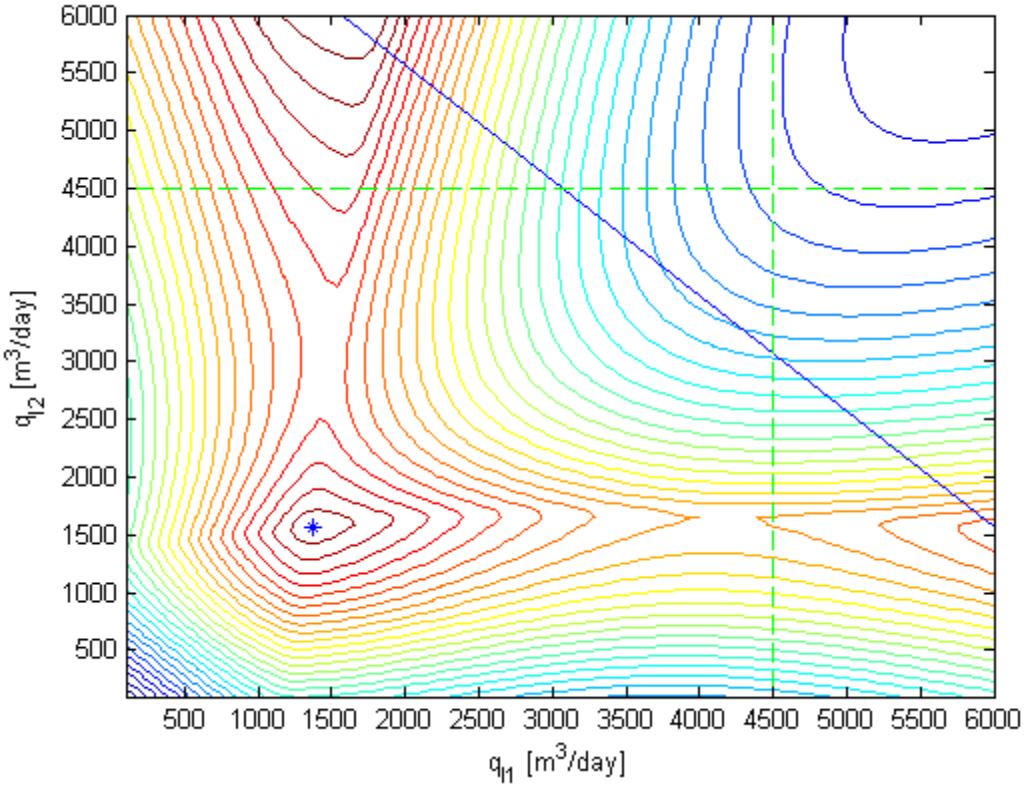

Figure 1.22: A contour plot of a slice through the objective function based on net present value of production. The slice is taken with $q_{I3} = 2617$ m^3/day and $q_{I4} = 1821$ m^3/day, which are the optimum values. A maximum total injection constraint of 12000 m^3/day is illustrated by the blue diagonal line. Maximum injection constraints of 4500 m^3/day for injectors I1 and I2 are shown by the green dashed lines. The optimum feasible point is shown as a blue star.

Based on the analytical temperature estimates, the value of the objective function increased by 14% compared to the initial allocation of 2500 m^3/day per well. However, it is more meaningful to look at the improvement based on the simulations, since they were meant to represent the actual outcome of the injection strategy. The simulation based net present value for the initial allocation was $21.6 million, while the optimized allocation yielded $33.6 million. Thus, a 55% increase was obtained over the initial allocation. Again, the fractional increase in the objective function was quite arbitrary because it was measured against an arbitrary initial allocation, which in this case was quite close to the optimal allocation. Importantly, however, the actual reservoir response behaved in a manner similar to that predicted by the analytical equations which resulted in a significant increase in the objective function, for both cases.

The predicted and simulated thermal breakthrough curves are shown in Figure 1.23 for the case when the flow was distributed evenly at 2500 m^3/day to each injector. The same curves for the optimal injection rates are shown in Figure 1.24. As the figures show, the predicted breakthrough lags a bit behind the simulated breakthrough. A possible way to fix this might be to reestimate the fracture apertures at the predicted optimal flow rate (say with a thermally degrading tracer method). Thus a couple of iterations of testing and readjusting the flow rates should quickly converge to a more accurate prediction.

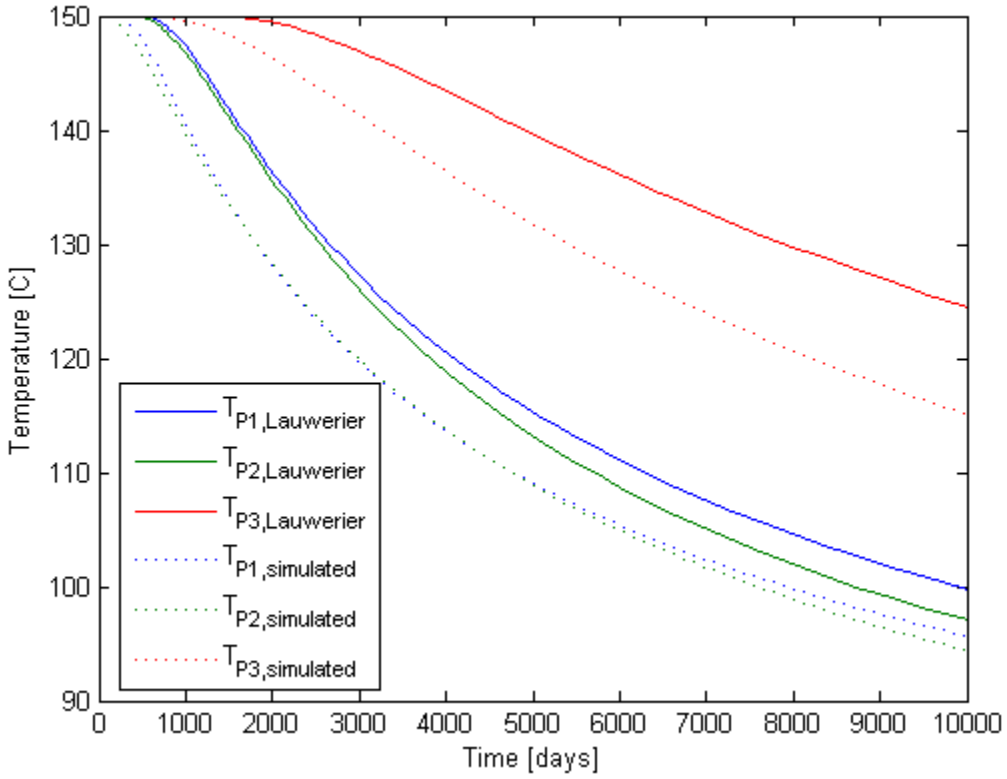

Figure 1.23: Comparison of simulated thermal breakthrough and thermal breakthrough as predicted by the Lauwerier (1955) analytical model. For this case water at 50 C was injected at 2500 m^3/day into each of the four injectors.

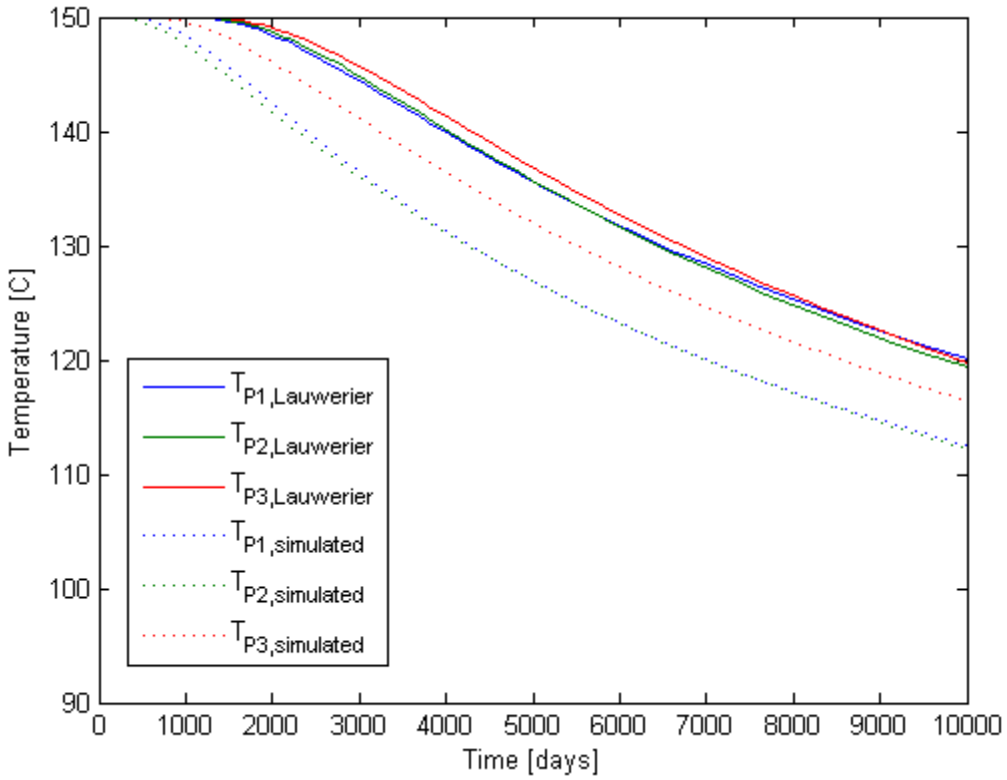

Figure 1.24: Comparison of simulated thermal breakthrough and thermal breakthrough as predicted by the Lauwerier (1955) analytical model. For this case water at 50 C was injected at the optimal flow rates given in Table 1.13.

1.4.4 Discussion

The example applications showed that the flow rate scheduling problem is reasonably well suited for optimization, i.e. it is not strongly nonconvex, and it was solved in a matter of seconds. The quality of the results depended greatly on the accuracy of the characterization methods, and as such the results in Example I were more accurate. The optimal flow rate configuration for Example II also yielded quite satisfactory results. Preliminary tests illustrated in Juliusson (2012) showed that the thermal drawdown model was not as well suited for characterizing three-dimensional fractured reservoirs. More research into analytical or semi-analytical ways to model such functions would be useful.

A slightly different topic of interest would be the application and modeling of thermally degrading tracer to determine the effective aperture or heat transfer area. Reimus et al. (2011) have made considerable progress on that front but their work is still in development. There seems to be room for improvement in the analytical modeling, and verification with data from full scale numerical simulations or laboratory experiments is still missing.

Injection and production scheduling models have been studied more thoroughly for oil and gas reservoirs. Researchers at the Stanford Department of Energy Resources Engineering are actively working on the topic, specifically within the Smart Fields Consortium. A few publications of

interest are those by Sarma et al. (2006), Cardoso et al. (2009) and Echeverria Ciaurri et al. (2011). Professor Jan-Dirk Jansen at the Delft University of Technology also runs an active research group with an interest in production optimization.

Much of the latest work on in the field of oil and gas has been focused on closed-loop optimization problems. In these problems, an objective function based on the net present value of production is usually defined, and then constrained by the arbitrarily complex discretized differential equations which represent the mass and energy balances that form the basis of a full scale numerical reservoir model. Further discussion of such problems is beyond the scope of this dissertation but interested readers are referred to Jansen (2011).

1.5 CONCLUSION

A novel method for utilizing tracer and flow-rate data to characterize flow paths in fractured medium has been developed. The method is useful for understanding well-to-well interactions, mapping and characterizing major flow paths, and designing injection schedules. Two major strengths of the method are that it can be applied to multiwell tracer transport scenarios and it works under variable flow-rate conditions.

The crux of the method is to: a) obtain the interwell connectivity (IWC) which describes how the injected fluids are distributed to each of the producers; b) obtain tracer kernels which are functions that describe how the geometry of the flow path affects the tracer return curve. The best way to obtain the tracer kernels is to perform tracer tests at constant flow-rate conditions. Advanced methods for inferring the tracer kernels are introduced for situations where well designed tracer test data is not available. This inverse problem can be quite challenging e.g. when both the tracer concentration and the flow-rate vary simultaneously, or when a large number of injection wells contribute to the concentration signal in a given production well.

The tracer kernel method was tested and validated with synthetic production data from discrete fracture reservoir models generated by the ground water simulator FEFLOW. The example applications showed that the inverse problem could be solved successfully for situations with a moderate number of wells (4-7 wells) where the fluid flow paths are strongly constrained by fractures.

A method for optimizing injection scheduling for geothermal reservoirs was developed. The method relies on information gathered from tracer and flow-rate data. These data are used to calibrate a thermal transport model for each injector-producer connection. The model was shown to be very efficient for optimizing flow-rates in strongly fracture-dominate reservoirs.

Table 1.14: Notation.

Symbol	*Description, unit.*
a	Dispersivity, m/day.
A	Cross-sectional area of flow path, m^2.
$\boldsymbol{A}$	Discrete producer-producer coefficient matrix, day^{-1}.
$\boldsymbol{A_c}$	Continuous producer-producer coefficient matrix, day^{-1}.
b	Fracture half aperture, m.
$\boldsymbol{B}$	Discrete injector-producer coefficient matrix, 1/day.

$\boldsymbol{B_c}$	Continuous injector-producer coefficient matrix, 1/day.
C	Specific heat capacity, J/(kg C).
D	Dispersion coefficient, m^2/day.
$\boldsymbol{F}$	Interwell connectivity matrix.
$\boldsymbol{H}$	Matrix that maps tracer kernel into produced concentration, g.
$\boldsymbol{J}$	Jacobian matrix.
L	Length of fracture.
m	Number of discretization points.
n	Number of measurements.
N_I	Total number of injection wells in a field, wells.
N_P	Total number of injection wells in a field, wells.
O	Objective function.
P	Electricity price, $/MWh.
Pe	Peclet number.
q_{Ii}	Injection rate for well i, m^3/day.
q_{Pj}	Production rate for well j, m^3/day.
$\boldsymbol{r}$	Residual vector, g/m^3.
R	Retardation factor.
$\boldsymbol{R}$	Regularization matrix, g m^3.
$S0$	Test statistic for significance of injector-producer connection.
t	Time, days.
T	Temperature, C.
u	Interstitial flow velocity, m/day.
w	Mixing weight.
x	Distance, m.
z	Specific power output function, kW/m^3/day.
α_{jk}	Weight for influence of producer k on producer j.
β_{ji}	Weight for influence of injector i on producer j.
γ_j	Response time constant for producer j, days.
κ	Tracer kernel, m^{-3}.
$\boldsymbol{\chi}$	Vector of unknown variables in parametric regression.
ν	Discrete time variable, days.
ϕ	Porosity.
ρ	Density, kg/m^3.
$\hat{\sigma}_r^2$	Sample variance of residuals, (g/m^3)^2.
$\hat{\sigma}_{\chi ij}^2$	Estimate of variance for parameter χ_{ij}.
$\hat{\Sigma}^2$	Estimate of covariance matrix for $\boldsymbol{\chi}$.
ς	Time factor for fluid mixing weight, days.
τ	Dimensionless time.
θ	Tuning parameter for regularization matrix, g m^3.
θ	Dimensionless ratio of heat capacities.
ξ	Dimensionless distance or pore volume.
Subscript	*Description*
a	Average.
f	Fracture.

i	Counter, often associated with injector.
I	Injector.
j	Counter, often associated with producer.
m	Matrix.
P	Producer.
r	Rock.
w	Water.

2. FRACTURE CHARACTERIZATION USING NANOPARTICLES

This research project has been conducted by Research Assistants Mohammed Alaskar and Morgan Ames, Senior Research Engineer Kewen Li and Professor Roland Horne. The objective of this study was to develop in-situ multifunction nanosensors for the characterization of Enhanced Geothermal Systems (EGS). The primary idea was to develop nanoparticles that undergo a specific, irreversible and detectable change at a specific temperature, and to use them as nanosensors to detect reservoir temperature during transport through the fractures of an EGS. By knowing where the nanosensors reached the specific temperature, it was shown to be feasible to infer the time of thermal breakthrough before it actually occurs.

2.1 SUMMARY

The principal findings of this study were that spherically shaped nanoparticles of certain size and surface charge compatible with that expected in porous media are most likely to be transported successfully through formation rock, without being trapped due to physical straining, chemical or electrostatic effects. We found that tin-bismuth nanoparticles of 200 nm and smaller were transported successfully through Berea sandstone. Larger particles were trapped at the inlet of the core, indicating that there was an optimum particle size range. We also found that the entrapment of silver nanowires was primarily due to their shape. This conclusion was supported by the recovery of the spherical silver nanoparticles with the same surface characteristics through the same porous medium used during the silver nanowires injection. The entrapment of hematite nanorice was attributed to its affinity to the porous medium caused by surface charge. The hematite coated with surfactant (which modified its surface charge to one compatible with the porous medium) flowed through the glass beads, emphasizing the importance of particles surface charge.

Preliminary investigation of the flow mechanism of nanoparticles through a naturally fractured greywacke core was conducted by injecting fluorescent silica microspheres. We found that silica microspheres of different sizes (smaller than fracture opening) could be transported through the fracture. We demonstrated the possibility of using microspheres to estimate fracture aperture by injecting a polydisperse microsphere sample. It was observed that only spheres of 20 μm and smaller were transported. This result agreed reasonably well with the measurement of hydraulic fracture aperture (27 μm) as determined by the cubic law.

Flow experiments were also carried out in a fractured Berea sandstone core plug using 2 μm and 5 μm fluorescent microparticles, to determine the effect of suspension concentration and fluid velocities. The recovery of 2 μm particles was found to be sensitive to suspension concentration, while that of the 5 μm was found to be sensitive to the fluid velocity (i.e. pressure gradient). The sensitivity of the recovery of 2 μm particles to concentration was likely due to a higher susceptibility of 2 μm particles to aggregation than that of 5 μm particles, leading to more aggregation at high concentrations and, subsequently, more trapping via straining. Meanwhile, the sensitivity of the recovery of 5 μm particles to fluid velocity was likely due to the larger gravitational forces and fluid drag forces acting on the larger particles and the fact that higher fluid drag forces corresponding to higher fluid velocities can directly offset gravitational forces. This explanation is in agreement with quantitative analysis using particle filtration theory,

Derjaguin-Landau-Verwey-Overbeek (DLVO), and metrics related to pore and grain size heterogeneity found in the literature.

The hypothesis that the reason for the large influence of concentration on the recovery of 2 μm particles was due to a susceptibility to aggregation is supported by observations of permeability reduction during these experiments (with both a higher degree and rate of reduction occurring at higher concentration). Flow experiments were also carried out in a silicon micromodel of a Berea sandstone pore space using 2 μm fluorescent microparticles as well as silica nanoparticles, in which the 2 μm particle straining at high concentrations was confirmed visually.

Two types of functional particles were also investigated: melting tin-bismuth nanoparticles and silica nanoparticles with attached dye. Tin-bismuth nanoparticles are attractive due to the fact that their melting point can be tuned anywhere from 139°C to 271°C, which encompasses a wide range of geothermal temperatures. The temperature sensing mechanism for such particles is size/shape change due to melting. Silica nanoparticles with a temperature sensitive linkage to fluorescent dye molecules could be used with a dye release sensing mechanism. An analytical model was constructed to demonstrate that such a sensing mechanism could potentially be used not only to measure temperature, but also to estimate the location of the measurement. Both tin-bismuth and dye-attached silica nanoparticles were synthesized, characterized, and used in heating experiments in order to evaluate their potential temperature sensitivity. The tin-bismuth nanoparticles experienced coarsening of their size distribution due to melting, demonstrating melting induced size change as a temperature sensing mechanism. The dye-attached silica nanoparticles experienced an irreversible shift in their fluorescence spectrum, indicating their promise as temperature sensors. The tin-bismuth nanoparticles were also used in a flow experiment in a Berea sandstone core plug, which resulted in limited recovery and permeability reduction. Particles were detected in the effluent using Scanning Electron Microscopy (SEM), but only at very low concentration. Only particles with diameters of 200 nm and smaller were recovered in the effluent. This indicates that larger particles experienced deposition due to some combination of straining, gravitational settling, interception, and an affinity of the particles to the rock surfaces. Tin-bismuth nanoparticles were also injected into a slim-tube packed with glass beads, which resulted in better recovery (including particles larger than 200 nm), possibly due to larger pore spaces.

Of the two types of functional particles investigated, dye-attached silica nanoparticles appear to have more promise due to their potential capability to estimate measurement location. The tin-bismuth nanoparticles have the advantage of easily tunable sensing temperature, but the sensing mechanism of particle growth due to melting can enhance deposition due to straining and gravitational settling. Because tin-bismuth nanoparticles are already denser than water by roughly one order of magnitude, gravitational settling could be particularly sensitive to particle growth induced by melting.

2.2 INTRODUCTION

In the development of enhanced geothermal systems (EGS), the characterization of the size, shape and connectivity of fractures is crucial. Unlike conventional geothermal systems, EGS do not require natural convective hydrothermal resources, but rather can be created in a hot, dry and

impermeable volume of rock. Hydraulic stimulation of fractures is the primary means of generating functional EGS reservoirs to allow economical heat recovery. The energy extraction rate is dependent on the creation of a fracture network within the targeted hot rock volume. However, existing tools and analysis methods are insufficient to characterize the fracture network that has been created. Temperature measurement can be obtained only in the near-wellbore region. Currently, there are no effective means to measure temperature far into the rock formation as a way to determine the efficacy of the fracture treatment. Thus, the objectives of this research are to provide new tools (nanosensors in the form of active nanoparticles or microparticles) and to develop reservoir engineering approaches to characterize fracture networks based on the measurements from these tools. This involves novel material syntheses to functionalize these particles and deep understanding of their transport mechanisms at macro- and microscale.

An initial investigation of the feasibility of synthesizing silica nanoparticles with dyes attached using a temperature-sensitive covalent linkage was performed (Alaskar et al., 2011). We demonstrated temperature sensitivity based on an observable change in the fluorescence spectrum of the dye upon heating. This work focused on the transport of inert particles, as a precursor for the transport of the functional nano- and/or microsensor. As an EGS reservoir is fracture-dominated, the transport of particles was conducted on porous as well as fractured rock cores.

The purpose of the study was to investigate the transport of particles in porous or fracture-matrix media. For this purpose, core-flooding experiments were conducted using porous and fractured sandstone core plugs and slim tubes packed with glass beads. Influences of particle size, shape, surface chemistry or surface charge, suspension concentration and fluid velocity on particle transport were investigated. Particle transport was assessed by measuring breakthrough curves, and results were discussed in light of physical transport mechanisms such as diffusion, interception, gravitational deposition and straining. Micromodels were also used. The main purpose of these microscale experiments was to visualize particle transport processes, especially straining, and to help explain findings from the core-flooding experiments.

The physical and chemical transport processes that determine the fate of particles flowing through saturated and unsaturated porous media have been studied extensively in colloid science. These processes affecting particle transport are the same as those that influence solute transport, i.e., advection, diffusion, dispersion, and adsorption (Bradford et al., 2002). Particle motion along fluid streamlines is advection. Due to heterogeneity of the fluid velocity field and tortuosity of paths within porous media, particle dispersion can occur, which may lead to earlier breakthrough for particles than for solutes. Investigators suggested that particle dispersion is partly caused by size exclusion or straining (Bales et al., 1989; Harter et al., 2000; Dong et al., 2002; Sirivithayapakorn and Keller, 2003). Straining is the trapping of particles of diameter larger than or equal to the pore throats to be entered. Because larger particles are excluded from smaller pore throats, they will travel through fewer pathways which in turn will reduce their travel time. Also, large particles tend to travel along higher velocity streamlines (excluded from lower velocity regions near pore walls), thus increasing particle velocity compared to conservative tracers (Auset and Keller, 2004). Interaction among particles (Brownian motion) will result in diffusion of particles, with large particles experiencing less diffusion than small

ones (Keller and Auset, 2006). Adsorption processes, which are commonly referred to as attachment through interactions (chemisorbed or physisorbed) leading to a filtration effect, are assumed to be the main processes that limit particle transport. Particle attachment is the removal of particles from solution by collision with and deposition onto a pore or fracture surface (Bradford et al., 2002). Particle removal by physical mechanisms includes Brownian diffusion, interception, and gravitational sedimentation. Interception occurs when a particle moving along a streamline comes in contact with a collector (grain) due to its finite size. Particles with densities greater than suspension fluid may experience settling or gravitational deposition onto the collector surface. Diffusion of particles into porous media can result in more contact with the grains (Tufenkji and Elimelech, 2004). Bradford et al. (2002) suggested that smaller particles are primarily removed by diffusive transport, while larger ones are removed by interception and sedimentation.

Filtration theory has been used to describe the transport of particles in porous media by predicting the single-collector contact efficiency (η_0), which is defined as the ratio of the number of collisions between particles and a filter medium grain to the total number of potential collisions in the projected cross-sectional area of the medium grain. The single-collector contact efficiency represents the sum of contributions of the individual physical transport mechanisms, i.e., diffusion, interception and gravitational sedimentation (Auset and Keller, 2006). The classical water filtration model was first presented by Yao et al. (1971) and modified by other authors (e.g., Rajagopalan and Tien, 1976; Rajagopalan et al., 1982). However, the model does not consider the influence of hydrodynamic (viscous) interactions and the universal van der Waals attractive forces. Colloid filtration was predicted accurately by solving the convective-diffusion equation numerically (Elimelech et al., 1995; Prieve and Ruckenstein, 1976), revealing the importance of the hydrodynamic interactions on colloid filtration. Tufenkji and Elimelech (2004) have proposed new correlation equation (Equation 2.1) based on a numerical solution of the governing convective-diffusion equation that incorporates the effect of hydrodynamic interactions and van der Waals attractive forces.

$$\eta_0 = 2.4A_s^{1/3}N_R^{-0.081}N_{Pe}^{-0.715}N_{vdW}^{0.052} + 0.55A_s\,N_R^{1.675}N_A^{0.125} + 0.22N_R^{-0.24}N_G^{1.11}N_{vdW}^{0.053} \qquad (2.1)$$

The three terms correspond to diffusion, interception and gravitational sedimentation, respectively. The dimensionless parameters are defined as:

$$N_R = \frac{d_p}{d_c} \qquad N_{Pe} = \frac{Ud_c}{D_\infty} \qquad N_{vdW} = \frac{A}{kT}$$

$$N_A = \frac{A}{12\pi\mu\left(d_p/2\right)^2 U} \qquad N_G = \frac{2}{9}\frac{\left(d_p/2\right)^2\left(\rho_p - \rho_f\right)g}{\mu U}$$

$$A_s = \frac{2(1-\gamma^5)}{2-3\gamma+3\gamma^5-2\gamma^6} \qquad where\ \ \gamma = (1-f)^{1/3}$$

where N_R is the aspect ratio, N_{Pe} is the Peclet number characterizing ratio of convective to diffusive transport, N_{vdW} is the van der Waals number characterizing ratio of van der Waals

interaction energy to colloid thermal energy, N_A is the attraction number which represents the combined influence of van der Waals attraction forces and fluid velocity on particle deposition rate due to interception and N_G is the gravity number which is the ratio of the Stokes particle settling velocity to the fluid velocity. A_s is a porosity-dependent parameter of Happel flow sphere-in-cell model and f is the porosity (Happel, 1958). The parameters in these dimensionless numbers are as follows: $d_p$and d_c are the particle and collector diameters in meters, respectively, U is the fluid approach velocity in meters per second, A is Hamaker constant in Joules, k is the Boltzmann constant in Joules per degree Kelvin, T is absolute temperature in degrees Kelvin, ρ_p and ρ_f are particle and fluid densities in kilograms per cubic meter, respectively, μ is the absolute fluid viscosity in kilograms per meter-second and g is gravitational acceleration in meters per square second. D_∞ is the particle bulk diffusion coefficient, which can be estimated from the Stokes-Einstein equation (Russel et al., 1989), given as:

$$D_\infty = kT/6\pi\mu\left(d_p/2\right) \tag{2.2}$$

Under practical conditions, the single-collector contact efficiency (η_0) is overestimated. The actual single-collector removal efficiency (η) is frequently expressed as a product of an empirical attachment efficiency(α), or sticking efficiency, and the single-collector contact efficiency:

$$\eta = \alpha\eta_0 \tag{2.3}$$

The attachment efficiency (α) is defined as the probability that successful collisions between particles and collector grains will result in attachment (Auset and Keller, 2006). The attachment efficiency is usually determined using experimental data for given physiochemical conditions (i.e. normalized concentration of the breakthrough curve) (Elimelech et al., 1995). The attachment efficiency is expressed as (Tufenkji and Elimelech, 2004):

$$\alpha = -\frac{2}{3}\frac{d_c}{(1-f)L\eta_0}ln(C/C_0) \tag{2.4}$$

where L is the filter medium packed length and C/C_0 is the ratio of effluent (outlet) concentration to the influent (inlet) concentration.

Interactions between particles and the surface of a porous medium are usually evaluated using the classical Derjaguin-Landau-Verwey-Overbeek (DLVO) theory (Derjaguin and Landau, 1941; Verwey and Overbeek, 1948). According to this theory, the total interaction energy is the sum of Lifshitz-van der Waals (LW) and electrostatic interactions (EL). The LW interactions are usually attractive and decay according to the square of the distance separating two infinitely long flat plates. Derjaguin's approximation of the LW interaction energy between a flat surface and spherical particle can be expressed as (Gregory, 1981):

$$U^{LW} = -\frac{A\left(d_p/2\right)}{6h}\left(1+\frac{14h}{\lambda}\right)^{-1} \tag{2.5}$$

where h is the surface to surface separation distance in meters, λ is the characteristic wavelength of the dielectric, usually assumed to be equal to 100 nm, A is Hamaker constant in joules and d_p is particle diameter in meters. The EL interaction energy (which decays with the separation distance) can be approximated from an expression derived by Hogg et al. (1966):

$$U^{EL} = \pi \varepsilon_r \varepsilon_0 \frac{d_p}{2} \left[2\zeta_1 \zeta_2 \, ln\left(\frac{1 + e^{-\kappa h}}{1 - e^{-\kappa h}}\right) + \left(\zeta_1{}^2 + \zeta_2{}^2\right) ln(1 - e^{-2\kappa h}) \right] \qquad (2.6)$$

where $\varepsilon_r \varepsilon_0$ is the dielectric permittivity of the suspending fluid J/V^2-m, κ is the Debye constant in 1/m and is given as $1/\kappa = 3.05\times10^{-10}\ I^{-0.5}$, I is the ionic strength (in pure water I$\approx 10^{-6}$), and $\zeta_1\zeta_2$ are surface potentials of interacting surface in Volts (usually replaced by zeta potentials). The total interaction energy, when plotted as function separation distance, demonstrates the magnitude and type of interactions (repulsive or attractive). Knowledge of interaction energy is of a particular interest when studying the transport of particles because it provides insight regarding what conditions are favorable for aggregation, attachment, and detachment of particles.

Experimental data of the transport of colloids and filtration theory are not always in agreement. Discrepancies have been attributed to soil surface roughness (Kretzschmar et al., 1997; Redman et al., 2001), charge heterogeneity (Johnson and Elimelech, 1995), and underestimation of attachment coefficients due to the existence of repulsive forces between particles and porous medium (Ryan and Elimelech, 1996). Bradford et al. (2002) attributed such discrepancies to the fact that filtration theory does not account for straining. The degree at which particles are excluded by straining is function of porous medium characteristics and particle size and/or concentration. Complete straining occurs when particles are excluded from all pore throats (McDowell-Boyer et al., 1986), resulting in a filter cake that may reduce the porous medium permeability (Willis and Tosun, 1980). Incomplete straining, on the other hand, occurs when particles are rejected from pore throats smaller than the critical size, resulting in permeability reduction that is less pronounced (Bradford et al., 2002).

Some studies have been conducted to investigate the relation between the size of particle and pore size distribution and its influence on particle straining. Sakthivadivel (1966 and 1969) proposed that particles larger than 5% of the median grain diameter were subjected to exclusion by straining. Matthess and Pekdeger (1985) extended this rule to include porous media consisting of a distribution of grain sizes. Their theoretical criteria suggested that particle to median grain size ratio should be greater than 18% for straining to occur in uniform sand. Experimental data by Harvey et al. (1993), however, was not in agreement with the criterion suggested by Matthess and Pekdeger (1985). Other researchers (e.g., Auset and Keller, 2006) studied the mechanisms of particle removal, including straining, by examining the relative particle size (i.e. throat to particle ratio T/C) using polystyrene beads (3-7 μm in diameter and particle density of 1.05 g/cm^3). They reported that straining was the primary attachment mechanism for T/C less than 1.8. For T/C greater than 2.5, only interception was observed for particles larger than or equal to 3 μm. For T/C ratios in between above values, straining and interception were the removal mechanism. Note that removal mechanism by gravity was not considered because the density of the polystyrene was similar to that of suspension fluid (i.e. water).

2.3 MATERIALS AND METHODS

2.3.1 Requirements for nanomaterials and characterization methods

Nanoparticles used in this study and ultimately in the reservoir must be safe to handle and environmentally benign. The optimum particle size should be verified to ensure particles are stable in suspension and disperse in solution. Moreover, the affinity of such particles to the reservoir formation should be verified and the particles must not interact with rock matrix (Kanj et al., 2009).

The quantity of the nanotracer produced at the sampling point should be sufficient to be recognizable and at concentrations greater than the lower detection limit of the devices used to analyze the effluent. In our experiments, characterization of the nanofluid prior to and after injection was carried out using various techniques. Dynamic Light Scattering (DLS), Fluorescence Spectrometry and Ultraviolet-visible Spectroscopy (UV-vis) were used to detect the nanomaterial particulates. Scanning Electron Microscopy (SEM) and Optical Microscopy were also used to confirm the findings.

Characterization of the rock pore spaces following the injection was carried out to study the nanoparticle dissemination inside the rock sample. The objective was to understand the particle size distribution and how the nanoparticles arranged themselves within the porous medium (Kanj et al., 2009).

2.3.2 Nanoparticle and microparticle

Fluorescent silica microspheres, silver nanowires, silver nanoparticles, tin-bismuth (Sn-Bi) alloy nanoparticles, iron oxide Fe_2O_3 nanoparticles (commonly known as hematite nanorice) and polyvinyl pyrrolidone (PVP) coated iron oxide nanoparticles were selected for initial experimentation with nanofluid injection.

Fluorescent silica microparticles were used as model particles in this experimental study, using three different sizes and colors (blue, green and red fluorescence particles). The blue and green microsphere particles had a narrow size distribution with an average diameter of 2 and 5 μm, respectively. The red silica spheres were polydisperse or polysized. The red silica sample had spheres with diameters ranging from 5 to 31 μm. The excitation and emission of the blue, green and red fluorescent dyes were at wavelengths of 360/430 nm, 480/530 nm and 550/580, respectively. These microspheres had a density in the range between 2.0 to 2.2 g/cm^3. The microspheres were negatively charged as specified by the manufacturer. Five different measurements of zeta potential (ζ) (i.e. conversion of electrophoretic mobility to zeta potential using the Smoluchowski equation, Bradford et al., 2002) were performed and the average zeta potentials were found to be -40.2 mV (standard deviation: 0.4 mV), -80.23 mV (standard deviation: 1.77 mV) and -56.30 mV (standard deviation: 1.32 mV) for particle size 2 μm, 5 μm and the polydisperse red spheres, respectively. All silica suspensions were diluted to three concentrations (C=0.5, 2C=1 and 4C=2 mg/cm^3).

In addition to silica microparticles, silica nanoparticles were also used in this study. The average particle size (350 nm) was determined by Dynamic Light Scattering (DLS) and confirmed by

SEM. The nanoparticles were negatively charged with zeta potential of -73.4 mV. The conditions for the preparation of monodisperse silica particles followed the study done by Bogush et al. (1988). The nanoparticle preparation was accomplished by the hydrolysis of tetraethyl orthosilicate (TEOS) in aqueous ethanol solutions containing ammonia. The details of the synthesis are well described in Bogush et al. (1988).

The study also investigated silver nanowires with diameters in the range of 50-100 nm, and lengths in the range of 5-10 μm. Silver nanoparticles can be made in different shapes allowing for the investigation of shape-related constraints to nanoparticle flow within porous media. In fact, our initial ideas of temperature-sensitive nanoparticles revolved around particles that change shape as their characteristic of temperature measurement. For example, a rod-like nanoparticle can transform to sphere once exposed to a certain temperature, hence the motivation for studying the flow of rod-like particles. The conditions for preparing uniform silver nanowires followed, for the most part, the study by Sun et al. (2002). The formation of silver nanowires was accomplished by reducing silver nitrate ($AgNO_3$) with ethylene glycol (EG) in the presence of silver (Ag) seeds. PVP was then added to direct the growth of silver into uniform nanowires. The longitudinal and lateral dimensions of the silver nanowires were controlled by changing the reaction conditions. Sun et al. (2002) reported that increasing the reaction temperature resulted in the formation of shorter nanowires. This synthetic method provided uniform nanowires with high yield (mass production) at relatively low temperature. The spherical silver nanoparticles synthesis is a protocol adapted from Kim et al. (2006).

Monodisperse hematite nanorice particles were synthesized using forced hydrolysis of solutions of ferric chloride, as suggested by Ozaki (1984). This hydrothermal synthesis was carried out by preparing 100 ml of aqueous solution of 2.0×10^{-2} M $FeCl_3$ and 4.0×10^{-4} M KH_2PO_4 and holding it at 100 ºC for 72 hours (Wang, 2006). The precipitated nanoparticles were centrifuged and washed several times, then dispersed in 100 ml of water. These nanoparticles were found to be roughly 500 nm in length and 100 nm in diameter, with 5:1 aspect ratio. Hematite was chosen for a number of reasons. First, it furthers the investigation of the feasibility of transporting nonspherical nanoparticles through porous media. Second, the particles can be made using a relatively simple synthesis. The surface chemistry and surface charge of these nanoparticles can be modified, and there are known processes for coating hematite nanorice with other materials, which makes it a valuable candidate for functional nanotracers (Connor, 2010). Hematite is also stable at reservoir conditions, and can be detected by its optical and magnetic signals. Finally, due to its unique geometry, nanorice can be distinguished visually from natural minerals that may be present in the geofluid, using SEM imaging. To coat the iron oxide with surfactant polyvinylpyrrolidone (PVP), a 0.1 M solution of PVP in ethanol was prepared. Iron oxide nanofluid was then added, sonicated for 1 hour, and soaked overnight. The coated particles were cleaned by centrifugation three times at 6.5 krpm to remove excess surfactant.

The tin-bismuth alloy nanoparticles were selected because of their potential to be used as temperature sensors due to their tunable melting temperature spanning a broad range of temperatures of geothermal interest. One promising idea is a core-shell particle with an inert, magnetic core and a shell that undergoes decomposition or phase change. One of the reasons hematite has been investigated is because of its behavior under an applied magnetic field. This would make it an ideal material for the inert core while the shell could be a metal alloy with a

low melting point such as Sn-Bi alloy. Sn-Bi alloys could be used as sensors in the temperature range between eutectic melting point of the alloy (139°C) and the pure melting points of Bi and Sn (271°C and 232°C, respectively). To perform the synthesis, Sn and Bi were melted together at the eutectic composition (~60 wt % Bi and ~40 wt % Sn). After the alloy was cooled to room temperature, 100 mg was sonicated in 10 ml of mineral oil, a slight variation of the sonochemical method suggested by Chen (2005). The VC-505 ultrasonic processor manufactured by Sonics & Materials, Inc. with a 0.75 in. diameter high gain solid probe was used. The sonicator was operated at 200 W (~95% amplitude) with a pulse setting of 20 s on, 10 s off. The mixture was cooled to room temperature. The particles were washed and centrifuged several times with a 1:1 mixture of hexane and acetone, rinsed in a solution of 0.1 M polyvinyl pyrrolidone (PVP) in ethanol, and finally suspended in ethanol. The centrifuge setting was 6000 rpm for 15 minutes each time.

Having proven silica particles to have been transported successfully through sandstone core, we further changed their surface properties to explore their temperature response. According to the report by Wu et al. (2008), when free fluorescent dye molecule was attached to the surface of silica nanoparticles, through energy transfer, the fluorescent properties of these molecules were changed. Therefore, when the covalent bond between fluorescent dye molecule and surface modified silica nanoparticle is broken under high temperature; the difference of fluorescent behavior before and after heating would be detected. First, silica nanoparticles (Nanogiant, LLC) were prepared by surface modification. In a typical reaction, 0.5ml of 3-Aminopropyltriethoxysilane (APTS) was added to 100mg silica nanoparticle suspended in 25 ml of toluene under nitrogen and heating to ~95 °C for 4 hours. The resulting particles were washed by centrifugation in ethanol and acetone (10min at 4,400 rpm). Then the particles were dried at ~95°C overnight. After that, we attached dye molecules (Oregon 488, Invitrogen) to the surface of the modified silica nanoparticles. A suspension of 1.0 mg of the amino-modified Silica nanoparticles in a mixture of 1ml of ethanol and 15 μl of a 10mmol/L phosphate buffer (pH 7.3) was reacted with 12.7 μl of dye molecule solution (1mg/ml water solution) in dark for 3 hours at room temperature. The resulting particles were washed by centrifugation (10min at 4,400 rpm) in ethanol and acetone. We also performed surface modification and dye attachment reaction on a monolayer of silica nanoparticles on quartz substrate using the same experiment parameters.

2.3.3 Rock core sample and slim tube characterizations

This section describes the measurements of the porosity, permeability and pore volume of Berea sandstone, fractured greywacke core and slim tube packed with glass beads.

2.3.3.1 Berea cores

The porosity was measured by mercury intrusion and confirmed by resaturation of the core samples with testing fluid (i.e. deionized water). The gas and liquid permeabilities were determined. The gas permeability was measured by introducing nitrogen at different flow rates and inlet pressures, and calculated by applying Darcy's law for compressible fluids. The Klinkenberg (gas slippage) effect was considered to evaluate the equivalent liquid permeability. After saturation, the liquid permeability for the same core samples was carried out. Darcy's law for horizontal flow was used to compute the water permeability. Porosity, permeability, pore volume and core dimensions are summarized in Table 2.1. Note that the nanofluid injection experiment for which the specific core was used is indicated in the table.

Table 2.1: Core characterization data

Property	*Measurement*	*Berea I* *Silver nanowires*	*Berea II* *Sn-Bi nanoparticle*	*Berea III* *Hematite nanorice*	*Berea IV* *Silver nanoparticle*
Core dimensions (cm)	Diameter	3.8	3.8	3.8	3.8
	Length	5.8	5.8	4.9	4.1
Porosity (%)	Hg intrusion	19.0	N/A	N/A	N/A
	Resaturation	18.2	17.5	17.1	17.1
Permeability (md)	Gas permeability	131	N/A	152	152
	Water permeability	94	125.4	60.7	60.7
Pore size (μm)	Mean pore size	10	10	10	10
Pore volume (cm^3)	Resaturation	12.0	10	9.1	8

2.3.3.2 Polypropylene slim tube packed with glass beads

To investigate the mobility of nanoparticles in the absence of the rock materials (such as clays), iron oxides and tin-bismuth nanoparticles were injected into two separate slim tubes packed with glass beads. The 30 cm long polypropylene tubes were packed with glass beads (Glasperlen 1 mm in diameter from B. Braun Biotech International) and fitted with screens and valves at each end. The porosity was measured by the saturation method. The water permeability was determined by the application of Darcy's law of horizontal flow. The dimensions, porosity, permeability and pore volume of the slim tubes are summarized in Table 2.2.

Table 2.2: Slim tube characterization data

Property	*Measurement*	*Tube I* *Sn-Bi nanoparticles*	*Tube II* *Hematite nanorice*
Tube dimensions (cm)	Inner diameter	0.4318	0.4318
	Length	30	30
Porosity (%)	Resaturation	58	48
Permeability (darcy)	Water permeability	18.1	19
Pore volume (cm3)	Resaturation	2.6	2.1

2.3.3.3 Fractured greywacke core characterization

The core sample tested was a fractured greywacke from The Geysers geothermal field, with 5.08 cm diameter and 3.01 cm length. The core sample was fitted between the two end-pieces and wrapped with Teflon shrink tube. An electric heating gun was used to bond the assembly together. To achieve proper sealing, the heat was applied evenly starting bottom up in a round motion. The assembly was positioned horizontally and polyethylene tubes (0.3175 cm in diameter) and fittings were used to connect the water pump and pressure manometer to the core assembly. As only a very low differential pressure was required to flow fluid through the

fractured core, the inlet pressure was measured using a manometer tube rather than a transducer. The flow rate was measured using a balance and stop watch.

Prior to saturation, the core was dried at 75°C under vacuum pressure of 0.09 MPa for about 3 days, using a vacuum oven. Then, the core and related system were saturated with dionized water. Initially, the system was evacuated using a vacuum pump under vacuum pressure of about 13 millitorr for about 4 hours. The vacuum pump was connected to the system from the inlet side of the core. A water column used to saturate the system was attached at the outlet side of the core assembly. The water column was positioned on a scale to observe the weight change and hence the water volume entered the system.

The pore volume of the fractured core sample was determined by subtracting the dead volume of connecting tubes, fittings and end pieces from the total volume displaced from the saturation water column. The dead volume of tubes and pore volume were calculated as follows:

$$V_p = V_{total} - V_d \tag{2.7}$$

$$V_{total} = \frac{W_{total}}{\rho_w} \tag{2.8}$$

$$V_d = \pi r^2 l \tag{2.9}$$

where V_p and V_d are the pore and dead volumes in cubic centimeters, respectively. V_{total} is the total volume of water entering the system in cubic centimeters, W_{total} is the total weight of water entering the system in grams, ρ_w is the density of water in grams per cubic centimeters, l and r are the length and inner radius of tubes, respectively, in centimeters.

Based on the pore volume estimation, the porosity of the core sample was calculated as the ratio of the pore volume to the core bulk volume.

$$\phi = \frac{V_p}{V_B} * 100 \tag{2.10}$$

$$V_B = \pi r^2 l \tag{2.11}$$

where ϕ is the porosity in percentage, V_B is the bulk volume in cubic centimeter, r and l are the radius and length of the core in centimeter, respectively. The core sample was found to have a pore volume of 1.8 cm^3 and porosity of 2.9%.

The hydraulic aperture of the fracture was determined using the cubic law. The cubic law is given as:

$$Q = \frac{b^2}{12}\frac{bD\Delta p}{\mu L} \tag{2.12}$$

$$k = \frac{b^2}{12} \tag{2.13}$$

where Q is the flow rate in cubic meters per second, b is the fracture aperture in meter, D is the fracture width in meter, Δp is the pressure drop across the core sample in Pascal, L is the length of the fracture in meter, μ is the test fluid viscosity in Pascal second and k is the permeability in square meters. The average of the hydraulic aperture of the fracture was found to be approximately 27 μm. The average permeability of the rock was found to be 60 darcy. The fracture hydraulic aperture and permeability, total volume of water entering the system, dead volume of tubes, dead volume of end pieces, pore volume and porosity are summarized in Table 2.3. The pore size distribution (Figure 2.1) was obtained from the capillary pressure-saturation curve measured by mercury intrusion and Laplace's equation of capillarity. According to this approach, the greywacke sandstone has pores in the range from few nanometers (5 nm) to 200 nm in diameter. The average pore size was approximately 60 nm.

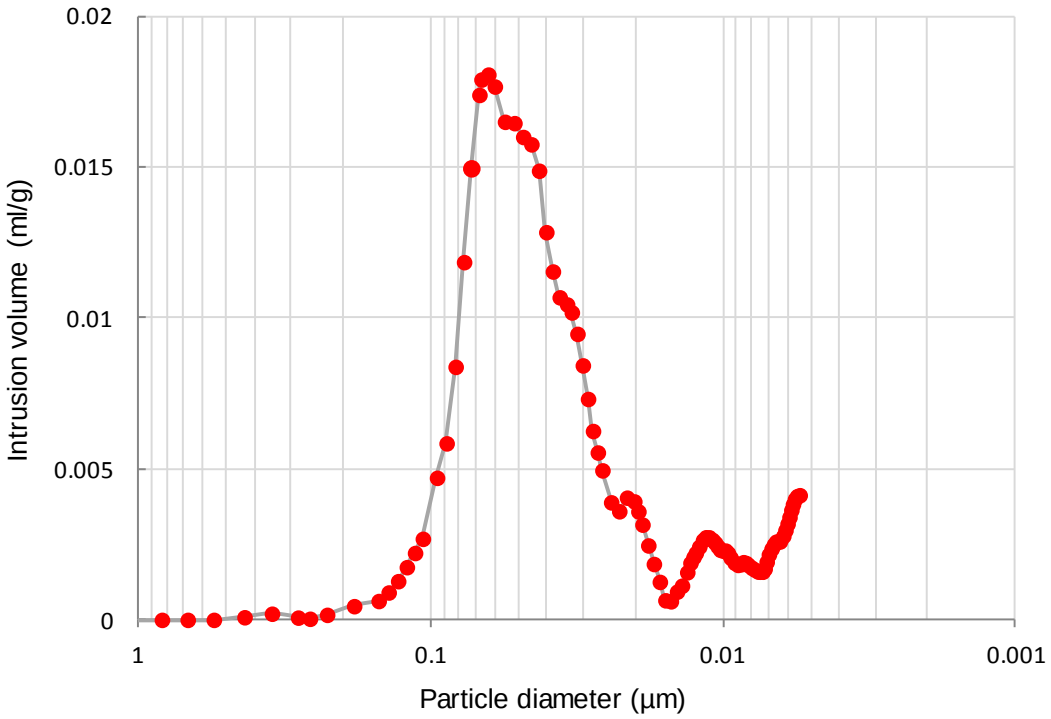

Figure 2.1: Pore size distribution of greywacke sandstone obtained by mercury intrusion, indicating an average pore diameter of about 60 nm.

2.3.3.4 Fractured Berea sandstone core preparation and characterization

The Berea sandstone core plug used this experimental study was 3.78 and 2.56 cm in diameter and length (Table 2.3), respectively. The core plug was fired at 700ºC for 2 hours. This firing

process was implemented because it stabilizes the indigenous fines and produces strongly water-wet conditions (Syndansk, 1980; Shaw et al., 1989). Prior to saturation, the core plug was dried under vacuum pressure of 0.09 MPa at 70ºC for 24 hours. The core was then saturated with testing fluid (i.e. ultrapure water prepared using Q-Millipore) inside the core-holder. The saturation was accomplished by evacuating the system (core plug and connecting tubing) to vacuum pressure below 50 millitorr. The system was left under vacuum for about 4 hours to ensure complete evacuation. The pure water was then introduced and the remaining vacuum was released to aid the process of saturation.

The rock sample was characterized in terms of its porosity, matrix permeability, grain density and pore size distribution. The porosity of the core plug was measured using by resaturation of the core (weight difference before and after saturation with testing fluid of known density), Helium expansion (gas pycnometer) and mercury intrusion methods and found to be 22%, 21.4% and 20.3%, respectively. The grain density measured by the gas pycnometer was 2.67 g/cm^3 and that by mercury intrusion was 2.57 g/cm^3. Matrix permeability was measured by introducing flow at different flow rates. The average matrix permeability was approximately 0.51 darcy. The pore size distribution (Figure 2.2) was obtained from the capillary pressure-saturation curve measured by mercury intrusion and Laplace's equation of capillarity. According to this approach, the Berea sandstone has pores in the range from few nanometers (5 nm) to as large as 50 µm in diameter, with the majority below 25 µm (d90). The average pore size (d_{50}) or (d50) was approximately 15.5 µm. The pore distribution also indicated that 10% of the total pores are smaller than 8 µm (d10).

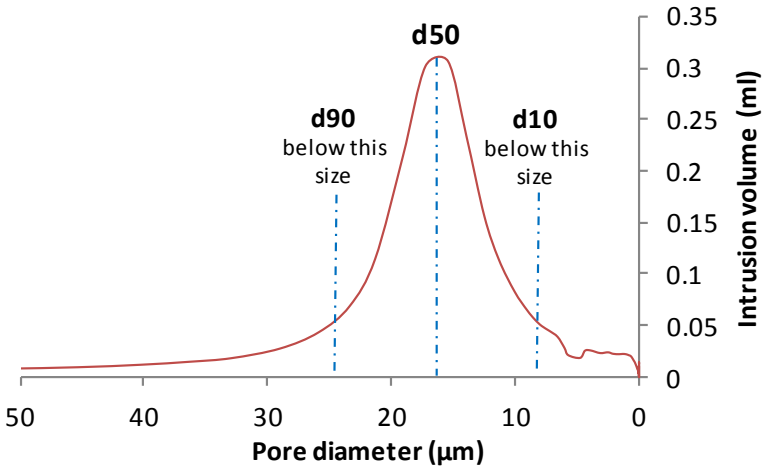

Figure 2.2: Pore size distribution of Berea sandstone obtained by mercury intrusion, indicating an average pore diameter of about 15.5 µm, 90% of pores are smaller than 25 µm and 10% are smaller than 8 µm.

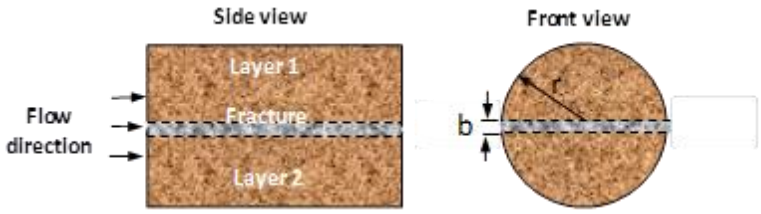

Figure 2.3: Schematic of the sandstone core plug with the location of the fracture. The fracture extends from the inlet to the outlet.

The fracture was initiated by saw-cutting the core plug into two pieces at the center. A schematic of the core showing the location of the fracture can be seen in Figure 2.3. The two pieces were then brought together using heat-shrink tubing. The hydraulic aperture of the fracture was estimated by considering the flow in parallel layers. Under conditions of flow in parallel layers, the pressure drop across each layer is the same. The total flow rate is the sum of flow rate in each layer. That is:

$$Q_t = Q_1 + Q_2 + Q_f \tag{2.14}$$

using Darcy's Law of incompressible horizontal fluid flow $Q = kA(\Delta p)/\mu L$,

$$k_t A_t = k_1 A_1 + k_2 A_2 + k_f A_f \tag{2.15}$$

Because $k_1 = k_2 = k_m$ and assuming $A_t = A_1 = A_2 = \pi r^2$, $k_f = b^2/12$ (cubic law) and $A_f = 2br$, then Equation 2.15 becomes:

$$b = \sqrt[3]{6\pi r(k_t - k_m)} \tag{2.16}$$

where r is the radius of the core plug in meter, k_t and k_m are the total and matrix permeability in square meters, respectively. Note that the matrix permeability (k_m) was determined before introducing the fracture. The hydraulic aperture of the fracture varied between 17.9 to 62.4 µm at different confining pressure ranging from 8.5 to 50 atmospheres. All particles injections were performed under confining pressure of 8.5 atmospheres. The maximum hydraulic aperture in these experiments was estimated to be 62.4 µm (k_t=1.20 darcy) using flow in parallel layers (Equation 2.16). The minimum aperture was approximated to be 3.79 µm by assuming the fracture permeability to be equal to the total permeability (1.2 darcy).

2.3.4 Micromodels Fabrication and Characterization

Micromodels have been developed to allow for flow visualization at the pore scale (Buckley, 1991). Micromodels are transparent networks of porous structures and channels. The porous structures can be an artificial pattern such as straight or staggered cylinders to simulate grains, or images based on real pore network found in natural rocks. Micromodels are two-dimensional systems and care must be taken when extrapolating the results to three-dimensional systems.

The etched silicon wafer micromodels used in this work were of the type described by Sagar and Castanier (1997). A pore network of a repeated pattern obtained from an SEM image of a Berea sandstone thin section (Figure 2.4a) was used. Continuity of repeated patterns was ensured by manipulating the image digitally (Figure 2.4b).

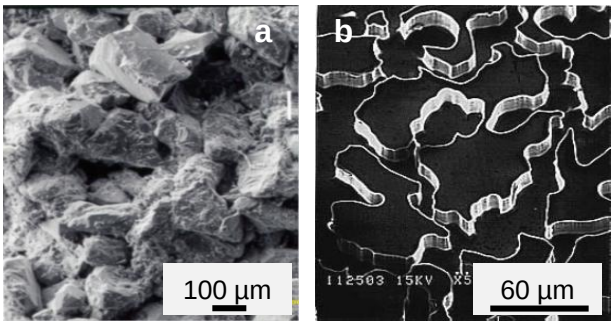

Figure 2.4: Berea sandstone thin section (a) SEM, and (b) digitally manipulated images (Rangel-Germán, 2002).

The micromodels we used are made of 4-inch silicon wafers, K Prime, 4P <100> B S42565. The micromodels in this study are etched pore patterns with two flow channels (fractures) (Rangel-Germán, 2002). Each pattern is about 490 µm by 400 µm repeated more than 100 times across each side of the 5 cm by 5 cm matrix region (Table 2.3). A schematic of the micromodel is shown in Figure 2.5. Grain sizes range from 30 to 300 µm and porosity of about 47% (Inwood, 2008). The absolute permeability was measured and found to be approximately 1 darcy (Inwood, 2008). The absolute permeability was remeasured and further details can be found later in this section.

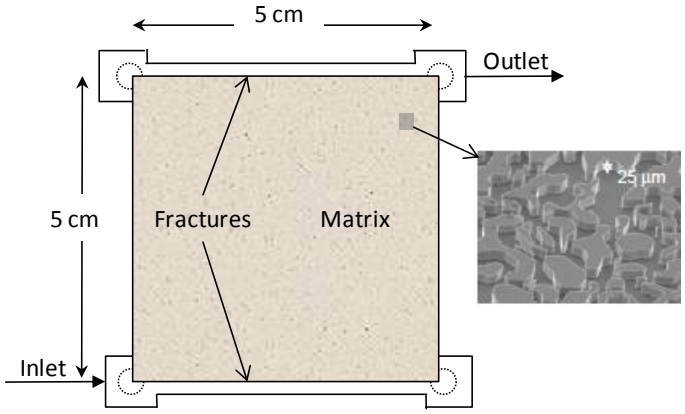

Figure 2.5: Schematic of the micromodel showing the repeated pattern and fracture channels (Rangel-Germán, 2002). Note that inlet and outlet port location were modified.

The fabrication of a micromodel begins with construction of a mask. The pore network image is reproduced as chrome on glass substrate. The grains on the glass replica are opaque while pores spaces are transparent. The image on the mask is transferred to the silicon wafer using a photoresist material (Hornbrook, 1991). Prior to the photoresist coating, the silicon wafer is dehydrated in an oven at 150ºC for about 30 minutes. Dehydration involves priming the wafer

with hexamethyldisilazane (HMDS) to improve the photoresist adhesion to the wafer (Alshehri, 2009).

A coating of the photoresist (Shipley 3612) is spun onto the wafer, resulting in 1.6 µm thick photoresist layer. The wafer is then baked at 90ºC for 2 minutes until dry. The wafer is exposed to the mask using Karlsuss MA-6 contact mask aligner. During exposure, ultraviolet light is passed through the mask, leaving only the photoresist coating at grains. Soft contact program with 2.6 seconds exposure time and 40-µm gap width is selected. The silicon wafer is developed using Shipley MF-26A surfactant to remove unexposed photoresist, and then baked at 110ºC for 2 minutes. After developing, the image transfer is completed and the wafer is removed from the photolithography area and is ready for etching.

The pore network image is dry etched using an inductive charged plasma deep reactive ion etcher. The etch process alternates between the passivating C_4F_8 plasma and the silicon etching SF6 plasma. The wafer is etched to a desired depth of approximately 25 µm. To isolate the individual flow channels, a borofloat glass wafer of 10.16 cm diameter and 0.1 cm thick is anodically bonded to the silicon wafer. In this work, 0.1 cm inlet and outlet ports were drilled, in the Stanford crystal shop, into the bonded glass substrate. Prior to bonding, wafers are cleaned in sulfuric acid/hydrogen peroxide (9:1 H_2SO_4:H_2O_2) solution bath at 120ºC for 20 minutes, followed by 6-cycle deionized water rinse and spin dry.

The anodic bonding forms an irreversible bond between the glass and unetched portions of the silicon wafer. The bonding process involves hotplate, electrodes and power supply. The materials are arranged from bottom up: anode, etched silicon wafer, glass wafer and cathode (Hornbrook, 1991). The bonding process starts by placing a clean silicon wafer (etched face up) on a hotplate preheated to 350ºC for about 30 minutes. The wafer is dusted using compressed ultrapure air to ensure that the etched side is particle-free. A clean glass wafer is then placed carefully on top of the silicon wafer. An aluminum plate wrapped with a copper mesh is positioned above the wafers. The hotplate is connected to one electrode (anode) of the power supply, while the positive electrode (cathode) is connected to the aluminum plate. The power supply is brought to 1000 volts and left for about 45 minutes (Rangel-Germán, 2002). The bonding is observed as gradual change in color of the wafer, bonded areas appear black whereas unbounded regions appear light gray (Hornbrook, 1991).

The permeability of the micromodel was measured at various flow rates ranging from 0.001 to 0.3 cm^3/min. Higher flow rates were avoided to avoid overpressurizing the micromodel. Initially, the micromodel and connecting tubes were all saturated fully with ultrapure water. Complete saturation of the micromodel was confirmed via image analysis. Darcy's Law of incompressible horizontal fluid flow was used to calculate the absolute permeability. Validity of Darcy's Law was confirmed by linearity between flow rates and measured pressure drop across the micromodel. The area used was the cross-sectional area at the fracture-matrix interface (i.e. 5 cm by 0.0025 cm, length and depth of micromodel). The average absolute permeability was found to be approximately 1.09 darcy, in agreement with previous measurements carried out by Inwood (2008), who used the same pore image mask.

Table 2.3: Summary of fractured Berea and Greywacke sandstones and micromodel properties.

Fractured Berea sandstone									
Diameter (cm)	Length (cm)	Porosity (saturation)	Pore volume (cm^3)	Matrix perm. (darcy)	Total perm. (darcy)	Aperture (µm)		Mean grain size (µm)	Mean pore size (µm)
						Max.	Min.		
3.78	2.56	0.22	6.3	0.51	1.2	62.4	3.79	150	15.5

Fractured Greywacke sandstone						
Diameter (cm)	Length (cm)	Porosity (saturation)	Bulk volume (cm^3)	Pore volume (cm^3)	Fracture perm. (darcy)	Aperture (µm)
5.08	3.01	0.029	61.1	1.8	60	27

Silicon micromodel						
Matrix area (cm^2)	Fracture area (cm^2)	Porosity (image analysis)	Pore volume (cm^3)	Permeability (darcy)	Grain size range (µm)	Channel depth (µm)
5x5	5x0.1	0.47	0.029	1.09	30-300	25

2.4 RESULTS

This section provides the results of the initial nanofluid injection experiments conducted on Berea sandstone, fractured Berea sandstone core and fractured greywacke core as well as slim tubes packed with glass beads, with different particle suspensions. We investigated the effect of the particle size and/or size distribution, shape and surface charge on their transport through various porous media. The effect of particle size, suspension concentration, fluid velocity and straining on particle recovery were investigated by injecting silica microspheres into the fractured Berea sandstone. Hypotheses made in relation to the specific experiment objective were also verified as applicable. The effect of the shape of the particles was explored through the injection of silver nanowires. The results were supported by injecting the same material of identical surface characteristics but with different shape (i.e. spherical silver nanoparticles). The surface charge was studied by injecting uncoated and PVP coated hematite nanorice. The affinity of nanoparticles to flow media was explored through the injection of tin-bismuth alloy nanoparticles. The effect of the particle size was investigated further by injecting polydisperse silica sample into fractured greywacke rock. Relation between recovered particles and fracture aperture was evaluated. Note that the influences of flow velocity, solution pH and ionic strength were not part of this study.

2.4.1 Silver nanowire and nanosphere injection

The objective of this experiment was to investigate the transport of rod-like nanoparticles through reservoir rock. We specifically explored the implication that the shape might impose on particle recovery. The silver nanowires injected had diameters in the range of 50-100 *nm*, and lengths in the range of 5-10 µm. Their surface charge was negative (i.e. same as the sandstone charge).

Silver nanowires were injected through the Berea sandstone core, however were not detected in the effluent. The effluent samples were analyzed and/or characterized using UV-visible spectrophotometry. Figure 2.6 shows the optical density measurements of the influent and selected effluent sample collected during injection. The influent had an optical signature (red curve) similar to typical silver nanowires reported in the literature (Sun et al., 2001). The optical density of selected effluent sample did not show any sign of silver nanowires. The spectrum of all effluent samples exhibited the behavior of pure water (flat lines). Note that effluent samples curves contain no further details than being flat lines, indicating that these effluent samples are free of any silver nanowires. This suggested that the silver nanowires were not transported, but rather trapped within the pore network of the sandstone core plug. The drop in the matrix permeability, as depicted in Figure 2.7, also suggested that flow paths were blocked by the silver nanowires. There was a drop in the permeability from approximately 94 to 51 md, or about 45% reduction. This drop began during the injection of the nanofluid and stabilized through the post-injection of the fifth pore volume. The core was backflushed by the injection of 11 pore volumes of pure water. The optical densities of representative backflushing samples of every pore volume were measured (not shown here). All exhibited the behavior of pure water, similar to that depicted earlier in Figure 2.6, indicating that the nanowires remained in the core and were not backflushed out.

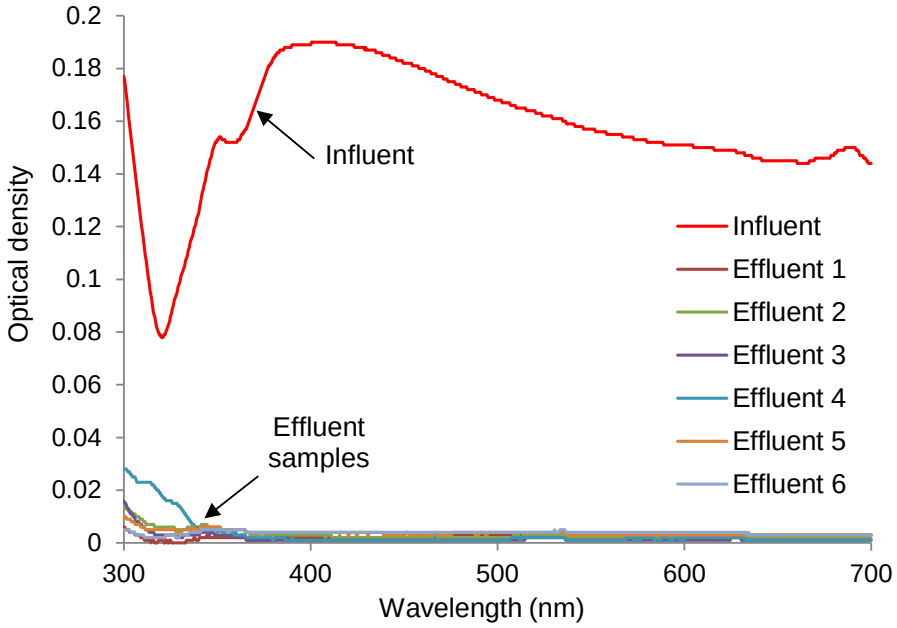

Figure 2.6: Optical density of silver nanowires influent (red curve) and selected effluent samples. Optical densities of effluent samples were flat lines indicating these samples are free of silver nanowires.

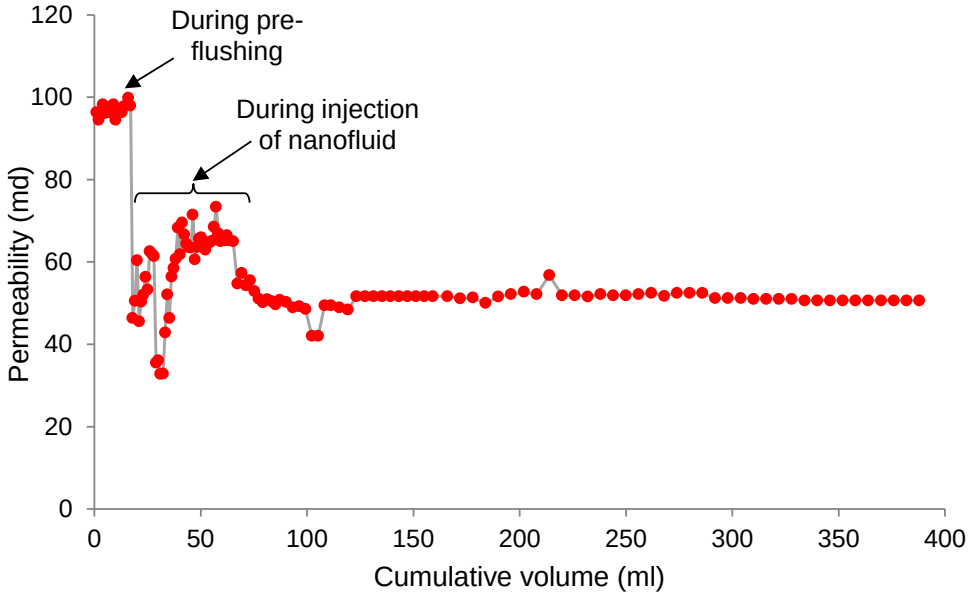

Figure 2.7: Permeability measurement during the silver nanowires injection experiment. Permeability dropped during the injection of the nanofluid until stabilized (plateau) at about 45% of initial permeability.

To investigate the hypothesis made regarding the entrapment of the silver nanowires, a 3 millimeter slice was cut at the inlet section of the core. The gas permeability was remeasured to assess the effect of the nanowires on the core after removing the few millimeters slice. The original gas and equivalent liquid permeabilities of the core were restored by cutting off that slice.

These findings suggested that the nanowires had been trapped within the removed slice. SEM imaging confirmed this unambiguously. The analysis was performed on the front and back sides of the slice. Figure 2.8 is SEM images of the front sides. The silver nanowires were clearly trapped at the front side. SEM micrographs (not shown) of the back side of the slice showed no sign of nanowires. This demonstrated that the nanowires could not pass through the pores of the core even for a couple of millimeters. It has been concluded that their geometry (longitudinal length) may have imposed constraint on their transport through the core. To verify this hypothesis, an injection of spherical silver nanoparticles into the same Berea sandstone (after removing the slice) was conducted.

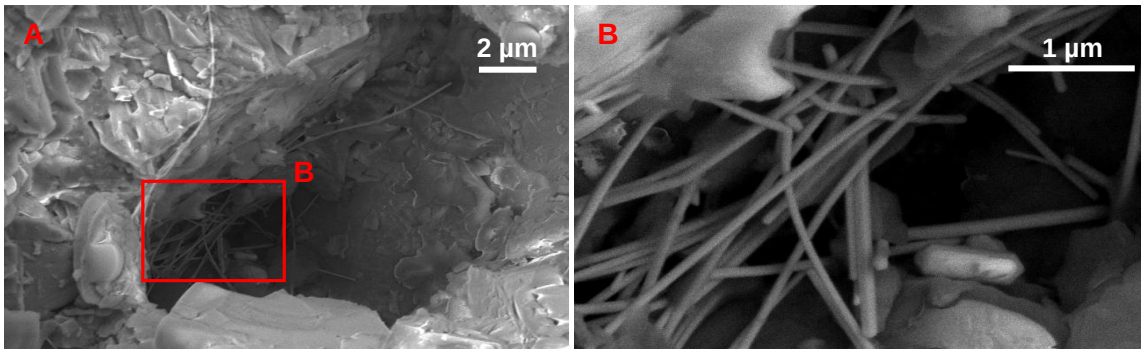

Figure 2.8: SEM imaging on the front side of the slice at different magnifications.

The spherically shaped silver nanoparticle size was around 40 nm ±10 with an average zeta potential of approximately negative 17 mV at pH of 7.9. The zeta potential for Berea sandstone saturated with pure water (ionic strength of 10^{-6}) was assumed to be -76.3 mV as suggested by Alkafeef et al. (1999). Pore size distribution measurement using mercury intrusion showed that Berea sandstone has pore sizes in the range of 0.1 to 50 *µm*. Note that the size of these nanoparticles was within the size of the pore spaces available for their flow. As the goal was to determine if nanoparticle shape would inhibit their flow, the main difference over the silver nanowires was the shape of the particles.

The spherical silver nanoparticles were transported through the pore spaces of the rock and were detected in the effluent. The concentration of the nanoparticles in the effluent samples was determined by measuring and correlating their absorbance to concentration using a calibration curve. The calibration curve was constructed by making few dilutions, each with accurately known concentration. For each dilution, the absorbance was measured and plotted against the sample concentration. This is the calibration curve. Following the determination of the effluent samples concentration, the production history curve of the silver nanoparticles was estimated as depicted in Figure 2.9. The initial breakthrough of nanoparticles occurred at about 30% of the first post injected pore volume and they were produced continuously until the bulk of the particles were displaced through the second pore volume.

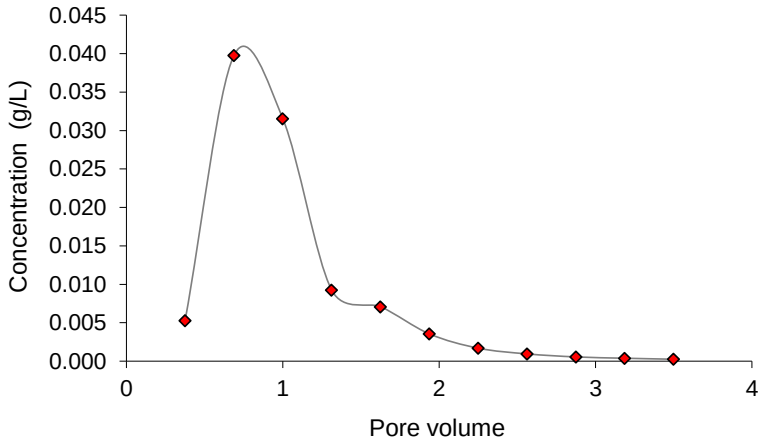

Figure 2.9: Production history (return curve) of silver nanoparticles.

The quantity of nanoparticles recovered was about 25%, calculated by integrating the area under the return curve. The low recovery was attributed to particle aggregation. Large aggregates or clusters can be physically trapped at small pore throats. Estimation of total interaction energy (Figure 2.10) indicated that the repulsive energy barrier is very shallow. When particles come at close proximity to each other, the energy barrier may be overcome by the attractive forces at the primary energy minimum. This would result in particle aggregation and the formation of large clusters. Clusters moving through narrow pore throats will be excluded from the flow by physical entrapment due to their size, and thus low recovery. The permeability of the core was not affected because entrapment of nanoparticles at pores would still allow water to flow. Despite the modest recovery of these nanoparticles, it was clear that the shape was an important factor for their transport through the pores of the sandstone core.

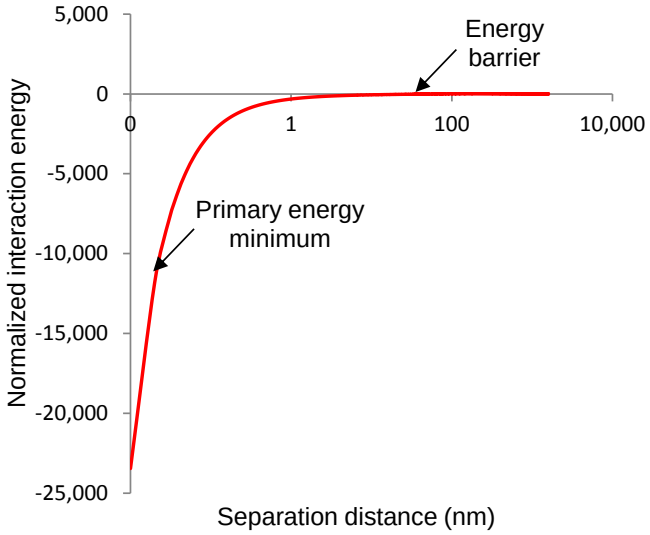

Figure 2.10: Total interaction energy between silver nanoparticles. The interaction energy is normalized to the thermal energy (Boltzmann constant and absolute temperature). Hamaker constant used is 28.2×10^{-20} J as per Israelachvili (1992) for silver-silver nanoparticle in water.

2.4.2 Hematite nanorice injection

Injection of hematite nanorice was conducted to investigate their mobility within the pore spaces of Berea sandstone. The purpose was to investigate the constraint imposed by the surface charge of nanoparticles. The nanoparticle size was roughly 500 *nm* in length and 100 *nm* in diameter, resulting in an aspect ratio of 5:1. By comparison, the hematite nanorice was at least an order of magnitude shorter than the silver nanowires injected previously, and was carrying a positive charge of 59.3 mV with pH of 3.3. Thus, the nanorice was also used to test the hypothesis made regarding the entrapment of the silver nanowires due to their geometry (length).

Hematite nanorice was not identified in the effluent. Light scattering, UV-visible spectroscopy and scanning electron microscopy were used to examine the effluent samples, in which no nanoparticles were detected. The hematite nanorice was, however, observed within the pores at the inlet side of the core as illustrated by SEM micrographs in Figure 2.11.

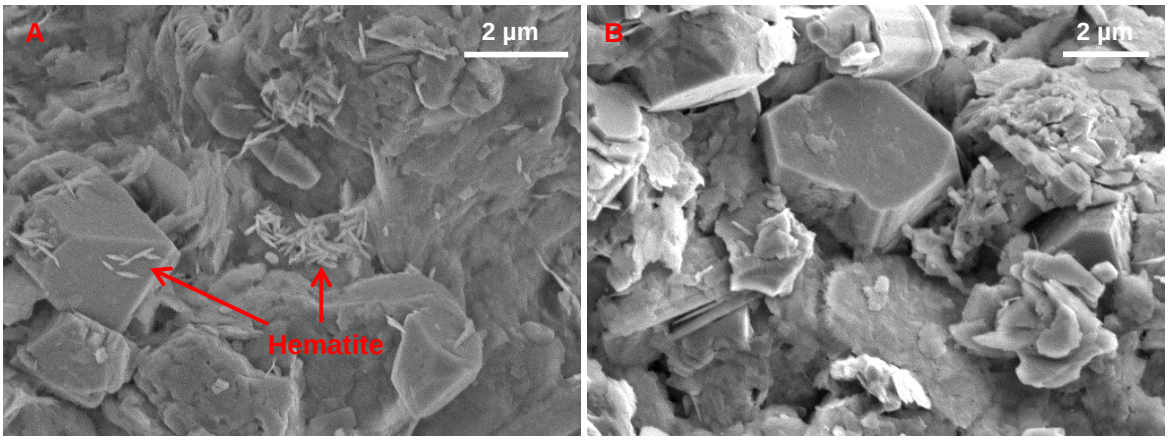

Figure 2.11: SEM imaging of hematite nanorice in Berea sandstone at (A) front side, (B) back side of the slice (free of nanorice).

Similar to the analysis for the silver nanowires, a thin slice of the core at the inlet was cut and SEM imaging was performed on both sides. Hematite nanorice were observed on the front face but not on the back face. We speculated that the entrapment of the nanorice resulted from interaction with core material due to either incompatibility of surface charges or chemical interaction of hematite with core constituents. The size of the nanorice (aspect ratio) and complexity of pore connectivity of Berea sandstone might have contributed to their entrapment, however, results of the nanorice injections into glass beads (explained later) suggested that surface charge effect was dominating. Poulton and Raiswell (2005) reported that the natural spherical iron oxides nanoparticles (10-20 nm) in sediments tend to aggregate at the edges of clay grains, most likely because of their surface charge characteristics. Tipping (1981) and Tipping and Cooke (1982) observed that iron oxides were negatively charged in fresh water while the edge of clay has positive charge which may explain the particle aggregation at that location. The micrographs in Figure 2.11 do not provide conclusive evidence of this interaction between the sandstone clays and the hematite nanorice. Nevertheless, this result suggested that there was interaction between hematite nanorice and the sandstone core materials and/or among the nanorice in the form of particle aggregation. To investigate the interaction of hematite with core materials, the hematite nanorice was injected into a porous medium that consisted of a tube packed with glass beads (in the absence of core materials). The glass beads were negatively charged, so the incompatibility of surface charges still exists.

An extremely low particle count was observed using SEM imagery of several effluent samples at different post-injected pore volumes. The particles were mostly found aggregated on the surface or within the surface defects of the glass beads themselves (Figure 2.12). The optical density of the hematite suspension during this injection could not be measured due to their low concentrations, and thus the concentration of hematite nanorice in the effluent relative to the concentration in the influent could not be determined. However, it was determined that in the absence of the clays (during hematite nanorice injection into glass beads), the nanorice exhibited very low mobility and thus interaction with core materials was not the main factor behind the nanorice entrapment within pore spaces of the Berea sandstone. Despite that fact that the pore connectivity in packed glass beads is less complex than that of Berea sandstone and the pore sizes in packed glass beads are expected to be larger, the recovery of the hematite nanorice was

negligible. This suggests that the entrapment of the nanorice was not due to the particle size or aspect ratio. Therefore, it was concluded that the incompatibility of surface charges was limiting the transportation of the hematite nanorice through the sandstone and glass beads.

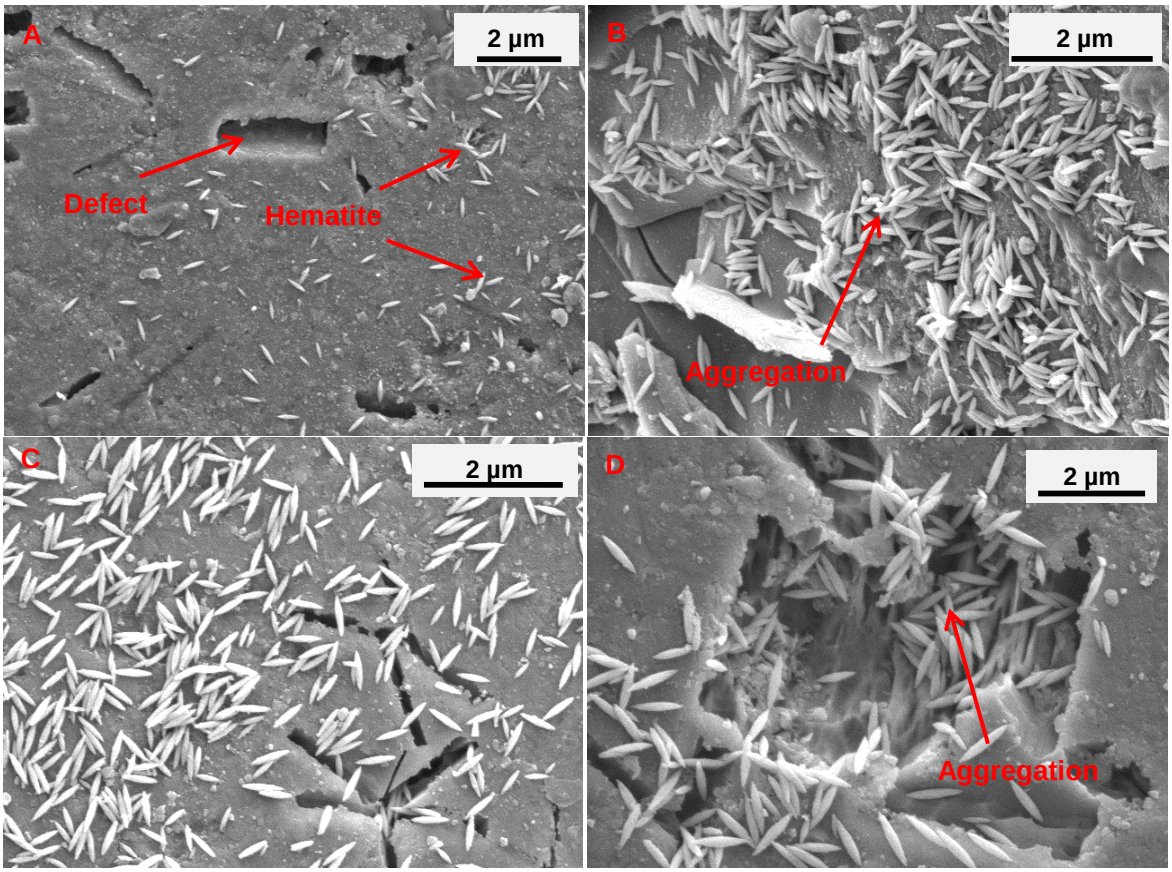

Figure 2.12: Hematite nanorice aggregation on the surface of glass beads at (A) & (B) inlet and (C) & (D) outlet side of the flow apparatus.

To confirm this conclusion, the hematite nanorice was coated with the surfactant (PVP) to modify its surface charge. The coated with PVP surfactant carried a negative charge of 9.5 mV with pH 4.8) compared to the uncoated nanorice (positive 59.3 mV, pH of 3.3). The coated hematite nanorice was then injected into a clean tube packed with glass beads. The nanorice was transported through the glass beads and was detected in the effluent. The recovery of coated hematite nanorice amounted to about 23% of influent concentration (Figure 2.13). The low recovery was attributed to size exclusion (particle removal by physical entrapment due to size) due to aggregation. As can be observed in Figure 2.7, the anisotropic hematite particles have a tendency to aggregate in clusters. Lu et al. (2002) reported that hematite nanorice often aggregate in large clusters as a result of anisotropic dipolar forces. This aggregation would limit the transport of the nanorice through pore networks, due to bridging of the pores. Because the nonspherical particles are anisotropic with respect to curvature, they are also anisotropic with respect to chemical potential, which is highest where the radius is smallest. Thus, nonspherical particles are more prone to aggregation than spherical ones with isotropic curvature. Furthermore, the aggregation can be expected to occur most where the radius of curvature is small in order to cover parts of the surface with high free energy. This can be observed in Figure 2.12. As a result of aggregation, large cluster forms. If the cluster flows along a streamline that

passes through pore throats smaller than the size of the cluster, it will be excluded from the flow based on its physical size.

While the recovery was not high, it was substantially higher than that achieved during the injection of the uncoated (positively charged) hematite, which confirms the influence of surface charge on the transport of nanoparticles (the objective of these experiments). This also confirms that the recovery was less sensitive to aspect ratio of nanorice because the coating of nanorice did not alter the size but only their surface charge. Based on this finding, it was concluded that the surface charge plays an important role on the transport of nanoparticles through porous media.

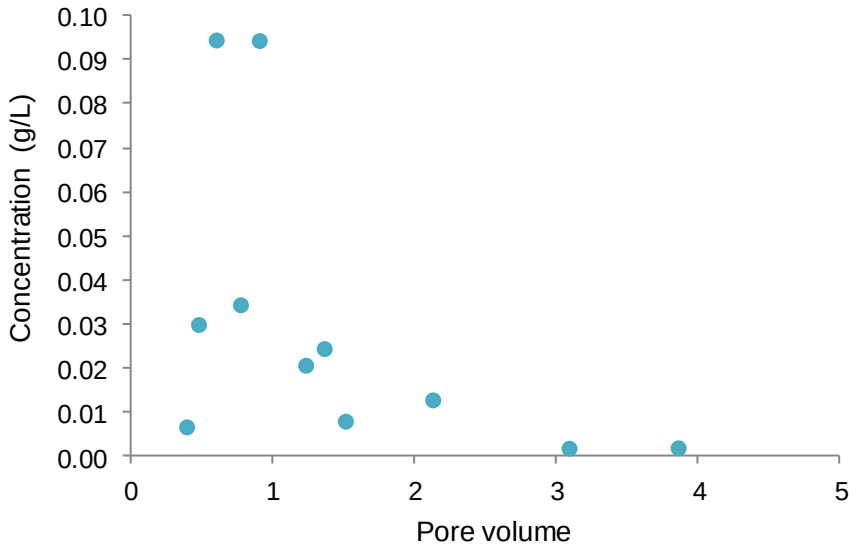

Figure 2.13: Production history (return curve) of PVP-coated hematite nanorice.

2.4.3 Tin-Bismuth alloy nanoparticles injection

The objective of the tin-bismuth injection experiment was investigate their transport through porous media. The affinity of nanoparticles to the flow medium was also addressed. The nanoparticle suspensions were injected into a slim tube packed with glass beads and into a Berea sandstone core. Alaskar et al. (2010) showed that spherically shaped silicon dioxide nanoparticles with narrow size distribution and surface charge similar to that of the porous medium can be transported and recovered. The synthesized tin-bismuth nanoparticles had comparable specification (spherically shaped and negatively charged, 30 mV), except that the influent contained a wider size distribution of particles from 50 to 600 nm.

Tin-bismuth nanoparticles were identified in a few effluent samples with very low concentrations. It was observed that only nanoparticles with diameters 200 nm and smaller were transported within the pore spaces of the rock, as shown in the SEM image in Figure 2.14A. Note that the influent sample contained nanoparticles as large as 600 nm. It was speculated that larger particles (greater than 200 nm) were trapped at the inlet of the core. In fact, SEM imaging of the backflushing effluents showed that there was entrapment of various nanoparticle sizes, including

the sizes greater than 200 nm (Figure 2.14B). The rock filtered the injected nanofluid allowing only a certain particle sizes to flow through it. It should be noted that this is a qualitative analysis in which the determination of the relative number of particles recovered was not attempted.

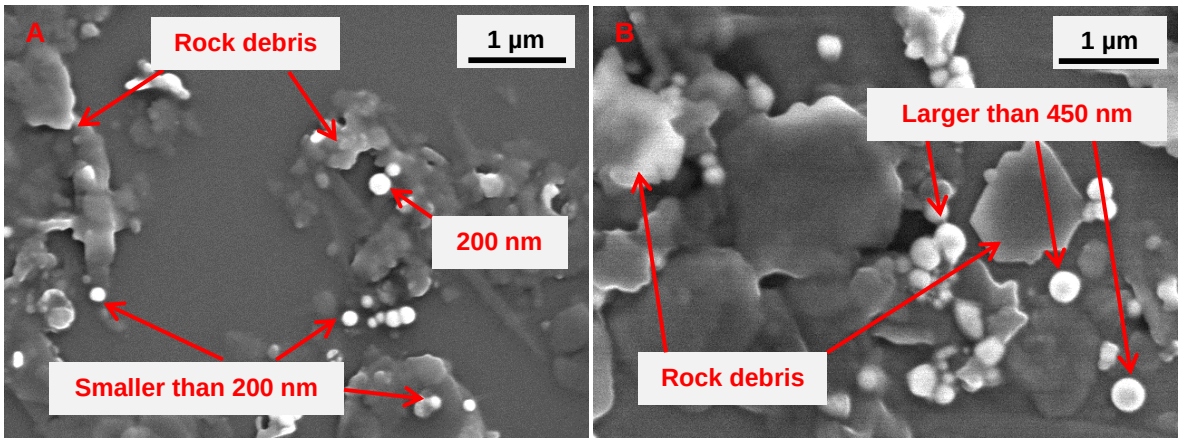

Figure 2.14: SEM imaging showing the tin-bismuth nanoparticles at the effluent during (A) injection and (B) backflushing of the Berea sandstone. Only particles smaller than 200 nm transported through pore spaces while larger particles trapped at the inlet of the core and mobilized during backflushing.

The permeability measurements during the injection agree with this finding. The permeability as a function of the injected volume is depicted in Figure 2.15. There was a sudden drop in permeability to about 56% of the original value, after which the permeability remained at that level during the first post-injected pore volume, indicating the partial plugging of the pores. Then, permeability started to increase until it reached a plateau at approximately 82% of its value prior to the nanofluid injection. At this time, only nanoparticles of 200 nm and smaller were observed in the effluent, using SEM imaging (Figure 2.14A). As mentioned earlier, the backflushing of the core mobilized some particles (but not all) and as a result the permeability of the rock improved slightly by 8% (i.e. back to 90% of its original value).

However, permeability improvement (from 56% to 90% of original value) does not imply a good recovery of the injected nanoparticles. If the injected nanofluid has a visible color, it is possible to observe the nanoparticles in the effluent visually. In the case of the tin-bismuth injection, the influent had a dark gray color that was characterized by being highly concentrated with nanoparticles. All effluent samples appeared colorless and transparent, so it was concluded that many of these nanoparticles were trapped within the rock pores, most likely at the inlet of the core.

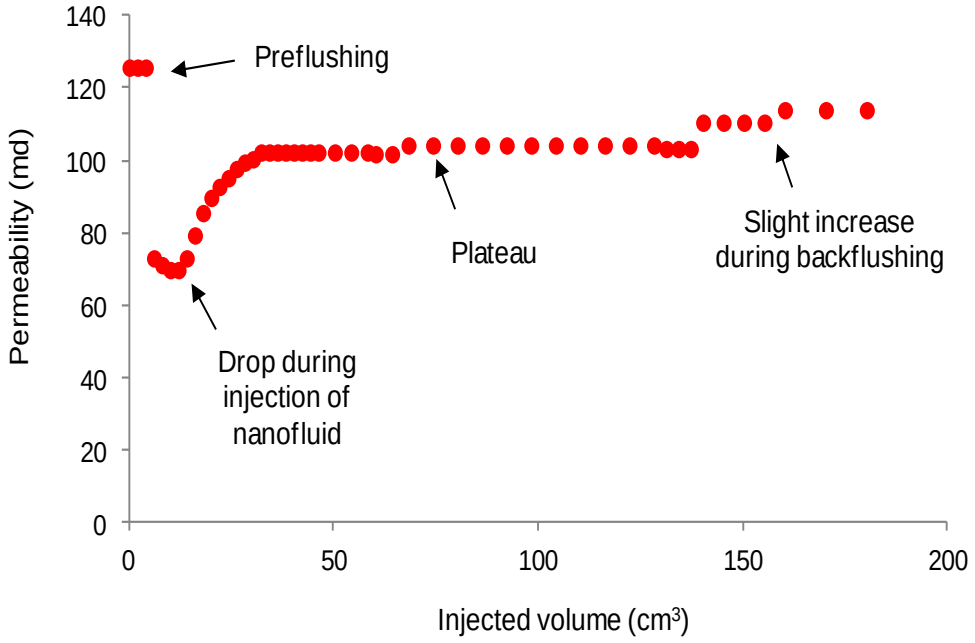

Figure 2.15: Permeability measurements during the injection of the tin-bismuth nanoparticles.

Further evaluation using SEM imaging (Figure 2.16) of the rock pore spaces demonstrated the bridging and plugging of the tin-bismuth nanoparticles in the pore throat entry. Kanj et al. (2009) suggested that small particles at high concentrations might bridge across the pore throat. The authors also added that large particles could result in direct plugging of the pore entry. Both phenomena would impact the rock permeability negatively. Particles shown in Figure 2.10 could not be mobilized either by increasing the injection flow rate or by backflushing and were probably responsible for the permanent reduction in the rock permeability. The SEM analysis did not provide conclusive evidence of the mechanism of particle entrapment. However, it was realized that the polydisperse nanofluid sample was more effective in plugging the pores. One could observe how smaller particles aggregate around larger ones to fill the tinier spaces and hence effectively plug the pore spaces.

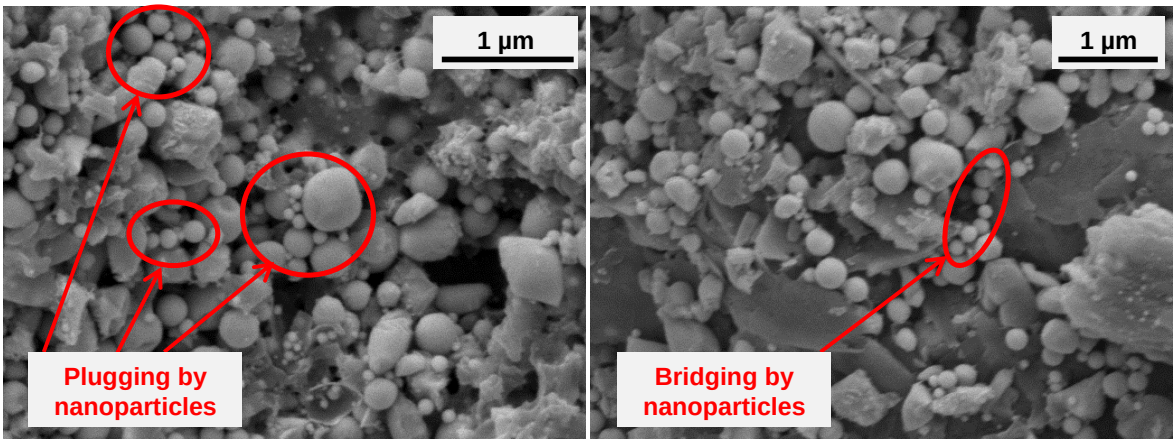

Figure 2.16: SEM images from within the pore spaces of the Berea sandstone. They demonstrate

the bridging and plugging phenomena.

Alaskar et al. (2010) reported that the spherical silicon dioxide (SiO_2) nanoparticles with narrow size distribution and surface charge compatible to that of the rock were transported successfully through the pore spaces of Berea sandstone. The tin-bismuth nanoparticles exhibit similar properties in terms of shape and surface charge (negatively charged), except that the tin-bismuth nanoparticles had a wider distribution of sizes between 50 to 600 nm. Thus, particle shape and surface charge should not impose flow constraints. The testing program suggested by Kanj et al. (2009) for nanoparticle flow in porous media emphasizes particle size, influent concentration and affinity of particles to rock matrix. In the case of tin-bismuth injection, although the influent sample had wide distribution of particle sizes that might have introduced difficulty for their delivery, the tin-bismuth nanoparticles affinity and/or concentration may be the primary cause of their entrapment.

Further investigation of particle affinity to Berea sandstone was carried out by injecting the same influent sample of the same concentration into a slim tube packed with glass beads. This allowed testing the transport of the tin-bismuth nanoparticles in the absence of the core material. One pore volume of the nanofluid was injected at the rate of 0.5 cm^3/min followed by continuous injection of pure water at the same rate. Several effluent samples were collected and analyzed by SEM imaging. It was found that the tin-bismuth nanoparticles of all sizes flowed through the slim tube. The increasing concentration of the nanoparticles in the effluent was observed visually through the injection of the first post-injected pore volume.

Thus, it has been demonstrated that the spherically shaped tin-bismuth nanoparticles can be recovered following their injection into glass beads without being trapped within the flow conduits, but not through the pore network of the rock (which has much smaller pores). This might be attributed to an affinity of these nanoparticles to the sandstone rock matrix and the wide size distribution imposing constraints to their flow. The complexity of the rock pore network compared to the large pores in the glass beads was not taken into consideration during this analysis. It should be noted that the pore network in glass beads is expected to be less complex compared to that of a natural rock such as Berea sandstone. The pore sizes are also larger than those in real rocks. This would aid the transport of large particle during the glass bead injection.

2.4.4 Fluorescent silica microspheres injection into fractured greywacke core

The objectives of this experiment were to investigate the transport and recovery of silica microspheres through fractured greywacke core sample, and study the relationship between the size of recovered microparticles and fracture aperture. Based on the previous experiments discussed earlier with regard to the transport of particles of various nanomaterials with different size, shape and surface charge, it has been found that spherically shaped particles of certain size and surface charge compatible to that of the flow medium are more likely to be transported. The fluorescent silica microspheres used during the fractured greywacke satisfy these conditions (i.e. spherically shaped with surface charge similar to that of fractured media). To investigate the optimum particle size and its relation to fracture aperture, silica microspheres of different sizes were injected.

The sequence by which the transport of the silica microspheres through the fractured greywacke core was investigated was as follows. Initially, the blue and green microsphere suspensions of concentration (C) were injected, followed by the injection of the blue and green microsphere suspensions of double the concentration (2C). Following each injection, effluent samples were collected. Due to the polydisperse nature of the red silica microspheres and concerns regarding plugging of the fracture by large spheres, particle suspensions (C and 2C) were injected at the end.

The fluorescent silica microspheres were transported through the fractured greywacke core successfully. As mentioned earlier, the silica microspheres influent samples of the same concentration (but different size) were consecutively injected. The silica microspheres were identified in the effluent samples using optical microscopy and fluorescence spectroscopy, confirming their delivery through the fracture.

The recovery of the silica microspheres was determined by measuring the emission spectrum and correlating it to the effluent concentration using a calibration curve. The samples were excited at a wavelength of 350 nm and the emission spectrum was measured between 350 to 600 nm, with a peak or maximum emission at a wavelength of about 434 nm. To construct the calibration curve, the emission spectra of a few samples of known concentrations were acquired. The concentrations of effluent samples were determined based on the maximum emission intensity at the peak. The return curves of the blue microspheres were then estimated as depicted in Figure 2.17. It was found that about 54% of the injected blue suspension at concentration (C) was recovered. The microspheres were produced throughout the post injection at roughly constant level ($\pm 1.5\times10^{-5}$ g/cm^3), with no clear or identifiable peak. On the other hand, only 19% of the (2C) blue suspension was recovered, mostly during the post injection of the first five pore volumes.

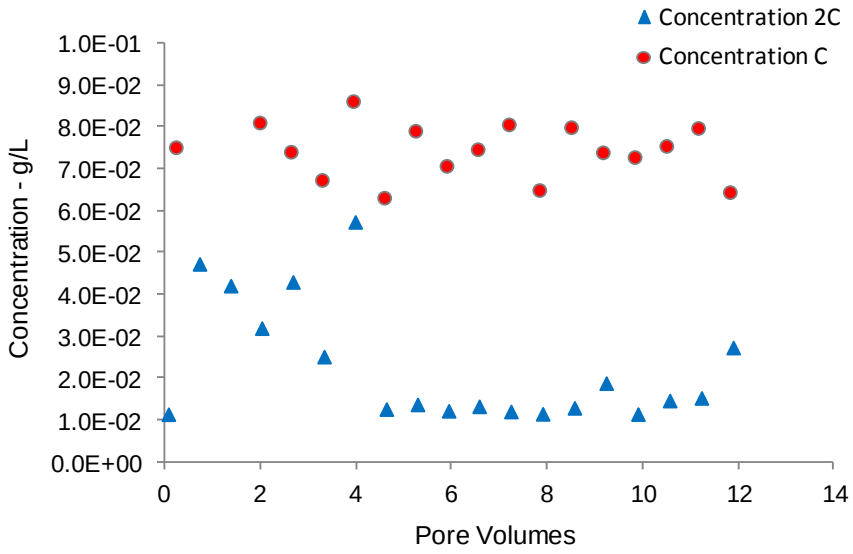

Figure 2.17: Blue silica microspheres return curves.

The return curves for the blue silica microspheres showed a very fast arrival. The first arrival of the particles occurred within 0.09 to 0.2 pore volume from the start of their injection. This suggests that the recovered particles were moving through the fracture, not the core matrix. The pore size distribution of greywacke sandstone (see Figure 2.1) indicated that the core has pores in the range of 5 to 200 nm. The largest pore is significantly smaller than the blue silica microsphere (2 µm), and thus trapped particles were most likely retained at the small pore spaces (at the inlet) in core matrix and fracture walls in regions with small apertures. It was observed that the recovery of the silica microspheres is inversely proportional to the particle suspension concentration. The recovery of the microspheres decreased with increasing particle suspension. This may suggest that there was particle-particle interaction, causing the microspheres to aggregate. As the suspension concentration increases, more particles are present, resulting in larger aggregates or clusters. When these clusters flow through areas of narrower aperture (areas where fracture surfaces are closer to each other), they will be trapped because of their physical size, and thus low recovery. The particle-particle interaction energy estimated for the blue silica microspheres, as depicted in Figure 2.18, shows low repulsive energy barrier, which might be overcome by the attractive forces at the primary energy minimum at small separation distances. This is consistent with the fact that the blue microspheres experienced lower recovery with increasing concentration (i.e. higher concentration resulted in larger clusters, due to aggregation, that led to further plugging and thus low recovery).

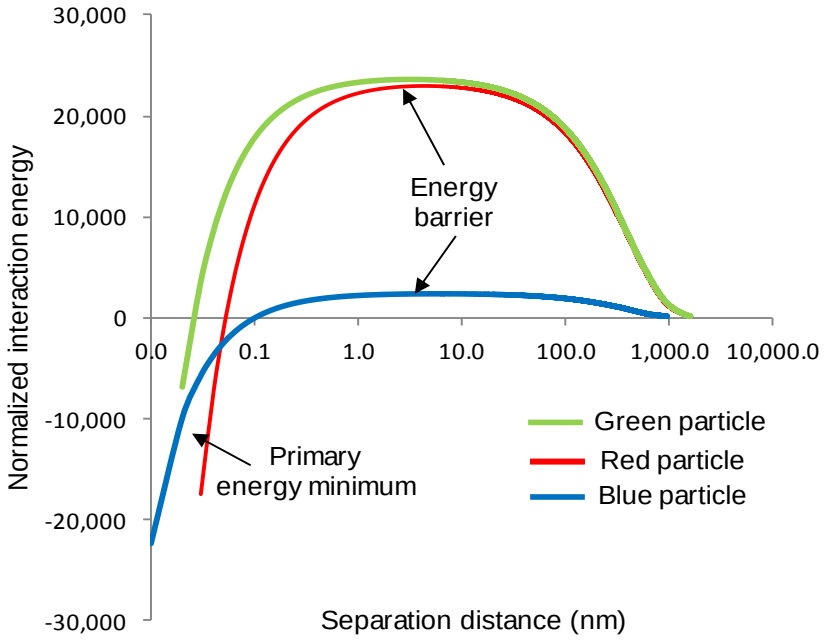

Figure 2.18: Total interaction energy between particle-particle of the blue, green and red microspheres. The interaction energy is normalized to the thermal energy (Boltzmann constant and absolute temperature). Hamaker constant used is 6×10^{-21} J as per Grabbe and Horn (1993) for silica-water-silica system. Note that an average particle size of 10 µm was used in the case of the red particles.

Estimating the recovery of the green silica microspheres based on concentration was not feasible due to discrepancies in the emission spectra measurement during the construction of the calibration curve. Instead, we attempt to estimate the average recovery of the green spheres by calculating the cumulative ratio of emission intensity of effluent (E_e) to emission intensity of influent (E_i), as shown in Figure 2.19. The effluent and backflushing samples were excited at wavelength 480 nm and the emission spectrum was acquired between 480 to 700 nm, with maximum emission at wavelength of about 525 nm. The transport of the green silica microspheres was mainly through the fracture as indicated by their early arrival. The recovery of the green microspheres was improved with increasing concentration. The influence of the green microsphere suspension concentration was totally opposite to that of the blue microsphere concentration (recovery decreasing with increasing concentration). The estimation of the total interaction energy (Figure 2.18) among the green microspheres suggests a high repulsive energy barrier, which would prevent the particles from aggregation. Instead, the particles will repel from fracture surfaces and from each other and remain disperse in solution. Therefore, increasing suspension concentration of the green microspheres may not cause in aggregation that often result in low recovery. We speculated that the low recovery of the green microspheres was related to transport by gravitational sedimentation. Note that the density of the silica microspheres is more than twice that of injected water (i.e. 2.2 g/cm^3). During transport by sedimentation, particle moves across streamlines, due to gravity forces and associated settling velocity, until it collides with fracture surface. The particle may attach to the surface if attachment conditions are favorable. In the case of the green microsphere injections, the attachment conditions are unfavorable (pure water and compatible surface charge between particles and flow medium). In fact, even if the microspheres collide with the fracture surface, the repulsive energy barrier should prevent them from attaching. Therefore, it was concluded that the low recovery of the green silica microspheres was primarily due to gravity settling. The drag forces at fluid velocity used during injection was not sufficient to offset gravity forces. The effect of fluid velocity was not assessed since the objectives of the fracture experiments were only to investigate the influence of the particle size and its relation to fracture aperture.

Owing to the existence of surface irregularities in fractures, it is very possible that a flow channel in the fracture at or below the size of injected microspheres exists along a preferential flow path. Consequently, entrapment of particles due to their physical size will result in their accumulation at narrow aperture areas and, therefore, the blockage of that flow path. Blocked flow paths are a dead-end for subsequent particles, which eventually results in reduction of particle recovery. The permeability measurements (i.e. pressure data) support the fact that the number of conductive flow paths available to particles decreased due to blockage. Figure 2.20 shows the permeability measurements conducted prior and during the injection of the blue and green silica particles at two different suspension concentrations. The permeability continued to decrease as more particles injected. The permeability decreased to approximately 22 darcy by the end of the green microsphere (of concentration C) injection. This reduction in permeability indicates a degree of blockage, supporting the argument that blockage occurred in some of the preferential flow paths. After that, the permeability decreased slightly as more particles were injected (during the injection of blue and green silica microspheres at concentration of 2C). The slight decrease in permeability following the injection of concentrated suspensions can be explained by the fact that small flow paths were already plugged during previous injections (injection of blue and

green suspensions at concentration C), and the flow of subsequently injected particles was redirected to areas of wider apertures where trapping by particle size is expected to be less.

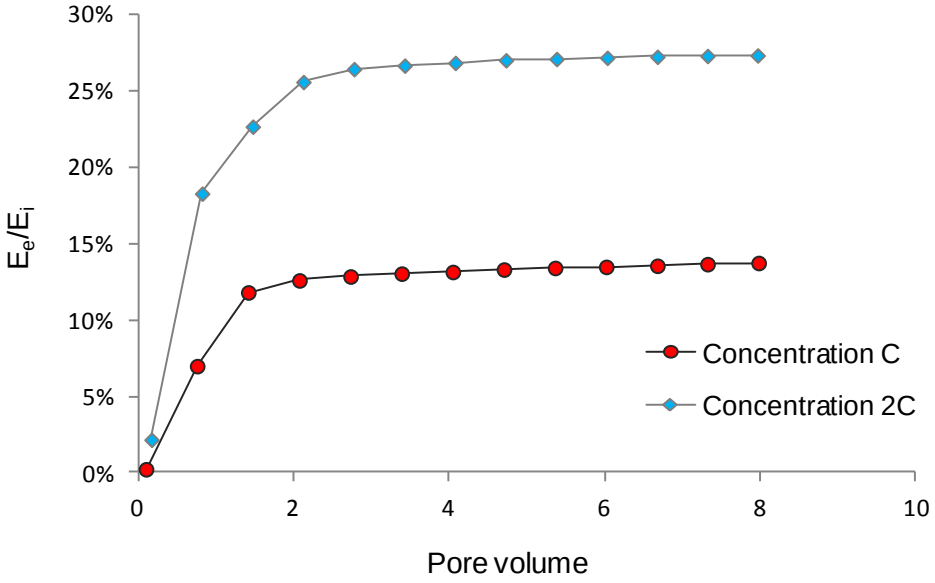

Figure 2.19: Green silica spheres cumulative ratio of emission intensity of effluent (E_e) to influent (E_i) as function of pore volumes injection. The backflushing samples start at about the seventh pore volume in this graph.

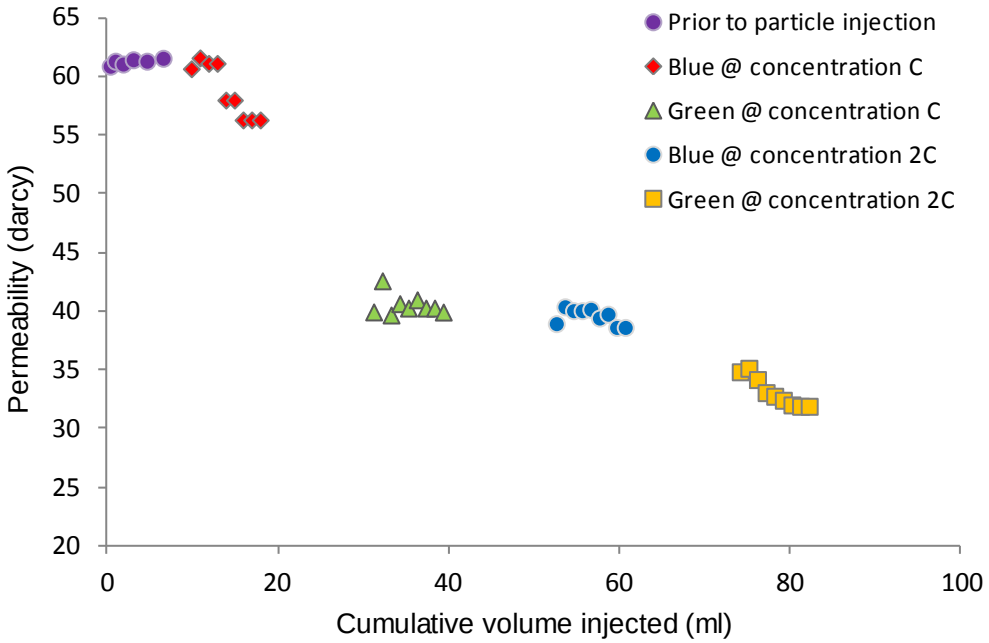

Figure 2.20: Permeability measurement prior and during the injection of the blue and green silica microspheres at different concentrations. The permeability is decreasing as more microspheres injected.

We have demonstrated the feasibility of transporting nanoparticles and/or microparticles through a fractured greywacke core. In terms of characterizing the fractures in the rock, which is a primary objective of the project, the preliminary experiments showed promise. The preliminary testing involved injection of silicon dioxide (SiO_2) nanoparticles through Berea sandstone. The details for the preliminary experimental work can be found in Alaskar et al. (2010). It was found that the nanoparticles passed through pores of sizes larger than themselves, but were unable to pass into the smaller natural fractures that existed within the rock structure. A smaller nanoparticle could have entered the fracture providing a direct correlation between the recovered particle size and fracture aperture. Therefore, it may be possible to use nanoparticles as a fracture aperture caliper.

Investigation into the idea of using particles to measure the fracture aperture was carried out by injecting the polydisperse red silica microspheres (diameter ranging from 5 to 31 μm) into the fractured greywacke core. It was found that only microspheres with diameters smaller than 20 μm were transported through the fracture. This suggested that the fracture has an aperture of at least 20 μm, but not as large as 31 μm. This result was in agreement with the hydraulic fracture aperture measurement (i.e. 27 μm as determined by the cubic law), and demonstrates the possibility of using particles to estimate the size of the fracture opening.

The recovery of the red silica microspheres was determined by calculating the ratio of fluorescence emission intensity of effluent to that of the influent. Two influent samples of different concentration of red spheres were injected one after the other. Note that the fractured core was flushed with many pore volumes prior to the injection of the red spheres; in attempt to mobilize remaining microspheres from previous injections (blue and green silica spheres). The core was also dried and resaturated again. The return curves based on the cumulative emission intensity ratio as function of pore volume injected were similar to those of obtained during the green silica microspheres injection. The particle recovery was dependent on the influent concentration. . The recovery of the most dilute influent was around 15.7%. Acquiring the emission spectrum of some effluent and backflushing samples was not possible, because fluorescence levels in these samples were below detection limit of the instrument. The recovery was improved to 47.5% when the concentration of influent was doubled (i.e. concentration 2C).

Similar to the blue and green silica microspheres, the red microspheres were transported through the fracture, as indicated by the very fast initial breakthrough. The recovery of the red microspheres was proportional to the suspension concentration. The particle recovery was increased by about a factor of three (from 15.7 to 47.5%). Conclusions with regard to the entrapment of the red microspheres were similar to those concluded for the green microspheres. To be specific, the transport of the red microspheres was dominated by gravitational sedimentation due to their density. Note that the red silica sample is polydisperse with diameter between 5 to 31 μm. Large particles are more susceptible to settling by gravitational forces, and hence sedimentation was prominent during the flow of the red microspheres through the fracture. Gravitational forces were higher than drag forces at injection flow rate or fluid velocity, which caused the particles to settle resulting in lower recovery. Interaction among particles was highly repulsive (Figure 2.12). The repulsive energy barrier would prevent particle aggregation that might result in trapping. However, a single particle can be trapped based on its size (not

aggregate size). This is consistent with the fracture caliper results where particles larger than 20 µm were not detected in the effluent samples. Large particles may have flowed along streamlines that pass through areas of narrow aperture between fracture surfaces. If the particle has comparable or larger diameter than the flow channel, it will be physically trapped.

2.4.5 Fluorescent silica microspheres injection into fractured Berea core and silicon micromodel

2.4.5.1 Silica injection into fractured Berea sandstone core

The transport of silica particles was investigated by flow experiments in the fractured Berea sandstone core plug. For this purpose, the particle suspension concentration, particle size and fluid velocity were varied. The effluent breakthrough curves are presented in Figure 2.21.

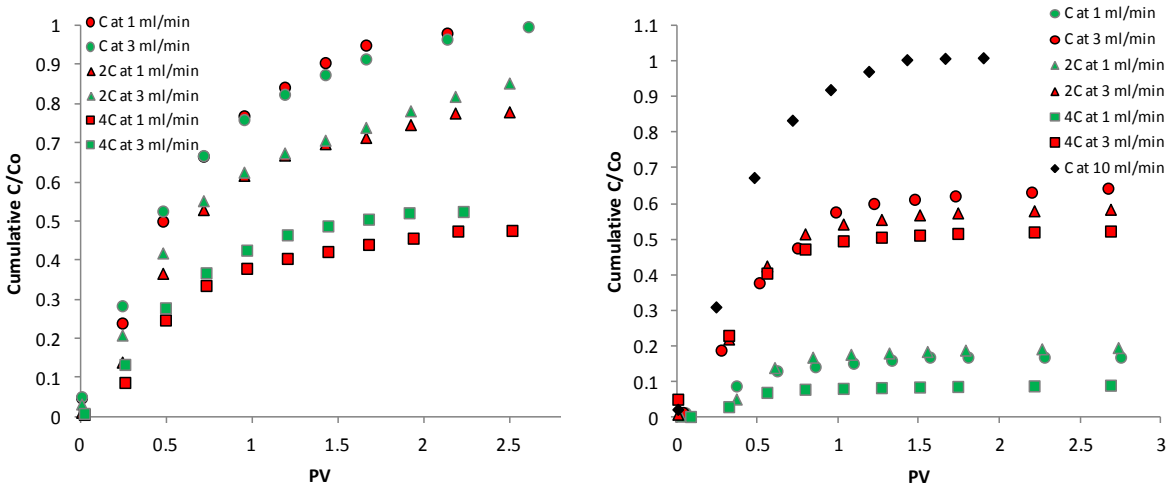

Figure 2.21: Breakthrough curves for silica microspheres with diameter of 2 µm (left) and 5 µm (right), at different flow rates and particle suspension concentration. Removal of particle is enhanced as particle size increase, which is indicative of straining.

Several observations can be made based on these breakthrough curves. The breakthrough time for both particle sizes was very similar. The return curves for both particle sizes showed a very fast arrival followed by gradually increasing (in the case of the 2 µm particles) or constant (for the 5 µm particles) concentrations. The first arrival of the 2 and 5 µm particles occurred within 0.02 to 0.04 and 0.03 to 0.08 pore volume from the start of their injection. This suggests that the recovered particles were, at least initially, moving through the fracture and large pores. Trapped particles were most likely retained in the small pore spaces in the core matrix and fracture walls in regions with small apertures. It was concluded that gravitational sedimentation, aggregation at the primary energy minimum (only for the 2 µm particles) and straining due to particle size were the main particle trapping mechanisms. Aggregation and straining mechanisms of the 2 µm particle were evident based on visual observation during micromodel experiments (details can be found later in the micromodel result section). For the 5 µm particles, the role of the balance between fluid drag and gravitational forces was apparent. The particle cumulative recovery decreases with increasing particle size at the same experimental conditions, which is indicative of straining. This finding is consistent with the observation made by Bradford et al. (2002) through the injection of fluorescent latex particles into saturated sand columns.

For the 2 μm silica particles (Figure 2.21, left), the recovery was inversely proportional to particle suspension concentration, and directly proportional to fluid velocity. Recovery was strongly sensitive to concentration, and slightly sensitive to fluid velocity. Detachment of particles by rolling, sliding or lifting was considered insignificant because increasing fluid velocity (drag forces) did not result in considerable recovery enhancement.

Similarly, with the larger particle size (5 μm), the recovery was also increasing with increasing fluid velocity and decreasing with increasing concentration. The degree by which the recovery was influenced by these parameters (fluid velocity and suspension concentration) was completely different at this particle size – it was observed that recovery is more sensitive to fluid velocity than concentration. In general, the particle recovery (Figure 2.21, right) was found to have a linear relationship with the fluid velocity used during injection. For example, the recovery of the 5 μm diameter particle particles had increased from below 20% to higher than 64% (about three times higher by increasing fluid velocity by factor of three). Further increase in fluid velocity had resulted in complete recovery of the 5 μm diameter silica particles (Figure 2.21, right). Large particles follow fast-moving streamlines (central streamlines) and therefore they are held away from grain or fracture walls. As fluid velocity decreases, the drag force exerted on particles by moving fluid also decreases, allowing gravity to play a larger role. Particles may also diffuse away from fast-moving streamlines toward the fracture walls, or near grains at the fracture-matrix interface, but this is not expected to play a dominant role in the transport of micron-scale particles. Based on all experimental data, it was hypothesized that gravitational sedimentation was playing an important role in the particle transport.

Based on the refined correlation for single-collector contact efficiency (η_0), the probability of collision of the silica particles with a grain can be estimated using Equation 2.1. Figure 2.22 represents the total single-collector contact efficiency, and the magnitude of individual collision mechanisms (diffusion, interception and sedimentation), calculated for the silica particles used in this study, with particle density of 2.2 g/cm^3, average grain size for Berea sandstone of 150 μm (Churcher et al., 1991) with porosity of 21%, fluid velocity of 1.5×10^{-5} m/s (corresponds to 1 cm^3/min), temperature of 21 ºC, Hamaker A constant for silica-water-silica system in the order of 6×10^{-21} J (Grabbe and Horn, 1993) and particle size ranging from 0.01 to 10 μm. At particle size of 2 μm, the total probability of collision was approximately 15%, of which gravitational sedimentation contributed around 9%. The diffusion and interception had equal effect (about 3% each). In contrast, the transport mechanism (predicated by the single-collector efficiency) of the 5 μm diameter particles was dominated by the gravitational sedimentation. The probabilities of collision based on gravity and interception mounted for 56% and 13% of the overall probability (70%), respectively, while diffusion was considered to be negligible.

Recall that the silica particles have density of about 2.2 g/cm^3, more than twice that of the suspension water, meaning that these particles are subject to a force due to gravity. The gravitational force on a particle is directly proportional to particle mass (and thus the cube of the particle diameter), so the 5 μm particles are more greatly affected by gravitational settling than the 2 μm particles. This helps to explain why the recovery of 5 μm particles is much more sensitive to fluid velocity than the 2 μm particles. Because the trapping of 5 μm particles is likely

to be dominated by gravitational sedimentation (which can be offset by increasing fluid velocity) and the trapping of the 2 µm particles is likely to be dominated by aggregation (which cannot necessarily be offset by increasing fluid velocity), it makes sense that the recovery of the 5 µm particles is more sensitive to fluid velocity than that of the 2 µm particles. Furthermore, the fluid drag force acting on a spherical particle (Figure 2.23) is directly proportional to the fluid velocity and the diameter of particle. Larger particles will be experience greater drag forces, and thus, they will be mobilized or detached more effectively from contact surface as velocity increases (Ryan and Elimelech, 1995). The lift force that also counters the adhesive force is also function of the fluid velocity. The combined effect of fluid velocity on those forces causes larger particles to be more sensitive to fluid velocity. Finally, as a result of increasing fluid velocity, the volume of low velocity regions (referred to as stagnant flow regions) will decrease, which will limit collision of particles between fracture surface crevasses or at the pore walls.

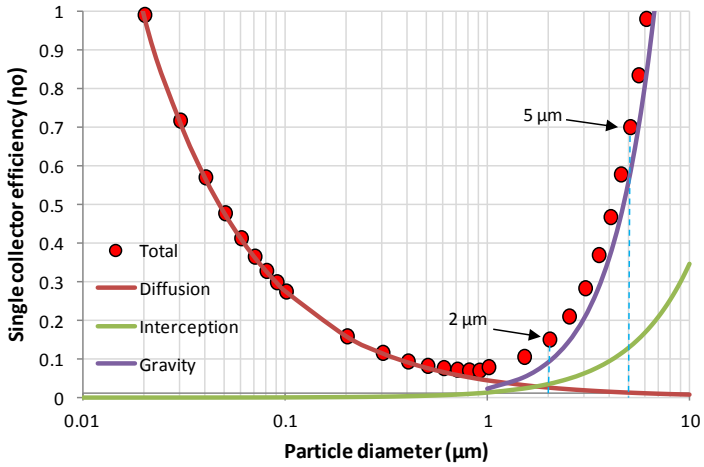

Figure 2.22: Semilog plot of single-collector contact efficiency, with respective contribution of each transport mechanism, calculated for all silica particles used in this study. Hamaker constant $A=6\times10^{-21}$ J, T= 21 ºC, ρ_p= 2.2 g/cm^3, d_c= 150 µm, f= 21%, U= 1.5×10^{-5} m/s.

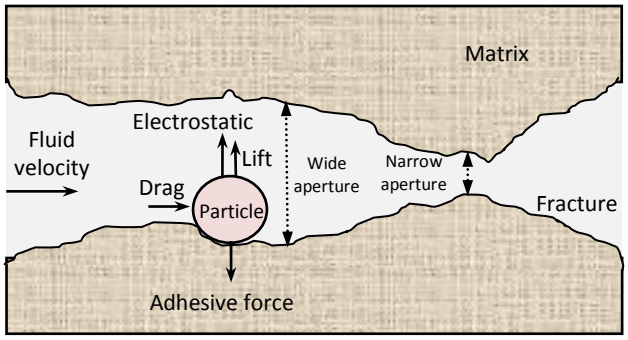

Figure 2.23: Illustration of forces acting on a particle attached to a rough surface.

Keller and Auset (2006), when studying the transport of polystyrene of various sizes (0.05, 1, 2.5 and 5 µm) through micromodels, estimated the relative importance of the contributing transport mechanisms as function of fluid velocity using Equation 2.1. Due to the fact that their polystyrene beads had density similar to that of the injected water (1.05 g/cm^3), the probability of collision based on gravity for all particle sizes was assumed to be insignificant. The transport mechanisms were predicted to be due to diffusion and interception, with interception being the dominant controlling mechanism. In the case of the silica particles used in this study, the effect of gravitational sedimentation is very prominent, especially at lower fluid velocities, as depicted in Figure 2.24. For the 2 µm particles, the collision probability as a result of gravity and diffusion decreases by an order of magnitude as Darcy velocity increases from 1.48×10^{-5} to 2.1×10^{-4} m/s (corresponding to flow rates of 1 and 3 cm^3/min), while probability of interception remained relatively the same (1% difference). For the 5 µm particles, collision probability due to gravity, at the highest fluid velocity of 7.1×10^{-4} m/s, diminished from 56% to 0.7%. Diffusion had no role in their transport at that fluid velocity, but collision by interception with grain or crevasses in fracture wall was probable. By comparison, fluid velocity played a more important role in offsetting gravity sedimentation for larger particles than smaller ones (from 56% to 0.7% for 5 µm and 9% to 0.4% for 2 µm, i.e. a factor of 6). This is consistent with the fact that larger particles are more susceptible to gravitational and fluid drag forces than smaller particles.

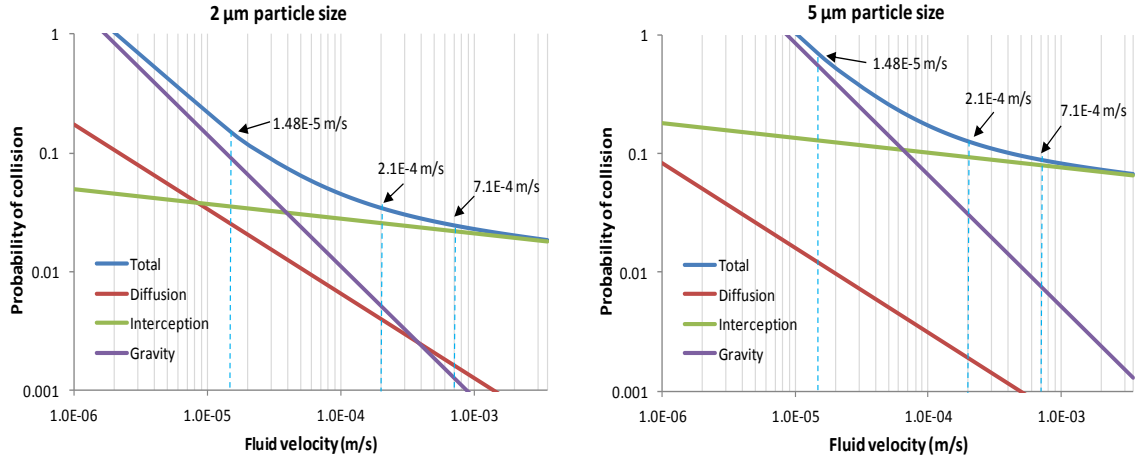

Figure 2.24: A log-log plot of the effect of fluid velocity on the physical transport mechanisms of diffusion, interception and gravitational sedimentation for both silica particle size 2 and 5 µm. Parameters used here are the same as those used in Figure 2.22.

The values of the attachment efficiency (α), the probability that collisions of a particle with a grain collector (or fracture wall in this study) will result in attachment, were calculated using Equation (2.4) and values are listed in Table 2.4. The calculation results indicated that the attachment efficiency values, for all experiments with changing particle sizes, concentrations and fluid velocities varied from 0.0077 to 0.08 with the majority of values in the range of 0.011 to 0.024. Other studies conducted in sand columns (Keller and Sirivithayapakorn, 2004; Bradford et al., 2002 and 2006) or sediment cores (Dong et al., 2002) reported values comparable to the values found in this study. The attachment efficiency in this study generally increased with increasing concentration of the particle suspension and fluid velocity. The values of actual-collector removal efficiency(η), also listed in Table 2.4, behaved somewhat differently. The actual efficiency values increased with concentrations (the larger the number of particles, the

higher the probability of collision) and decreased with increasing fluid velocities (except for one data point). This was anticipated because the silica particles at sizes of 2 and 5 µm are expected not to diffuse much but rather follow the higher velocity streamlines, and thus the probability to collide with the fracture or grain walls is lower. Filtration theory accounts for the dependency of particle and grain sizes in the actual-collector removal efficiency and that of surface chemistry in the attachment efficiency. It should be mentioned that all experiments were conducted under unfavorable attachment conditions (i.e. at low ionic strength, $I=10^{-6}$, using pure water) to minimize the physicochemical factors that determine particle immobilization. According to filtration theory, the attachment efficiency should not change with varying particle and grain sizes for experiments conducted at the same set of chemical conditions. Deviation from this condition suggests that significant straining may be occurring (Bradford et al., 2006). In this work, variability of the attachment efficiency values was observed.

Table 2.4: Summary of attachment, single-collector contact and actual efficiencies calculated for all experiments.

Particle size d_p (µm)	*Concentration (g/L)*	*Fluid velocity (m/s)*	η_0	$\alpha \times 10^2$	$\eta \times 10^3$	*C/Co*
2	1.92	1.48×10^{-5}	0.16	0	0	1.00
2	0.98	1.48×10^{-5}	0.16	0.77	1.22	0.78
2	0.49	1.48×10^{-5}	0.16	2.34	3.73	0.47
2	1.92	2.1×10^{-4}	0.04	0	0	1.00
2	0.98	2.1×10^{-4}	0.04	2.10	0.78	0.85
2	0.49	2.1×10^{-4}	0.04	8.80	3.19	0.53
5	1.92	1.48×10^{-5}	0.74	1.37	10.05	0.17
5	0.98	1.48×10^{-5}	0.74	1.10	8.00	0.19
5	0.49	1.48×10^{-5}	0.74	1.63	11.90	0.09
5	1.92	2.1×10^{-4}	0.13	1.65	2.20	0.64
5	0.98	2.1×10^{-4}	0.13	2.00	2.60	0.58
5	0.49	2.1×10^{-4}	0.13	2.40	3.20	0.52
5	1.92	7.1×10^{-4}	0.09	0	0	1.00

Ryan and Elimelech (1996) reported that the existence of repulsive forces between particles and surfaces of porous media would result in inaccurate prediction of attachment efficiency. The total interaction energy between particle-surface (particle-Berea sandstone and particle-micromodel) was calculated using Equations 2.5 and 2.6 and plotted in Figure 2.13. In this calculation, the measured zeta potentials of -40.2 and -80.23 mV for 2 and 5 µm particles were used. The zeta potential for Berea sandstone and the silicon micromodel saturated with pure water (ionic strength of 10^{-6}) were assumed respectively to be -76.3 mV as suggested by Alkafeef et al. (1999), and -30 mV as per Baumann and Werth (2004). The estimation of the total interaction energy indicated that the attractive forces of van der Waals were negligible. This was indicative that the silica particles did not interact with Berea sandstone or silicon micromodel surfaces via the secondary energy minimum. Both particle sizes showed a repulsive energy barrier,

considerably higher for the 5 µm diameter particles. Unless these forces are overcome by gravitational forces, particle attachment would be unfavorable. For the 2 µm particle, the height of the energy barrier was much shallower and might be overcome by attractive forces at the primary energy minimum at shorter separation distance resulting in attachment (consistent with the micromodel observations). This may also explain the variability of attachment efficiency when calculated for different particle sizes under the same set of chemical conditions.

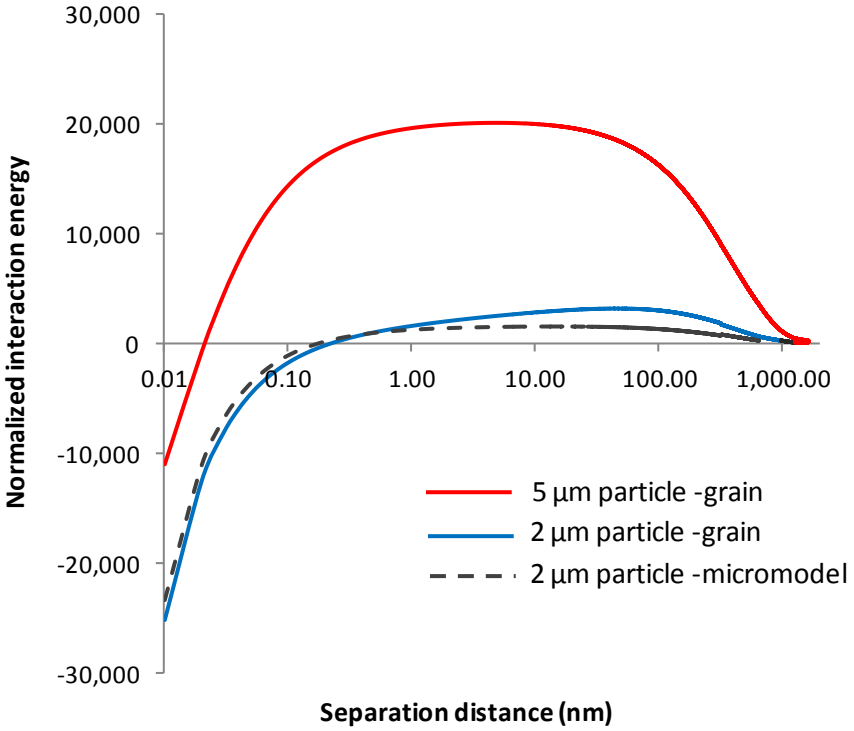

Figure 2.25: Classical DLVO interaction energy between particles and Berea sandstone grain as well as particles and silicon micromodel. The interaction energy is normalized to the thermal energy (k_BT) of suspension. Magnitude of parameters used in the calculation can be found in the text.

Surface chemistry or functional groups on the particle surface may result in acid-base energy interactions. These acid-base interactions (not accounted for by classical DLVO theory) describe the hydrogen bonding properties of interacting surfaces with water. Water molecules structure themselves by hydrogen bonding upon interaction, resulting in attractive particle-surface and particle-particle interactions for hydrophobic particles and repulsive particle-surface and particle-particle interactions for hydrophilic particles. Silica microspheres used in this study have no functional groups in their surfaces and retain hydrophilic properties as provided by the manufacturer, and thus repulsive hydrophilic interactions are expected. The particle-particle total interaction energy (van der Waals attractive and electrostatic repulsive interactions) was calculated and plotted as depicted in Figure 2.18. Note that the particle-particle interaction energies are similar to those of the particle-surface (Figure 2.25), because the surface potentials were very comparable to those of particles. Specifically, the 5 µm particle-particle interaction

curve is similar to that of the 5 µm particle-grain, and the 2 µm particle-particle curve is similar to that of the particle-micromodel. The 5 µm particles may have had a sufficiently large repulsive energy barrier to hinder particle aggregation. When particles are at close proximity to each other while entering a pore throat or near a fracture wall, they may repel each other until one or the other flows through or physically strain based on their size. Therefore, due to the resistance of the 5 µm particles to aggregation, the suspension concentration had a smaller effect on their recovery compared to the 2 µm particles. In the case of the 2 µm particles, the attractive interactions at the primary energy minimum are large compared to the repulsive energy barrier. This suggested that there could be an attractive interaction between particles at this size and separation distance. As a result, particle aggregation is favored. The relative sensitivity of recovery of 2 µm particles to concentration compared to 5 µm particles may be explained on this basis. When aggregation is occurring, particles attach to each other to form a cluster. The size the cluster is dependent on number of particles forming that cluster: the more particles available, the larger the cluster size. Thus, size exclusion may occur not based on the size of the individual particle but the size of the cluster. The cluster would be excluded from all pores smaller than its own size. Evidence of increasing straining as a function of increasing concentration of the 2 µm particles was confirmed visually during the micromodel flow experiments which are discussed later in the micromodel section. Clustering was observed visually in the micromodel experiments, despite the fact that very low ionic strength water (pure water) was used. Keller and Auset (2006) observed particle clustering at the same conditions.

Unlike attachment, where a particle requires one solid-water interface to attach to surface, straining involves at least two solid-water interfaces or surface roughness (Bradford et al., 2006). Straining or size exclusion inside the fracture may be present, either in areas between fracture surfaces or at the fracture-matrix interface. When fracture surfaces come into contact, irregularities of those surfaces (crevasses) result in a fracture with varying aperture. Areas where surfaces are further apart are candidate sites for particle attachment (one solid-water interface), while closer surfaces (two solid-water interfaces) promote straining. The removal mechanisms by collision with attachment to fracture walls or straining between fracture surfaces are analogous to those occurring within a pore throat. We shall discuss some of the criteria suggested by other authors with regard to particle straining inside pore structure and employ whichever applicable to assess straining occurring in the fracture area. In this discussion, the fracture is treated as a single pore with a maximum width of 62.4 µm as calculated from flow in parallel layers using Equation 2.9 or a minimum width of 3.79 µm as estimated by the cubic law assuming that the fracture permeability is equal to the total permeability. This is a conservative estimate because matrix permeability is high (approximately 0.51 darcy).

As mentioned earlier, the general disagreement between prediction of filtration theory and experimental work (Bradford et al., 2002) was attributed to the fact that the filtration theory does not take into account the influence of pore structure on particle removal by straining. Xu et al. (2006) studied the effect of straining on the mobility of particles within groundwater aquifers and granular filters. They suggested that accurate description of particle mobility requires considering the effects of straining when the ratio of particle diameter to the median grain size (d_p/d_{50}) exceeds 0.008. Bradford et al. (2007) investigated the influence of (d_p/d_{50}) on the recovery of latex microspheres on the basis of straining under unfavorable attachment

conditions. They reported that as (d_p/d_{50}) ratio increased, the recovery declined and more particles were deposited, especially adjacent to the sand column inlet. For example, for the (d_p/d_{50}) ratio of 0.007, 0.008, 0.013 and 0.020 (at fluid velocity of 0.1 cm/min), the peaks of the return curves were approximately at 100%, 70%, 20% and 10%, respectively. It is well understood that smaller grain size corresponds to smaller pore size for certain types of grain packing. For the Berea sandstone used in this study, an average grain size of 150 μm was assumed, based on Churcher et al. (1991). Considering the silica particles of 2 and 5 μm, the ratio of (d_p/d_{50}) would be 0.013 and 0.033, respectively. This suggested that the silica particles which entered the pore network at the inlet or fracture-matrix interface were likely to be trapped due to straining, especially larger particles. Additionally, the pore network in sedimentary rocks such as Berea sandstone would have far more complex pore connectivity which might lead to additional reduction in effective pore size at pore junctions. In other words, this criterion is regarded as conservative when applied to sedimentary rocks.

The ratio of throat size to particle size (T/C) was used as a criterion by Auset and Keller (2006). They performed experiments in micromodels, the results of which suggested that the T/C of 1.8 and smaller would result in particle removal solely by straining. For T/C ratios between 1.8 and 2.5, interception and straining were observed. For higher T/C, straining was not observed. For Berea sandstone, we apply the T/C criteria based on the pore size distribution range obtained from capillary pressure data (Figure 2.2) and particle sizes (2 and 5 μm) used in this study. Recall that the Berea sandstone has pore sizes in the range of 0.005 to 50 μm. According to this criterion, the threshold pore size for the straining of 2 μm particles is 5 μm, and that of 5 μm particles is 12.5 μm. In other words, in pores that are smaller than this threshold size, the particles will be trapped within the porous medium primarily due to straining. Similarly, the T/C criteria can be applied to evaluate straining within a fracture by treating the fracture regions with small apertures as pore throats. Our estimate of the fracture hydraulic aperture indicated that the apertures could be as small as 3.79 μm in areas of closely matching fracture surfaces. This aperture size (or throat) would result in T/C ratio of 1.9 and 0.8 for particle sizes of 2 and 5 μm, respectively, suggesting a high probability of straining. Owing to the complexity of the pore network and the existence of surface irregularities in fractures, it is very possible that a pore throat (or a flow channel in the fracture) at or below the threshold size exists along a preferential flow path. Consequently, straining of particles will result in their accumulation at pore junctions and, therefore, the total blockage of the connecting pore. Blocked pores are a dead end for subsequent particles, which eventually results in reduction of particle recovery. The permeability measurements (i.e. pressure data) support the fact that the number of conductive flow paths available to particles decreased due to blockage. Figure 2.26 shows an example of the permeability measurements conducted during the injection of the 2 μm silica particles at flow rate of 3 cm^3/min using three different suspension concentrations. The permeability continued to decrease as particle concentration increased. Although there was only a slight decrease, the result indicates a certain degree of blockage (i.e. incomplete straining). Bradford et al. (2002) reported that incomplete straining would have less pronounced reduction in permeability because it occurred in part of the pore network. This supports the argument that the blockage occurred in some of the preferential flow paths. The decrease in permeability was consistent with the decline in recovery (the rock is less permeable with as more particles retained inside). Also, the rate of reduction in permeability (from initial values to the end of injection) was closely related to the amount of recovered particles. This means the permeability decreased faster as more particles

were introduced to the porous medium, possibly due to blockage by aggregation and straining. The rate of reduction was the largest (from 1.2 to 0.92 darcy) during the injection of particle suspension with the highest concentration, the experiment in which only 53% of the influent concentration was recovered. The reduction rate was shallower (from 1.02 to 0.97) during the injection of particle concentration of (2C), where recovery was 85%. For the injection of the most dilute suspension (C), the permeability remained almost constant with an average value of about 1.10 darcy, after a slight decrease at the beginning of the experiment.

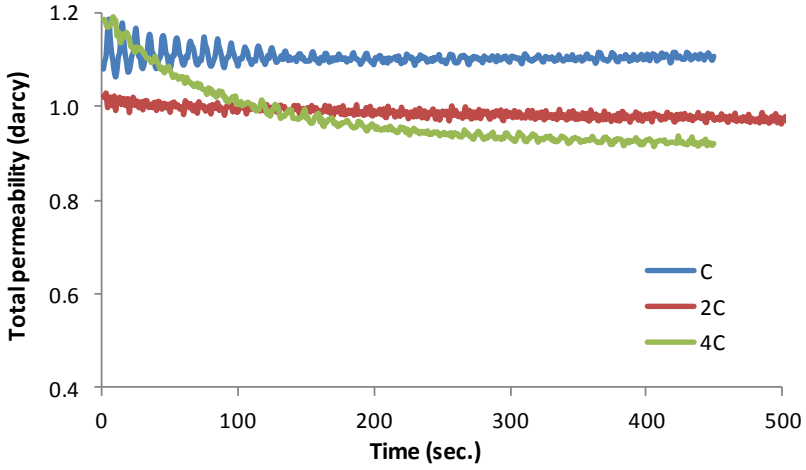

Figure 2.26: Permeability measurements during the injection of the 2 µm silica particles at different suspension concentrations, C, 2C and 4C. Flow rate was 3 cm^3/min.

2.4.5.2 Silica injection into silicon micromodel

Micromodels were used to assess the flow mechanism of silica particles, at the pore scale, within the fracture and fracture-matrix interface. Particles of 2 µm in diameter at two different concentrations (C and 4C) were injected at flow rate of 0.001 cm^3/min (1.33×10^{-5} m/s). The particles were transported through the fracture, but trapped along the fracture-matrix interface (Figure 2.27). The particles were not able to infiltrate through the matrix for more than few grains downstream of the fracture-matrix interface, depending on the concentration. Note that straining was more pronounced with increasing concentration. This was consistent with the recovery measurements (i.e. the recovery of the 2 µm particles was decreasing with increasing particle concentration during core-flooding experiments). The total recovery of particles was observed based on concentration measurements of effluent samples using the fluorimeter. SEM micrographs obtained for effluent samples confirmed this finding. Further investigation of particle straining was carried out by injecting silica nanoparticles of an average size of 350 nm (about six times smaller than the 2 µm particles). The silica nanoparticles were negatively charged (zeta potential of -73.4 mV) with surface chemistry similar to the 2 µm particles. The existence of the silica nanoparticles in the effluent was confirmed by SEM. The recovery of nanoparticles was not determined because the influent concentration was unknown and because the nanoparticles were not fluorescent. Visual observation of the nanoparticles was not possible due to the physical limitation imposed by the light optics to resolve particles at that size. This injection was conducted as a precursor of straining only, so further details are omitted.

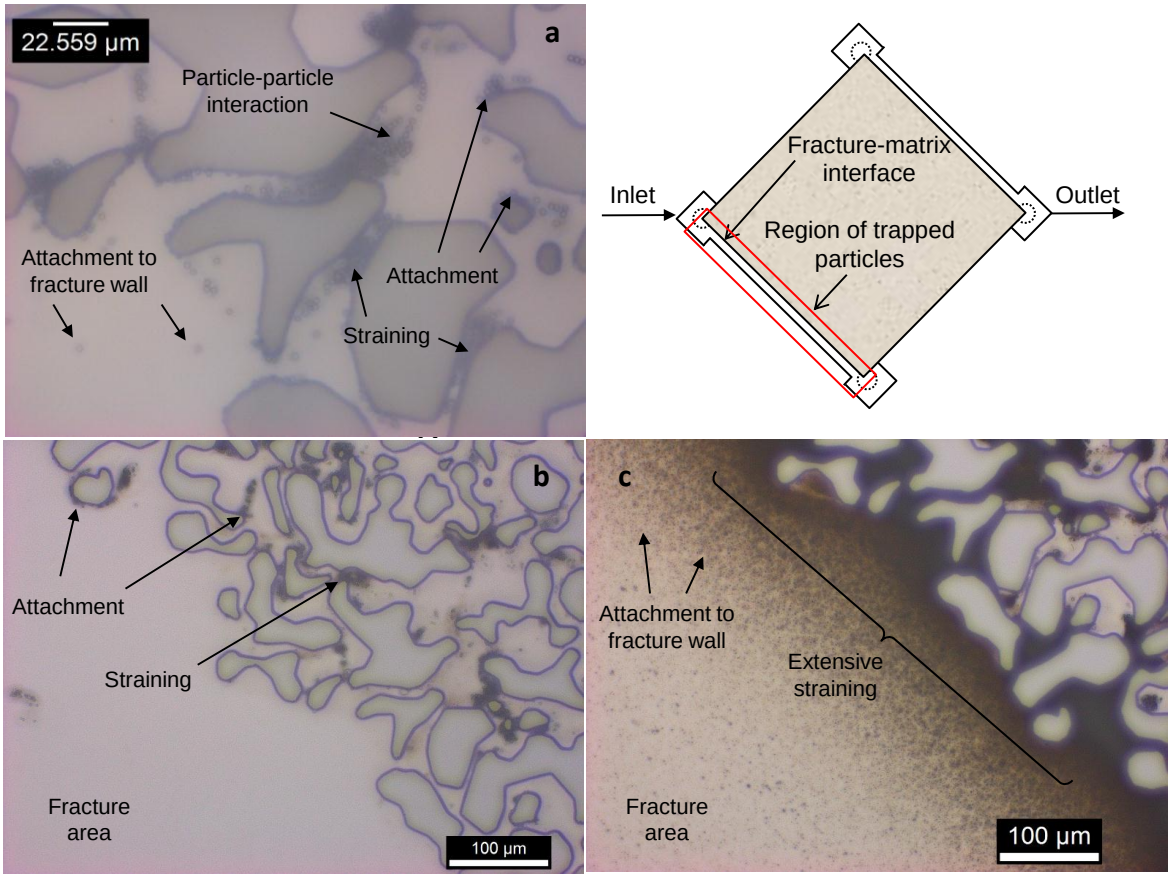

Figure 2.27: Schematic of micromodel showing the general region of particles entrapment along the fracture-matrix interface. Image (a) showing particle-particle interaction (aggregation), particle attachment to grain surface and straining. Images (b) and (c) showing straining during the injection of most diluted (denoted as C) and concentrated (denoted as 4C) particle concentrations, respectively. Note that in images (a and c), the particles represented by dark dots were attaching to the fracture wall.

By visual observation (Figure 2.27), it was evident that significant straining had occurred, with some attachment. Attachment aided straining because particle attachment decreased the effective pore throat size for subsequent particles to flow for a given pore throat. The particles attachment to fracture walls was also observed (Figure 2.27 a and c). The collision of the particle with the wall was attributed to gravitational sedimentation, and the actual attachment to the fracture wall was attributed to the attractive interaction at the primary energy minimum. Hydrodynamic forces represented mainly by fluid drag may have not been sufficient to overcome gravity and adhesion forces, and hence particle attachment. Note that the fracture walls in the micromodel (silicon-glass walls) are smoother and more uniform compared to the fracture in the real rock (e.g. fractured Berea sandstone). In fractured rocks, fracture walls are expected to have some degree of surface roughness. Rougher grain surfaces are expected to be more efficient particle collectors. Auset and Keller (2006) observed significant influence of rough grain surface in particle capturing. Irregularities in matching fracture surfaces would result in varying size and orientation of flow paths, resulting in a larger collision probability, and a higher overall

probability of attachment to fracture walls. Thus, the particle attachments to the fracture walls in Berea core were expected to be more pronounced than in the micromodel. Filtration theory, using single-collector contact efficiency, suggested that the probability collision of the 2 µm particles (density of 2.2 g/cm^3) with varying collector (grain) size from 30 to 300 µm (as per the fabrication of the micromodel) is below 20% (Figure 2.28). Note that under these experimental conditions, the probability of collision changed only slightly with the grain size in this range (from 14% to 20%) at the same fluid velocity. According to filtration theory, gravitational sedimentation dominates the transport of particles for the majority of the grain size distribution of the micromodel. Transport by interception and diffusion was estimated to decrease with increasing grain size, with the former decreasing more rapidly with increasing grain size.

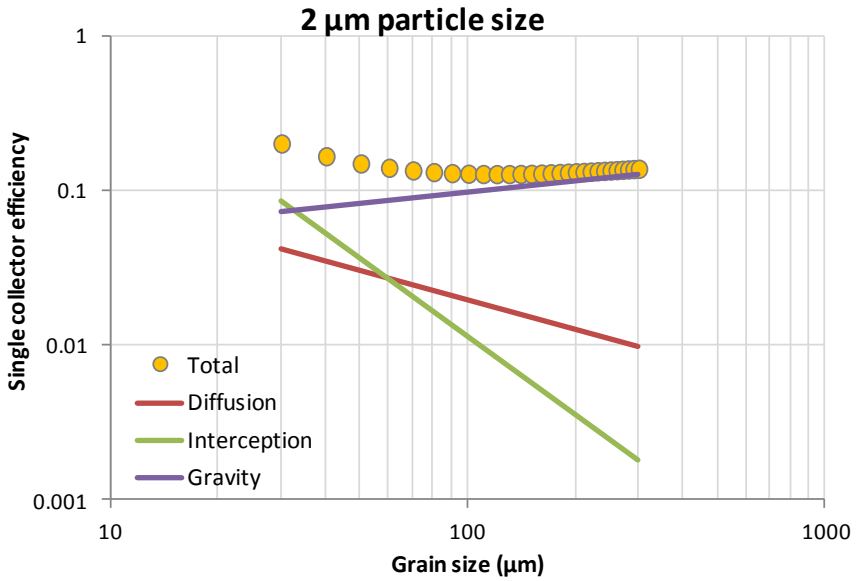

Figure 2.28: A log-log plot of the effect of grain size on the physical transport mechanisms of diffusion, interception and gravitational sedimentation for silica of particle size 2 µm in the micromodel.

In this work, most of the micromodel inlet pore throats are about 8 to 12 µm, corresponding to T/C ratios higher than 4. Keller and Auset (2006) showed experimentally that filtration theory is appropriate for T/C ratios greater than 2.5, but not at lower T/C ratios where straining was occurring. Sedimentation and interception of particles were observed visually in our micromodel experiments. Some silica particles strayed from the central streamlines toward grain walls, indicating gravitational sedimentation, while others flowing near grain walls were intercepted. This was consistent with the filtration theory prediction. Within the fracture region of the micromodel, the T/C ratio was estimated to be about 12.5 (the ratio of the aperture to particle size), suggesting that particle entrapment would be a result of particle interception or gravitational settling. This was also consistent with visual observations (Figure 2.15 A and C).

The ratio of particle to grain size is in the range of 0.0067 to 0.067. At grain sizes of 250 µm and smaller, the particle to grain size ratio exceeded the value of 0.008, threshold proposed by Xu et al. (2006), above which straining affects particle mobility. This implies that straining dominated the transport in the micromodel. This is also consistent with the findings of Bradford et al. (2007)

in their study of transport of latex microspheres through sand columns, each packed with single grain size sand (ratios in the range of 0.007 to 0.02 with respective recovery diminishing from 100% to 10%). Thus, heterogeneity of the pore network in our micromodel, represented by the mixture of grain sizes, augmented the effect of straining. In order to predict of particle recovery successfully, the influence of the spatial distribution of pore or grain size must be included.

2.4.6 Tin-bimuth nanoparticle heating experiment

The tin-bismuth alloy nanoparticles were characterized in terms of size and shape using DLS and SEM imaging. It was determined from three consecutive DLS measurements that there was a wide distribution of the particle hydrodynamic diameter, as shown in Figure 2.29.

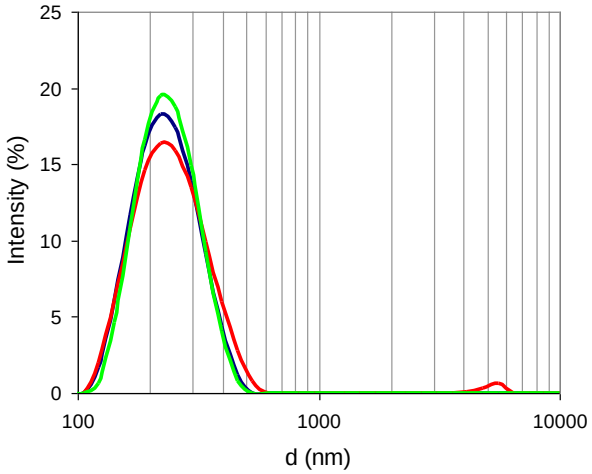

Figure 2.29: Logarithmic particle size distribution based on hydrodynamic diameter for original tin-bismuth nanoparticle sample. (Three consecutive measurements.)

The three measurements are in reasonable agreement, with an average modal value of 235 nm. The hydrodynamic diameter ranged from ~100 nm to ~600 nm, with one measurement showing a small peak at ~5500 nm. This indicates that there may have been large particles in the sample, either due to aggregation or from the original synthesis.

The SEM images of the sample show good agreement with the DLS measurements, as shown in Figure 2.30. It is apparent from Figure 2.30 that the tin-bismuth nanoparticles range from 50 nm to less than 600 nm. Furthermore, although many of the nanoparticles seem to be spherical as expected, the presence of nonspherical crystalline structures indicates that the sonochemical synthesis did not reach completion. Aggregation on the substrate is observed in both figures, but it is unclear whether this aggregation occurs in solution or upon drying on the substrate. The DLS results suggest that the latter may be the case.

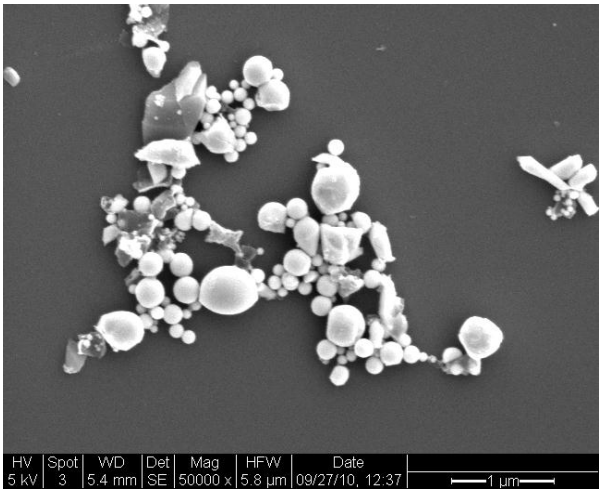

Figure 2.30: SEM image showing the wide range of tin-bismuth nanoparticle sizes.

To begin investigating the melting behavior of tin-bismuth nanoparticles within the temperature range of interest, a sample of the nanofluid (tin-bismuth in mineral oil) was subjected to a preliminary heating experiment. Although ultimately we are interested in the melting behavior of the tin-bismuth nanoparticles in water, the heating experiments were performed in oil due to the complications associated with the boiling of water at experimental conditions. From the phase diagram, at the eutectic composition, the tin-bismuth alloy melts at 139°C. In fact, the nanoparticles likely melt at a slightly lower temperature than this due to melting point depression due to their size.

The sample was heated using a heating mantle connected to a temperature controller with a feedback thermometer, as shown in Figure 2.31.

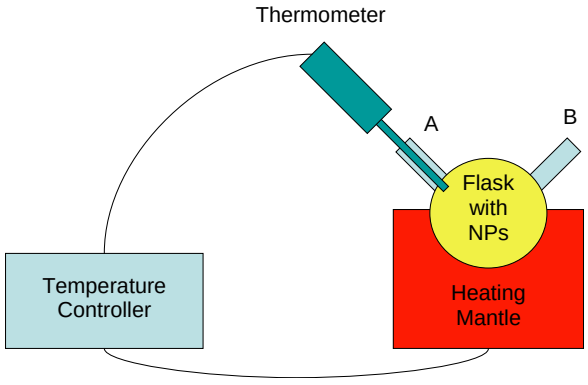

Figure 2.31: Experimental apparatus for tin-bismuth heating experiment

The flask containing the tin-bismuth nanoparticles in oil was placed in the heating mantle, which was connected to the temperature controller. The temperature controller was also connected to a thermometer, the feedback from which affected whether the mantle was heated, cooled, or maintained and the rate at which this was done. The thermometer was positioned in port A.

The sample was heated in steps to the expected melting point of 139°C. The sample was monitored for a color change near the expected melting point, and when none occurred, the sample was heated in steps to 210°C. No color change ever occurred, but the heating was stopped to prevent the mineral oil from burning. It is apparent that melting occurred regardless of the absence of color change. Finally, when the apparatus was at room temperature, the sample was removed from the flask.

The sample was then washed and centrifuged several times with a 1:1 mixture of hexane and acetone, rinsed in a solution of 0.1 M PVP in ethanol, and finally suspended in ethanol. The centrifuge setting was 6000 rpm for 15 minutes each time. This sample was characterized using DLS and SEM imaging. The DLS results of the sample subjected to heating are shown in Figure 2.32.

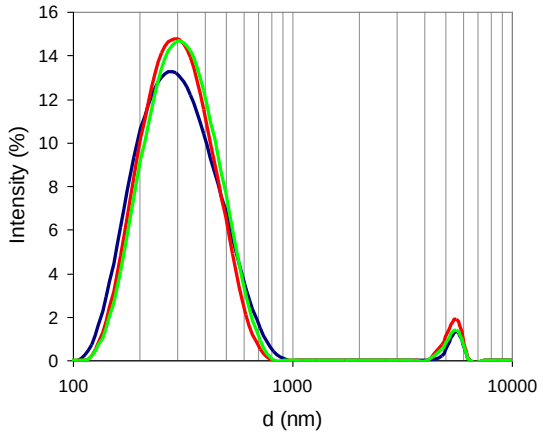

Figure 2.32: Logarithmic particle size distribution based on hydrodynamic diameter for heated tin-bismuth nanoparticle sample.

The three measurements are in relatively close agreement, with an average modal value of 321 nm. The hydrodynamic diameter ranged from ~100 nm to ~1000 nm. Appreciable secondary peaks in the range of ~4100 nm to ~6400 nm were observed for all runs. This indicates that there are large particles in the sample, most likely due to aggregation and fusion of the particles. Selected particle size distribution curves for comparison of the original and heated samples are shown in Figure 2.33.

As shown in the figure, the particle size distribution peak shifted noticeably to a larger size. Also, the secondary peak in the micron scale is noticeably larger, indicating that there are more large aggregates. SEM images of the heated sample are shown in Figures 34 and 35.

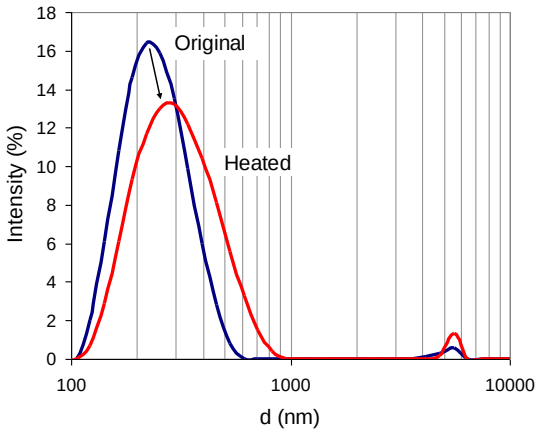

Figure 2.33: Comparison of logarithmic particle size distribution based on hydrodynamic diameter for original and heated tin-bismuth nanoparticle samples.

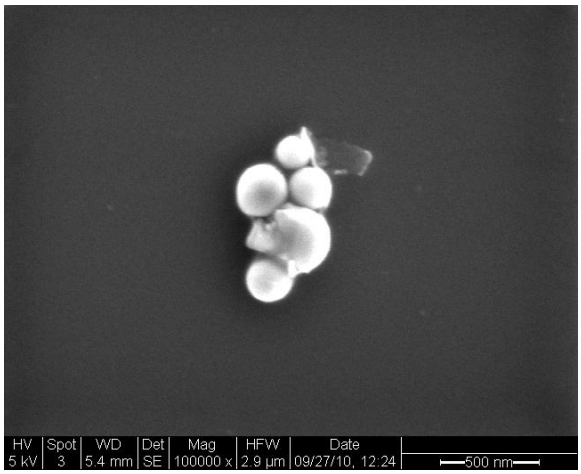

Figure 2.34: SEM image showing heated tin-bismuth nanoparticles.

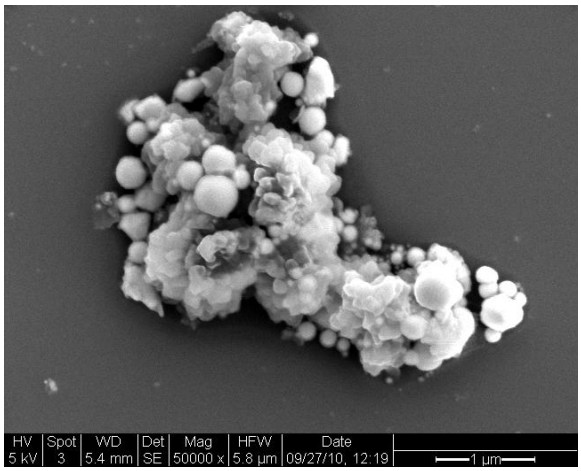

Figure 2.35: SEM image showing large aggregate of heated tin-bismuth nanoparticles.

Fusion of melted particles can be observed in both figures, and the sizes of both particles and large aggregates are within the range suggested by DLS results. While the fusion of melted particles could account for the shift in particle size distribution, it is difficult to reach any definite conclusions from the SEM results due to the very wide particle size distributions of both the heated and unheated samples.

2.4.7 Dye-attached silica nanoparticle heating experiment

Dye-attached silica nanoparticles (Figure 2.36) were subjected to a heating experiment, and fluorescence spectra of the particles were measured before and after heating.

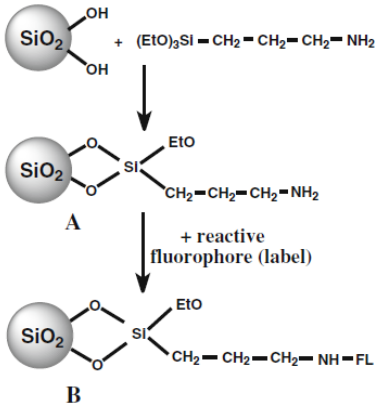

Figure 2.36: Schematic representation of silica nanoparticle surface modification and dye attachment by Saleh, et al. (2010).

We used Fluorescent Microscopy, SEM and Fluorescent Spectrum to characterize the dye-attached silica nanoparticles. Fluorescent microscopy characterization as shown in Figure 2.37 was done using the substrate base dye-attached silica nanoparticle sample. We can see clearly that the dye molecules were attached successfully to the surface of silica nanoparticles. The whole substrate was fluorescent although not uniformly (some spots were brighter with more fluorescent molecules attached).

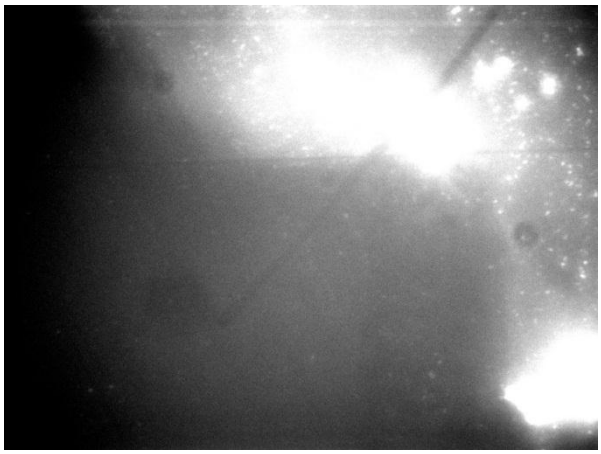

Figure 2.37: Fluorescent microscopy image of dye-attached silica nanoparticles on quartz substrate.

We also measured the fluorescence spectra of free dye molecule solution, silica nanoparticle suspension, dye-attached silica nanoparticles both on substrate and in solution. We used 400nm as the excitation wave length. We could see from the fluorescence spectrum of Oregon 488 solution that its emission peak is at ~530nm, shown in Figure 2.38. As control, we measured the fluorescence spectrum of silica nanoparticles in water without dye attachment. We also measured the fluorescence spectra of dye-attached silica nanoparticles in water and on substrate. We used 400nm as excitation wavelength, shown in Figure 2.39. The results showed that, without dye attachment, there was no fluorescence response of the silica nanoparticles and after dye attachment, two peaks at ~425nm and ~530nm were observed in the spectrum.

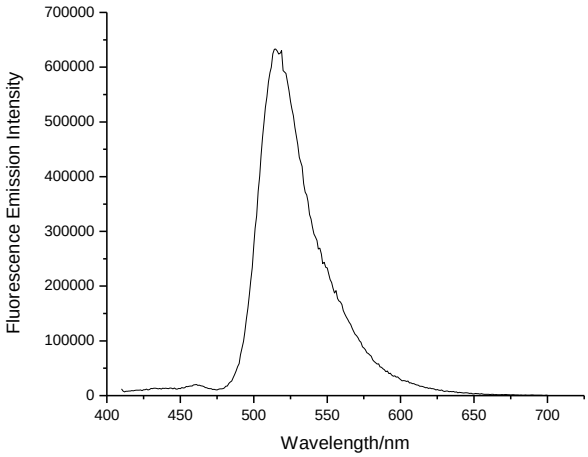

Figure 2.38: Fluorescence spectrum of Oregon 488 dye molecule solution (excitation wavelength 400nm).

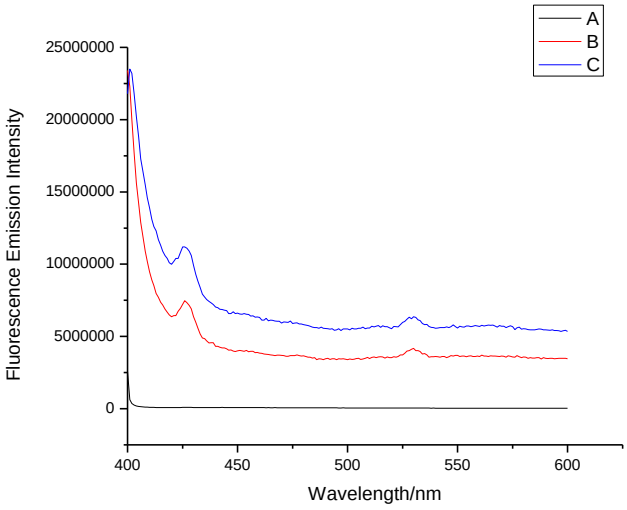

Figure 2.39: Fluorescence spectrum (excitation wavelength 400nm): (A) Silica nanoparticle without dye attachment as control; (B) Dye-attached silica nanoparticles in water; (C) Dye-attached silica nanoparticles on quartz substrate.

A heating experiment was conducted using the sample of dye-attached silica nanoparticles on quartz substrate. We heated the substrate on a hot plate at 200°C for 15min. Then we soaked the substrate in ethanol and acetone respectively and washed the substrate both with ethanol and acetone. The substrate was dried in air. We used Fluorescence Spectrum to characterize this sample.

The fluorescence spectrum of the particles was measured after the heating experiment, shown in Figure 2.40. We used an excitation wavelength of ~360nm. We can observe a wide peak at ~425nm of the heated sample which was obviously different from the sample before heating. Besides that, we observed at ~380nm and ~475nm there were two shoulder peaks and at ~575nm there was a small peak in both spectra. Hence, a clearly identifiable property change (fluorescence) is available as a temperature indicator using this kind of nanoparticle.

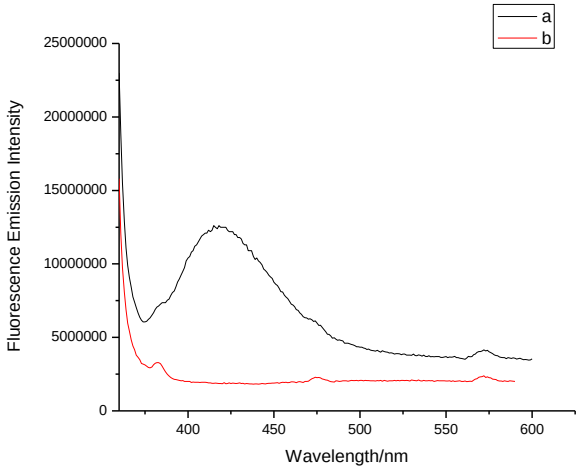

Figure 2.40: Fluorescence spectrum (excitation wavelength 360nm): (a) Dye-attached silica nanoparticle after heating experiment at 200°C for 15min; (b) Dye-attached silica nanoparticle without heating experiment.

2.4.8 Using dye-releasing nanoparticles to estimate measurement location

Simply knowing that some region of the reservoir has a certain temperature without knowing the location of the measurement is of limited use to reservoir engineers. If this location could be estimated accurately, the reservoir temperature distribution could be mapped. This could make it possible to predict thermal breakthrough in a reservoir and would allow reservoir engineers to make more informed decisions. The potential capability of nanosensors with a dye-release sensing mechanism to estimate measurement location via analysis of the return curve of released dye is addressed in this section.

2.4.8.1 Simple Analytical Model for Return Curve Analysis

A thought experiment was conceived consisting of two hypothetical tracer tests performed in a well doublet: one with a conservative solute tracer and one with dye-releasing nanosensors.

Synthetic tracer return curves for these hypothetical tests were generated using an analytical solution to the advection-dispersion equation, which is often used to describe tracer flow in porous and fractured media. Juliusson and Horne (2011) expressed the one-dimensional form of this equation as:

$$R\frac{\partial C}{\partial t} = \alpha u \frac{\partial^2 C}{\partial x^2} - u\frac{\partial C}{\partial x} \tag{2.17}$$

where C is tracer concentration, x is the spatial coordinate, t is time, u is the flux velocity, and α is the dispersion length, and R is the tracer retardation factor. For this initial investigation, the simple case with a constant flux velocity v (i.e. constant flow rate) was considered, and it was assumed that R is constant with respect to t, x, and C for both the solute tracer and the nanoparticles. It may be more realistic to assume that R varies spatially, as is suggested by Chrysikopoulos (1993), and that nanoparticle flow likely requires even more complex treatment. With these caveats in mind, it was decided to first examine the simplest possible case.

Kreft and Zuber (1978) provided a solution to the advection-dispersion equation with flux injection and detection boundary conditions, and Juliusson and Horne (2011) rewrote this solution to include the retardation factor R:

$$C = \frac{mV_x}{qt\sqrt{4\pi V_\alpha qt}} \exp\left(-\frac{\left(qt - V_x\right)^2}{4V_\alpha qt}\right) \tag{2.18}$$

$$V_x = RA\phi x \tag{2.19}$$

$$V_\alpha = RA\phi\alpha \tag{2.20}$$

where m is the mass injected, q is the volumetric flowrate, t is time, V_x is the pore volume modified by the retardation factor R, V_α is the dispersion volume modified by R, A is cross-sectional area, ϕ is porosity, and α is the dispersion length.

Consider a flow-path in a geothermal reservoir between a well doublet that consists of a fractured zone with length L, cross-sectional area A, and porosity ϕ. Before the beginning of heat extraction, the reservoir had a uniform temperature distribution with a temperature of T_1. Some years after the onset of extraction, the thermal front has advanced to the position x_f, and the portion of the reservoir behind the front has cooled to temperature T_2, as shown in Figure 2.41. Note the implicit assumption that cooling advances as a sharp front rather than the more gradual temperature distribution associated with the cooling of a single isolated fracture. Suppose a nanosensor has been designed to release a fluorescent dye at the threshold temperature T_1, and assume that this release occurs almost instantaneously upon exposure to this threshold.

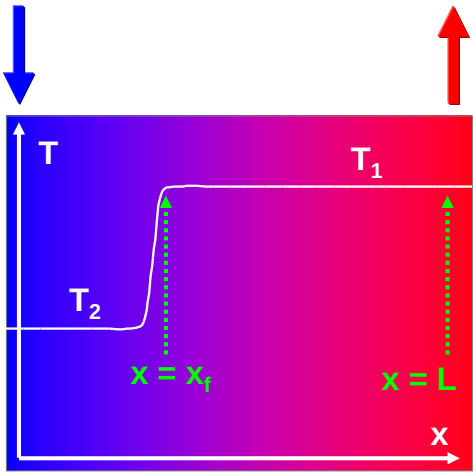

Figure 2.41: Cartoon of temperature distribution in a geothermal reservoir with a thermal front at position x_f.

Suppose that two tracer tests are performed. In one test, a mass m_c of a conservative tracer with a retardation factor R_c is injected into the reservoir. The tracer is sampled at the production well (i.e. $x = L$), and the return curve can be described by Equations 2.21 through 2.23.

$$C_c = \frac{m_c V_{x,c}}{qt\sqrt{4\pi V_{\alpha,c} qt}} \exp\left(-\frac{\left(qt - V_{x,c}\right)^2}{4V_{\alpha,c} qt}\right) \tag{2.21}$$

$$V_{x,c} = R_c A\phi L \tag{2.22}$$

$$V_{\alpha,c} = R_c A\phi\alpha \tag{2.23}$$

where the subscript c denotes the conservative solute tracer.

In the second test, a slug of the dye-releasing nanosensors with retardation factor R_n is injected into the reservoir. Upon reaching exposure to the threshold temperature T_1 at position x_f, the nanosensors release a mass m_r of the attached dye, which itself behaves like the conservative solute tracer in the previous tracer test, and has a retardation factor R_c. The released dye is sampled at the production well. The return curve of the released dye is influenced by both R_n and R_c, because it travels with the nanosensor retardation factor R_n from $x = 0$ to $x = x_f$ and the solute retardation factor R_c from $x = x_f$ to $x = L$. Thus, the return curve of the released dye can be described by convolution, as shown in Equations 2.24 through 2.27.

$$C_r = \int_0^t \frac{m_r V_{x,n}}{qt\sqrt{4\pi V_{\alpha,n} q(t-\tau)}} \exp\left(-\frac{\left(q(t-\tau) - V_{x,n}\right)^2}{4V_{\alpha,n} q(t-\tau)}\right) \bullet \frac{qV_{x,r}}{qt\sqrt{4\pi V_{\alpha,c} q\tau}} \exp\left(-\frac{\left(q\tau - V_{x,r}\right)^2}{4V_{\alpha,c} q\tau}\right) \partial\tau \tag{2.24}$$

$$V_{x,n} = R_n A\phi x_f \tag{2.25}$$

$$V_{\alpha,n} = R_n A\phi\alpha \tag{2.26}$$

$$V_{x,r} = R_c A\phi\left(L - x_f\right) \tag{2.27}$$

where the subscript *n* denotes the nanosensors and the subscript *r* denotes the released dye. Note that $V_{x,r}$ can be rewritten as:

$$V_{x,r} = V_{x,c} - \frac{V_{\alpha,c}}{V_{\alpha,n}} V_{x,n} \tag{2.28}$$

Thus, the return curves for the conservative tracer can be fit to Equation 2.21 by adjusting the values of unknowns $V_{x,c}$ and $V_{\alpha,c}$ (i.e. minimizing the norm of the differences between the return curve data and the model with the unknowns as decision variables). Subsequently, the return curves for the released dye can be fit to Equation 2.24 by adjusting the values unknowns $V_{x,n}$ and $V_{\alpha,n}$. Note that $V_{x,r}$ is not explicitly adjusted here because it can be expressed in terms of the other unknowns (Equation 2.28). Once the values of the unknowns have been determined, one can calculate the location of the thermal front using Equation 2.29:

$$x_{f,d} = \frac{x_f}{L} = \frac{V_{x,c} - V_{x,r}}{V_{x,c}} \tag{2.29}$$

where $x_{f,d}$ is the dimensionless position of the thermal front.

2.4.8.2 Example Problem

This analysis was demonstrated successfully in an example problem with the parameter values shown in Table 2.5.

These values were chosen somewhat arbitrarily for the purposes of this demonstration. However, values of R_c and R_n were used such that the nanosensors experience no retardation and the solute tracer does experience retardation. This is based on studies of colloid transport in fractures which showed that nonadsorbing colloids exhibit breakthrough more rapidly than solute tracers because they tend to stay in fluid streamlines and do not experience matrix diffusion (Reimus 1995). Also, the volumetric flow rate q and the masses of the tracer m_c and m_r were based on values reported by Gentier et al. (2010) for the 2005 tracer test performed in the Soultz-sous-Forets reservoir.

Synthetic return curve data for the conservative tracer and the nanosensors were generated for various values of x_f using Equations 2.21 and 2.24, and Gaussian noise was added for the sake of realism. An optimization solver was then used to find the best fit to Equations 2.21 and 2.24 by adjusting the unknowns. The results are tabulated in Table 2.6, and select return curves are plotted in Figure 2.42.

Table 2.5: Parameter values used in return curve analysis demonstration problem

Parameter	*Value*
R_c	2
R_n	1
A	200 m^2
φ	0.10
L	1000 m
α	25 m
Pe = L / α	40
m_c	123.75 kg
m_r	123.75 kg
q	43.2 m^3/hr

Table 2.6: Estimates of temperature measurement locations in demonstration problem for various true values of $x_{f,d}$.

$x_{f,d}$ *true*	$x_{f,d}$ *estimate*	*Error*
0.05	0.037	26%
0.15	0.155	3.2%
0.25	0.248	0.8%
0.35	0.382	9.1%
0.45	0.431	4.3%
0.55	0.517	5.9%
0.65	0.632	2.7%
0.75	0.746	0.6%
0.85	0.852	0.2%
0.95	0.925	2.7%

Reasonably good estimates of the location of the thermal front were obtained for all scenarios except for x_f = 0.05. This is physically intuitive, because the return curves for the conservative tracer and the released dye are almost identical when the thermal front is still close to the injection well, making it difficult to estimate the front location quantitatively. The poor fit of the return curve of the released dye can be attributed mathematically to the problematic nature of the optimization surface for this scenario, which is shown in Figure 2.43.

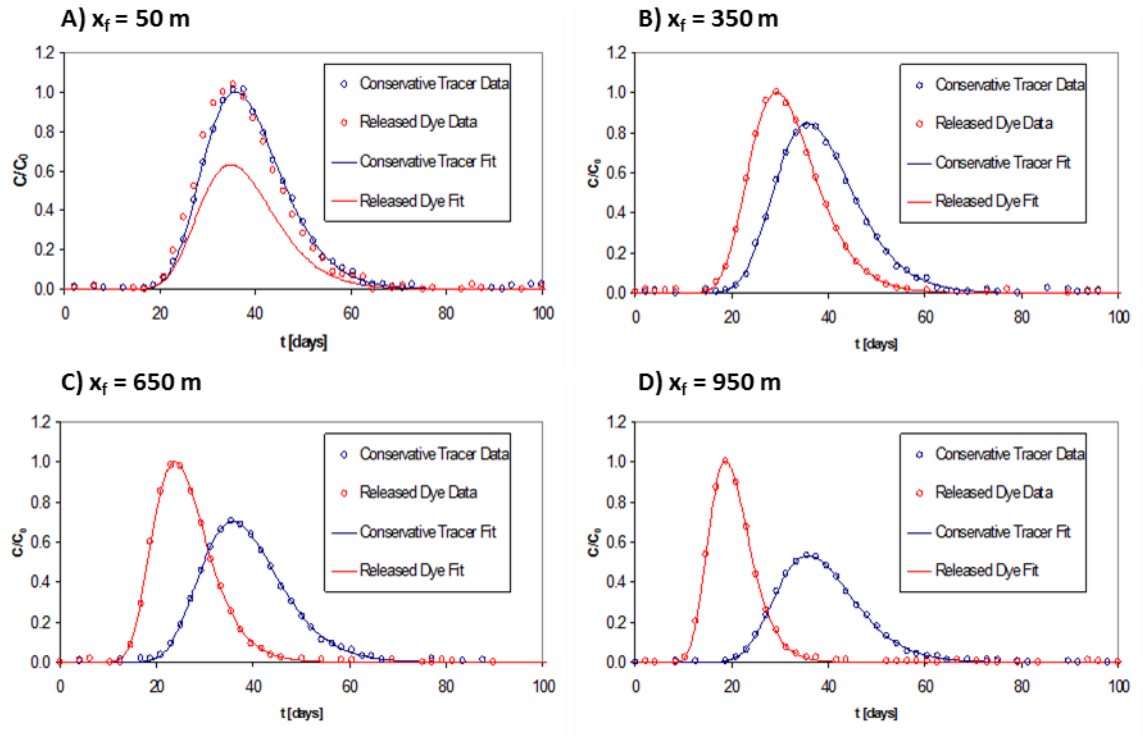

Figure 2.42: Return curve data and fits for (A) x_f = 50 m, (B) x_f = 350 m, (C) x_f = 650 m, and (D) x_f = 950 m. Note that released dye experiences breakthrough first because it is carried a distance x_f by the nanosensor, which has a retardation factor of 1, while the conservative tracer has a retardation factor of 2.

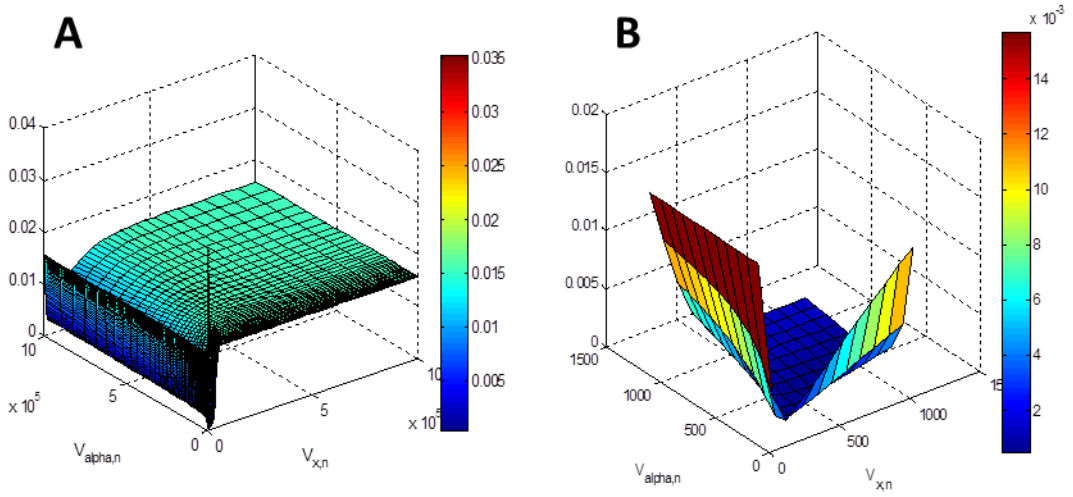

Figure 2.43: Objective function surface for fitting the return curve of the reactive tracer when x_f = 50 m (A) for entire parameter range of optimization and (B) zoomed in near the minimum of ($V_{x,n}$ = 1000 m^3, $V_{\alpha,n}$ = 500 m^3). Note that the point chosen by the solver was ($V_{x,n}$ = 268.3 m^3, $V_{\alpha,n}$ = 180.8 m^3).

The large trough along the $V_{\alpha,n}$ axis in Figure 2.43A indicates that for large initial guesses of $V_{\alpha,n}$, the solver might get stuck far from the minimum (since change in the objective function is the termination criteria). Moreover, the values of the objective function vary very little near the minimum, as shown in Figure 2.43B. This explains why the solver terminated at the point ($V_{x,n}$ = 268.3 m^3, $V_{\alpha,n}$ = 180.8 m^3) and resulted in a poor fit.

2.5 CONCLUSION

To investigate the feasibility of using nanosensors to determine reservoir properties in general and fracture network properties in particular, it was essential to verify their transport through typical formation rock. Initial testing with nanoparticles was also required to develop the understanding of best injection procedures, sampling strategies and characterization techniques. Accordingly, various laboratory-scaled core-flooding and micromodel experiments with inert nanoparticle and microsphere suspensions were conducted.

Functional tin-bismuth nanoparticles and dye-attached silica nanoparticles were synthesized, characterized, and used in heating experiments. Tin-bismuth nanoparticles experienced size distribution coarsening due to melting, and dye-attached silica nanoparticles exhibited a permanent fluorescence change, possibly due to dye release. The potential capability of a dye-releasing nanoparticle to estimate location of temperature measurement and thus map the temperature distribution in geothermal reservoirs was explored using an analytical model. Dye-attached silica nanoparticles show more promise as temperature sensors than tin-bismuth nanoparticles due to their potential capability to estimate measurement location and the fact that the growth of tin-bismuth nanoparticles due to melting and colliding could enhance deposition by straining and gravitational settling.

This study has shown that the particles size and/or size distribution, shape, surface charge, suspension concentration and fluid velocity were influential parameters governing the transport of nanoparticles through porous and fractured media.

1. **Shape:** We explored the significance of the nanoparticle shape by flowing silver nanowires through the pore spaces of Berea sandstone. The silver nanowires were trapped at the inlet of the core and could not flow through. Subsequently, spherically shaped silver nanoparticles with the same surface characteristics were injected into the sandstone. It was found that the silver nanospheres were able to flow with 25% recovery. The low recovery was attributed to the aggregation of the particles that resulted in entrapment due to their physical size.

2. **Surface charge:** The surface charge effect on the transport of nanoparticles was studied by injecting hematite nanorice into sandstone. Initially the hematite nanorice sample had surface charge opposite that found in the sandstone. Analysis of the effluent and pore spaces showed that the nanorice was trapped within the pores and was not detected in the effluent. Testing on a tube packed with glass beads (in the absence of core materials) revealed that nanorice still experienced low mobility. We modified the hematite surface charge by surfactant coating. As a result, the hematite nanorice flowed with approximately 23% recovery. Despite the modest recovery, it was concluded that the affinity of the nanorice to the porous medium was primarily related to its surface charge.

3. **Particle size:** This study has also shown that there is an optimum particle size for the transport of tin-bismuth alloy nanoparticles through Berea sandstone. The rock filtered the injected nanofluid allowing only certain particle sizes to flow across it, as opposed to the glass bead injection where tin-bismuth particles of all sizes were produced. Testing with glass beads has also confirmed that the tin-bismuth nanoparticles had affinity to the rock materials.

4. **Suspension concentration:** It was observed that the recovery of the 2 µm particles was affected adversely by suspension concentrations (decreasing recovery with increasing suspension concentration). It was found that the increasing concentration of the 2 µm particles had resulted in more pronounced aggregation, which led to trapping by straining. This conclusion was supported by the degree and rate of reduction in permeability occurring at higher concentration, and visual observations during micromodel flow experiments. This finding would be significant in the design of a tracer test using these particles as nanosensors.

5. **Fluid velocity:** In the micromodel, **t**he recovery of the 5 µm particles was influenced more by fluid velocity than by suspension concentration. This effect was attributed to the degree by which larger particles are influenced by the hydrodynamics of the system (drag and gravitational forces) compared to smaller particles. This observation was in agreement with quantitative analysis using particle filtration and DLVO theory, and metrics related to pore and grain size heterogeneity found in the literature.

6. **Fracture caliper:** Investigation of the transport of microspheres through fractures was carried out. We demonstrated the transport and recovery of fluorescent silica microspheres of different sizes through a naturally fractured greywacke core. We also demonstrated the feasibility of estimating the fracture aperture by correlating the size of largest recovered spheres to fracture opening, through the injection of a polydisperse sample with a range of particle sizes.

3. FRACTURE CHARACTERIZATION USING RESISTIVITY

This research project was conducted by Research Assistant Lilja Magnusdottir and Professor Roland Horne. The objective of this project was to investigate ways to use resistivity to infer fracture properties in geothermal reservoirs.

3.1 SUMMARY

In this project, the aim was to use Electrical Resistivity Tomography (ERT) to characterize fracture properties in geothermal fields. The resistivity distribution of a field can be estimated by measuring potential differences between various points while injecting an electric current into the ground and resistivity data can be used to infer fracture properties due to the large contrast in resistivity between water and rock. The contrast between rock and fractures can be increased further by injecting a conductive tracer into the reservoir, thereby decreasing the resistivity of the fractures. In this project, the potential difference has been calculated between wells as conductive fluid flows through fracture networks. The time history of the potential field depends on the fracture network and can therefore be used to estimate where fractures are located and the character of their distribution.

A two-dimensional resistivity model was developed to calculate a potential field due to point sources of excitation for a nonuniform rectangular grid. The resistivity model was used with flow simulations of a conductive tracer to study how the time history of the electric potential difference between wells depends on the fracture paths in the reservoir. Then, the possibility of using flow simulator TOUGH2 to not only simulate the tracer flow through the reservoirs but to also solve the electric potential was studied, due to the analogy between Ohm's law that describes electrical flow and Darcy's law describing fluid flow. The EOS9 module in TOUGH2 was used successfully to solve the electric field because it allows for the viscosity, density and compressibility to be independent of pressure, unlike the EOS1 module used for tracer flow. However, it was also shown that the EOS1 module was capable of calculating the electric potential with sufficient accuracy. Using TOUGH2 to solve the electric field increases the efficiency by allowing for the same nonrectangular grid to be used for all simulations. Next, a discrete-fracture model introduced by Karimi-Fard et al. (2003) was used to create discrete-fracture networks with fractures of realistic dimensions and the time-dependent potential difference between two or more wells was analyzed for different networks. One of the fracture networks was modeled as an electric circuit to verify that the electric field calculations from TOUGH2 were accurate for the discrete-fracture network. Finally, some preliminary work was done in finding ways to use the electric potential with inverse modeling to characterize fracture patterns. Geometric fractal dimensions were determined for two fracture networks using inverse analysis but more examination needs to be done to test and improve the accuracy of the method.

3.2 INTRODUCTION

Fracture characterization in Enhanced Geothermal Systems (EGS) is crucial to ensure adequate supply of geothermal fluids and efficient thermal operation of the wells. The flow path characteristics control mass and heat transport in the system and inappropriate placing of injection or production wells can lead to premature thermal breakthrough. Such premature thermal breakthroughs have occurred in numerous geothermal reservoirs, as described by Horne (1982), and observed in The Geysers (Beal et al., 1994).

The goal of this study was to find ways to use direct current resistivity measurements to characterize fractures in geothermal reservoirs. Pritchett (2004) demonstrated based on a theoretical study that hidden geothermal resources can be explored by electrical resistivity surveys because geothermal reservoirs are usually characterized by substantially reduced electrical resistivity relative to their surroundings. The rock is normally a good insulator so the electrical current moving through the reservoir passes mainly through fluid-filled fractures and pore spaces. In these surveys, a direct current is sent into the ground through electrodes and the voltage differences between them are recorded. The input current and measured voltage difference give information about the subsurface resistivity, which can then be used to infer fracture locations. Other geophysical surveys commonly used to find hidden geothermal resources are self-potential and magnetotelluric surveys. Garg et al. (2007) described how self-potential, magnetotelluric and direct current surveys were all used to explore the Beowawe geothermal field in the Basin and Range Province of western USA. However, these surveys are usually performed on the surface with very low resolution when exploring deeper portions of the reservoirs, making it impossible to characterize fractures that are small-scaled compared to the size of the reservoir. Therefore, the possibility of placing the electrodes inside geothermal wells has been considered in this study, in order to measure the resistivity more accurately in the deeper parts of the reservoir. Due to the limited number of wells (i.e. measurement points), the study includes investigating ways to enhance the process of characterizing fractures from sparse resistivity data.

In order to increase the contrast in resistivity between the rock and fracture zones, a conductive tracer could be injected into the reservoir and the time-dependent potential difference is measured as the tracer distributes through the fracture network. Slater et al. (2000), and Singha and Gorelick (2005) have shown a way of using tracer injection with Electrical Resistivity Tomography (ERT) to observe tracer migration in experimental tanks with cross-borehole electrical imaging. In previous work, usually many electrodes were used to obtain the resistivity distribution for the whole tank at each time step. The resistivity distribution was then compared to the background distribution (without any tracer) to see resistivity changes in each block visually. These resistivity changes helped locate the saline tracer and thereby the fractures. Using this method for a whole reservoir would require a gigantic parameter space, and the inverse problem would likely not be solvable, except at very low resolution. However, in the approach considered in this study, the electrodes would be placed inside two or more geothermal wells and the potential differences between them studied. The potential difference between the wells which corresponds to changes in apparent resistivity would be measured and plotted as a function of time while the conductive tracer flows through the fracture network. The goal is to find ways to use that response, i.e. potential difference vs. time, with the tracer return curves in an inverse modeling process to characterize fracture patterns.

In this report, a two-dimensional resistivity model used to calculate a potential field due to point sources of excitation is described and examples shown where two different fracture networks give different time histories of the potential difference between wells. The analogy between water flow and electrical flow is also defined and the possibility of using EOS9 and EOS1 modules in TOUGH2 to calculate the electric potential is explored. Next, the resistivity of a saline tracer is interpreted and the time history of the electric potential difference is studied for

discrete-fracture networks to illustrate further how the potential difference response corresponds to realistic fracture networks. A discrete-fracture network is also modeled as an electric circuit and the analytical results compared to results from TOUGH2. Then, some preliminary work to find ways to use inverse analysis to characterize fracture networks is described and geometric fractal dimensions are determined using inverse analysis.

3.3 RESISTIVITY MODEL

A two-dimensional resistivity model was developed to calculate a potential field due to point sources of excitation. In resistivity modeling, one of the main problems is to solve the Poisson equation that describes the potential field and to complete the inversion iteration efficiently. The Poisson equation can be derived from basic electrical relationships as described by Dey and Morrison (1979). Ohm's Law defines the relationship between current density, *J*, conductivity of the medium, σ, and the electric field, *E*, as:

$$J = \sigma E \tag{3.1}$$

The stationary electric fields are conservative, so the electric field at a point is equal to the negative gradient of the electric potential there, i.e.:

$$E = -\nabla \phi \tag{3.2}$$

where ϕ is the scalar field representing the electric potential at the given point. Hence,

$$J = -\sigma \nabla \phi \tag{3.3}$$

Current density is the movement of charge density, so according to the continuity equation, the divergence of the current density is equal to the rate of change of charge density,

$$\nabla J = \frac{\partial Q(x, y, z)}{\partial t} = q(x, y, z) \tag{3.4}$$

where *q* is the current density. Combining equations (3.3) and (3.4) gives the following Poisson equation which describes the potential distribution due to a point source of excitation,

$$\nabla \left[\sigma \nabla \phi\right] = -q(x, y, z) \tag{3.5}$$

This partial differential equation can then be solved numerically for the resistivity problem.

3.3.1 Finite difference equations in two dimensions

Finite difference method is used to approximate the solution to the partial differential equation (3.5) using a point-discretization of the subsurface (Mufti, 1976). The computational domain is discretized into $Nx \times Ny$ blocks and the distance between two adjacent points is *h* in x-direction and *l* in y-direction, as shown in Figure 3.1.

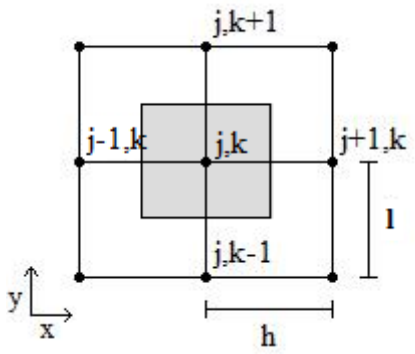

Figure 3.1: Computational domain, discretized into blocks.

The grid used is rectangular and nonuniform so the fracture elements can be modeled smaller than the elements for the rest of the reservoir, in order to decrease the total number of elements. Taylor series expansion is used to approximate the derivatives of equation (3.5) about a point (*j*,*k*) on the grid,

$$\left.\frac{\partial}{\partial x}\left(\sigma\frac{\partial\phi}{\partial x}\right)\right|_{(j,k)} \approx \frac{\left[\begin{array}{l}\phi(j+1,k)\sigma\left(j+\frac{1}{2},k\right)+\phi(j-1,k)\sigma\left(j-\frac{1}{2},k\right)\\ -\left[\sigma\left(j+\frac{1}{2},k\right)\sigma\left(j-\frac{1}{2},k\right)\right]\phi(j,k)\end{array}\right]}{h^2} \tag{3.6}$$

$$\left.\frac{\partial}{\partial y}\left(\sigma\frac{\partial\phi}{\partial y}\right)\right|_{(j,k)} \approx \frac{\left[\begin{array}{l}\phi(j,k+1)\sigma\left(j,k+\frac{1}{2}\right)+\phi(j,k-1)\sigma\left(j,k-\frac{1}{2}\right)\\ -\left[\sigma\left(j,k+\frac{1}{2}\right)\sigma\left(j,k-\frac{1}{2}\right)\right]\phi(j,k)\end{array}\right]}{l^2} \tag{3.7}$$

The point (*j*,*k*) represents the shaded area in Figure 3.1 (area = *hl*) so the current density due to an electrode at that point is given by,

$$q(j,k)=\frac{I}{hl} \tag{3.8}$$

where *I* [A] is the current injected at point (*j*,*k*). Combining Equations (3.5)-(3.8) and solving for the electric potential ϕ [V] at point (*j*,*k*) gives,

$$\phi(j,k)=\frac{\left[Ihl+\phi(j+1,k)c_1l^2+\phi(j-1,k)c_2l^2+\phi(j,k+1)c_3h^2+\phi(j,k-1)c_4h^2\right]}{\left[c_1+c_2\right]l^2+\left[c_3+c_4\right]h^2} \tag{3.9}$$

The parameters c_i represent the conductivity averaged between two adjacent blocks, i.e.

$$c_1=\frac{2}{\rho(j,k)+\rho(j+1,k)} \tag{3.10}$$

$$c_2=\frac{2}{\rho(j,k)+\rho(j-1,k)} \tag{3.11}$$

$$c_3 = \frac{2}{\rho(j,k) + \rho(j,k+1)} \tag{3.12}$$

$$c_4 = \frac{2}{\rho(j,k) + \rho(j,k-1)} \tag{3.13}$$

where $\rho(j,k)$ is the resistivity [Ωm] of the node at grid coordinates j,k.

3.3.2 Iteration method

In order to solve Equation (3.9) numerically and obtain the results for electrical potential ϕ at each point on the grid, the iteration method called Successive Over-Relaxation was used (Spencer and Ware, 2009). At first, a guess is made for $\phi(j,k)$ across the whole grid, for example $\phi(j,k)=0$ for all j,k. That guess is then used to calculate the right hand side of equation (3.9) (*Rhs*) for each point and the new set of values for $\phi(j,k)$ is calculated using the following iteration scheme,

$$\phi_{n+1} = \omega Rhs + (1-\omega)\phi_n \tag{3.14}$$

The multiplier ω is used to shift the eigenvalues so the iteration converges better than simple relaxation. The number ω is between 1 and 2, and when the computing region is rectangular the following equation can be used to get a reasonable good value for ω,

$$\omega = \frac{2}{1+\sqrt{1-R^2}} \tag{3.15}$$

where

$$R = \frac{\left(\cos\left(\frac{\pi}{Nx}\right) + \cos\left(\frac{\pi}{Ny}\right)\right)}{2} \tag{3.16}$$

The natural Neumann boundary conditions are used on the outer boundaries, i.e. $\frac{\partial\phi}{\partial n} = 0$.

3.3.3 Time-dependent potential difference simulated for two reservoirs

A flow simulation was first performed using TOUGH2 reservoir simulator to see how a tracer, which increases the conductivity of the fluid, distributes after being injected into a reservoir. The simulation was carried out on a two-dimensional grid with dimensions 1000 × 1000 × 10 m^3 with fractured rock modeled as a squared area (green blocks), first in the lower right corner and then in the upper left corner, as shown in Figure 3.2.

The goal was to study the difference in potential field between these two cases as conductive fluid is injected into the reservoir. The reservoir was modeled with porosity 0.4 and permeability 10^5 md (10^{-10} m^2) while the fractured rock had porosity 0.65 and permeability 5×10^{10} md (5×10^{-5} m^2).

No-flow boundary conditions were used and 100 kg/s of water was injected in the upper left corner with enthalpy 100 kJ/kg, and 0.1 kg/s of tracer with enthalpy 100 kJ/kg. The production well was set to produce at a constant pressure, 8 bar. The initial pressure was set to 9.6 bar,

temperature to 150°C and initial tracer mass fraction to 10^{-9} because the simulator could not solve the problem with zero initial tracer mass fraction.

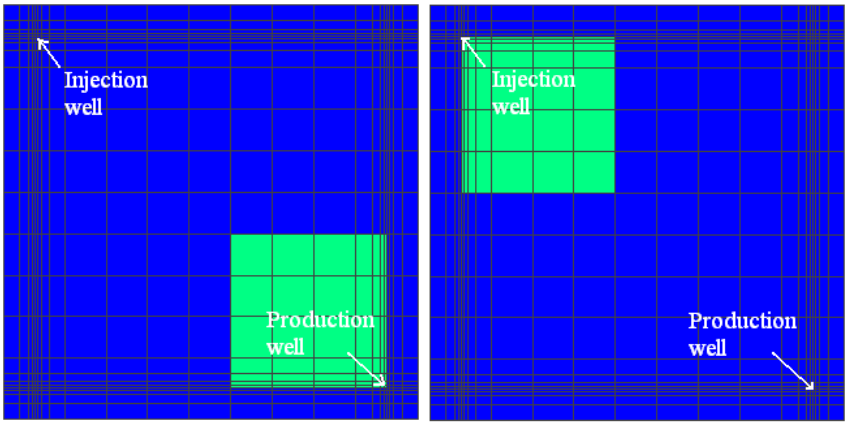

Figure 3.2: Fractured rock (green blocks) modeled in the lower right corner of the reservoir (to the left) and in the upper left corner (to the right).

The following equation was used to calculate the electrical conductivity, $1/\rho_w$, of a NaCl water solution (Crain, 2010),

$$\rho_w = \frac{400{,}000}{\left(\frac{9}{5}T + 32\right)Ws} \tag{3.17}$$

in order to define conductivity values in the resistivity model as NaCl tracer flows through the reservoir. T is the formation temperature (assumed to be 150°C) and Ws is the water salinity [ppm NaCl].

The resistivity for the rock before fluid had been injected was set as 100 Ωm for the fractured area (assuming fractures were filled with water) and as 2000 Ωm for the rest of the reservoir. Figure 3.3 shows how the potential difference between the injector and the producer changes with time for the reservoirs shown in Figure 3.2.

The potential difference in the graph on the left in Figure 3.3 drops very rapidly for the first 10 days, but then decreases more slowly when the tracer front has reached the fractured area. On the graph to the right in Figure 3.3, the potential difference drops more slowly, as the conductive fluid first fills up the fractured rock, modeled with much higher porosity then the rest of the reservoir. These preliminary results indicated that different fracture properties give different potential difference histories between two wells, and could therefore be used to indicate fracture characteristics.

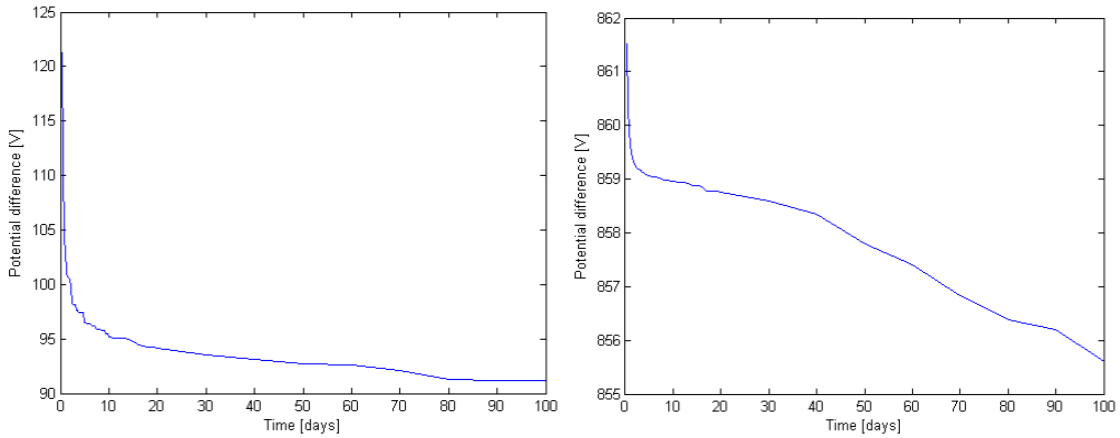

Figure 3.3: Potential difference between injection and production wells for reservoirs in Figure 3.2.

3.4 THE ELECTRIC FIELD SOLVED USING TOUGH2

In the previous case, flow simulator TOUGH2 was used to calculate the flow of conductive fluid and the resistivity model used to calculate the electric field at each time step while the fluid distributed through the reservoir. This section describes how the flow simulator can also be used to solve Ohm's law describing the flow of an electric current due to the analogy between Darcy's law and Ohm's law (Muskat, 1932). The potential distribution in steady-state flow through a porous medium is exactly the same as the potential distribution in an electrically conducting medium. Therefore, the efficiency could be increased by using TOUGH2 for both the fluid flow simulations and to simulate the electric current. That way, the same grid could be used when calculating the distribution of a conductive tracer in the reservoir as well as when solving the electric difference between the wells at each time step.

3.4.1 Water flow analogy of electrical flow

The steady-state flow of an electric current through a conducting medium due to differences in energy potential is analogous to the steady-state flow of a fluid through porous medium. Darcy's law is an empirical relationship similar to Ohm's law (equation 3.3) but instead of describing electrical flow Darcy's law describes fluid flow through a porous medium,

$$q = -\frac{k}{\mu}\nabla p \tag{3.18}$$

where q is the flow rate [m/s], k is permeability [m^2], μ is viscosity of the fluid [kg/ms] and p is pressure [Pa]. Table 3.1 presents the relations between the variables of Darcy's law and Ohm's law.

Table 3.1: Analogy between electric current flow and water flow.

	Darcy's law:	Ohm's law:
Flux of:	Water q [m/s]	Charge J [A/m^3]
Potential:	Pressure p [Pa]	Voltage φ [V]
Medium property:	Hydraulic conductivity $\frac{k}{\mu}$ [m^2/Pa·s]	Electrical conductivity σ [1/Ωm]

The similarities between these two equations show that it is possible to use a flow simulator like TOUGH2 to solve an electric field due to flow of an electric current. Then, the pressure results from TOUGH2 correspond to the electric voltage, the current density to the flow of water and the electrical conductivity corresponds to the hydraulic conductivity, i.e.

$$\sigma = \frac{k}{\mu} \tag{3.19}$$

Consequently, the permeability written in the TOUGH2 input file is defined as the conductivity of the field under study, multiplied by the appropriate viscosity which corresponds to the pressure (i.e. electric potential) conditions existing in the TOUGH2 simulation. However, it must be recognized that viscosity depends on pressure while conductivity of a reservoir does not depend on the electric voltage used. Also, some of the electric parameters need to be scaled when using TOUGH2 in this way.

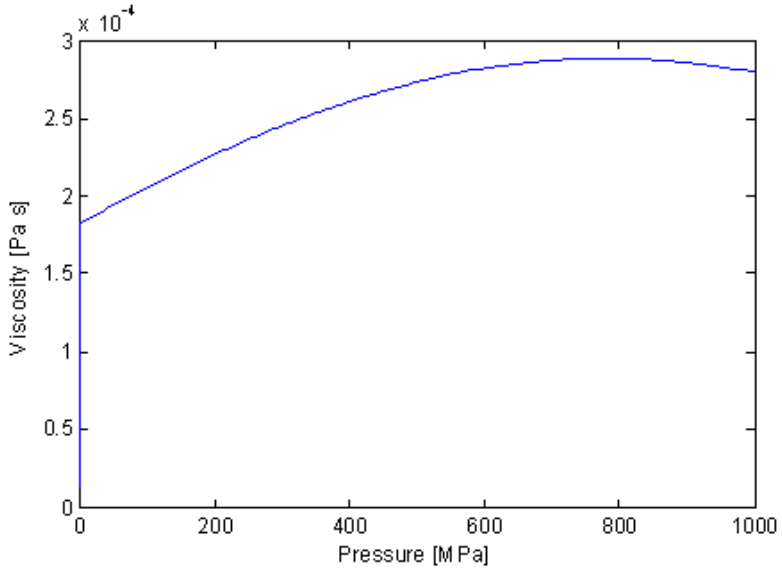

Figure 3.4: Viscosity [Pa·s] as a function of pressure [MPa].

3.4.2 Pressure dependence of viscosity

When the EOS1 module in TOUGH2 is used the viscosity of the fluid is pressure dependent. For example, Figure 3.4 shows how viscosity of water at 150°C changes with pressure. The electric conductivity which corresponds to the permeability divided by viscosity does however not

depend on the electric potential corresponding to the pressure, so the EOS1 module might not give accurate results when calculating the electric potential.

In order to take the pressure dependence into account EOS9 module in TOUGH2 was studied. It considers flow of a single aqueous phase consisting of a single water component. The conditions are assumed to be isothermal so only a single water mass balance equation is solved for each grid block and the thermal properties of water can be overwritten. Therefore, liquid viscosity, density and compressibility can be defined constant and reference pressure and temperature can be overwritten, making the imitation of electric flow possible.

In TOUGH2, Darcy's law is solved using the following discretization,

$$F_{nm} = \rho u_{nm} = -k_{nm}\left[\frac{k_r \rho}{\mu}\right]_{nm}\left[\frac{P_n - P_m}{D_{nm}} - \rho_{nm} g_{nm}\right] \tag{3.20}$$

where ρ is density and g_{nm} is gravity in direction from m to n. Suitable averaging are used at the interface between grid blocks n and m, and D_{nm} is the distance between the nodal points n and m (see Figure 3.5).

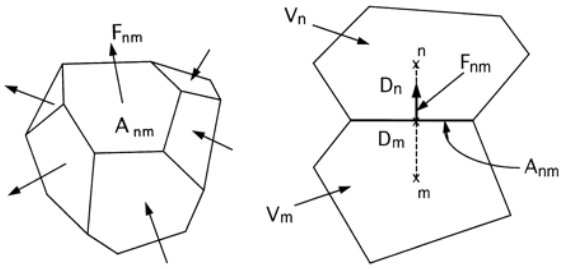

Figure 3.5: Space discretization, grid blocks n and m.

In order to calculate the flow simulation the following equation is solved using Newton/Raphson iteration:

$$R_n^{K,K+1} = M_n^{K,K+1} - M_n^{K,K} - \frac{\Delta t}{V_n}\left[\sum_m A_{nm} F_{nm}^{K,K+1} + V_n q_n^{K,K+1}\right] \tag{3.21}$$

where $R_n^{K,K+1}$ are residuals between time step t^k and $t^{k+1} = t^k + \Delta t$, M is mass accumulation, A is the surface area of the grid block, V is the volume and q denotes sinks and sources.

The electric field was calculated for a 3 × 3 block matrix, see Figure 3.6, using EOS9 and the results compared to the resistivity model described in section 3.3 (Resistivity Model) and an analytical solution. The resistivity of the middle block (green) was set as 0.0025 Ωm and the resistivity of the blue blocks was set as 0.005 Ωm and the initial electric potential was defined as zero.

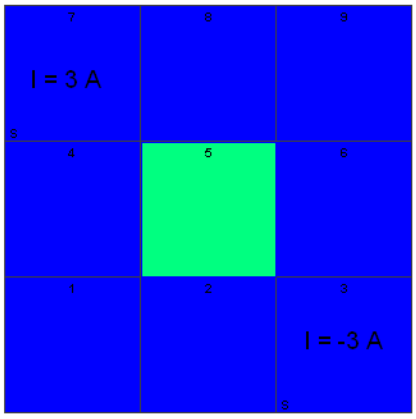

Figure 3.6: Inhomogeneous electric model with the current set as 3 A in the upper left corner and as -3 A in the lower right corner.

The analytical solution and the solution from the resistivity model were the same as when EOS9 was used. Results are shown in Table 3.2. Therefore, it was shown that EOS9 module in TOUGH2 can be used to calculate the electric field accurately by defining the water density and viscosity constant.

Table 3.2: Electric potential calculated using the resistivity model, EOS9 module in TOUGH2 and the analytical solution.

0.0107 V	0.0032 V	0 V
0.0032 V	0 V	-0.0032 V
0 V	-0.0032 V	-0.0107 V

In order to study further the effects of pressure dependence on the simulated electric potential, EOS1 and EOS9 were both used to calculate the electric field for a simple inhomogeneous 9 × 9 grid shown in Figure 3.7.

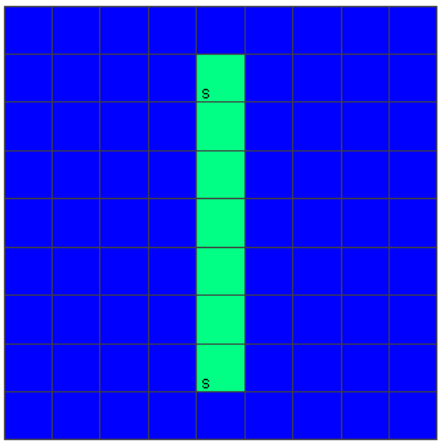

Figure 3.7: Inhomogeneous 9 × 9 grid.

The two-dimensional grid was modeled with dimensions 100 × 100 × 1 m^3 and permeability 1 × 10^{-13} m^2 (blue blocks) and with a fracture in the middle with permeability 1 × 10^{-8} m^2 (green blocks). The initial pressure was set as 10^6 Pa and the temperature as 150°C. Equation 3.19 shows how the conductivity of the field was defined as the permeability divided by the viscosity, so when EOS1 was used the conductivity changed by a small amount as the viscosity changed with pressure. In EOS9 the viscosity, density and compressibility were defined constant making it possible to model constant conductivity values for the reservoir. Figure 3.8 shows the electric potential for the grid blocks calculated using EOS1 and EOS9 in TOUGH2.

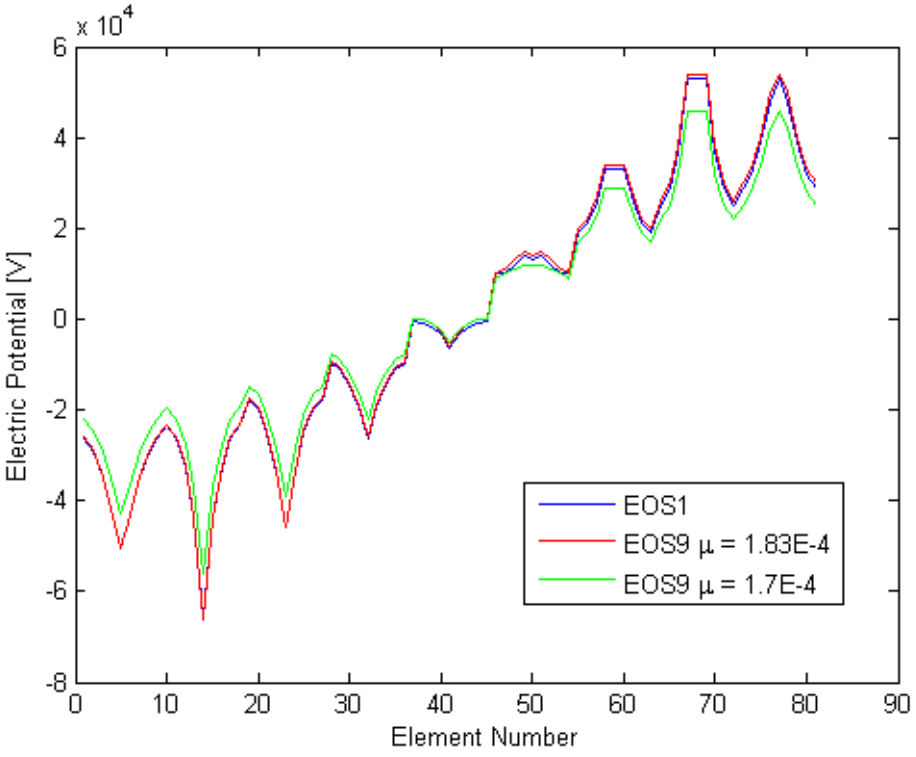

Figure 3.8: Electric potential for the reservoir calculated using EOS1 and EOS9

The electric potential calculated using EOS1 is almost the same as the electric potential calculated using EOS9 with μ = 1.84 × 10^{-4} Pa·s. However, if the viscosity is set as 1.7 × 10^{-4} Pa·s the electric potential results are slightly different from the EOS1 results because EOS1 uses the viscosity of water at the appropriate pressure and temperature conditions. In this case, the pressure is ranging from 0.996-1.0 × 10^6 Pa and the temperature is 150°C so the viscosity is ranging from 1.85-1.83 × 10^{-4} Pa·s. Therefore, it has been shown that EOS1 module in TOUGH2 can be used to calculate the electric field instead of using EOS9 as long as the permeability is defined as the conductivity multiplied with the appropriate viscosity that corresponds to the pressure and temperature conditions in the simulation. The EOS9 module was used when possible but problems occurred when using EOS9 with a Discrete-Fracture Method (DFN) by Karimi-Fard et al. (2003) so in those cases EOS1 module was used instead.

3.4.3 Two simple fracture networks studied

Two simple fracture networks were studied to examine the difference in the time histories of the potential field between these two cases as conductive fluid was injected into the reservoir. First, flow simulations were performed using the EOS1 module in TOUGH2 to see how a conductive tracer, distributes after being injected into different reservoirs. The simulations were carried out on two-dimensional grids with dimensions 2000 × 2000 × 1 m^3 with fractures first modeled as a long path from the injector to the producer as shown in Figure 3.9 and then as a path straight from the injector to the producer, shown in Figure 3.10.

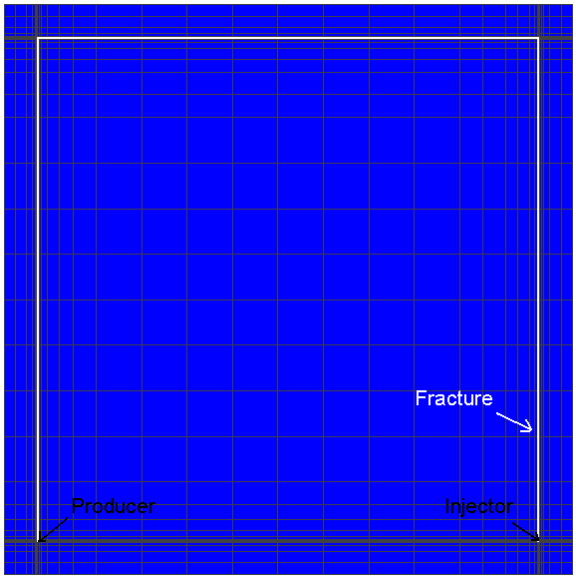

Figure 3.9: Reservoir with a fracture from the injector, around the reservoir and to the producer.

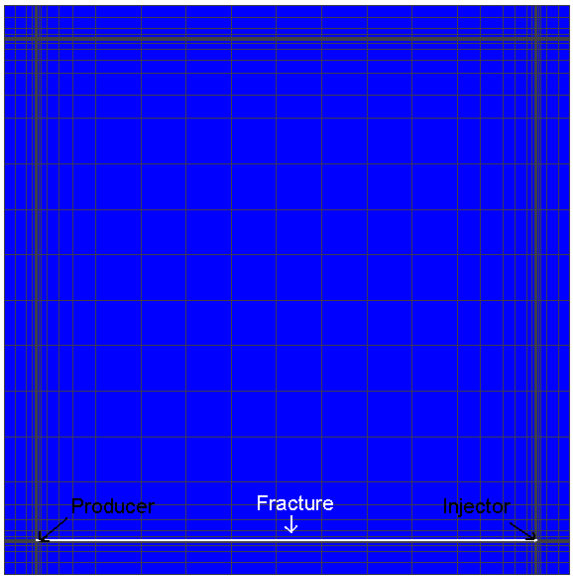

Figure 3.10: Reservoir with a fracture straight from the injector to the producer.

The reservoir was modeled with a porosity of 0.2 and a permeability of 10^6 md (10^{-9} m^2) while the fractures have a permeability of 10^{11} md (10^{-4} m^2). No-flow boundary conditions were used

and 100 kg/s of water was injected in the lower right corner with enthalpy 100 kJ/kg, and 0.1 kg/s of tracer with enthalpy 100 kJ/kg. The initial pressure was set to 10^6 Pa, temperature to 150°C and initial tracer mass fraction to 10^{-9}.

The tracer injected into the reservoir is a NaCl solution whose resistivity changes with temperature and concentration. Ucok et al. (1980) have established experimentally the resistivity of saline fluids over the temperature range 20-350°C and their results for resistivity of NaCl solution calculated using a three-dimensional regression formula is shown in Figure 3.11.

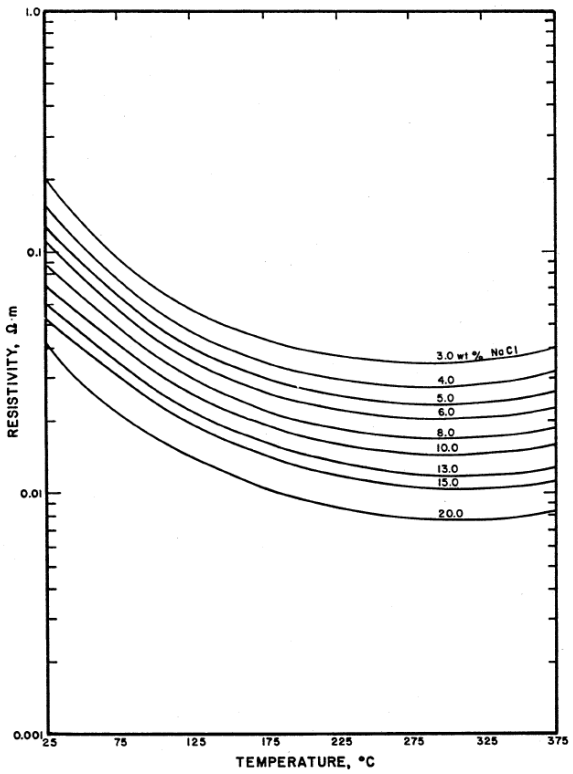

Figure 3.11: Resistivity of NaCl solution as a function of temperature and concentration (Ucok et al., 1980).

Ucok et al. (1980) calculated that the dependence of resistivity is best represented by the formula:

$$\rho_w = b_0 + b_1 T^{-1} + b_2 T + b_3 T^2 + b_4 T^3 \tag{3.22}$$

where T is temperature and b are coefficients found empirically. The best fit for the concentration dependence was found to be:

$$\rho_w = 10/(\Lambda c) \tag{3.23}$$

where:

$$\Lambda = B_0 - B_1 c^{1/2} + B_2 c \ln c + higher\ \ order\ \ terms \tag{3.24}$$

Coefficients B depend on the solution chemistry and c is the molar concentration.

In this project, the tracer concentration resulting from the flow simulation is changed into molar concentration and the following B coefficient matrix for the three-dimensional regression analysis of the data studied by Ucok et al. (1980) is used to calculate the resistivity of the NaCl solution,

$$B = \begin{matrix} 3.470 & -6.650 & 2.633 \\ -59.23 & 198.1 & -64.80 \\ 0.4551 & -0.2058 & 0.005799 \\ -0.346E\text{-}5 & 7.368E\text{-}5 & 6.741E\text{-}5 \\ -1.766E\text{-}6 & 8.787E\text{-}7 & -2.136E\text{-}7 \end{matrix}$$

Then, the resistivity of water saturated rock, ρ, is calculated using Archie's law (Archie, 1942),

$$\rho = a\phi^{-b}\rho_w \tag{3.25}$$

where ϕ is the porosity of the rock and a and b are empirical constants, here a is set as 1 and b as 2. The resistivity value of each block therefore depends on the tracer concentration in that block and the value decreases as more tracer flows into the block.

The EOS9 module in TOUGH2 was used to calculate the electric potential distribution for the reservoirs in Figures 3.9 and 3.10. A current was set equal to 1 A at the injector and as -1 A at the producer and the potential field calculated based on the resistivity of the field at each time step. Figure 3.12 shows how the potential difference, which corresponds to the changes in resistivity, between the injector and the producer changed with time for the reservoirs in Figure 3.9 and Figure 3.10.

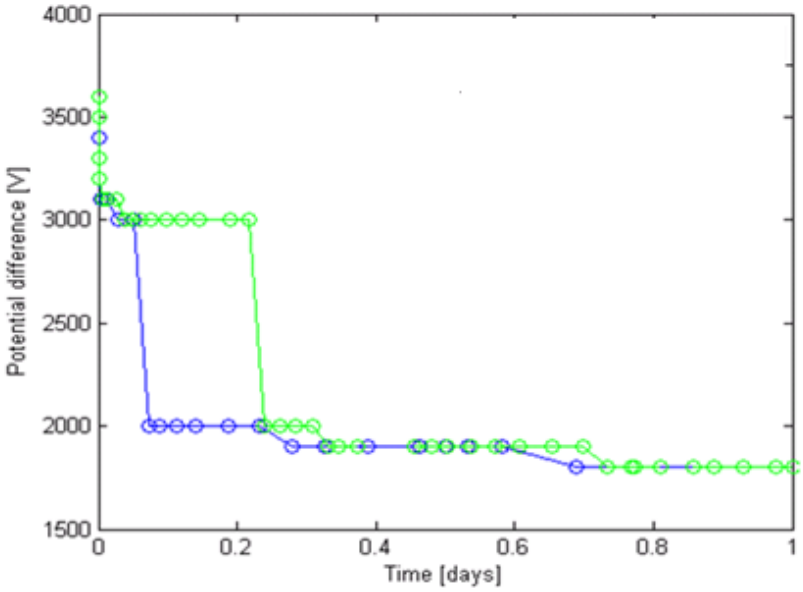

Figure 3.12: Potential difference between wells for reservoirs in Figure 3.9 (green) and Figure 3.10 (blue).

Figure 3.12 illustrates clearly that the electric potential history is different for the two fracture networks. After 0.239 days the potential difference plotted in green drops from 3000 V to 2000

V but the potential difference plotted in blue drops the same amount much earlier, or after 0.074 days. Therefore, these histories of the potential differences show that the conductive tracer flows faster through the fracture network in Figure 3.10 than in Figure 3.9 which tells us that the fracture path from the injector to the producer is shorter for that fracture network. In these examples, it is assumed that the reservoir does not have any water until the conductive water is injected into the reservoir. The resistivity between the injector and the producer is therefore very high until the tracer reaches the production well, allowing the current to flow easily between the wells. When the tracer has gone fully through the fracture networks for both cases the potential differences are the same. For realistic fracture networks, defining fractures by high permeability values in course-scale grid blocks would not be feasible so a discrete approach was explored.

3.5 DISCRETE-FRACTURE NETWORKS

A Discrete-Fracture Network (DFN) approach introduced by Karimi-Fard et al. (2003) was used to create realistic fracture networks by treating the fractures discretely. The method is based on an unstructured control volume finite-difference formulation where the element connections are assigned using a connectivity list. A MATLAB code written by Juliusson (2009) was used to generate a two-dimensional stochastic fracture network, run flow simulations on the network with TOUGH2, and plot the tracer flow results. In these cases, EOS1 module in TOUGH2 was used to solve the tracer flow as well as the electric flow. Figure 3.13 shows the fracture network generated, where the computational grid was formed using the triangular mesh generator Triangle, developed by Shewchuk (1996).

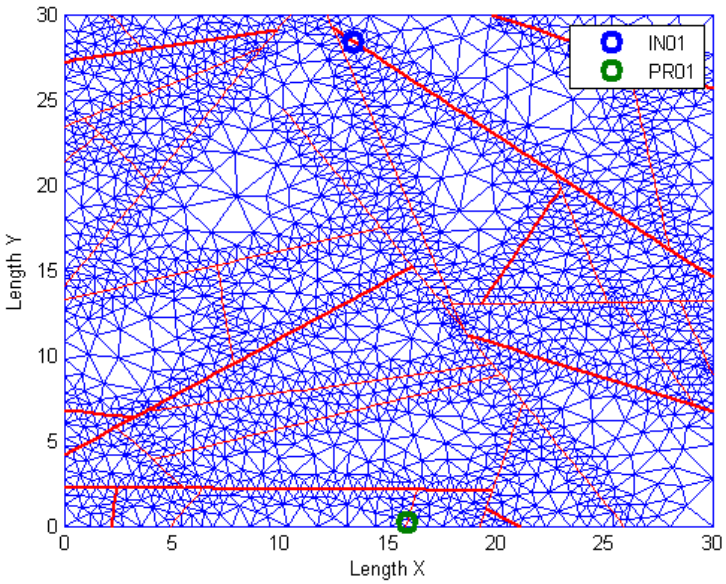

Figure 3.13: A two-dimensional discrete-fracture network.

The dimensions of the two-dimensional grid were 30 × 30 × 1 m^3 and closed (no-flow) boundary conditions were used. The porosity of the fractures was set to 0.9 and the width, w, was assigned as a function of the fracture length L,

$$w = L \cdot 10^{-4} \tag{3.26}$$

The corresponding permeability was determined by:

$$k = \frac{w^2}{12} \tag{3.27}$$

The matrix blocks were given a porosity value of 0.1 and a very low permeability value so the conductive fluid only flows through the fractures.

By using the DFN approach every element (both triangles and fracture segments) was given a transmissibility value which is related to the flow between two adjoining elements as,

$$Q_{ij} = T_{ij}(p_j - p_i) \tag{3.28}$$

where Q is the flow rate between gridblocks i and j, T is the transmissibility and p is the pressure. More details on the approach can be found in the reference by Karimi-Fard et al. (2003).

In Figure 3.13 an injection well was placed at the top of the figure and a production well at the bottom. Water was injected at the rate of 5.6×10^{-2} kg/s with enthalpy 3.14×10^5 kJ/kg and the tracer injected was 0.1% of the water injected. The production well was modeled to deliver against a bottomhole pressure of 10^6 Pa with productivity index of 4×10^{-12} m^3 (as specified for TOUGH2). The initial pressure was set to 10^6 Pa and the temperature to 25°C and the initial tracer mass fraction was set to 5.42×10^{-3}, which corresponds to ground-water. For the resistivity calculations the pores and fractures were modeled to be filled with ground-water before any tracer was injected into reservoir. The tracer was assumed to be a NaCl solution and the resistivity calculated using the three-dimensional regression formula as before (equations (3.22)-(3.24)) and the resistivity of water saturated rock was calculated using Archie's law, see equation (3.25). Archie (1942) concluded that for typical sandstones of oil reservoirs the coefficient a is approximately 1 and b is approximately 2 but Keller and Frischknecht (1996) showed that this power law is valid with varying coefficients based on the rock type. In this case, a was set as 3.5 and b as 1.4.

Figure 3.14 shows how the tracer concentration in the producer (green) changed with time as more tracer was injected into the reservoir.

The electrical resistivity method was used to examine how the potential difference history, which corresponds to the changes in resistivity, relates to the fracture network. The current was set as 1 A at the injector and as -1 A at the producer and the potential field calculated using EOS1 module in TOUGH2, see Figure 3.15.

The potential difference drops relatively quickly until about 0.25 days when it starts decreasing more slowly as a result of the entire fracture path from the injector to the producer becoming saturated with tracer. The relationship between the fractures and the time history of the electric potential can be made more visible by looking at the derivative of the potential difference, see Figure 3.16.

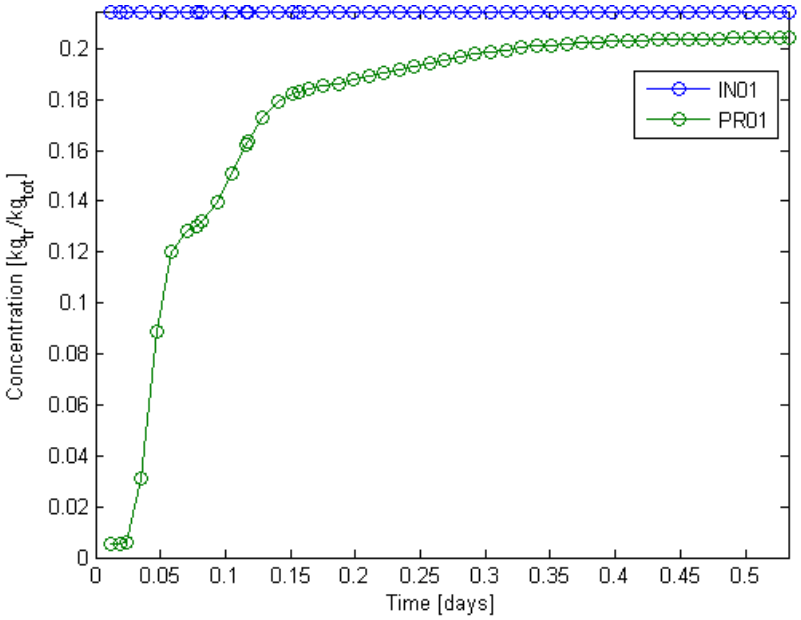

Figure 3.14: Tracer history at the injector (blue) and at the producer (green).

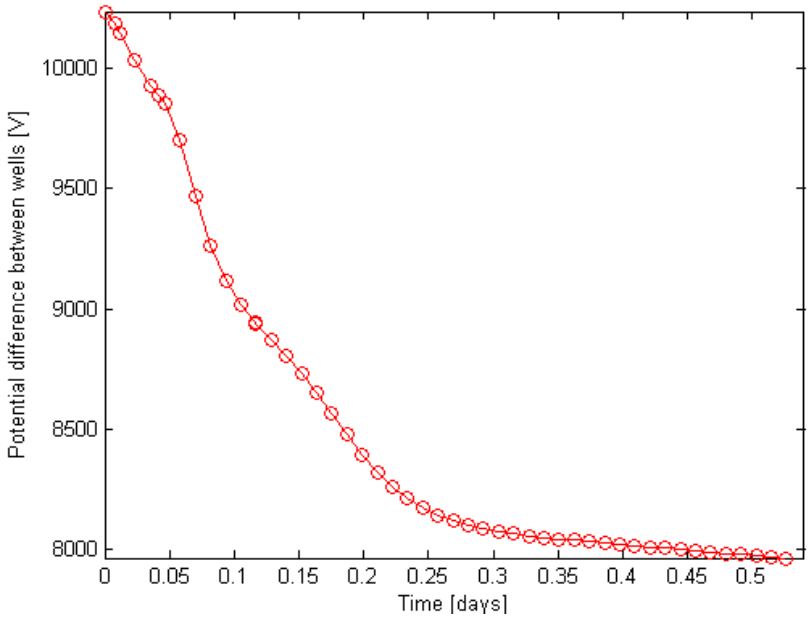

Figure 3.15: Potential difference between the injector and the producer.

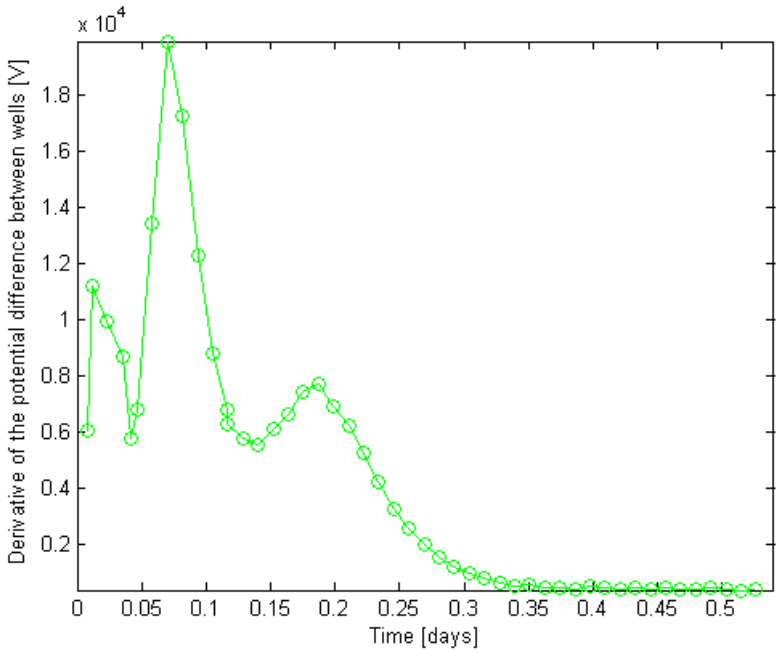

Figure 3.16: Derivative of the potential difference between the wells.

The first peak is after about 0.02 days when the conductive tracer reaches the production well. Figure 3.14 shows that the tracer concentration at the production well starts increasing at 0.02 days causing the resistivity to decrease and a low conductivity path to form between the injector and the producer, shown in Figure 3.17a). The electric current therefore flows through the low conductivity path, causing the electric potential difference between the wells to drop. Other peaks can be seen in Figure 3.16, for example after approximately 0.08 days and approximately 0.18 days. The peak after 0.08 days corresponds to a new low conductivity path formed to the left of the producer, see Figure 3.17c), and another path has been formed to the right after 0.18 days, see Figure 3.17d). The peaks of the derivative of the potential difference therefore correspond to the fracture network which verifies that the history of the electric potential could be used for fracture characterization.

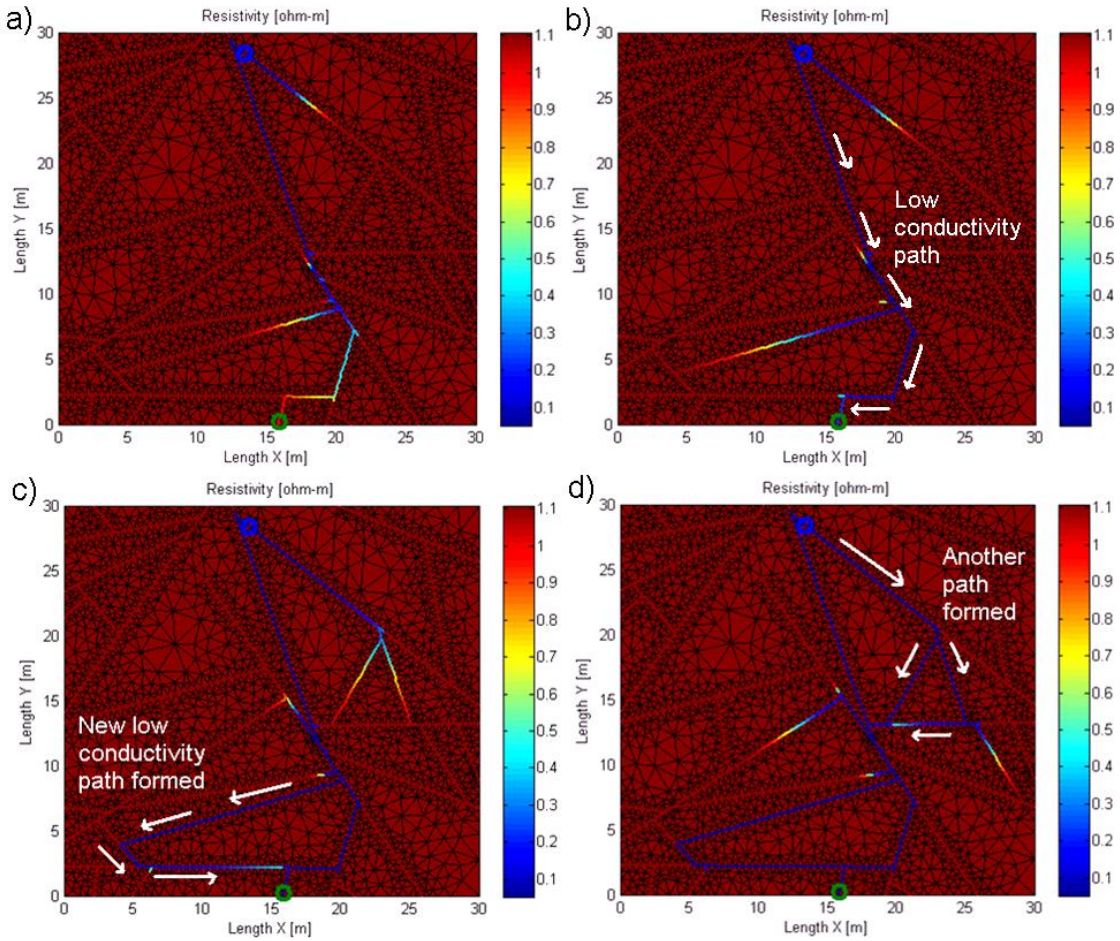

Figure 3.17: Resistivity of the field after a) 0.01 days, b) 0.02 days, c) 0.08 days and d) 0.18 days.

3.5.1 Fracture network analyzed as an electric circuit

The reservoir in Figure 3.13 acts in many ways like an electric circuit because the fractures form low-resistivity paths from the injector to the producer. The electric current travels mainly through these paths due to the high resistivity of the reservoir. Figure 3.19 demonstrates the electric circuit that corresponds to the fracture network in Figure 3.18 which is the same network previously studied (Figure 3.13) except the width of the fractures was set as 2×10^{-3} m. All the fractures are assumed to be filled with ground-water with NaCl concentration equal to 5.42×10^{-3} and no conductive tracer has been injected into the reservoir.

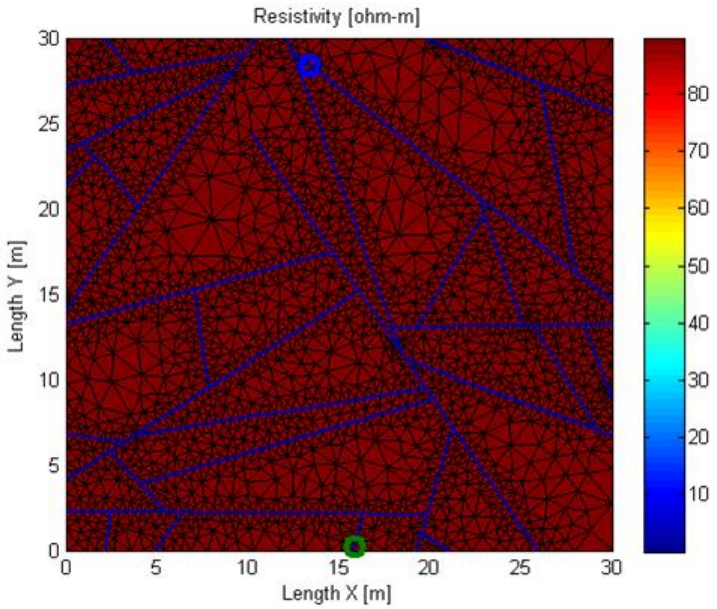

Figure 3.18: A fracture network with water-filled fractures.

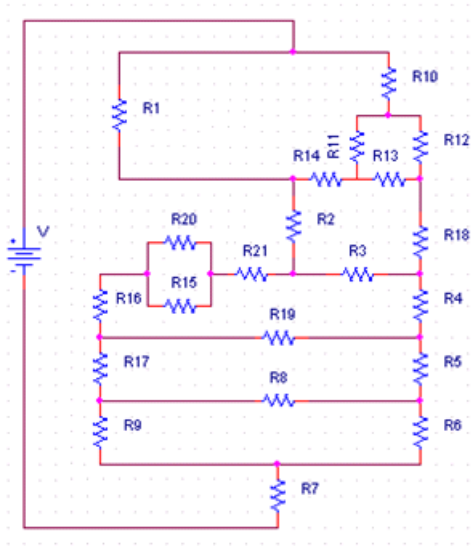

Figure 3.19: An electric circuit that corresponds to the fracture network in Figure 3.18.

The resistance, R [ohm], of the resistors in the electric circuit was calculated using the following relationship,

$$R = \frac{\rho L}{A} \tag{3.29}$$

where L [m] is the length and A [m^2] is the cross sectional area of the corresponding water-filled fracture. The Y-Δ transformation theory published by Kennelly (1899) was used to simplify the resistors into a single equivalent resistor equal to $R = 1.2 \times 10^4$ ohm. The electric current at one end of the resistor was set as -1 A and as 1 A at the other end to simulate the current flow through the fractures between the injector and the producer. The voltage drop in the electric

circuit was calculated using Ohm's law (Equation 3.1) and compared to the voltage drop for the fracture network computed using module EOS1 in TOUGH2, see results in Table 3.3.

Table 3.3: Voltage drop for a fracture network and corresponding electric circuit.

	Voltage drop [V]
Electric circuit	1.1964×10^4
TOUGH2	1.1980×10^4

The voltage drop calculated for the electric circuit is equivalent to the voltage drop computed using TOUGH2, so the EOS1 module in TOUGH2 can successfully be used to calculate the electric potential for discrete-fracture networks with sufficient accuracy for the procedure in this project. The difference is likely due to the pressure dependency of the viscosity, density and compressibility in EOS1, as previously analyzed, but should not affect the overall results of the fracture characterization.

3.5.2 Fracture network with multiple production wells

Another Discrete-Fracture Network (DFN) was modeled, this time with one injection well and three production wells, and the apparent resistivity between them was studied. The width of the fractures was set as 10^{-2} m and the grid dimensions were $1000 \times 1000 \times 1$ m^3, see Figure 3.20.

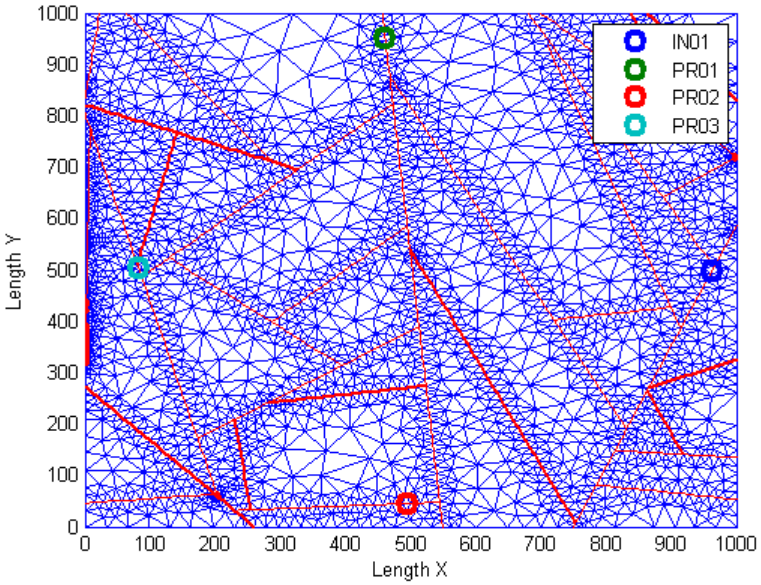

Figure 3.20: A discrete-fracture network with one injector and three producers.

A NaCl solution of 0.9 wt% was injected at the rate of 1.1×10^{-2} kg/s with enthalpy 3.14×10^5 kJ/kg and the production wells modeled to deliver against a bottom hole pressure of 10^6 Pa with productivity index of 4×10^{-12} m^3. The initial pressure was set to 10^6 Pa and the temperature to 25°C. Closed (no-flow) boundary conditions were used and the fractures were initially assumed

to be filled with ground-water with 5×10^{-4} NaCl concentration. The electric potential differences between the wells were calculated and the apparent resistivity, ρ_a [ohm-m], solved using Ohm's law,

$$\rho_a = \frac{\Delta\varphi}{I} k \tag{3.30}$$

where $\Delta\varphi$ [V] is the potential difference between the wells, I [A] is the intensity of the current flowing through the network and k [m] is a geometric factor. In resistivity studies in geophysics, the total current is assumed to flow away from or toward each electrode across the surface of a half sphere, or a whole sphere if electrodes are placed underground. Here, the current flow is significantly different, because the rock is a good insulator so the current only flows through the thin fractures. Therefore, if a conventional geometric factor which only depends on the electrode spacing is used, the apparent resistivity values calculated would be very different from the true resistivity values. The volume considered for electrodes placed far apart (i.e. defined by the sphere shaped flow paths) would be much larger than for electrodes placed closer to each other, while the true increase in fracture flow path volume because of a larger distance between electrodes would be relatively small. Finding the true geometric factor is a very difficult task because the fracture characteristics are unknown, but in order to find a suitable geometric factor the potential differences between the wells before any tracer has been injected is used. It is assumed that all the wells are connected with fractures and that the resistivity of the fractures is ρ = 36.59 ohm-m, corresponding to fractures with porosity 0.9 and filled with 9 ohm-m ground-water. Therefore, all the current flows through the fractures because of the high resistivity of the rock. The geometric factor, k [m], between each well pair is then calculated using Equation 3.30 as well as the assumed resistivity of the water-filled fractures, the known injected current, and the measured potential differences between the wells. If the fracture network was expressed as a simplified electric circuit, this geometric factor would represent the cross-sectional area of the wire, divided by its length, i.e. the length of the current path. Therefore, it corresponds to the current flow path and could possibly be used to gain information about the fracture network. Here, it is used to calculate the apparent resistivity for the fractures, which is used for comparison at different time steps to locate where the conductive fluid is flowing.

The apparent resistivity was mapped by kriging and the general exponential-Bessel variogram was used to fit the data. Kriging is an optimal method for estimation of unknown values within known data points and was developed by Krige (1951). In this case, very few data points are known because of the few numbers of measurement points, i.e. few wells, but mapping by kriging helps illustrate the changes in resistivity as conductive tracer is injected into the reservoir. A test well is assumed to be located in a fracture in the middle of the reservoir, between all the wells to get more measurement points. First, the flow simulator TOUGH2 was used to calculate the flow of the tracer for 450 days and then to solve the electric field at different times as the tracer distributes through the network. Figure 3.21 shows the tracer return curves at the producers and the injected tracer concentration.

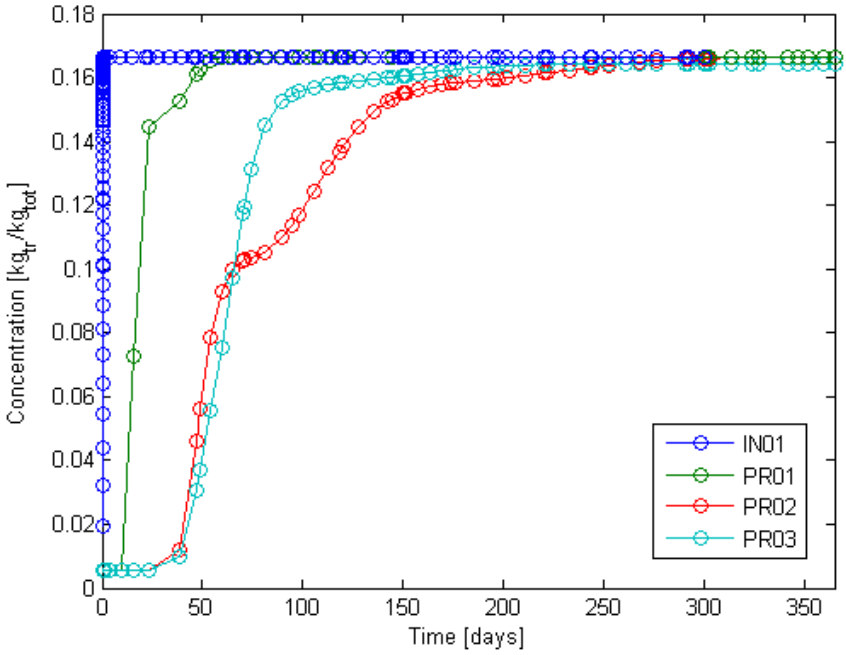

Figure 3.21: Tracer return curves.

The conductive fluid travels fastest towards producer 1 because of the relatively straight path between the injector and producer 1, see Figure 3.20. The tracer return curves indicate more tortuous flow paths between the injector and producers 2 and 3. Figure 3.22 illustrates the changes in the apparent resistivity between the wells, mapped by kriging, as the conductive fluid flows through the fracture network. At the beginning, all the fractures are filled with ground-water and therefore have the same resistivity, equal to 36.59 ohm-m. After 24 days of injection, the apparent resistivity has decreased in the upper part of the figure. Then, after 200 days of injection, as well as after 450 days, the upper right corner has the lowest resistivity and it has changed significantly in the lower right corner as well. These changes in resistivity indicate good fracture connection from the injector to producer 2, then from producer 2 to producer 3, but lower connection towards producer 3.

Figure 3.23 shows the true resistivity distribution after 70 days, which is in accordance with previous results. The fracture path between producer 2 and producer 3 is the last one to fill up with conductive tracer, which causes high potential difference between these producers and therefore high apparent resistivity in Figure 3.22.

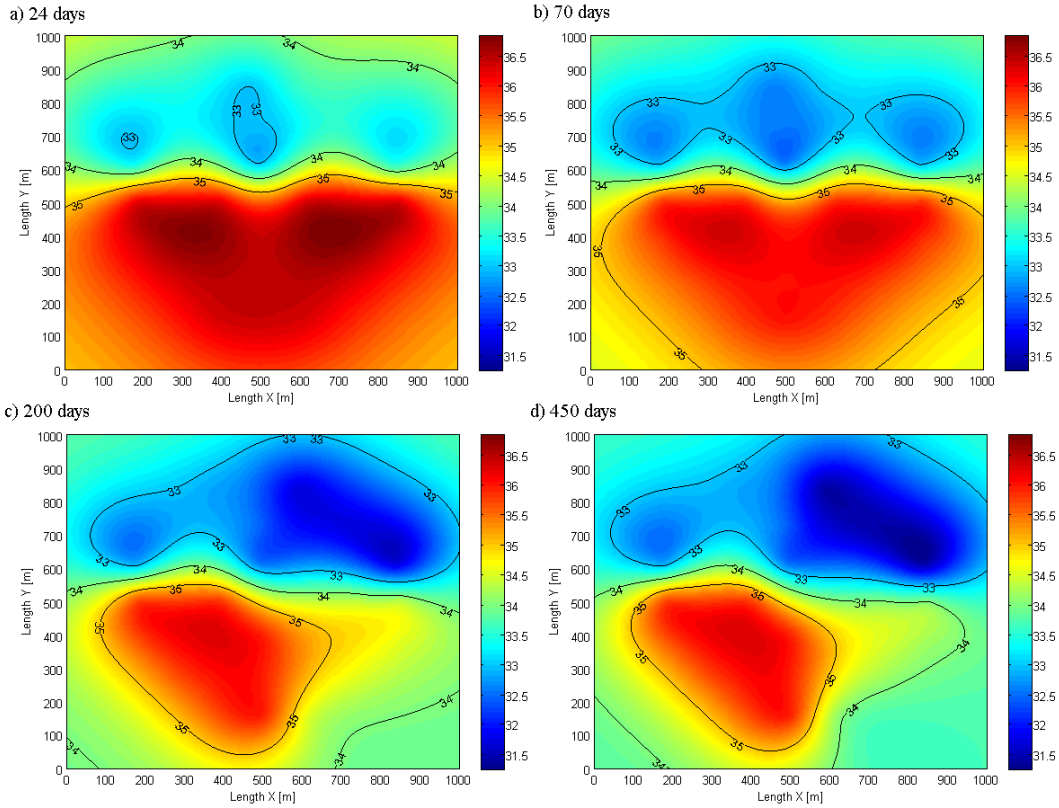

Figure 3.22: Apparent resistivity [ohm-m] calculated from potential measurements between wells after a) 24 days, b) 70 days, c) 200 days and d) 450 days.

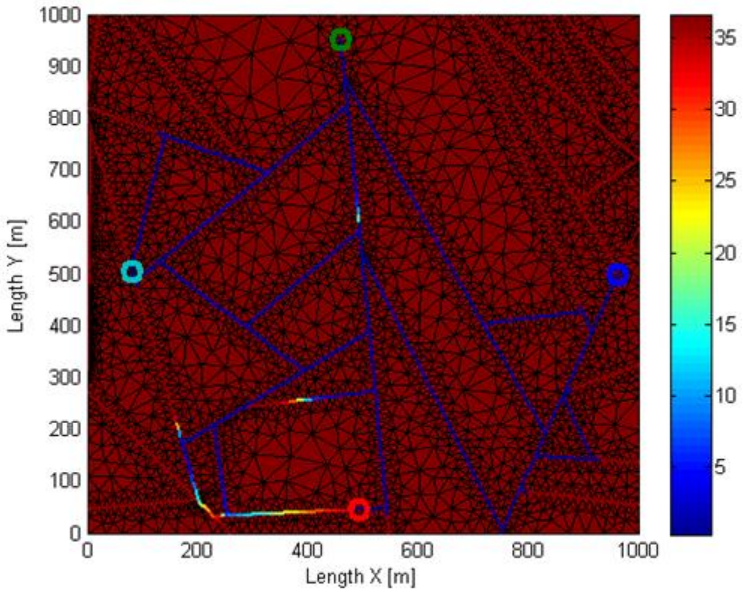

Figure 3.23: Resistivity [ohm-m] after 70 days of injection.

In reality, the produced fluid is likely to be reinjected into the reservoir, causing the injected fluid to be elevated in NaCl concentration with time due to the separation of steam. Therefore, the same case was studied but with the injected tracer concentration increasing in steps after 100 days. Figure 3.24 shows the injected tracer concentration and the tracer return curves for the three producers.

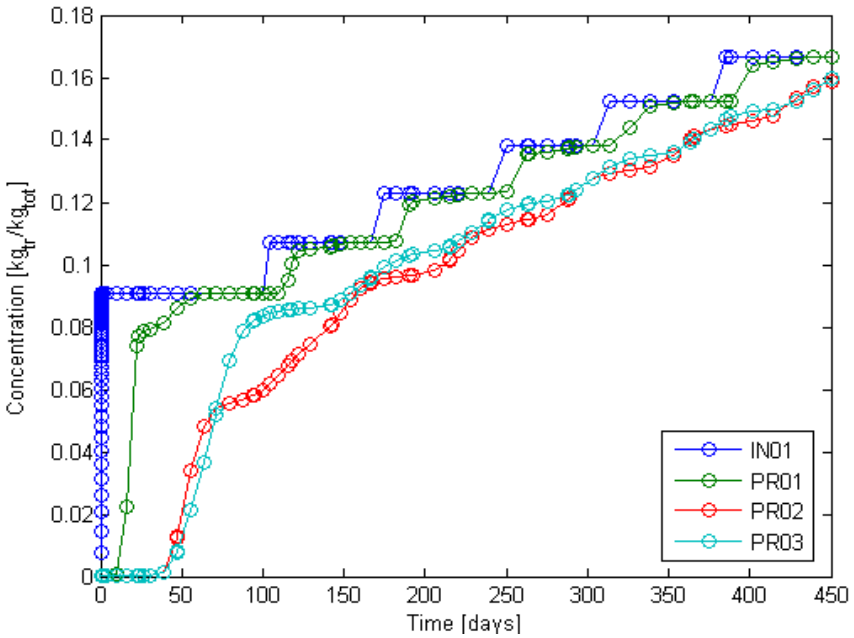

Figure 3.24: Tracer return curves with increasing tracer injection.

The tracer return curves indicate good connection between the injector and producer 1, but due to a weaker connection towards producers 2 and 3 the tracer concentration in these wells does not reach the injected concentration. As a result, the contrast in resistivity between the strongest and the weakest connections remains high, see Figure 3.25, because the majority of the tracer will always be flowing through the best connected flow path from the injector to the producers. In the previous case, where the injected water had a constant NaCl concentration, the weaker connected paths became greatly saturated as well once all the stronger connected paths were fully saturated with tracer. Therefore, the connection between injector 1 and producer 2 could be observed after about 200 days of injection, while the mapped apparent resistivity at the same time for the reinjection case does not indicate the same connection, see Figure 3.25 (left). However, both examples gave some good information about the fracture connections between the wells and indicated that the time histories of the apparent resistivity between the wells could be used for fracture characterization.

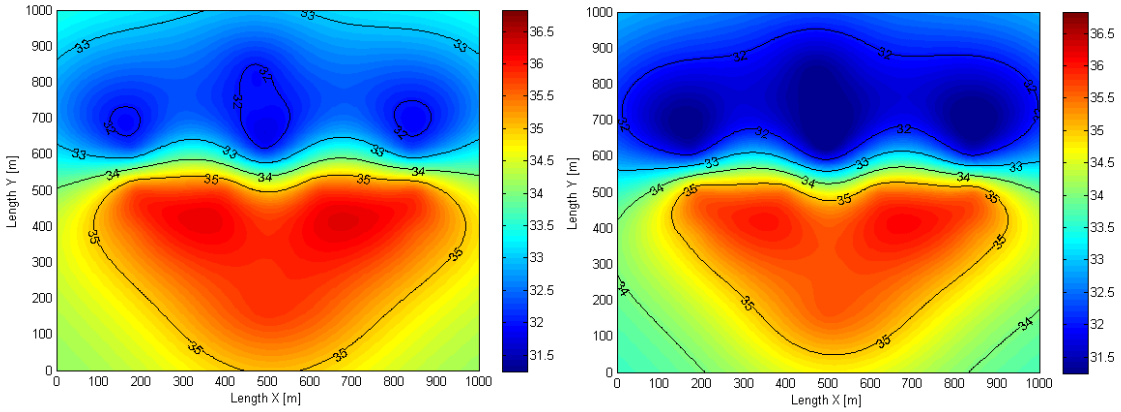

Figure 3.25: Apparent resistivity [ohm-m] for reinjected fluid with elevated NaCl concentration, calculated from potential measurements between wells after 200 days (to the left) and 450 days (to the right).

3.6 INVERSE ANALYSIS

One of the goals of this project is to use the tracer concentration simulations and electrical potential calculations from TOUGH2 with inverse modeling to estimate the dimensions and topology of a fracture network. In inverse modeling the results of actual observations are used to infer the values of the parameters characterizing the system under investigation. In this study, the output parameters would be the tracer return curves at the producer and the potential differences between wells as a function of time while the input parameters would include the dimensions and orientations of the fractures between the wells. The objective function measures the difference between the model calculation (the calculated voltage difference between the wells and tracer return) and the observed data (measured potential field between actual wells and actual tracer return), as illustrated in Figure 3.26, and a minimization algorithm proposes new parameter sets that improve the match iteratively.

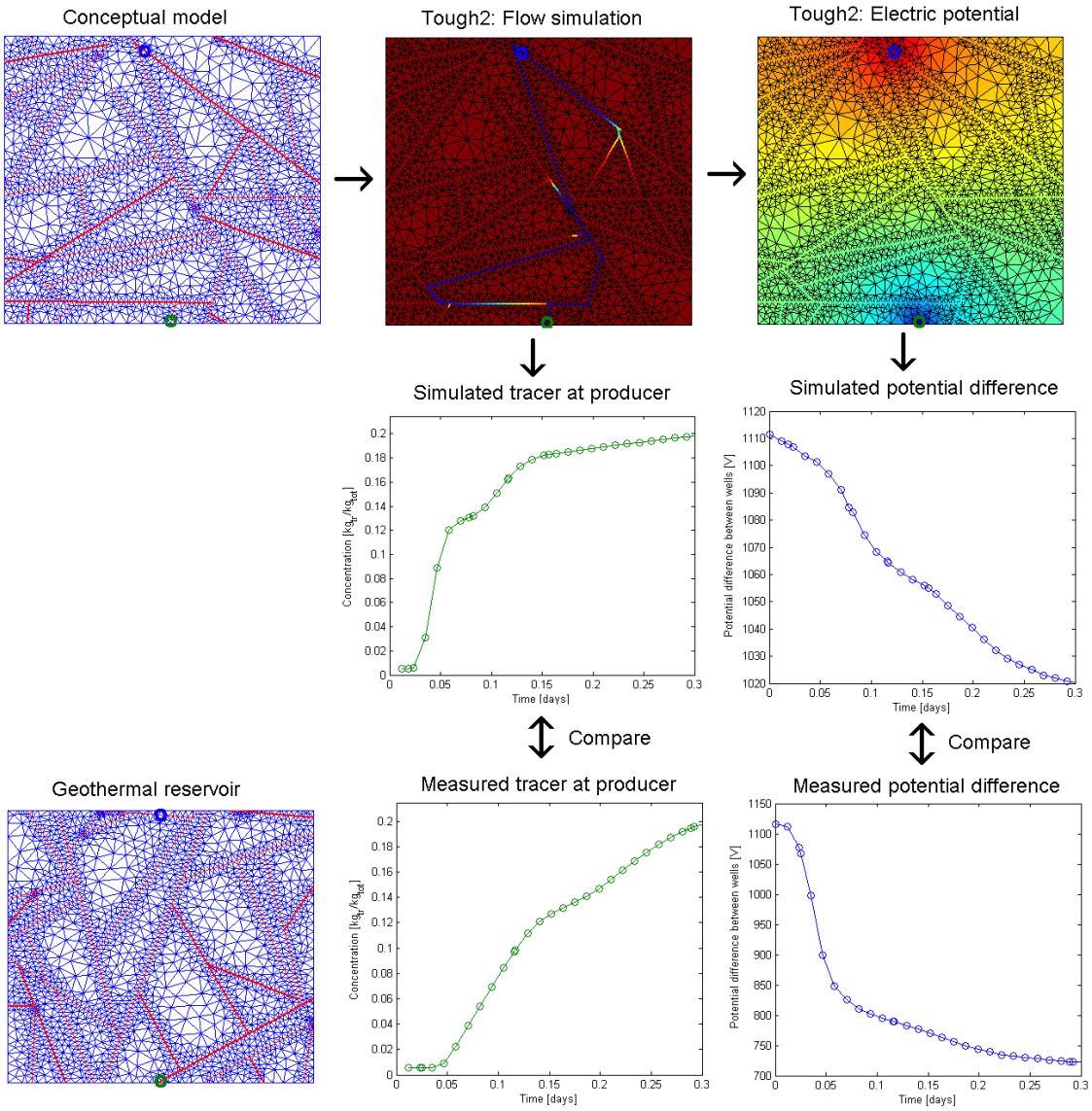

Figure 3.26: The inverse analysis.

3.6.1 Inverse analysis studied for four discrete-fracture networks

Among optimization algorithms in inverse analysis, a genetic algorithm has the advantage that it can search the global minimum value and it can be modified to handle both discrete and continuous variables. Genetic algorithm was proposed by Holland (1975) as an optimization method that imitates natural evolution. A solution to the inverse problem is represented as a chromosome and the genetic algorithm creates a population of chromosomes that evolve through mutation and crossover in order to find the best one.

The possibility of using a genetic algorithm to characterize fracture patterns was explored by performing a very simple inverse analysis using a genetic algorithm to identify a given fracture

network from four possible networks. The four networks have dimensions 30 × 30 m^2 and are shown in Figure 3.27.

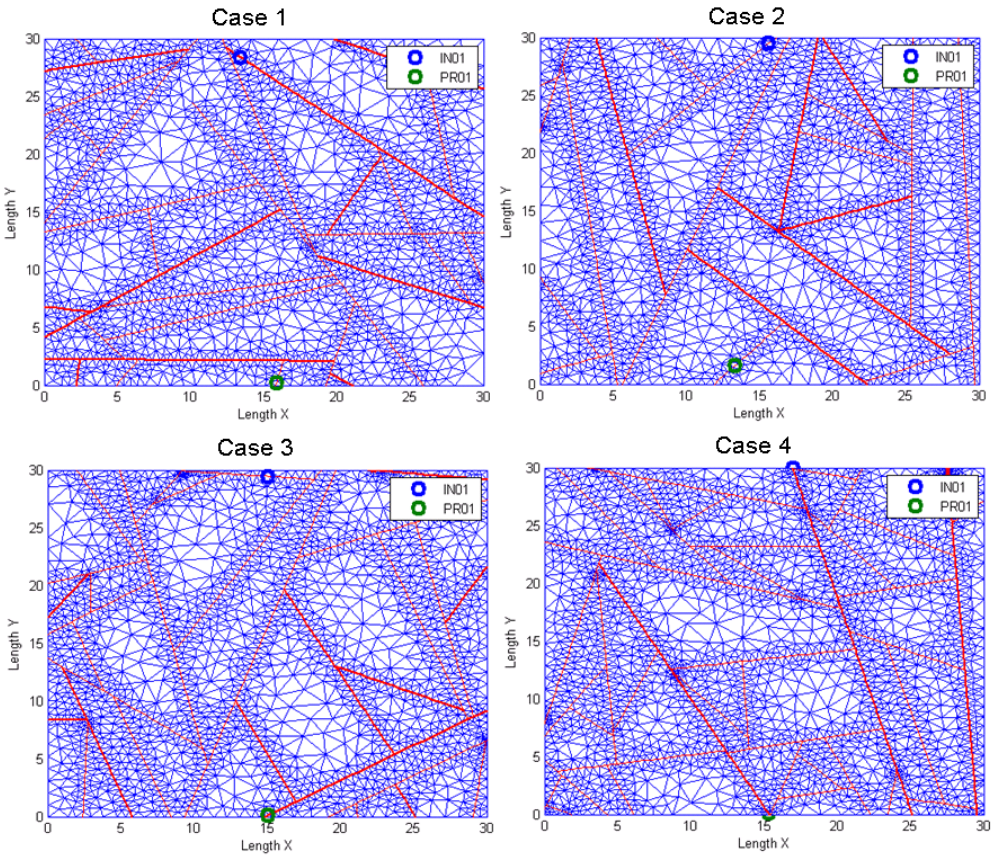

Figure 3.27: Discrete-fracture networks.

The reservoir and injection/production properties were the same as for the fracture network decribed in Section 3.5 except that the width of the fractures was defined as,

$$w = 3.33L \times 10^{-4} \tag{3.31}$$

First, a flow simulation of a NaCl tracer was carried out and the resistivity of the reservoir defined from the tracer distribution. Next, the electric field was calculated for different timesteps, from before any tracer had been injected into the reservoir and up to 3 days of injection. The tracer production histories and the electric potential differences for the four cases in Figure 3.27 are shown in Figure 3.28 and Figure 3.29.

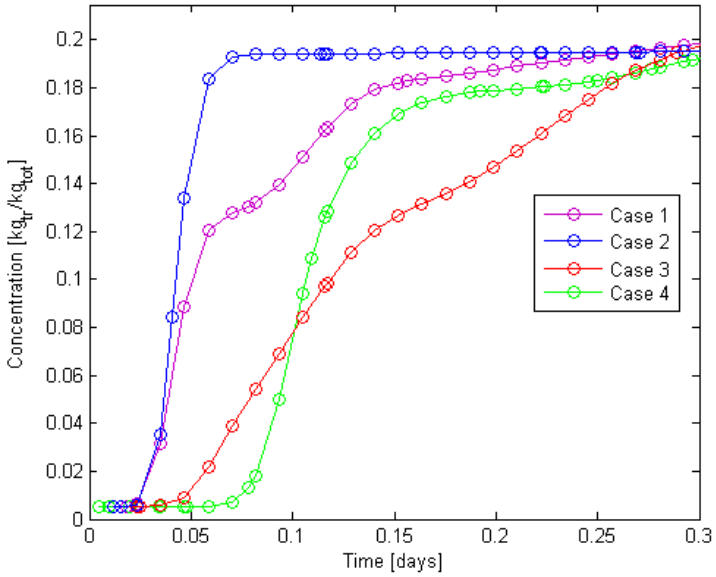

Figure 3.28: Tracer production history for Cases 1-4.

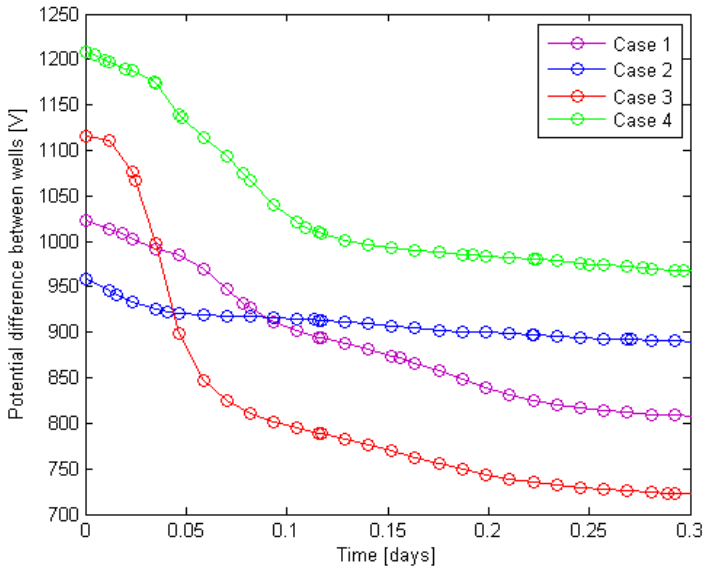

Figure 3.29: Potential difference between wells for Cases 1-4.

The conductive tracer reaches the production well fastest through the fracture network in Case 2 but the potential difference drops the most in Case 3. These differences in the histories of the tracer production and of the potential difference are due to the previous conclusion that the electric potential and tracer production depend on the fracture networks and can therefore give information about the fracture characteristics. The objective function of the inverse analysis was defined as the sum of the difference between the tracer production histories and the difference between the histories of the potential difference between the injector and the producer. The genetic algorithm was modified to force the chromosomes to be integers between 1 and 4, where the integer corresponds to Cases 1-4. One of the four cases was chosen and the inverse analysis used to identify the chosen fracture pattern. The genetic algorithm was able to identify the correct fracture patterns in all cases. However, because the variable being optimized is an integer

corresponding to different fracture networks, the genetic algorithm acts like a grid search algorithm where each fracture network needs to be tested unless a perfect match has been found. An increase in the variable, i.e. the case number, does not indicate a certain change in the fracture pattern because all the patterns were randomly generated. Therefore, it can be impossible to find the best fitted fracture network without checking all the possible networks. In reality, it would not be applicable to use grid search to try all networks because of the gigantic number of possible fracture patterns, so a relationship needs to exist between a certain change in the integer being optimized and the equivalent change in the corresponding fracture network. Therefore, the possibility of using inverse analysis with fractal geometry was explored.

3.6.2 Inverse analysis using fractal geometry

Several field studies performed on fault systems at different length scales have demonstrated that fracture populations follow a power-law length distribution (Shaw and Gartner, 1986, and Main et al., 1990). Therefore, the relationship between a fracture length r and the number of fractures N with lengths equal to or larger than r can be represented by a fractal equation,

$$N = Cr^{-D} \tag{3.32}$$

where D is the fractal dimension and C is a fracture density parameter. A method described by Watanabe and Takahashi (1995) was used to create discrete-fracture networks with fractal dimensions ranging from D = 1.0 to 1.7 with 0.1 increments. The fracture locations were randomly determined and the angles normal to the fractures were randomly chosen to be either 100° or 135° with a standard deviation of 5°. The length of the fractures must satisfy equation (3.32) so r was determined from,

$$r_i = (C / i)^{1/D} \tag{3.33}$$

and the total number of fractures n was determined using,

$$n = \frac{C}{r_{\min}^{\ D}} \tag{3.34}$$

where r_{min} is the smallest length of the fractures observed, here set as 0.05 m. The fracture density C can be determined from actual field data by looking at the number of fractures observed per unit length or depth, here it was set as 2 fractures per meter. The aperture was defined by

$$d_{\max} = K \cdot r^{e} \tag{3.35}$$

where d_{max} is the aperture and K is a constant. Olson (2003) describes how this power law equation was used to fit various fracture datasets of different sizes, usually with e = 0.4. Here, e was set as 0.4, K as 0.002 $m^{3/5}$ and the size of the reservoir was set as 1000 × 1000 m^2. Ten different fracture networks were created for each fractal dimension D, ranging from D = 1.0 to 1.7 and a similar method as described in Section 3.6.1 used to try to find the fractal dimension of a certain fracture network using inverse analysis. Now, if the integer variable being optimized is increased enough, the corresponding fractal dimension is increased as well. Therefore, the genetic algorithm does not act as a grid search as in the previous case. Figure 3.30 shows an example of a fracture network created with D = 1.5, the corresponding tracer injection and production history, the potential difference between the wells, and the derivative of the potential difference.

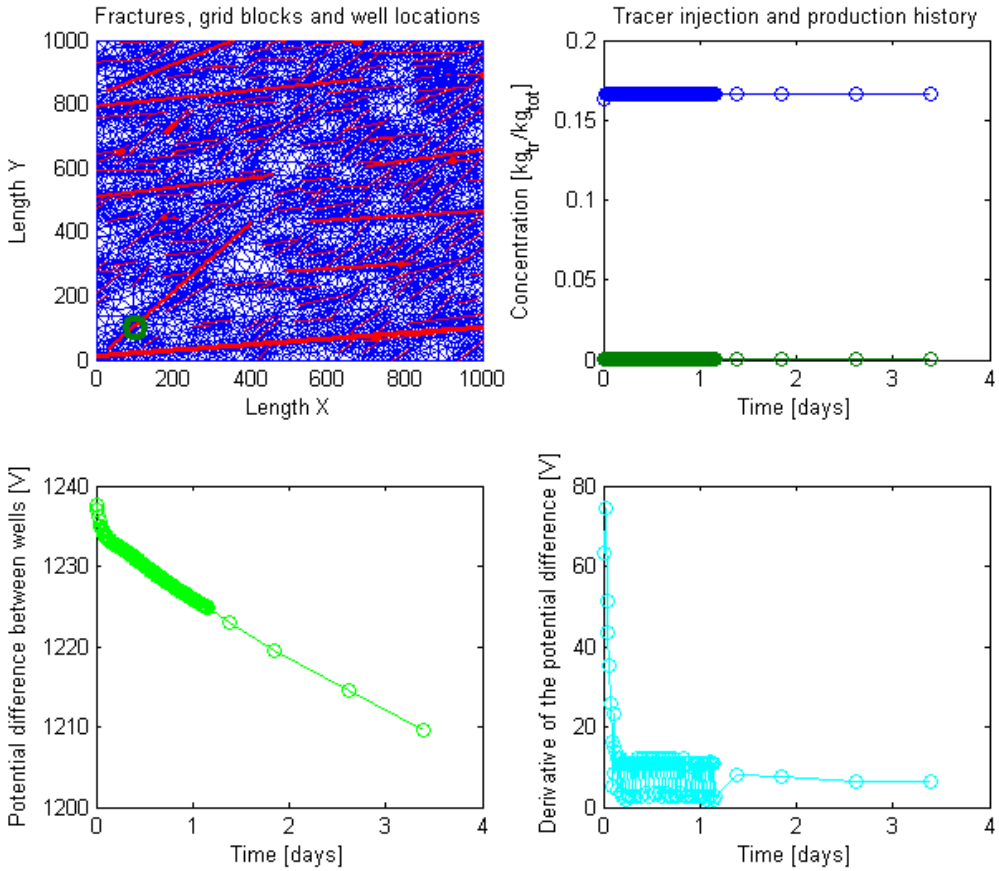

Figure 3.30: A fracture network with D = 1.5 and a producer in lower left corner and an injector in upper right corner, a tracer injection and production history, potential difference between the wells, and the derivative of the potential difference.

The objective function consisted of the sum of the differences in the tracer production, potential differences, and the normalized potential differences, between the network in Figure 3.30 and the other fracture networks. Genetic algorithm was used to find the network with the most similar characteristics, seen in Figure 3.31.

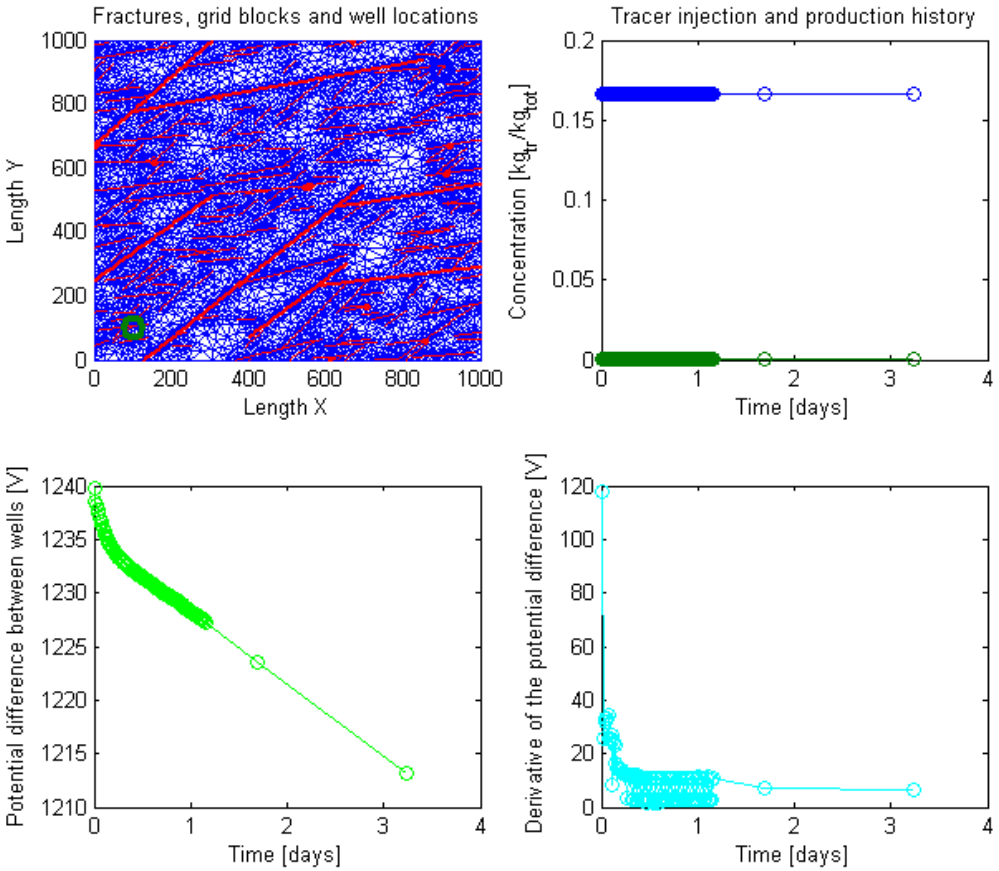

Figure 3.31: A fracture network with D = 1.5 and a producer in lower left corner and an injector in upper right corner, a tracer injection and production history, potential difference between the wells, and the derivative of the potential difference.

The fracture network in Figure 3.31 is different from the fracture network in Figure 3.30 but also has fractal dimension D = 1.5. Therefore, the inverse analysis was used successfully to predict the fractal dimension of the fracture network in Figure 3.30. The potential difference curves for the two networks are very similar and both start at around 1240 V. The starting point can give some information about the network because the fractures are assumed to be filled with water in the beginning so lower potential difference corresponds to more fractures/fracture paths between the wells. Also, the faster the potential difference drops, the better path between the wells because the potential difference drops significantly when a high conductivity path has been formed between the injector and the producer as previously studied, and also when new paths are formed. Another example is seen in Figure 3.32 with D = 1.2.

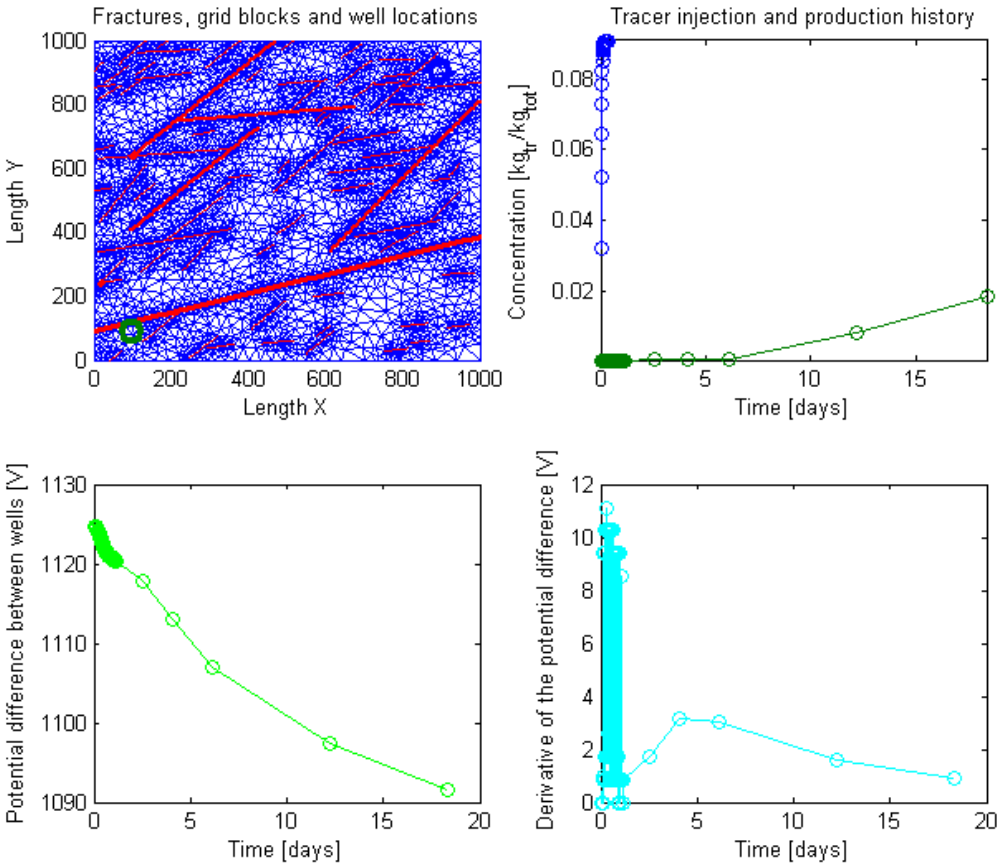

Figure 3.32: A fracture network with D = 1.2 and a producer in lower left corner and an injector in upper right corner, a tracer injection and production history, potential difference between the wells, and the derivative of the potential difference.

The best fit for this fracture network determined by the inverse analysis is the fracture network in Figure 3.33, which has D = 1.1. The networks are somewhat similar and the potential difference curves show similar behavior, which can be seen more clearly when the derivatives are studied. The magnitude of the derivatives for these cases are much lower than for previous cases with D = 1.5, because of fewer fractures so the potential difference does not drop as fast. The different networks were also run for different amount of time, depending on for how long TOUGH2 could simulate the conductive tracer flow, so it is important to take that into account when comparing the graphs. In the inverse analysis, the objective function is divided by the total number of points being compared each time, and the number of points depends on the network with shorter time simulated out of the two networks being compared each time.

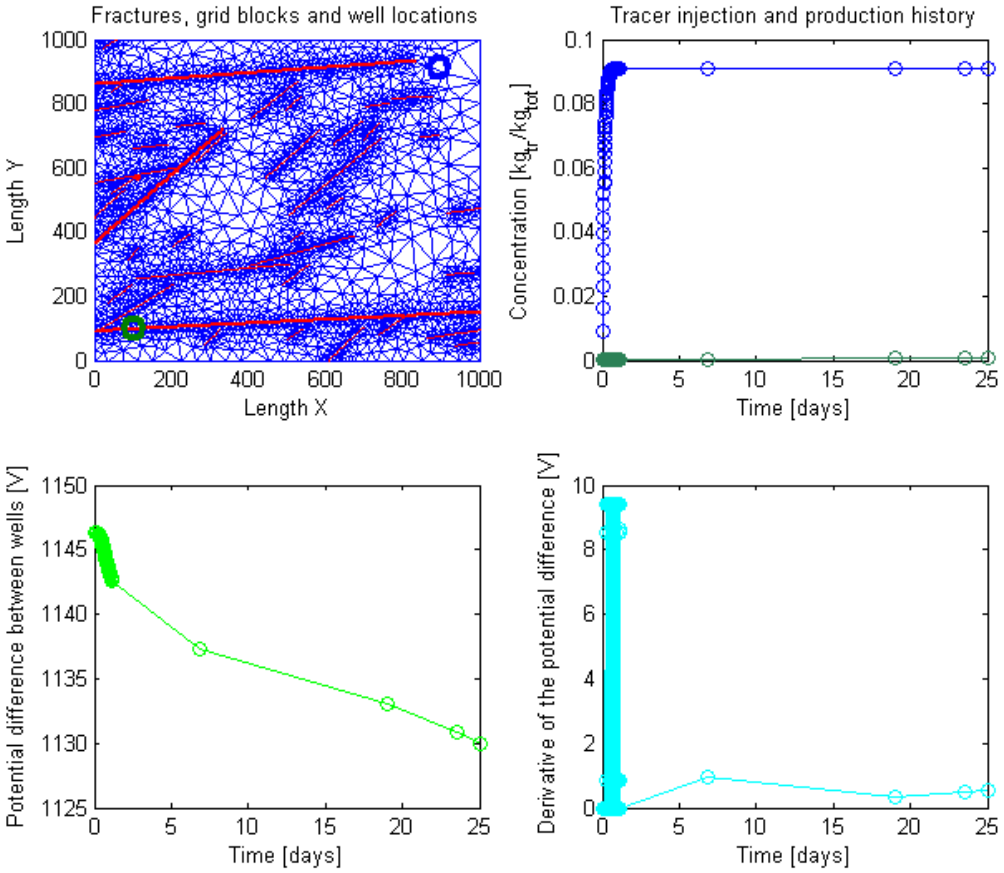

Figure 3.33: A fracture network with D = 1.1 and a producer in lower left corner and an injector in upper right corner, a tracer injection and production history, potential difference between the wells, and the derivative of the potential difference.

Although in many cases the inverse analysis was used successfully to determine the right fractal dimension, the fractal dimension was also often slightly different, especially when studying networks with lower fractal dimension. That is likely because there is a smaller number of fractures when the fractal dimension is lower and many completely different fracture patterns are possible with the same fractal dimension. Therefore, it might not always be possible to find a similar network out of the ten cases for each fractal dimension and a fracture network with a different fractal dimension might give a better fit. The defined fractal dimension might also not be correct because when the networks are created some of the long fractures that intersect the reservoir boundaries are made smaller to fit inside the reservoir. This method has shown some possibilities for fracture characterization but needs to be studied further to test and increase the accuracy of determining the fractal dimension.

It is important to recognize that the meaning of the fractal dimension D used so far is different from the fractal dimension calculated by the box-counting method, D_B, where,

$$N_B = C_B r^{-D_B} \tag{3.36}$$

Here N_B signifies the number of boxes with edge length R that are entered by fractures and C_B is a constant. Therefore, the fractal dimension in equation 3.32 is a measure of the geometry of the fractures (length distribution) while the fractal dimension calculated by the box-counting method is a measure of the spatial distribution of the fractures. When Equation 3.36 holds for natural fracture systems the fractal dimension D_B represents the spatial distribution of fractures ranging between 1 and 2 (Watanabe and Takahashi, 1995). When D_B = 1, the fractures cluster in a narrow band and if D_B = 2, they completely fill the area being studied. Therefore, this fractal dimension provides valuable information regarding the fracture system and it is of interest to study whether it can be determined using the same approach previously used to determine D.

3.7 FUTURE WORK

Future work could include investigation of further ways to use inverse analysis with tracer concentration simulations and electric potential calculations from TOUGH2 to characterize fractures. The possibility of defining the reservoirs using fractal dimensions as a measure of the spatial distribution seems promising. Other future paths could be to study the use of nanotracers and different chemical tracer as well as to explore the influence of injecting varying tracer concentration. Different well arrangements could be studied to estimate the minimum number of measurement locations necessary to solve the inverse problem efficiently. The objective would be to develop a method which can be used to find the character of the fracture distribution.

4. FRACTURE CHARACTERIZATION USING THERMAL AND TRACER DATA

This research project was conducted by Research Assistant Carla Kathryn Co and Professor Roland Horne. The overall objective of this study was to develop a methodology to estimate fracture dimensions. Our focus was on utilizing temperature, tracer, and borehole imaging data to determine relevant fracture parameters.

4.1 SUMMARY

This study aimed to describe interwell connections through characterization of permeable zones in geothermal wells. Several model configurations were described and investigated. A single fracture model was used to represent the connectivity between injection and production well pairs. An analytical model derived by Gringarten and Sauty (1975) was used to estimate the fracture aperture from thermal breakthrough time and mean tracer arrival time. Estimated effective fracture aperture values were from 2.1 cm to 42.6 cm.

To further understand the characterization of fractures, a literature review was undertaken. Fields included in this study were: Desert Peak, Nevada; Dixie Valley, Nevada; Soultz, France; The Geysers, California; and Wairakei, New Zealand. Fracture properties were determined from acoustic imaging techniques. Feed zone locations identified through Pressure, Temperature, and Spinner (PTS) data were then correlated to these properties. Results showed that feed zone locations correspond to depths with higher apertures. Fracture density, however, was not found to be relevant to fluid entry zones.

An extensive literature review was undertaken to investigate the possibility of integrating scaling relationships with heat and mass transport to improve the single effective fracture model. The main goal was to model fracture networks that were more consistent with the observed patterns in the field. Scaling relationships between relevant fracture properties such as aperture, length, and density were envisioned to become useful in constraining the possible models derived from tracer analysis and temperature matching. Field studies revealed that scaling had been observed in numerous geothermal fields in various scales ranging from thin sections to aerial photographs. Furthermore, stratigraphy was found to be important mainly for shallow permeable zones only. Moreover, fractures most relevant to flow were optimally-oriented and critically-stressed. In addition, either high fracture aperture or high fracture density values could be used to identify permeable zones depending on the degree of fracture overlap in the borehole image logs.

This study also investigated using coupled tracer and temperature nonlinear least squares optimization to determine unknown parameters from a porous model. Five main parameters for the porous channel model were: channel half-aperture (b), channel height (H), porosity (ϕ), saturated pore diffusivity (D), and equivalent injection temperature (T_{inj}). There were several scenarios simulated for this model. The five parameter scenario did not take scaling correlations into account. In the six parameter scenario, the half-aperture (b) was correlated to the channel length (L) using the scaling coefficient (α) and the scaling exponent or the fractal dimension (β). For four parameter scenarios, both α and β were specified using data from literature. Three

scaling correlations were available. The scaling correlations were: $b = 0.0004L^1$; $b = 0.0039L^1$; and $b = 0.1689L^{0.4}$.

Overall, the coupling of thermal and tracer response analyses resulted in the detailed characterization of interwell connectivity which could be used to predict future thermal response to injection. Models derived from tracer analysis alone consistently gave the most pessimistic results for both high and low injection cases. The most optimistic model was the configuration with the lowest aperture. For the injection case tested, the different models gave a wide range of thermal drawdown forecasts.

4.2 INTRODUCTION

Injection of spent brine and condensate is widely practiced in geothermal fields for pressure support and wastewater disposal (Horne, 1996). However, premature thermal breakthrough can occur if this is not managed properly. Therefore, determination of interwell connectivity is important for proper reservoir management. Connectivity between production and injection wells can be represented by different permeable zone configurations with their corresponding tracer and heat transport analytical models. Figure 4.1a describes a single fracture connection model (Co and Horne, 2011; Horne, 1996). The second model (Figure 4.1b) uses a well-developed major fault with an impermeable core and permeable damage zones (Massart et al., 2010; Paul et al., 2009, Paul et al., 2011; Johri et al., 2012). A third model, shown in Figure 4.1c, utilizes sheared fracture planes or porous channels (Bullivant and O'Sullivan, 1985; Lauwerier, 1955; Gringarten and Sauty, 1975) that can be attributed to secondary structures subparallel to major faults. In addition, horizontal sheared fracture planes can be used to model lithological boundaries. Lastly, the fourth model (Figure 4.1d) describes the intersection of cross-cutting sheared fracture planes as possible geothermal permeable zones. These could be represented by parallel plate models (Gringarten et al., 1975, Rivera et al., 1987). The focus of this report will be on the first two models.

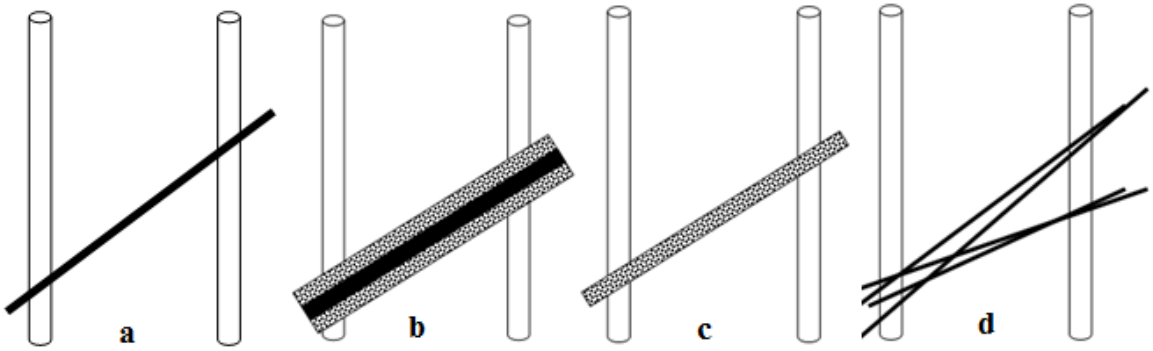

Figure 4.1 Interwell connectivity configurations: (a) single fracture connection; (b) well-developed fault with damage zone with a low permeability core; (c) secondary structures subparallel to faults or stratigraphy based connections; (d) cross-cutting sheared fracture planes.

Fracture aperture is an important parameter in geothermal reservoirs. Aperture influences transport and thermal behavior of the reservoir, both in EGS and in conventional hydrothermal

systems. An important application is the determination of the degree of interwell connectivity. Of critical importance is the prevention of thermal breakthrough from injection wells to production wells.

During the 1980s, several unsuccessful attempts were made to estimate fracture aperture by matching tracer test data. This was because the parameter estimation problem had multiple degrees of freedom, which made it difficult to separate fracture aperture from other unknown reservoir parameters. To constrain the degrees of freedom, thermal response data could be used. This was proposed in the 1980s; however at the time no data existed that provided both tracer and thermal responses. Now that several EGS and fractured reservoirs have been monitored to provide these data, the possibility exists to estimate fracture aperture in those fields. A single fracture model was used to describe the connectivity of an injection and production well pair. Tracer and thermal data were used to estimate the fracture width for this simplified model.

The objective of the initial work done was to determine whether it would be feasible to derive reasonable estimates for the fracture aperture using both temperature data and tracer test results. Another objective was to document existing analytical models and field data available in literature. Calculated fracture width values were compared to those derived from other datasets to check for consistency.

Focus last year has been on understanding the significance of the fracture aperture in predicting possible fracture network models. A comprehensive literature review of the scaling of fracture properties in geothermal reservoirs was undertaken to define the relationships among fracture properties such as aperture, length, and density. Moreover, acoustic imaging data was used to correlate these fracture properties to feed zone locations. Furthermore, the influence of fracture orientation and lithology on feed zone locations was investigated. In addition, scaling correlations for damage zone fracture density were used to derive an effective permeability for faults.

There were two analytical models included in this study. One was a single fracture connection model which was the focus of research efforts last year. The second model consisted of a sheared fracture plane or a brecciated porous channel. For the first model, an analytical model was derived to relate both the thermal breakthrough and mean tracer arrival times to the effective fracture aperture. The second model was a porous model that used a combination of thermal and tracer response analyses to determine unknown parameters using nonlinear least squares optimization. There were two scenarios simulated for the porous model. The first scenario did not take scaling correlations into account. In the second scenario, scaling correlations used were: $b = 0.0004L^{1}$; $b = 0.0039L^{1}$; and $b = 0.1689L^{0.4}$.

4.3 COMBINED TRACER AND TEMPERATURE ANALYTICAL MODELS

4.3.1 Single Fracture Model

Fracture Aperture

Gringarten and Sauty (1975) derived a solution that can be used for unsteady-state one-dimensional heat transfer through a fracture as shown in Figure 4.2. The solution was similar to that for a porous medium, derived by Lauwerier (1955). The solution assumes a thin, uniform reservoir with an adiabatic boundary. Heat is transferred by conduction from the rock layers and the entering fluid. As no mixing is assumed, the result is a stream-like channel flow.

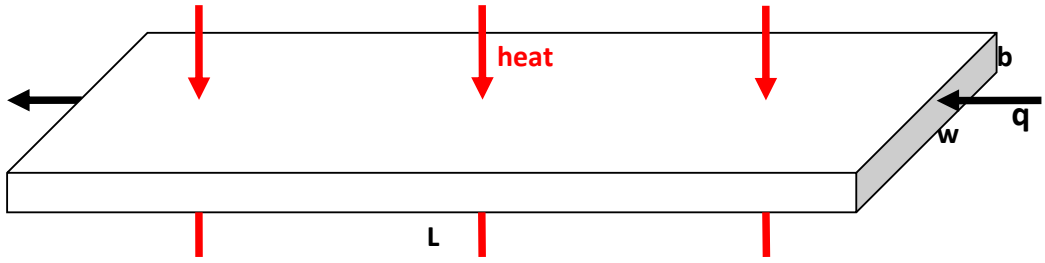

Figure 4.2 Model schematic for the Gringarten and Sauty (1975) derivation

Horne (1996) derived the resulting analytical solution for this model as Equation 4.1 where t_c is the tracer front arrival time, t_{th} is the thermal breakthrough time, and b is the fracture aperture. On the left hand side of Equation 4.1 is the relative temperature ratio T_{ratio}. Here, T_o is the original reservoir temperature, T_w is the reservoir temperature at x, and T_{inj} is the injected fluid temperature. Thus, the fracture aperture can be determined using the thermal and tracer breakthrough data. Knowledge of the fracture aperture can then be used to predict temperature drawdown in producing wells.

$$T_{ratio} = \frac{T_o - T_w}{T_o - T_{inj}} = erfc\left\{\left[\frac{(\rho_w C_w)^2}{K_r \rho_r C_r}\left(\frac{b}{t_c}\right)^2 (t_{th} - t_c)\right]^{-\frac{1}{2}}\right\} \tag{4.1}$$

$$b = \left\{\left(erfc^{-1}\left[\frac{T_o - T_w}{T_o - T_{inj}}\right]\right)^{-2} \frac{t_c^2}{(t_{th} - t_c)} \frac{K_r \rho_r C_r}{(\rho_w C_w)^2}\right\}^{1/2} \tag{4.2}$$

These are the analytical expressions used to model a single fracture connection between an injector and producer well pair. Equation 4.2 calculates the effective fracture aperture from the thermal arrival time t_{th}; tracer front arrival time t_c; and relative temperature ratio T_{ratio}.

Cooling Rate Predictions

$$T_w = T_o - (T_o - T_{inj})\,erfc\left\{\left[\frac{(\rho_w C_w)^2}{K_r \rho_r C_r}\left(\frac{qb}{A_{tracer}x}\right)^2\left(t - \left(\frac{\rho_A C_A}{\rho_w C_w}\right)\frac{A_{tracer}x}{q}\right)\right]^{-\frac{1}{2}}\right\} \tag{4.3}$$

$$\rho_A C_A = \phi\rho_w C_w + (1-\phi)\rho_r C_r \tag{4.4}$$

$$A_{tracer} = \phi A_{cross\,section} \tag{4.5}$$

$$A_{\max} = \frac{q_{total}}{v_{mean}} \tag{4.6}$$

$$q = q_{total}\left(\frac{A_{tracer}}{A_{\max}}\right) \tag{4.7}$$

The general equation for temperature versus time as derived by Gringarten and Sauty (1975) is shown in Equation 4.3. Here, x is the distance between the injection well and producer well. Thus, once the aperture b is determined, this equation describes the cooling of producing feed zones due to injection with constant volumetric rate (q) and temperature (T_{inj}). Note that q specified here is not the total injection rate. It is the rate of effective injected volume that goes to a particular producer. This is approximated by getting the ratio of the area derived from tracer analysis to the maximum area based on the total injection rate and the observed mean velocity from tracer data. Equations 4.5 to 4.7 illustrate these in more detail.

4.3.2 Porous Channel with Heat Loss Model: Cooling Rate Predictions

Maturgo et al. (2010) use tracer analysis to determine the effective area (A_{tracer}) for two injector and producer well pairs. These are NJ3D-SG2RD and NJ2RD-NJ5D. Using parameters from the general equation and the effective cross sectional area, thermal velocity without heat loss (v_{th}) can be defined as shown in Equation 4.8. From this definition, Equation 4.3 can be rearranged to get Equation 4.9 which describes the cooling effect of injection for a porous connection model. As explained in the previous section, q is the effective volumetric injection rate.

$$v_{th} = \frac{q}{A_{tracer}}\frac{\rho_w C_w}{\rho_A C_A} = v_w\phi \tag{4.8}$$

$$T_w = T_o - (T_o - T_{inj})\,erfc\left\{\left[\frac{(\rho_A C_A)^2}{K_r \rho_r C_r}\frac{v_{th}^2 b^2}{x^2}\left(t - \frac{x}{v_{th}}\right)\right]^{-\frac{1}{2}}\right\} \tag{4.9}$$

4.3.3 Single Porous Channel

Nonlinear Optimization

In order to couple both the tracer returns concentration and temperature responses for the analytical models, the measured data were scaled to have the same order of magnitude. This was to ensure that both tracer and temperature responses would be given equal weights in the optimization. Scaling was done by using the normalized concentration ($\bar{C}$) and temperature ($\bar{T}$) data vectors as described in Equations 4.10 and 4.11, respectively. Here, the maximum and minimum subscripts referred to the maximum and minimum values for the tracer concentration and temperature datasets. Thus, both normalized data vectors had values that ranged from 0 to 1. The same scaling was done with the calculated values of the model.

Nonlinear least squares optimization was used to determine the relevant geometric and fluid flow parameters defined as the y vector in Equation 4.12. Parameters included were: channel half width (b), channel height (H), channel porosity (ϕ), saturated rock pore diffusivity (D), and equivalent injection temperature in the porous channel (T_{inj}). The total residual error vector, $\vec{F}(\vec{p})$, was a combination of the error vectors for the normalized concentration and temperature as shown in Equation 4.13. Error was defined as the absolute difference between the calculated values from the model and the measured data points. Using the square of the 2-norm of the vector $\vec{F}$ as the objective function or the residual norm (f), nonlinear least squares optimization was used to determine the parameter vector ($\vec{p}$) that minimized f as defined by Equation 4.14. Levenberg-Marquardt and Trust-Region-Reflective algorithms were applied. These minimized the objective function that was bounded. A first-order optimality measure was used as the stopping criterion (Equation 4.15). Iterations were done until the change in value of the objective function during an iteration step ($i+1$) was less than 10^{-10}. This method was applied to field data as will be described in the next section.

$$\bar{C} = \frac{\vec{C}}{C_{maximum}} \tag{4.10}$$

$$\bar{T} = \frac{\vec{T} - T_{minimum}}{T_{maximum} - T_{minimum}} \tag{4.11}$$

$$\vec{p} = [\ b \quad H \quad \phi \quad D \quad T_{inj}] \tag{4.12}$$

$$\vec{F}(\vec{p}) = \{|\bar{C}_{calc}(\vec{p}) - \bar{C}_{data}| \quad , \quad |\bar{T}_{calc}(\vec{p}) - \bar{T}_{data}|\} \tag{4.13}$$

$$\min_{\vec{p}} f = \min_{\vec{y}} \left\|\vec{F}(\vec{p})\right\|_2^{\ 2} = \min_{\vec{y}} \sum_k {F_k}^2(\vec{p}) \tag{4.14}$$

$$|f(\vec{y}_i) - f(\vec{y}_{i+1})| < 10^{-10} \tag{4.15}$$

Tracer and Heat Transport Equations

From the governing advection-dispersion equation for the impulse boundary condition on the left side and a semi-infinite plane boundary in the x-axis, the well-known solution of tracer

concentration dependency on distance (x) and time (t) can be derived (Equation 4.16). This solution has also been derived in previous studies (Bullivant and O'Sullivan, 1985; Kreft and Zuber, 1978). Another form of Equation 4.16 can be derived in terms of the Peclet number (w), which is the dimensionless ratio of the advection and diffusion terms; as well as the mean tracer arrival time (t_m) (Equation 4.17). Definitions of these two parameters are shown in Equations 4.18 and 4.19 with volumetric injection rate (q), the cross-sectional area (A), and porosity (ϕ). For tracer analysis alone, the Peclet number and mean tracer arrival time are used to obtain a match for Equation 4.17. This implies that the parameters are lumped together, which makes it difficult to isolate individual values. Hence, coupling the tracer and temperature data analyses will yield a better match by constraining the possible geometric configurations and providing more data calibration points. This can then be used to generate more reliable temperature response predictions for different injection schemes.

$$C(x,t) = \frac{m\phi}{q}\frac{1}{2}\frac{x}{\sqrt{D}}\frac{1}{\sqrt{\pi t^3}}\left[e^{\frac{-(x-vt)^2}{4Dt}}\right] \tag{4.16}$$

$$C(x,t) = \frac{m\phi}{2q}\sqrt{\frac{t_m w}{\pi}}\frac{1}{t^{1.5}}\ exp\left\{-\frac{w}{4}\frac{(t-t_m)^2}{tt_m}\right\} \tag{4.17}$$

$$t_m = \frac{\phi x A}{q} \tag{4.18}$$

$$w = \frac{qx}{vA} = \frac{qx}{D\phi A} \tag{4.19}$$

Several studies have modeled the temperature drawdown caused by constant cold water injection into a porous channel in hot geothermal systems (Lauwerier, 1955; Gringarten and Sauty, 1975). The temperature of the low permeability matrix or host rock is (T_r) and the temperature of the fluid saturated rock is (T_w). Specific heat capacities (by mass) for the fluid saturated rock and water are c_A and c_w, respectively. Densities of the fluid saturated rock and water are ρ_r and ρ_w such that ($\rho_A c_A$) is the saturated rock specific heat capacity by volume as defined in Equation 4.20. K_r is the rock thermal conductivity and the other variables related to geometry have the same definition as described in the tracer transport section.

Heat is transported by the convection within the porous zone in the x direction and conduction from the rock matrix to this permeable zone in the z direction. One important assumption of this model is the instantaneous thermal equilibrium between the rock matrix and the fluid saturated rock. Another assumption is that the rock and fluid properties are constant. The first boundary condition is instantaneous thermal equilibrium and the second boundary condition is constant injection temperature on the left side. Initial conditions for these systems are the same initial temperature for the rock matrix and saturated rock (T_o) as well as the constant injection temperature on the left (T_{inj}). Using iterative Laplace transform, the solution to these two partial differential equations can be derived as shown in Equation 4.21. Typically, the temperature drawdown at the producer is defined in terms of the temperature ratio (T_{ratio}) of the resulting temperature decrease due to injection ($T_w - T_o$) and the difference between the injection and initial temperatures ($T_{inj} - T_o$). In the next section, the results will be discussed.

$$\rho_A c_A = \phi\rho_w c_w + (1-\phi)\rho_r c_r \tag{4.20}$$

$$T_{ratio}(x,t) = \frac{T_w(x,t) - T_o}{T_{injection} - T_o} = erfc \frac{\frac{1}{b}\sqrt{\frac{K_r}{\rho_w c_w v}}x}{2\sqrt{\frac{\rho_A c_A}{\rho_r c_r}\left(\frac{\rho_w c_w v}{\rho_A c_A}t - x\right)}} \quad (4.21)$$

4.4 RESULTS FROM COMBINED TRACER AND TEMPERATURE ANALYSIS

4.4.1 Single Fracture Model

Available Data

Results from tracer tests in EGS and conventional fractured geothermal reservoirs have been reported frequently in the literature. However, thermal breakthrough data are not as widely published. For EGS fields, thermal data are obtained usually from long-term circulation tests, as for example in Hijiori, Matsunaga et al. (2002) and Matsunaga et al. (2005). Historic silica geothermometer data are used from Palinpinon field which is a conventional liquid-dominated reservoir, Maturgo et al. (2010). Matsukawa is a conventional vapor-dominated field, Fukuda et al. (2006). Table 4.1 provides a summary of the field data used in this study. The thermal breakthrough time t_{th} here corresponds to the time it takes to reach a T_{ratio} of 0.5.

Table 4.1: Thermal and tracer breakthrough times from field data.

Field	Injector	Producer	t_c	t_{th}	Source
			Days	days	
Hijiori	HDR-1	HDR-2A	1	175	Matsunaga et al. (2002)
	HDR-1	HDR-3	4	266	Matsunaga et al. (2005)
Palinpinon	NJ2RD	NJ5D	15	730[1]	Maturgo et al. (2010)
	SG2RD	NJ3D	28	365	
Matsukawa	M-6	M-8	1.5	146	Fukuda et al. (2006)

As described in the previous section, fracture aperture can be estimated directly from the thermal and tracer breakthrough times. Assumptions for the values of the other parameters are listed in Table 4.2. These are the values assigned to these properties in the estimation of fracture aperture. Actual temperature ratios for the injector-producer pairs derived from long term circulation test results are shown in Table 4.3. Estimated fracture aperture values are given in the same table.

Table 4.2: Assumptions used in calculations.

Rock thermal conductivity	K_r	2	W/m-C
Rock density	ρ_r	2200	kg/m^3
Water density	ρ_w	900	kg/m^3
Rock heat capacity	C_r	0.712	kJ/kg-C
Water heat capacity	C_w	4.342	kJ/kg-C

[1] Assumed that injection in NJ2RD started in 1998 or 1 year before the start of drawdown in NJ5D based on the Palinpinon injection and production history discussed by Bayon and Ogena (2005).

Results

To determine the relative temperature for M-6 and M-8 in Matsukawa, a 60°C injection temperature was assumed. Estimates of effective fracture aperture *b* varied from 2.1 cm to 42.6 cm. Though the HDR-1 and HDR-2A well pair in Hijiori exhibited the shortest mean tracer arrival time, it had the lowest calculated effective aperture value because of the long thermal breakthrough time. This observation demonstrated the value of using both tracer and thermal results to constrain the effective aperture. Using this analytical solution also provided an alternative method to characterize the flow path between wells.

Results from finite element heat and mass transfer modeling (FEHM) of the Hijiori field demonstrates fracture aperture values of about 2 mm (Tenma et al., 2005). This is significantly lower than the calculated aperture values. Further investigation of results from aperture estimates from numerical modeling will be undertaken. However, effective fracture aperture derived from acoustic imaging logs show a range of values consistent with those calculated. The next section will describe these studies in detail.

Table 4.3: Relative temperature ratios and calculated fracture aperture from thermal and tracer breakthrough times.

Field	Injector	Producer	T_{ratio}	Calculated *b* cm
Hijiori	HDR-1	HDR-2A	0.46	2.1
	HDR-1	HDR-3	0.14	6.9
Palinpinon	NJ2RD	NJ5D	0.17	15.7
	SG2RD	NJ3D	0.07	42.6
Matsukawa	M-6	M-8	0.29[2]	3.5

4.4.2 Porous Channel Model

Available Data

Table Table 4.4 lists the injection and production well pairs with tracer and temperature data available in published literature. All were used in this study. Hijiori is an EGS field while Palinpinon is a conventional liquid-dominated reservoir. Tracers test results are often readily available in literature; however thermal breakthrough data are infrequent. In Hijiori, temperature data were derived from long-term circulation tests (Matsunaga et al., 2002; Matsunaga et al., 2005). Reservoir temperatures for the Palinpinon field were reported by Maturgo et al. (2010). Rock and fluid thermal transport properties and fluid densities are assumed to be constant with values from Table 4.2.

[2] Assumed an injection temperature of 60°C

Table 4.4: Injection-production well pairs analyzed.

Field	Injector	Producer	Source
Hijiori	HDR-1	HDR-3	Matsunaga et al. (2002)
Palinpinon	NJ2RD	NJ5D	Maturgo et al. (2010)
	SG2RD	NJ3D	

Results

Results from the nonlinear optimization are shown in Table 4.5. This nonlinear least squares optimization for the coupled tracer and temperature data analysis is a five parameter scenario run. Channel geometry related parameters are the following: half-aperture (b), height (H), and porosity (ϕ). The channel half-aperture (b) described the degree of heat transfer from the matrix to the porous channel. The total channel pore volume represents the strength of connectivity of a well pair. Saturated pore diffusivity (D) and equivalent channel injection temperature (T_{inj}) are related to transport. Pore diffusivity (D) is an indication of the amount of diffusion within the channel. Lastly, the equivalent injection temperature (T_{inj}) at the channel models the amount of fluid mixing with other permeable zones.

Because it is an EGS reservoir, the Hijiori well pair (HDR-1 and HDR-3) is expected to have a lower injection temperature as calculated. Both Palinpinon field well pairs have high T_{inj} values because they are from a conventional geothermal reservoir, where there are multiple high enthalpy feed zones expected. In terms of pore diffusivity, the Hijiori well pair value is smaller by an order of magnitude compared to the other two at 0.01 m^2/s. This can be attributed as well to the nature of the EGS reservoir, where a few flow paths are present and advective transport dominates. In contrast, relative values of porosities and channel heights are similar for the three well pairs. Porosity values range from 0.15 to 0.19, which is consistent with either secondary damage zone or brecciated zone models. Channel half-aperture values for HDR1-HDR-3 and SG2RD-NJ3D well pairs have the same order of magnitude. On the other hand, NJ2RD-NJ5D has the largest half-aperture at 5.64m. This well pair likewise has the largest pore diffusivity of 0.230 m^2/s. Therefore, one can conclude that this well pair has the greatest connectivity among the three.

Table 4.6 shows the parameters derived by Maturgo et al. (2010) from tracer analysis of the same Palinpinon field data. There is significant difference for all the parameters when compared to those derived from the nonlinear least squares optimization. Because it is based solely on tracer analysis, one would not be able to match the thermal response using these values. This illustrates the importance of constraining the possible configurations of the porous model.

Table 4.5: Geometric and fluid flow parameters derived from the five parameter scenario analysis.

Injector	Producer	b m	H m	ϕ	D m^2/s	T_{inj} C
HDR-1	HDR-3	0.73	1246	0.23	0.010	100
NJ2RD	NJ5D	5.64	1296	0.15	0.230	236
SG2RD	NJ3D	0.51	1127	0.19	0.138	259

Table 4.6: Geometric and fluid flow parameters from tracer analysis (Maturgo et al., 2010).

Injector	Producer	b m	H m	ϕ	T_{inj} C
NJ2RD	NJ5D	2.44	104	0.10	160
SG2RD	NJ3D	2.18	91	0.10	160

Table 4.7 shows the 95 percent confidence intervals of the five parameters used in the nonlinear least squares fitting for the HDR-1 (injector) and HDR-3 (producer) well pair using the porous model. The equivalent residual norm (f) for this case is 0.6745 while the average error is 114 percent. Residual norm (f) is defined as the square of the 2-norm of the residual error vector $\vec{F}(\vec{p})$. The results show that both the half-aperture (b), equivalent injection temperature (T_{inj}), and channel height (H) exhibit the highest error percentages. A high error percent signifies a higher uncertainty on the value of the parameter. Looking at the confidence intervals for b, the minimum and maximum values are -1.3m and 2.76m, respectively. Though the parameters values are bounded for the nonlinear optimization, the nonphysical negative values are obtained from the high percent errors. The high error percent values can be attributed to the limited number of data points in the measured temperature and tracer values as can be observed from the residual plot for HDR1-HDR3 (Figure 4.3).

Table 4.7: Confidence interval and percent error values for HDR1(Injector)-HDR3(Producer) for the five parameter scenario analysis.

Parameter	Minimum	Value	Maximum	% Error
$b\ (m)$	-1.30	0.73	2.76	277
$H\ (m)$	-262	1264	2790	121
ϕ	0.19	0.23	0.28	20
$D\ (m^2/s)$	0.008	0.010	0.011	15
$T_{inj}\ (C)$	-36	100	236	136

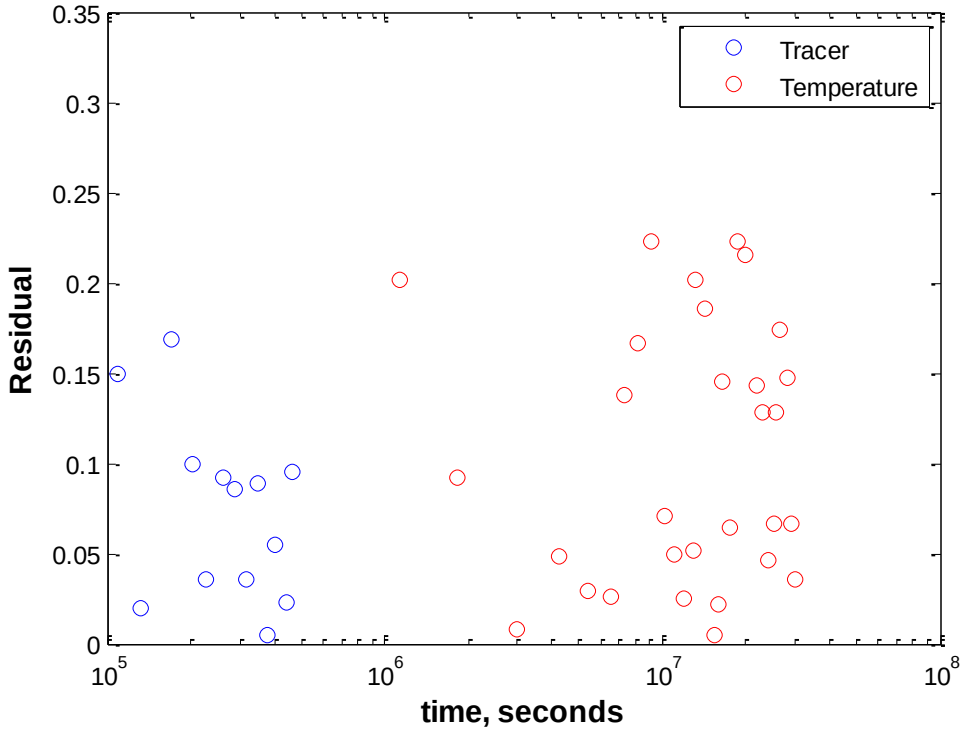

Figure 4.3 Residual Plot for HDR1(Injector)-HDR3(Producer) for the five parameter scenario.

On the other hand, Table 4.8 shows the 95 percent confidence interval and percent error values for the NJ2RD(Injector)-NJ5D(Producer) well pair. The residual norm (f) value is 0.5595 and the average error is 36 percent. Compared to the Hijiori case, this well pair exhibits lower errors and smaller confidence interval values. In this scenario, the half-aperture (b) value ranges from 0.17m to 11.11m with an average value of 5.64m. Similar to the HDR1-HDR3 case, the half-aperture (b) and height (H) have the highest error percent values. Thus, both b and H can take on a wide range of values that will satisfy the both the tracer and temperature data sets given. However, the injection temperature (T_{inj}) for the NJ2RD-NJ5D porous model run has a low error of 10 percent. Aside from T_{inj}, porosity (ϕ) and saturated pore diffusivity (D) values have a narrow confidence interval and low error values. Low error values indicate that the calculated parameters are unique. The residual plot (Figure 4.4) shows higher residual errors for temperature values as compared to tracer values. This trend is expected because temperature measurements have higher measurement error ranges than tracer concentration data.

Table 4.8: Confidence interval and percent error values for NJ2RD(Injector)-NJ5D(Producer) for the five parameter scenario analysis,

Parameter	Minimum	Value	Maximum	% Error
$b\ (m)$	0.17	5.64	11.11	97
H (m)	563	1296	2029	57
ϕ	0.14	0.15	0.16	8
$D\ (m^2/s)$	0.213	0.230	0.246	7
$T_{inj}\ (C)$	212	236	260	10

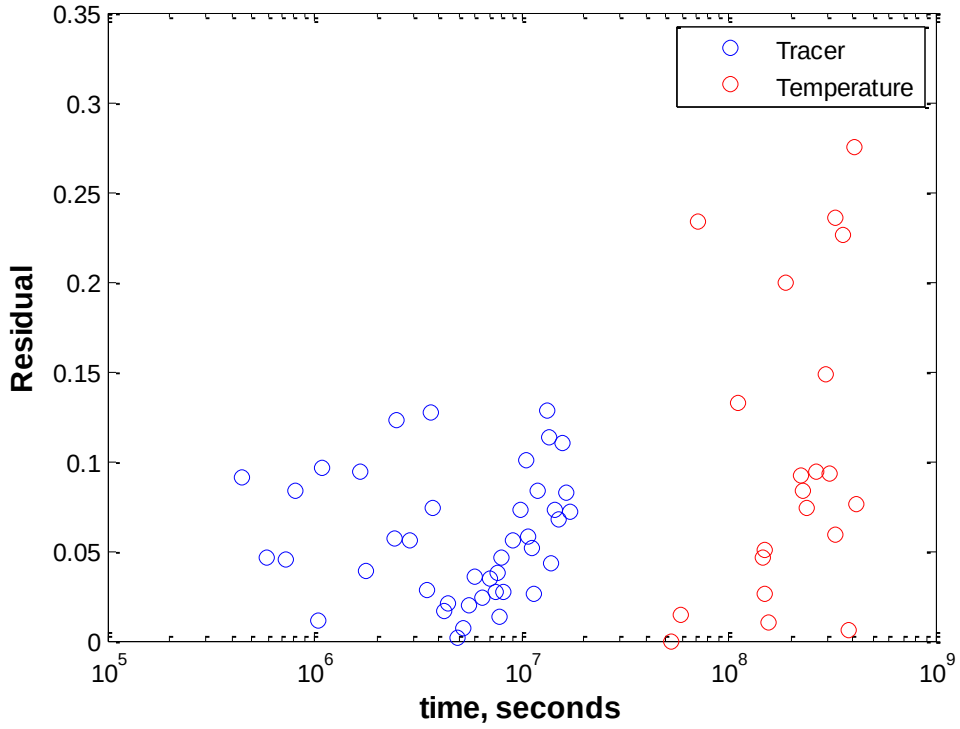

Figure 4.4 Residual plot for NJ2RD(Injector)-NJ5D(Producer) for the five parameter scenario.

For the SG2RD-NJ3D well pair from the Palinpinon geothermal field, the confidence interval and error values are shown in **Error! Reference source not found.**Table 4.9. The residual norm is 2.2260 and the average error is 133 percent. Consistent with the other two well pairs, the half-aperture (b) value had the highest percent error. Moreover, the channel height (H) had the second highest error value. Conversely, the porosity error value of 93 percent is higher than that from the other well pairs. As expected, the residual plot for the SG2RD-NJ3D well pair (Figure 4.5) also showed significant residual error values. From this plot, it can be observed that the temperature value residual errors values are significantly higher than for the tracer ones.

Table 4.9: Confidence interval and percent error values for SG2RD(Injector)-NJ3D(Producer) for the five parameter scenario analysis.

Parameter	Minimum	Value	Maximum	% Error
$b\ (m)$	-1.65	0.51	2.68	422
$H\ (m)$	-333	1127	2587	130
ϕ	0.01	0.19	0.36	93
$D\ (m^2/s)$	0.113	0.138	0.163	18
$T_{inj}\ (C)$	250	259	269	4

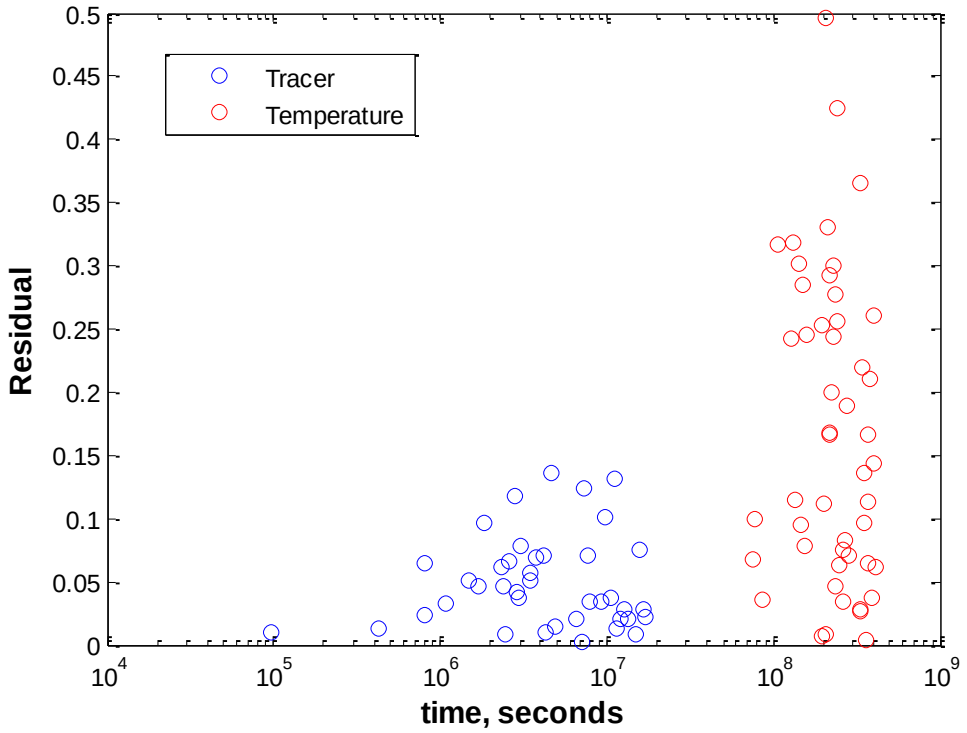

Figure 4.5 Residual plot for SG2RD(Injector)-NJ3D(Producer) for the five parameter scenario.

Figure 4.6 shows the normalized tracer response (C_{ratio}) curve fit versus time using the parameters for the HDR-1 and HDR-3 well pair. The tracer response curve is flat with no sharp peaks. On the other hand, Figure 4.7 shows the thermal response curve fit. Red circles are the measured data points while the blue line represents the optimized curve. Overall, a good match can be observed. However, because all the data points are honored by the optimization, outliers force the match towards the middle of all the data. This is more pronounced in the temperature data because they are generally more scattered. The same phenomenon can be observed for the normalized tracer concentration (Figure 4.8) and temperature response (Figure 4.9) curve fit for the NJ2RD-NJ5D well pair. For this case, the typical single peak tracer returns behavior with a tail can be observed. Aside from meeting the objective function tolerance per step, the tracer return curve fit should match the peak concentration time effectively. Measured thermal response data for this well pair are also slightly scattered but a sufficient match is obtained. Similarly, a standard tracer return profile can be noticed for the SG2RD-NJ3D well pair (Figure

4.10). The resulting model matches this extremely well. Equivalent thermal response curve fit is shown in Figure 4.11. There is significant scattering of measured data but the model still matches them adequately.

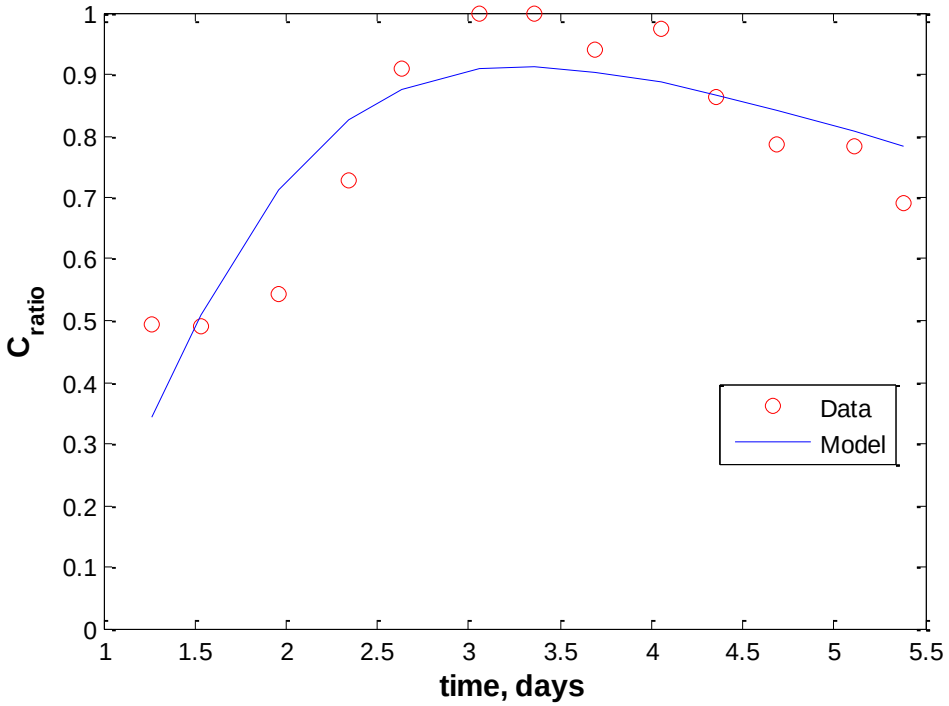

Figure 4.6 Normalized tracer response curve fit for HDR1(Injector)-HDR3(Producer) for the five parameter scenario. Measured data points are in red while the analytical model result is represented by the blue line.

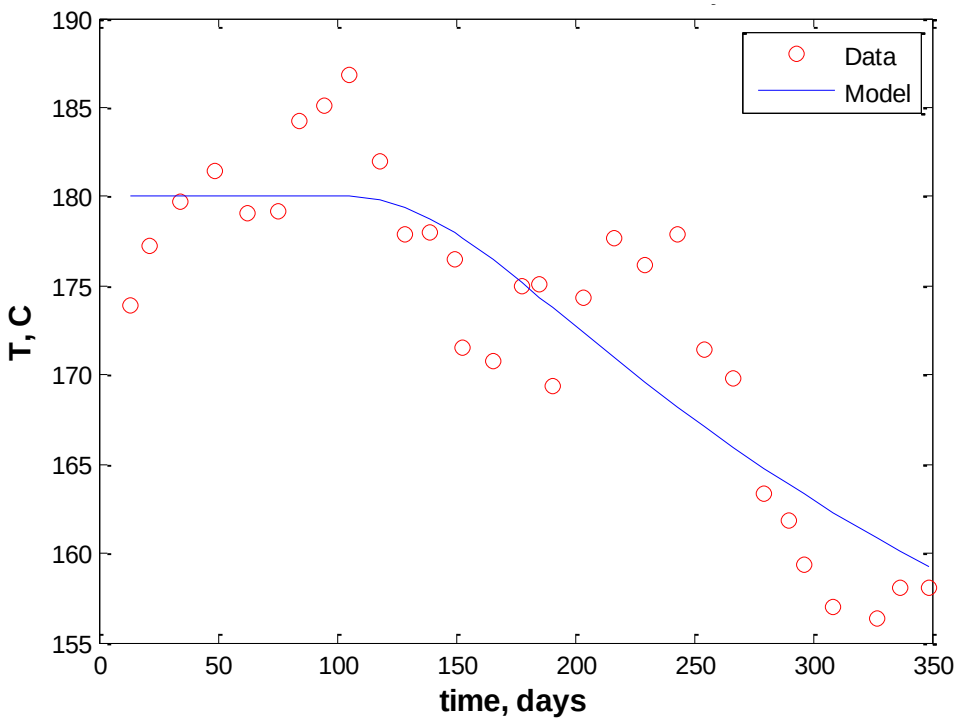

Figure 4.7 Thermal response curve fit for HDR1(Injector)-HDR3(Producer) for the five parameter scenario

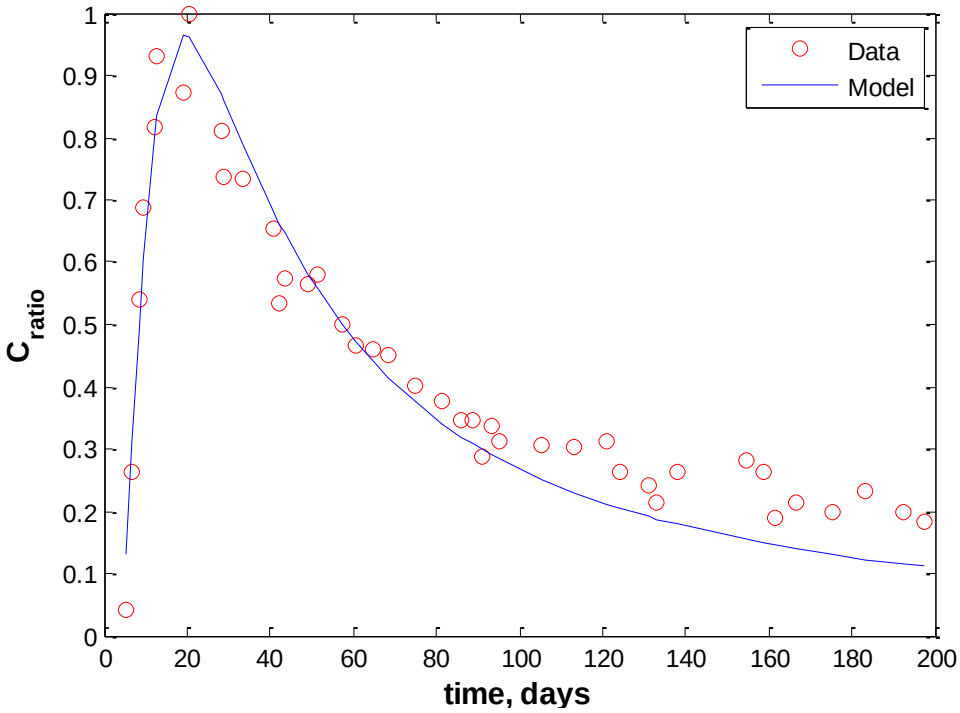

Figure 4.8 Normalized tracer response curve fit for NJ2RD(Injector)-NJ5D(Producer) for the five parameter scenario.

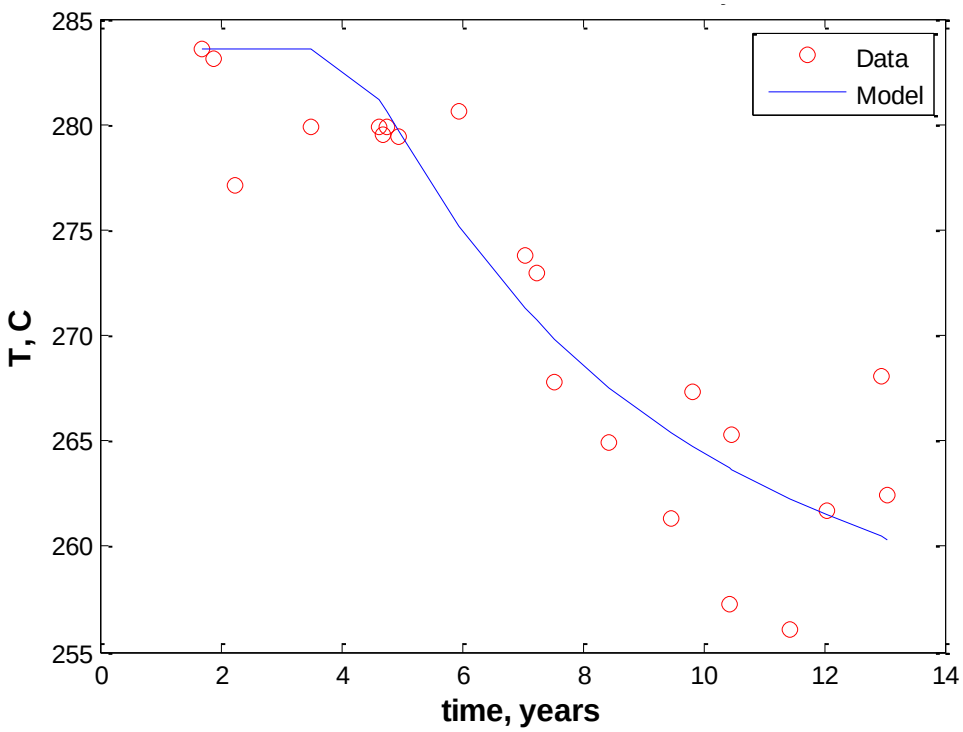

Figure 4.9 Thermal response curve fit for NJ2RD(Injector)-NJ5D(Producer) for the five parameter scenario.

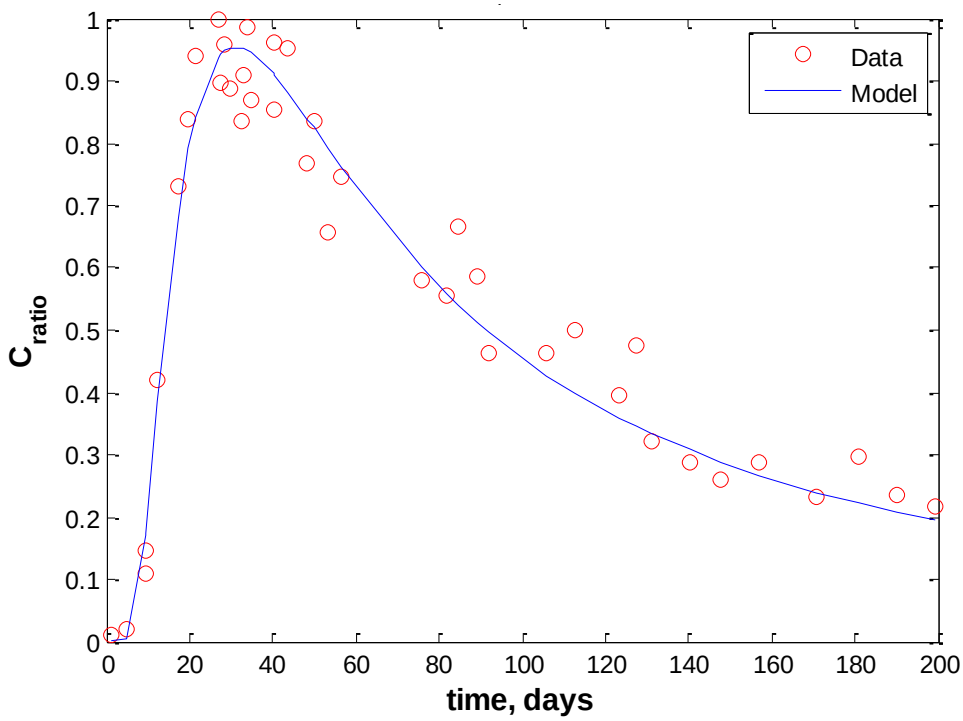

Figure 4.10 Normalized tracer response curve fit for SG2RD(Injector)-NJ3D(Producer) for the five parameter scenario.

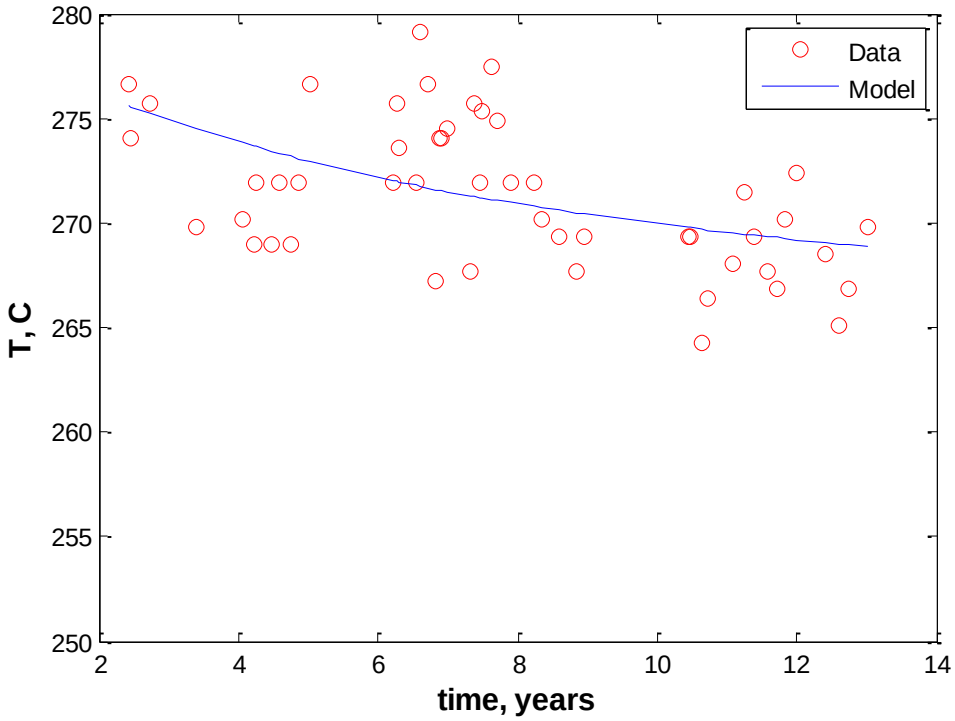

Figure 4.11 Thermal response curve fit for SG2RD(Injector)-NJ3D(Producer) for the five parameter scenario.

4.4.3 Porous Channel Model with Scaling Correlations

Scaling Correlations

Table 4.10 describes the scaling correlation coefficient values derived from literature. These are values derived from fitting of data for opening mode joints across various length scales. The expression found in literature follows the form given in Equation 4.22. In Equation 4.22, D_{max} is the maximum total aperture of the fracture which is equivalent to twice the maximum half-aperture value (b_{max}). A and B are the scaling constant coefficient and scaling exponent or fractal dimension, respectively. To convert these scaling coefficients from literature to the standard form, the ratio of the measured half-aperture (b) to the maximum value (b_{max}) must be taken into account as shown in Equation 4.23**.** Hence, the equivalent definition of the scaling constant coefficient (α) is given in Equation 4.24.

$$D_{max} = AL^B = 2b_{max} \quad \textbf{(4.22)}$$

$$b = \frac{\pi}{4}\, b_{max} = \frac{\pi}{8} AL^B = \alpha L^{\beta} \quad \textbf{(4.23)}$$

$$\alpha = \frac{\pi}{8} A \quad (4.24)$$

Table 4.10: Scaling correlation coefficients found in literature

α	β	Source
0.0004	1	Scholz (2010)
0.0039	1	Scholz (2010)
0.1689	0.4	Olson (2003)

These scaling coefficients were used as an additional constraint in the nonlinear least squares optimization of the coupled tracer and temperature data analysis. Each scaling coefficients combination was treated as a separate scenario run. Aside from scaling correlation scenarios, the equivalent value of α and β were determined using nonlinear least squares optimization. The half-aperture (b) can be replaced by the scaling coefficients (α and β). Hence, the six parameters during optimization include the following: channel height (H); porosity (ϕ); saturated pore diffusivity (D); equivalent injection temperature (T_{inj}); scaling constant coefficient (α); and scaling exponent (β). In other words, this six parameter scenario depicts the determination of the relationship between the half-aperture (b) and the channel height (H) by obtaining the equivalent scaling coefficients α and β.

Table 4.11 shows the equivalent values of the scaling coefficients determined from the nonlinear least squares optimization of the coupled tracer and thermal data analysis with bounded parameters. The scaling exponent or fractal dimension (β) value ranges from 0.64 to 1.00 which is within the range of values obtained from literature described in the previous subsection. Furthermore, the scaling coefficient (α) is also within the specified range from literature.

Table 4.11: Equivalent scaling coefficients from nonlinear optimization.

α	β	Well Pair
0.0117	0.85	HDR1-HDR3
0.0039	1.00	NJ2RD-NJ5D
0.0011	0.64	SG2RD-NJ3D

Results

This subsection describes the use of scaling correlations to relate the fracture half-aperture (b) to the channel length (L). Scaling correlation coefficients were obtained from reported values empirically determined in literature as described in the previous subsection. Thus, the number of fitting parameters to be determined reduced from six parameters to four parameters in total. These model fitting parameters are the following: channel height (H); porosity (ϕ); saturated pore diffusivity (D); and equivalent injection temperature (T_{inj}). For each of the three well pairs, three scenarios with different sets of scaling coefficients were used (α and β).

Table 4.12 shows the 95 percent confidence interval and percent error values for the HDR1-HDR3 well pair using $b = 0.0004L^1$ (Scholz, 2010). Percent error values for this case are lower than that of the five- parameter model. The residual norm for this scenario is 0.8219 and the average error is 24.85 percent. The maximum residual error values for both tracer and temperature data sets are lower for $b = 0.0039L^1$ (Scholz, 2010) as shown in Table 4.13. Average error for this scenario is slightly higher than for $b = 0.0004L^1$ at 28.7 percent. On the other hand, the residual norm is lower at 0.6889. Finally, the last scaling correlation is $b = 0.1689L^{0.4}$ from Olson (2003). Table 4.14 lists the confidence interval estimates and percent error values for each of the matching parameter. The average error value for this scenario is 22.7 percent which is less than the values for the other two scaling correlation scenarios.

All three scaling correlations used for the four parameter model fitting for the HDR1-HDR3 well pair showed the same value of the saturated pore diffusivity (D) at $0.01\ m/s^2$ and equivalent injection temperature (T_{inj}) at 100C. Moreover, there was also a narrow range for the determined porosity (ϕ) values from 0.13 to 0.23. In contrast, the channel height (H) values adjusted with the scaling correlation. For scaling correlations with low scaling constant coefficient (α), the channel height values were higher as can be seen from the $b = 0.0004L^1$ case.

Table 4.12: Confidence interval and percent error values for HDR1(Injector)-HDR3(Producer) using $b = 0.0004L = 0.05m$ (Scholz, 2010).

Parameter	Minimum	Value	Maximum	% Error
$H\ (m)$	1023	1367	1712	25
ϕ	0.19	0.23	0.27	17
$D\ (m^2/s)$	0.008	0.010	0.011	15
$T_{inj}\ (C)$	58	100	142	42

Table 4.13: Confidence interval and percent error values for HDR1(Injector)-HDR3(Producer) using $b = 0.0039L = 0.51m$ (Scholz, 2010).

Parameter	Minimum	Value	Maximum	% Error
$H\ (m)$	2171	2668	3164	19
ϕ	0.11	0.13	0.16	19
$D\ (m^2/s)$	0.008	0.009	0.011	17
$T_{inj}\ (C)$	40	100	160	60

Table 4.14: Confidence interval and percent error values for HDR1(Injector)-HDR3(Producer) using $b = 0.1689L^{0.4} = 1.18m$ (Olson, 2003).

Parameter	Minimum	Value	Maximum	% Error
$H\ (m)$	849	1120	1391	24
ϕ	0.19	0.23	0.28	18
$D\ (m^2/s)$	0.008	0.010	0.011	15
$T_{inj}\ (C)$	67	100	133	33

Average error is 11.30 percent while the residual norm is 0.5597 for the NJ2RD-NJ5D well pair using $b = 0.0004L^1$ (Scholz, 2010). All of the parameters have error values less than or equal to 15 percent as shown in Table 4.15. The narrow range of parameter values for the 95 percent confidence intervals show the uniqueness of the values. Using $b = 0.0039L^1$ from Scholz (2010), has a lower average error value of 7.43 percent with a residual norm of 0.5979. Confidence interval estimates and error values are shown in Table 4.16. For this scenario, the equivalent injection temperature (T_{inj}) has the lowest average error of two percent. The Olson (2003) scaling correlation is $b = 0.1689L^{0.4}$. Table 4.17 lists the confidence interval estimates and error values for this scenario with an average error value of 8.64 percent.

Similar to the HDR1-HDR2 well pair, both the saturated pore diffusivity (D) and equivalent injection temperature (T_{inj}) values remained the same for all scenarios. Diffusivity value from

optimization was 0.229 m/s^2 to 0.230 m/s^2 and the T_{inj} was 197C to 244C. Additionally, the porosity (ϕ) also remained relatively constant for all three scenarios with a value of 0.14 to 0.15. There was also a close correspondence between the channel height (H) and the resulting half-aperture (b). Higher equivalent half-aperture (b) values lead to higher channel height values (H).

Table 4.15: Confidence interval and percent error values for NJ2RD(Injector)-NJ5D(Producer) using $b = 0.0004L = 0.59m$ (Scholz, 2010).

Parameter	Minimum	Value	Maximum	% Error
$H\ (m)$	2122	2507	2892	15
ϕ	0.13	0.14	0.15	8
$D\ (m^2/s)$	0.212	0.229	0.246	7
$T_{inj}\ (C)$	169	197	226	15

Table 4.16: Confidence interval and percent error values for NJ2RD(Injector)-NJ5D(Producer) using $b = 0.0039L = 5.89m$ (Scholz, 2010).

Parameter	Minimum	Value	Maximum	% Error
$H\ (m)$	793	904	1014	12
ϕ	0.14	0.15	0.17	8
$D\ (m^2/s)$	0.213	0.229	0.246	7
$T_{inj}\ (C)$	239	244	250	2

Table 4.17: Confidence interval and percent error values for NJ2RD(Injector)-NJ5D(Producer) using $b = 0.1685L^{0.4}$ (Olson, 2003).

Parameter	Minimum	Value	Maximum	% Error
$H\ (m)$	1455	1684	1914	14
ϕ	0.14	0.15	0.16	8
$D\ (m^2/s)$	0.213	0.230	0.246	7
$T_{inj}\ (C)$	211	224	237	6

The average error curve fit using $b = 0.0004L^1$ (Scholz, 2010) for the SG2RD-NJ3D well pair is still acceptable at 13.46 percent but the residual norm can be considered high at 2.2265. Confidence interval ranges and the average error values for the parameters are listed in Table 4.18. A narrow range of values can be observed for all parameters with the equivalent injection temperature (T_{inj}) having the smallest average error. For the $b = 0.0039L^1$ case (Scholz, 2010), the average error is lower at 12.78 percent and the residual norm is slightly higher at 2.8291. Despite the relatively high error values for temperature, narrow confidence intervals can be observed from Table 4.19. Looking at the $b = 0.1689L^{0.4}$ (Olson, 2003) scenario, the average error for this scenario is 14.07 percent and the residual norm is 2.3025. Table 4.20 describes the confidence intervals as well as the average error values for this run. Overall, the average error values of the parameters for this scenario are higher than that of the other scaling correlations except for the equivalent injection rate (T_{inj}).

Because the calculated channel height (H) is significantly less than the distance between wells (L), three additional scaling correlations scenarios are done using H instead of L. The first

scenario is $b = 0.0004H^1$ from Scholz (2010). The average error is 12.22 percent and the residual norm is 2.2264. Confidence intervals and average error values are shown in Table 4.21. Scenario two uses $b = 0.0039H^1$ (Scholz, 2010). In this scenario, the average error is 12.05 percent and the residual norm is 2.2838. Table 4.22 shows the confidence intervals and average error values of the matching parameters. The third scenario employs $b = 0.1689L^{0.4}$ (Olson, 2003). Confidence intervals and error values for all the parameters are given in Table 4.23 with an average error value of 13.15 percent and a residual norm of 2.2779.

Overall, the average error values were significantly less for the scaling correlations related to the channel height (H) than from the channel length (L). There is also a narrow range of values across all the scenarios for the saturated pore diffusivity (D), porosity (ϕ) and equivalent injection temperature (T_{inj}) as evidenced by the consistent small error percent for these. Consistent with the other well pairs, the value for the half-aperture (b) and channel height (H) are closely related. Scaling correlations which lead to lower half-aperture (b) values also have higher channel height values (H). Thus, the channel height (H) compensates for the adjustments in the half-aperture (b) value.

Table 4.18: Confidence interval and percent error values for SG2RD(Injector)-NJ3D(Producer) using $b = 0.0004L = 0.59m$ (Scholz, 2010).

Parameter	Minimum	Value	Maximum	% Error
$H\ (m)$	795	1075	1356	26
ϕ	0.17	0.19	0.22	13
$D\ (m^2/s)$	0.121	0.139	0.156	12
$T_{inj}\ (C)$	253	260	267	3

Table 4.19: Confidence interval and percent error values for SG2RD(Injector)-NJ3D(Producer) using $b = 0.0039L = 5.89m$ (Scholz, 2010).

Parameter	Minimum	Value	Maximum	% Error
$H\ (m)$	609	768	926	21
ϕ	0.20	0.24	0.27	14
$D\ (m^2/s)$	0.121	0.140	0.160	14
$T_{inj}\ (C)$	249	256	262	3

Table 4.20: Confidence interval and percent error values for SG2RD(Injector)-NJ3D(Producer) using $b = 0.1685L^{0.4} = 3.15m$ (Olson, 2003).

Parameter	Minimum	Value	Maximum	% Error
$H\ (m)$	390	559	729	30
ϕ	0.20	0.23	0.25	12
$D\ (m^2/s)$	0.123	0.140	0.158	13
$T_{inj}\ (C)$	262	266	269	1

Table 4.21: Confidence interval and percent error values for SG2RD(Injector)-NJ3D(Producer) using $b = 0.0004H$ (Scholz, 2010).

Parameter	Minimum	Value	Maximum	% Error
$b\ (m)$	0.37	0.46	0.55	19
$H\ (m)$	954	1174	1394	19
ϕ	0.16	0.18	0.21	14
$D\ (m^2/s)$	0.120	0.138	0.155	13
$T_{inj}\ (C)$	252	259	267	3

Table 4.22: Confidence interval and percent error values for SG2RD(Injector)-NJ3D(Producer) using $b = 0.0039H$ (Scholz, 2010).

Parameter	Minimum	Value	Maximum	% Error
$b\ (m)$	1.89	2.44	2.99	22
$H\ (m)$	482	621	761	22
ϕ	0.20	0.22	0.25	12
$D\ (m^2/s)$	0.122	0.140	0.157	12
$T_{inj}\ (C)$	262	265	268	1

Table 4.23: Confidence interval and percent error values for SG2RD(Injector)-NJ3D(Producer) using $b = 0.1685H^{0.4}$ (Olson, 2003)

Parameter	Minimum	Value	Maximum	% Error
$b\ (m)$	1.99	2.26	2.48	10
$H\ (m)$	480	653	827	27
ϕ	0.20	0.22	0.25	12
$D\ (m^2/s)$	0.123	0.140	0.157	12
$T_{inj}\ (C)$	261	264	268	1

4.4.3 Predicted Thermal Drawdown Comparison

Figure 4.12 shows the comparison of the HDR1-HDR3 well pair thermal drawdown predictions over ten years for the different model configurations. Here, the low injection case scenario is used with an injection rate (q) of $20\frac{kg}{s}$ or $0.020\frac{m^3}{s}$. Equivalent injection temperature is 150C and the initial temperature is 250C. The most optimistic model is the $b = 0.0004L^1$ (Scholz, 2010) case because it results to the smallest value of the half-aperture (b). This small value improves the heat conduction from the hot matrix rock towards the porous channel or fracture. Among the porous channel models, the $b = 0.1689L^{0.4}$ (Olson, 2003) case gives the most pessimistic thermal drawdown forecast. This can likewise be attributed to the higher half-aperture (b) value for this run. Overall, the fracture model has the lowest predicted temperature drawdown. For this model, the total temperature decline is 70C over a period of ten years. Having all the different model configurations enables one to cover the uncertainty range in the expected temperature decline caused by a particular injector to a producer.

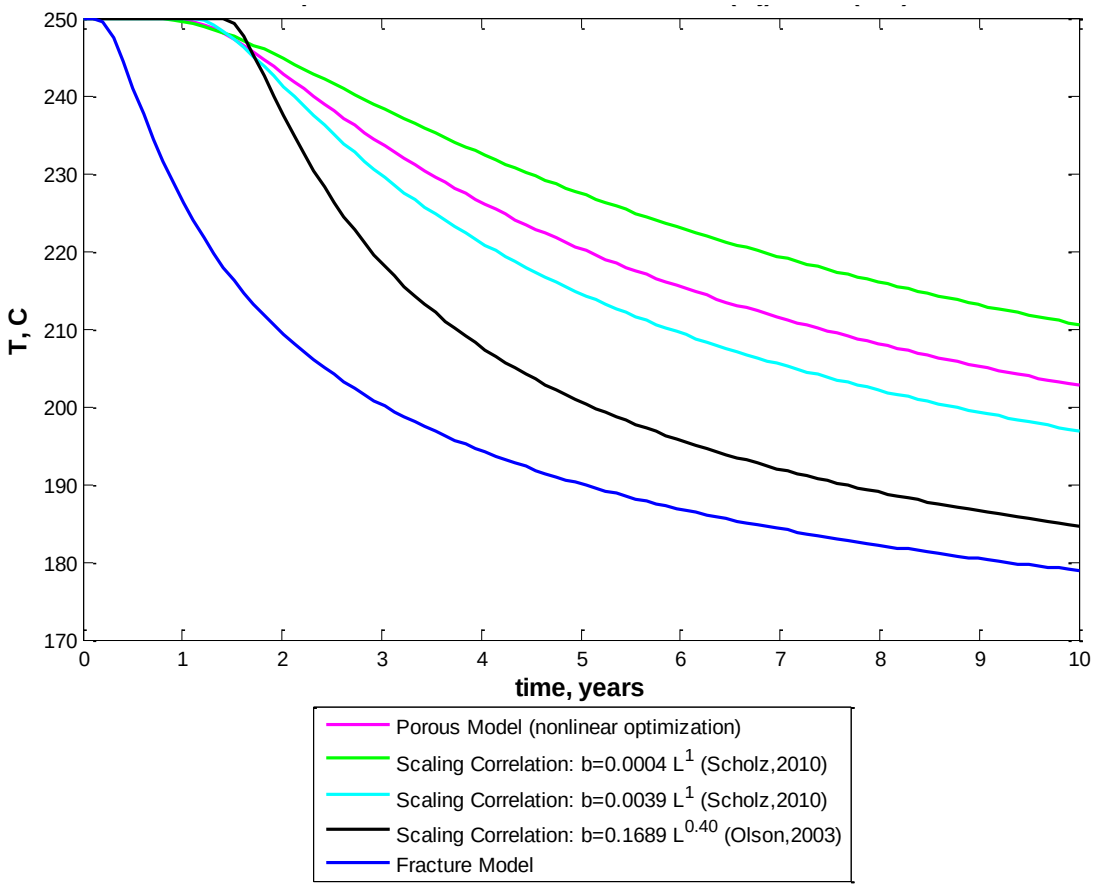

Figure 4.12: Temperature drawdown curves for HDR1(Producer)-HDR3(Injector): low injection case (q=0.020 m^3/s; T_{inj}=150C; T_o=250C).

For the NJ2RD-NJ5D well pair case, there is another porous channel model derived from tracer tests alone (Maturgo et al., 2010). Figure 4.13 shows the results for the low injection case scenario using the same set-up as in the HDR1-HDR3 case. Contrary to the result for HDR1-HDR3, the fracture model has the most optimistic thermal drawdown prediction with just a 10C temperature drop in ten years. The fracture model has the smallest fracture aperture which increases heat transfer through conduction from the rock to the fluid in the fracture. Among the porous channel models, the $b = 0.0004L^1$ (Scholz, 2010) case has the most optimistic thermal drawdown prediction. This model has a 40C temperature decline in ten years.

As expected, the model based on tracer data alone gave the most pessimistic temperature drawdown forecast. The temperature drops drastically from 250C to 160C after four months of 150C injection. This demonstrates the value of using more than one data set to constrain the model dimensions further. Coupled analysis of tracer and temperature data sets allows one to obtain a more robust model that can be used to predict future well response more effectively.

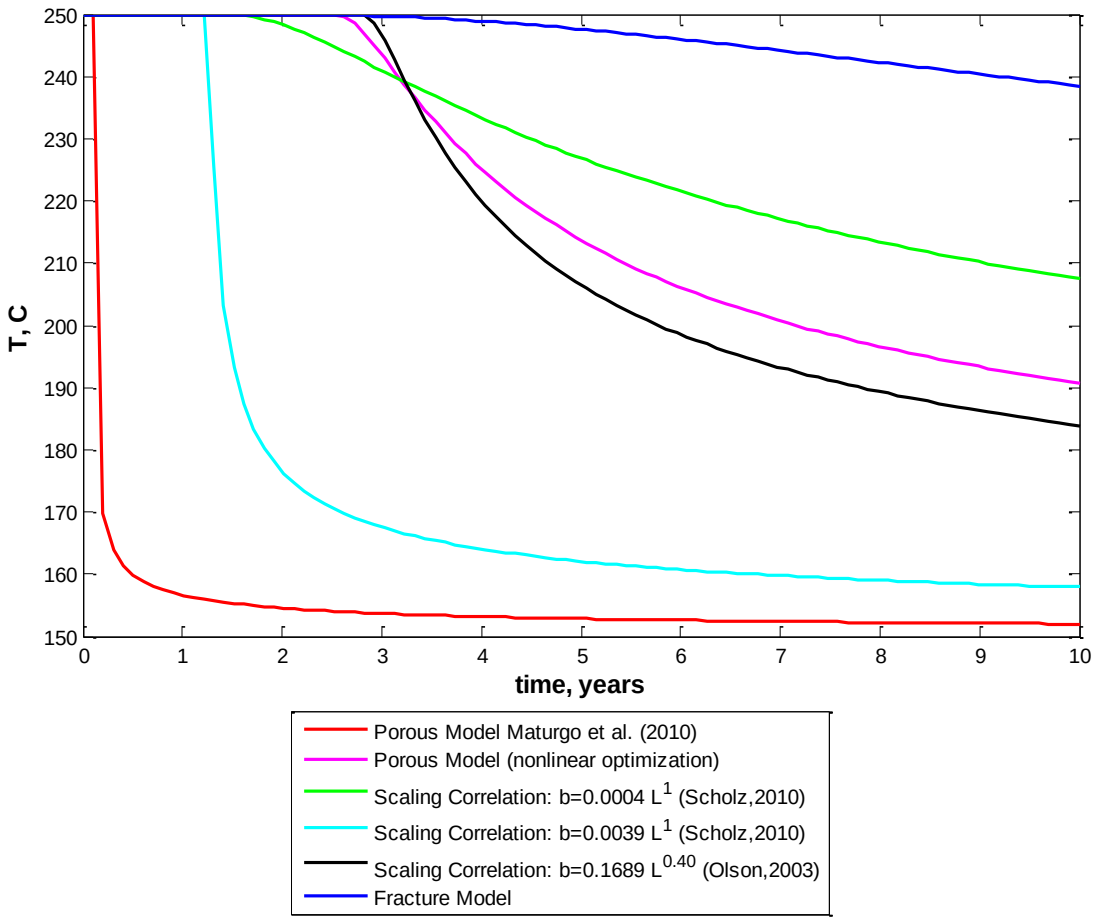

Figure 4.13: Temperature drawdown curves for NJ2RD(Producer)-NJ5D(Injector): low injection case (q=0.020 m^3/s; T_{inj}=150C; T_o=250C).

Figure 4.14 shows the temperature drawdown curve for SG2RD-NJ3D using the different model configurations in this study for the low injection rate case. This plot also includes the tracer-derived model by Maturgo et al. (2010). The low injection rate case has an injection rate (q) of $20\frac{kg}{s}$ or $0.020\frac{m^3}{s}$, injection temperature (T_{inj}) of 150C, and initial reservoir temperature (T_o) of 250C. Dotted lines represent model configurations that use the channel height (H) instead of the channel length (L) for the scaling correlations. Among all the models, the fracture model has the least amount of temperature drop of 4C after ten years of injection. On the other hand, the model derived solely from tracer data (Maturgo et al., 2010) exhibited the fastest temperature decline. This behavior is similar to the observations for the NJ2RD-NJ5D well pair. All the porous models have endpoint temperature predictions within 172C to 190C. For this group, the most pessimistic model is $b = 0.0039L^1$ (Scholz, 2010) because it has the highest aperture value.

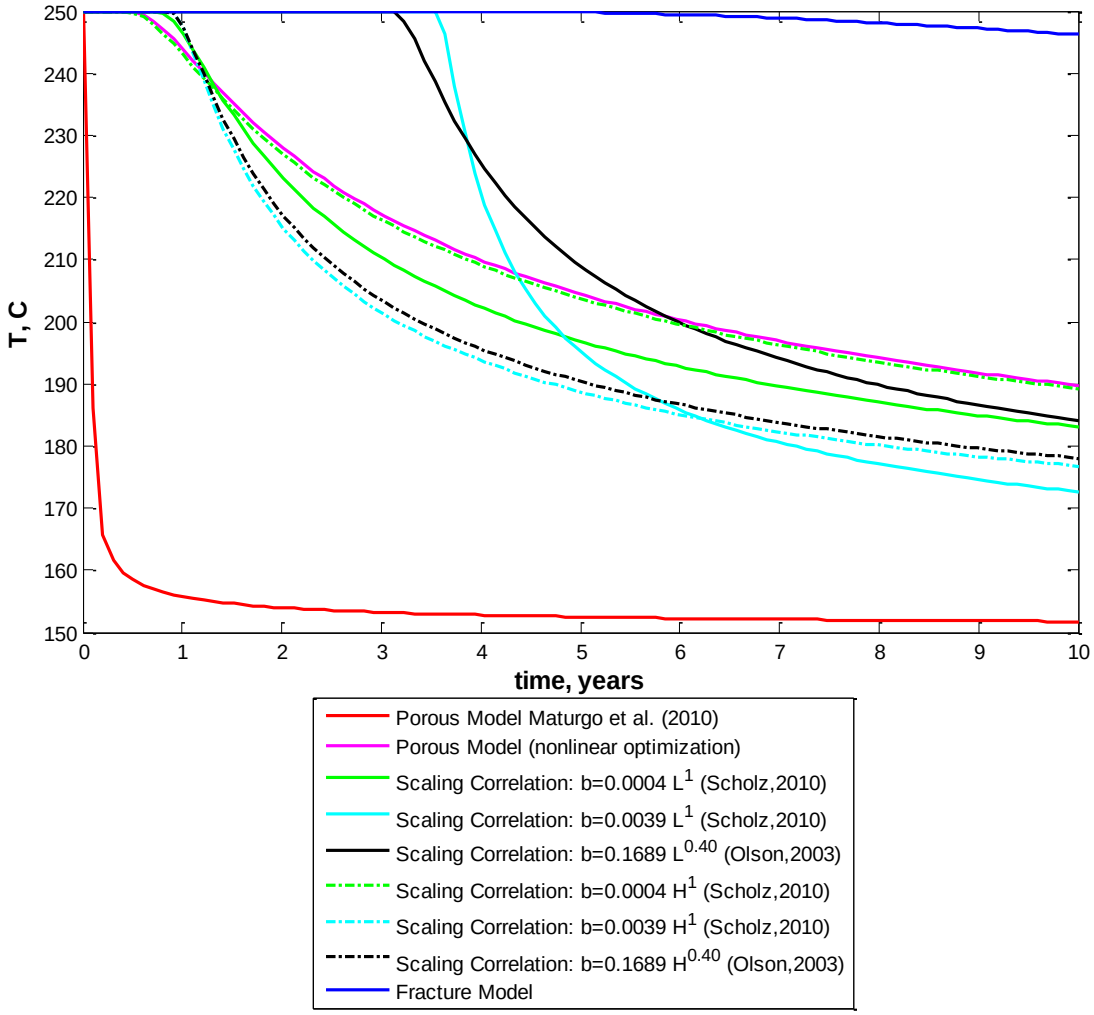

Figure 4.14: Temperature drawdown curves for SG2RD(Producer)-NJ3D(Injector): low injection case(q=0.020 m^3/s; T_{inj}=150C; T_o=250C).

4.5 SCALING CORRELATIONS AND GEOMECHANICS CONCEPTS

4.5.1. Aperture Related Scaling Correlations

Olson (2003) describes the different mechanisms that lead to linear and sublinear scaling of aperture versus length for opening mode cracks. The two most relevant linear elastic fracture mechanics (LEFM) equations are the following:

$$\frac{b_{max}}{L} = \Delta\sigma \frac{2(1-v^2)}{E} = \left[p_f - \sigma_n\right] \frac{2(1-v^2)}{E} \quad \textbf{(4.25)}$$

$$\Delta\sigma = \frac{K_I}{\sqrt{\frac{\pi L}{2}}} \quad (4.26)$$

Equation 4.25 describes the relationship of the aperture (b_{max}) to the fracture length (L) for non-interacting opening mode fractures under plane strain conditions (Pollard and Segall, 1987). The other relevant parameters are: opening mode driving stress ($\Delta\sigma$), Poisson's ratio (v), and Young's modulus (E). Another definition for the driving stress is $\left(p_f - \sigma_n\right)$ where, p_f is the

internal fluid pressure and σ_n is the remote normal compressive stress perpendicular to the crack. Furthermore, the driving stress ($\Delta\sigma$) for a uniformly loaded fracture can be expressed in terms of the stress intensity factor at the crack tip (K_I) and fracture length (L) as shown in Equation 4.26.

$$b_{max} = \Delta\sigma \frac{2(1-\gamma^2)}{E} L = CL \tag{4.27}$$

Linear scaling can be derived from Equation 4.10 assuming a constant driving stress condition (Equation 4.27). Additionally, C is a constant representing material properties and external stress conditions. The possibility of reaching an unstable dynamic crack growth condition increases as the crack propagates. This is because at constant driving stress, the stress intensity factor (K_I) is proportional to the fracture length (L) (Equation 4.26). Moreover, the minimum requirement for crack propagation is for K_I to be equal to the intrinsic fracture toughness of the material (K_{Ic}). Therefore, extensive crack tip branching behavior should be observed where linear scaling is applicable. Olson (2003) states that this is only possible when there is relaxed loading such as after propagation. In contrast, Scholz (2010) argues that this is the predominant mode of scaling based on the reanalysis of data. Calculated (C) values range from 0.1 to 0.001 (Scholz, 2010).

$$b_{max} = \frac{K_{Ic}(1-\gamma^2)}{E\sqrt{\pi/8}} \sqrt{L} \tag{4.28}$$

On the other hand, Olson (2003) claims that sublinear scaling is considered to be the most prevalent mechanism for most geologic conditions. Furthermore, Olson and Schultz (2011) insist that square root scaling provides the best fit for each data set. Sublinear or square root scaling can be derived from the assumption of constant stress intensity factor (K_I) equal to the intrinsic fracture toughness of the material (K_{Ic}) for critical crack propagation as presented in Equation 4.28 (Olson, 2003). Fracture arrest will occur once the internal fluid pressure goes down or the remote stresses are relieved due to propagation. In addition, sublinear scaling can also happen for subcritical crack growth where the rock has less resistance to failure due to corrosive fluids and long-term loading.

$$b_{max} = CL^e \tag{4.29}$$

$$b_{max} = \frac{4}{\pi} b_{measured} \tag{4.30}$$

Fracture data from various fields across multiple length scales (1 cm to 2 km) were fitted to a power law equation (Equation 4.29). The maximum aperture (b_{max}) can be derived from the measured aperture ($b_{measured}$) using Equation 4.30 for an elliptical opening distribution. Here, e was the scaling exponent and C was a constant. Values calculated by Olson (2003) for e ranged from 0.38 to 0.41. The deviation from the predicted exponent value of 0.5 could be due to several other interfering factors. One example of this was the mechanical interaction of multisegment features. Thus, overlapping multisegment fractures would behave like one long fracture. Another was the presence of strata boundaries such that the aperture scales with the fracture height (H) instead of length (L).

Renshaw and Park (1997) examined data from the Krafla fissure swarm in Iceland and observed a break in slope for the aperture (b) versus length (L) when L reaches the maximum value. They postulated that this threshold value was the length at which the smaller apertures were affected by stress perturbations of larger fractures. Superlinear scaling was observed for smaller fractures while linear scaling was observed for larger ones.

Ishibashi et al. (2012) evaluated the scale dependency of various parameters such as: tortuosity, permeability, fraction of area contacted by fluid, and the geometric mean of the aperture. This was done using confined pressure flow experiments and subsequent numerical modeling of sheared versus mated fracture planes in multiple scales (37.5 cm^2, 150 cm^2, and 600 cm^2). These fracture planes were created in a cube of Inada granite from Ibaraki, Japan using a wedge with a shear displacement of 5 mm in the radial direction for the sheared fracture. Their results showed that for the mated fracture, there was a scaling effect only for tortuosity and the mean aperture. On the other hand, sheared fractures planes exhibited sublinear scaling for all the parameters examined except for the fluid contacted area fraction. Moreover, channeling flow within the fracture plane was observed due to a log-normal distribution of aperture within it. Therefore, high aperture connections would be the dominant flow paths such that the contacted area fraction would not depend on the scale. Another important finding of this study was that sheared fractures had calculated permeability values that were three orders of magnitude higher than the equivalent mated one even though the shear displacement was just 5mm. This was consistent with the notion that sheared fracture planes models were more appropriate than opening mode ones for fractures obtained through borehole imaging.

4.5.2. Density Related Scaling Correlations

Density-Aperture Scaling

Statistical analysis of borehole imaging data from the Soultz Geothermal Field revealed an inverse linear scaling of fracture density and mean width across scales ranging from 1 to 1000 cm with a fractal dimension of 1.04 (Massart et al., 2010). Strong clustering was inferred from the low fractal dimension value. This result was consistent with Marrett et al. (1999), which analyzed data sets from natural faults and extension fractures and validated that the data follow power-law scaling in multiple-observational scales. Results from their study showed that the power-law scaling applied across six ranges of scale within reasonable uncertainty limits. Therefore, zones with higher fracture aperture values would have smaller fracture density values. Based on this, regions with fluid entry zones should have lower fracture densities.

Sammis et al. (1991) observed the same behavior at the Geysers Geothermal Field where it was found that fracture patterns in shear zones exhibited fractal geometry. Fracture networks on an outcrop from a freshly cut vertical wall (dm scale) were mapped and analyzed for the fractal dimension using the box counting method. The calculated fractal dimensions had values that ranged from 1.87 to 1.926 (Sammis et al., 1991). Two additional maps from larger scales were analyzed for self-similarity (Sammis et al., 1992). One was from a road-cut outcrop (m scale) and the other was from a regional map of the area (km scale). Density versus fracture length scaling was likewise observed in all length scales. It was observed from core analysis that most of the small fractures were sealed. One conclusion was that transport occurred through large shear fractures.

Damage Zone Fracture Density-Perpendicular Fault Distance Scaling

Fracture density scaling in damage zones of the San Andreas Fault and faults in the Suban Gas Field were investigated by Johri et al. (2012). Image and geophysical logs were used to ascertain properties of the damage zones at depth. It was found that the damage zone fracture density (F) versus perpendicular distance from the fault (r) followed an inverse power-law scaling behavior (Equation 4.31). F_o was the fault constant and n was the fractal dimension. Based on the data, n had values from 0.68 to 1 with an average value of 0.8. This fractal dimension was dependent on the lithology.

$$F = F_o r^{-n} \tag{4.31}$$

Paul et al. (2009) used dynamic-rupture propagation modeling to calculate the scope of damage zone along a fault for the CS field located between Australia and Indonesia. Secondary faults developed were oriented parallel to the major fault with higher dip angles. These faults, therefore, were at an optimal orientation for failure. This meant that they would be conduits for flow as described by Barton et al. (1995). Similar to Johri et al. (2010), this study found that damage intensity decreases with distance from the fault plane. Higher permeability values would be expected in the direction parallel to the strike of the major fault. In contrast, the direction perpendicular to the fault strike would have lower permeability if the fault were sealing due to a well-developed core. This would create field-scale permeability anisotropy that must be taken into account for reservoir simulation as modeled by Paul et al. (2011). Inclusion of fault damage zones in reservoir simulation led to a better history match and the uncertainty in simulation was investigated using multiple equally probable models (Paul et al., 2011).

Figure 4.15 describes the schematic for the parallel network configuration of porous channels to model this anisotropy. An equivalent inverse power-law scaling of the damage zone permeability with distance is shown in Equation 4.32. k_D is the damage zone permeability at a distance (y) away from the fault, k_o is the permeability right outside the core, and k_m is the low fault core permeability. To characterize the field-scale anisotropy, an approximate equivalent permeability for flow in the x ($\overline{k_x}$) and y ($\overline{k_y}$) directions can be derived (Equations 4.33 and 4.34) where, u is the velocity, μ is the fluid viscosity, and p is the pressure. Assuming that c is very small compared to the total width of the damage zone, equivalent parallel (x direction) and series (y direction) permeability values are defined by Equations 4.35 and 4.36, respectively. Expressing these two equations in integral form and substituting the inverse power-law scaling correlation, Equations 4.37 and 4.38 can be derived. For the x direction or flow parallel to the strike of the fault, the permeability increases with damage zone width (W_T) and decreases with core width (c). In addition, the matrix permeability has little effect on the overall permeability because flow in this direction can go through the other more permeable zones. However, flow in the y direction perpendicular to the fault plane exhibits a possible sealing effect when the fault core permeability (k_m) is very small.

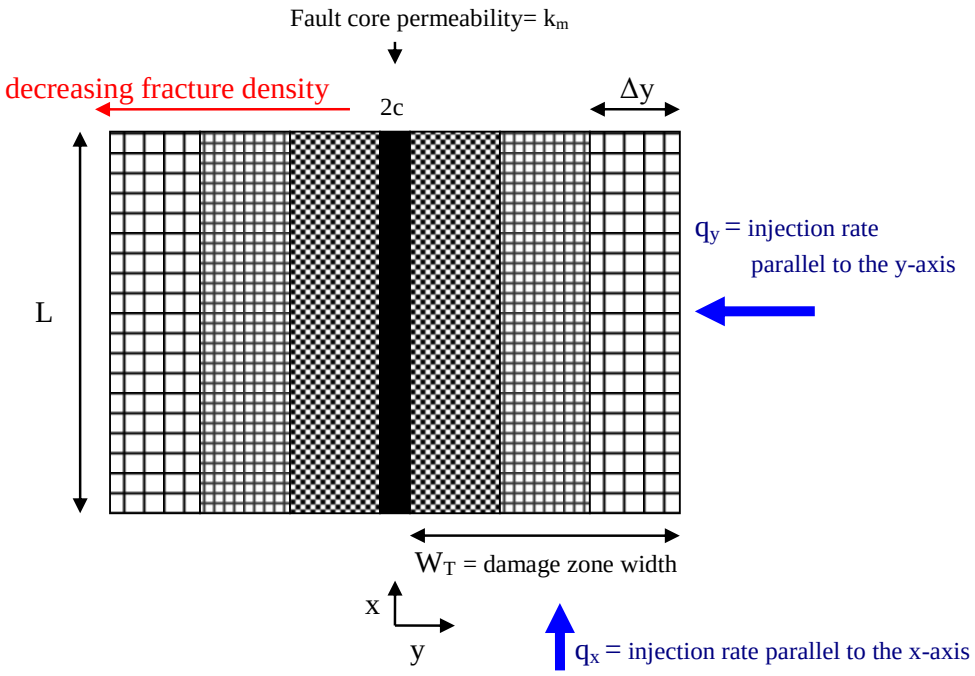

Figure 4.15 Schematic for a fault damage zone model.

$$k_D = k_o y^{-n} \tag{4.32}$$

$$u_x = -\frac{\overline{k_x}}{\mu}\frac{dp}{dx} \tag{4.33}$$

$$u_y = -\frac{\overline{k_y}}{\mu}\frac{dp}{dx} \tag{4.34}$$

$$\overline{k_x} = \frac{2\sum_i k_{f,i}\Delta y_i + 2k_m c}{2\sum_i \Delta y_i + 2c} \tag{4.35}$$

$$\overline{k_y} = \frac{2\sum_i \Delta y_i + 2c}{2\sum_i \frac{\Delta y_i}{k_{f,i}} + 2\frac{c}{k_m}} \tag{4.36}$$

$$\overline{k_x} = \frac{\int_c^{W_T} k_o y^{-n} dy + k_m c}{W_T + c} = \begin{cases} \dfrac{k_o\left(\dfrac{W_T^{1-n} - c^{1-n}}{1-n} + \dfrac{k_m}{k_o}c\right)}{W_T + c} & n \neq 1 \\ \dfrac{k_o\left(\ln\left[\dfrac{W_T}{c}\right] + \dfrac{k_m}{k_o}c\right)}{W_T + c} & n = 1 \end{cases} \tag{4.37}$$

$$\overline{k_y} = \frac{W_T + c}{\int_c^{W_T} \frac{dy}{k_o y^{-n}} + \frac{c}{k_m}} = \frac{k_o (W_T + c)}{\left(\frac{W_T^{1+n} - c^{1+n}}{1+n} + \frac{k_o}{k_m} c \right)} \tag{4.38}$$

4.5.3. Fractal Dimension Determination

Sammis et al. (1991) also observed that fracture patterns in shear zones were self-similar which meant that they could be characterized using fractal geometry. This rendered classical differential equations of transport for non-fractal media as inadequate. Hence, fracture networks on an outcrop from a freshly cut vertical wall (dm scale) were mapped and analyzed for the fractal dimension using the box counting method. Results confirmed self-similarity with the calculated fractal dimensions ranging from 1.87 to 1.926 (Sammis et al., 1991).

On a follow-up study (Sammis et al., 1992), similarity was investigated for other scales by analyzing two additional maps from larger scales. The first was from a road-cut outcrop (m scale) and the other was from a regional map of the area (km scale). Density versus fracture length scaling was observed in all length scales. Core observations were also performed. It was observed that most of the small fractures are sealed so a tentative conclusion was that transport occurs through large shear fractures. Using statistical analysis of the steam zone distributions, it was determined that the spacing of the relevant fractures was between 300 and 900 m (Sammis et al., 1992). Lastly, depths with high rate of penetration (ROP) over short distances in drilling logs were consistent with steam feed zone locations because they represent highly sheared rocks.

Different fractal analysis methods on various scales for two geothermal reservoirs, Germencik and Kizildere, in southwestern Turkey were done by Babadagli (2000). Analysis was done on four scales. Aerial photographs were used for the km scales and the calculated fractal dimensions were 1.575 and 1.583. Similarly, outcrop photos were used for the m scale and fractal dimensions ranged from 1.07 to 2. Furthermore, rock samples were analyzed for the cm scale which resulted to a fractal dimension range of 1.161 to 1.257. Lastly, thin sections were examined for the micrometer scale and the fractal dimension ranged from 1.011 to 1.039. Overall, linear scaling was consistently observed across all scales.

Tateno et al. (1995) studied cores from the Kakkonda geothermal field and also concluded that the fractures can be described by fractals. Another conclusion was that fractal dimensions varied with the fracture type and location due to the difference in fracture formation processes. Calculated fractal dimensions ranged from 0.38 to 0.53.

4.5.4. Critically-Stressed Fault Identification

Equation 4.39 describes the critical shear stress magnitude for frictional sliding of faults using the Coulomb failure criterion (Zoback, 2007). Here, μ is the coefficient of friction along the plane and S is the cohesion. Normal and shear stresses on the plane are σ_N and τ, respectively. P_p is the pore pressure within the fault. Faults are optimally oriented when the stress ratio of shear and effective normal stresses $\left(\tau / \left(\sigma_N - P_p\right)\right)$ is at a maximum. Assuming that there is no cohesion and using a normal faulting regime (applicable to all the field cases in this study), sliding will occur at a critical minimum horizontal compressive stress value ($S_{h\min crit}$) shown in

Equation 4.40. Here, μ is the coefficient of friction of preexisting faults. For conjugate normal faults, the critical stress orientation has a strike parallel to the maximum horizontal principal stress (S_{Hmax}) and a dip of 60 degrees for μ=0.6 (Zoback, 2007).

$$|\tau| = \tau_{crit} = \mu(\sigma_N - P_p) + S \tag{4.39}$$

$$S_{h\min\, crit} = \frac{(S_V - P_p)}{\left((\mu^2 + 1)^{1/2} + \mu\right)^2 + P_p} \tag{4.40}$$

Pore pressure versus depth can be calculated from the water density versus depth logs. Typical values used for μ range from 0.6 to 1.0 (Zoback, 2007; Hickman et al., 1997). The magnitude of the minimum horizontal compressive stress (S_{hmin}) can be determined from the instantaneous shut-in pressure (ISIP) (Hickman et al., 1997; Zoback, 2007). It is the pressure, after the well is shut-in during hydraulic fracture tests, at which the pressure drawdown curve deviates from the initial linear behavior. Contrary to this, the magnitude of S_{Hmax} is harder to obtain. S_{Hmax} values can be constrained using a stress polygon with the following information: presence or absence of wellbore breakouts and tensile fractures; rock strength; and faulting regime (Zoback, 2007). Overburden stress (S_v) can be derived from geophysical density logs and laboratory measurement of surface rock density (Hickman et al., 1997). In terms of orientation, drilling-induced tensile fractures along the borehole wall occur when the stress concentration around the wellbore becomes greater the tensile strength of the rock (Barton et al., 2009). These will propagate parallel to the direction of S_{Hmax} and perpendicular to S_{hmin} (Zoback, 2007; Barton et al., 2009; Hickman et al., 1997).

4.6 CORRELATION OF FRACTURE PROPERTIES AND LITHOLOGY TO PERMEABLE ZONE LOCATIONS

Characterization of fluid flow in fractures is an important area of study in geothermal reservoir engineering. Overall permeability in these reservoirs is fault-dominated (Massart et al., 2010). Relevant fracture parameters to fluid flow are: orientation, aperture, extension, and density. These parameters influence transport and thermal behavior of the reservoir, both in enhanced geothermal systems (EGS) and in conventional hydrothermal systems. Recent advances in borehole imaging technology have made it possible to measure fracture properties with greater accuracy.

For the Wairakei geothermal field, McLean and McNamara (2011) used a high temperature acoustic formation imaging tool (AFIT) to collect fracture data. Confidence, azimuth, and amplitude filters were applied to the data prior to analysis. A borehole televiewer (BHTV) similar to AFIT was used in the Desert Peak EGS project. In addition, formation microscanner (FMS) image logs were utilized (Devatzes, 2009). Published fracture data from various geothermal fields were collected and analyzed. Data sets examined for this study were fracture aperture, density, and orientation. These were then compared to locations of feed zones to determine their correlation with fluid flow properties.

4.6.1 Fracture Aperture

Fracture data from the various geothermal fields showed consistent correspondence between fracture apertures and feed zone locations for most of the data points. In Wairakei, fracture apertures for the feed zones ranged from 10 to 60 cm in wells WK-404, WK-318, and WK-407 (McLean and McNamara, 2011) as shown in Figures 4.16 to 4.18. Moreover, it was found that the narrower azimuth filter yielded a better match of large fractures to permeable zones. There were some cases, however, where the depths of the permeable zones from completions testing did not align perfectly with the large aperture fractures. Minor depth discrepancies can be attributed to wireline stretching and slight depth measurement errors between logging runs.

A similar trend was observed from the Desert Peak data. Collected data included the following: permeable zone locations, PTS data, and fracture apertures from borehole imaging data. Because the injection rate used was small and the well diameter was large, spinner data could not be interpreted (Devatzes and Hickman, 2009). Thus, temperature gradient anomalies were used to identify permeable zones. Data for well 27-15 (Figure 4.19) had aperture values from 1 to 10 cm at fluid entry zones (Devatzes and Hickman, 2009).

There are two possible explanations for this observation. Using a parallel-plate model, fracture permeability is proportional to b^2, where b is the fracture aperture (Jourde et al., 2002). Fluid entry, associated to fractures in geothermal reservoirs, occurs at depths with high permeability. Therefore, permeable zone locations will be at depths with high apertures. Another rationale is the power-law scaling between joint length and width described by Scholz (2010). He argues that for opening mode in rocks, fracture toughness scales linearly with $\sqrt{L}$ and b scales linearly with L, where L is the length. Therefore, a larger fracture width will correspond to a longer fracture which implies a farther reach for the fluid source.

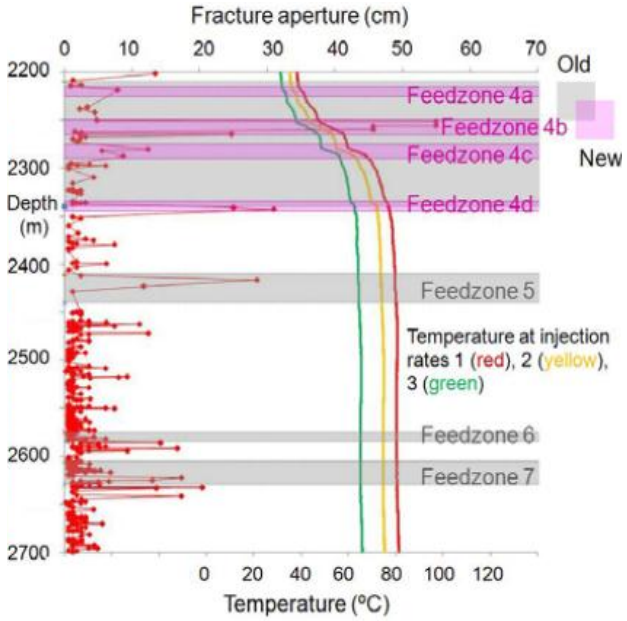

Figure 4.16 Fracture aperture (red) and temperature versus depth for well WK-404 in the Wairakei Geothermal Field (McLean and McNamara, 2011)

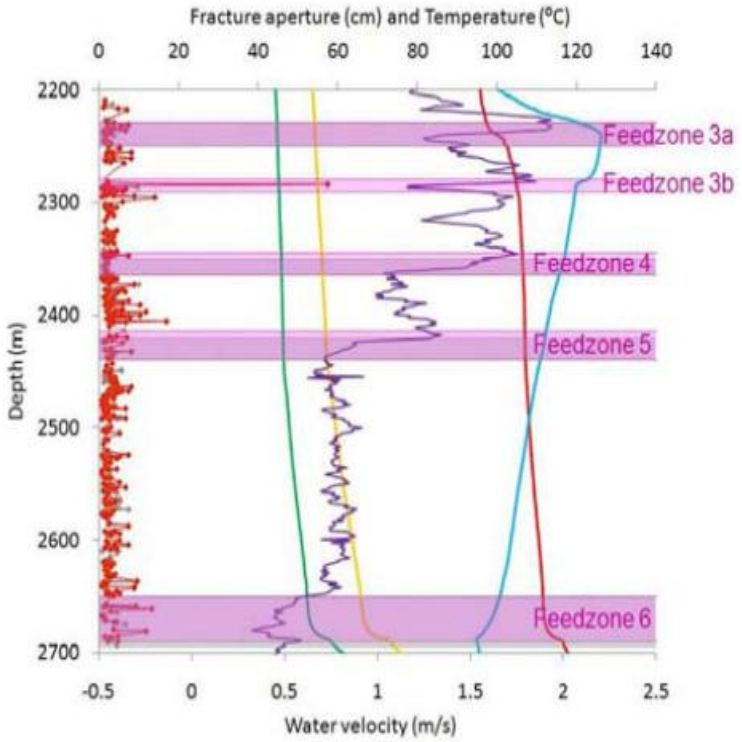

Figure 4.17 Fracture aperture (red), temperature, and spinner velocity (blue) versus depth log for well WK-317 in the Wairakei Geothermal Field (McLean and McNamara, 2011)

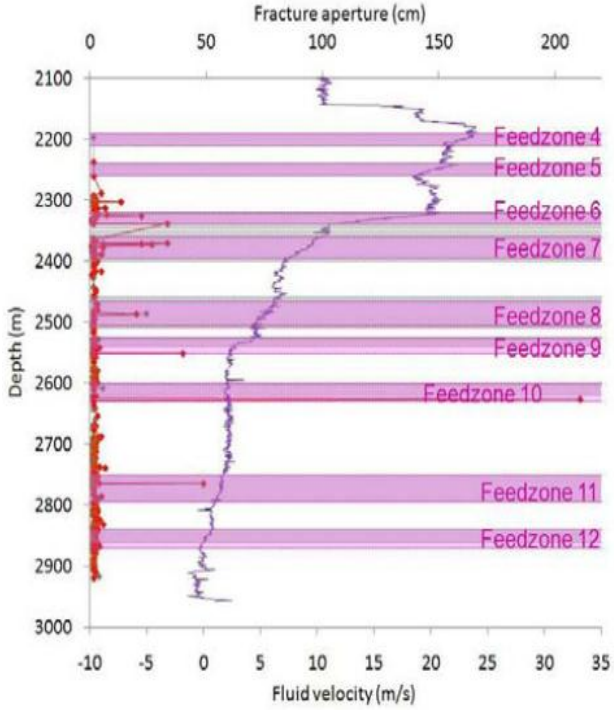

Figure 4.18 Aperture (red) and spinner velocity (blue) versus depth log for well WK-407 in the Wairakei Geothermal Field (McLean and McNamara, 2011)

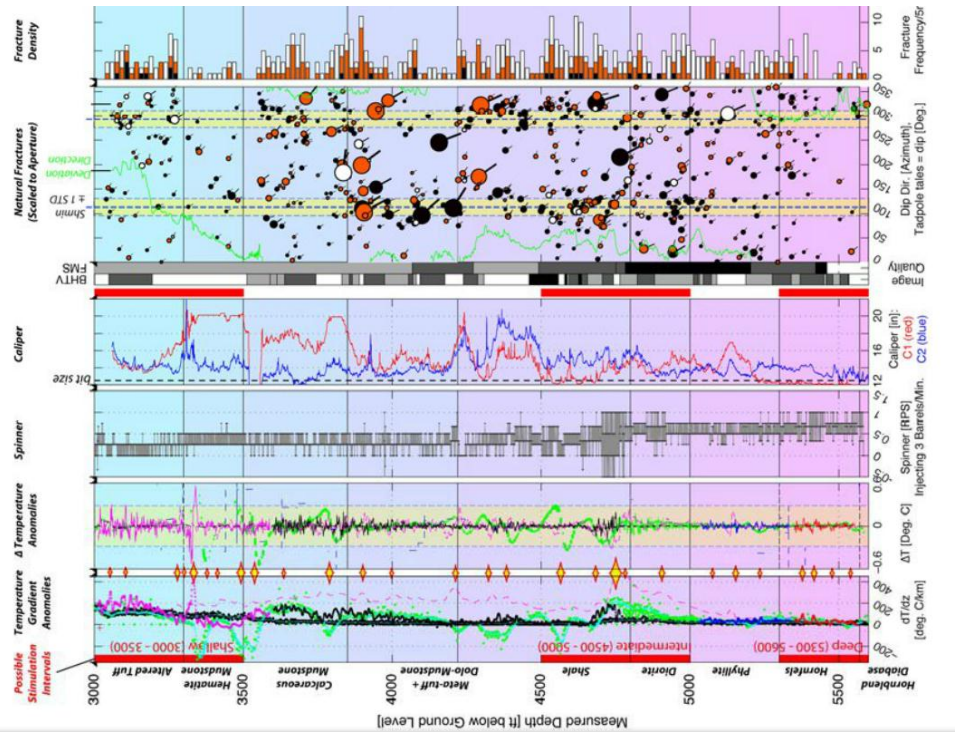

Figure 4.19 Well Log data for well 27-15 in the Desert Peak Geothermal Field, Nevada. Yellow diamonds indicate feed zones derived from temperature anomalies and spinner velocities (Devatzes and Hickman, 2009)

4.6.2 Fracture Orientation

For the Wairakei Geothermal Field (McLean and McNamara, 2011), two additional azimuth filters were employed to include only fractures at optimal orientations. Here, structures were controlled by normal faulting so the optimal fault orientation was parallel or subparallel to S_{Hmax}. Based on the direction of drilling induced tensile fractures, the S_{Hmax} orientation ranged from 035 to 045 degrees strike. Azimuth filters utilized were 45 degrees and 30 degrees from this S_{Hmax} direction. This filtering narrowed the fault orientations to those that were critically-stressed in the current stress regime and would therefore be most likely slip. Permeable zones in this study followed the dominant S_{Hmax} direction within 30 degrees with steep average dips ranging from 66 to 84 degrees.

Hickman et al. (1997) investigated the relationship between permeable zones from temperature gradient anomalies and fracture properties from borehole imaging for the Dixie Valley Geothermal Field. The S_{Hmax} direction was N33^{o}E which was subparallel to the Stillwater fault. It was ascertained that most of the hydraulically conductive faults were critically-stressed and optimally-oriented with respect to the current stress field striking northeast with varying dips ranging from 15 to 70 degrees. Furthermore, spinner logs showed that only six fractures dominated fluid flow in well 73B-7 and they occurred at a narrow depth range of 2.5 to 2.7 km. Isolated spinner flow meter and pressure logs at two depths (2.614 and 2.637 km) revealed high permeability values of 21 and 48 darcys, respectively. These were inferred to be part of the damage zone of the Stillwater fault. A follow-up study by Barton et al. (1998) used the same analysis for six wells to compare the orientations of fractures in productive and nonproductive

geothermal wells. Hydraulically conductive fractures for good producers and segments of the Stillwater fault zone were critically-stressed. On the other hand, hydraulically conductive faults of poor producers were below the Coulomb failure line for μ=0.6 in the Mohr circle.

A similar analysis was done for well 27-15 from the Desert Peak Geothermal Field which was a candidate for hydraulic fracturing (Devatzes and Hickman, 2009; Hickman and Devatzes, 2010). The azimuth of S_{hmin} was 114 ± 17^o which was consistent with the E-SE and W-NW striking orientation of the Rhyolite Ridge normal fault zone in the area with a stress magnitude of 1995 ± 60 psi. However, normal faulting regime in the well was not confirmed but was assumed based on the regional stress regimes. Hydraulic fracturing was planned for intervals that had a significant number of critically-stressed faults.

A previous study on the Cajon Pass scientific drill hole data demonstrated that optimally oriented faults control the overall permeability for reservoirs with low rock matrix permeability such as granite (Barton et al., 1995). Additionally, it was found that relatively few fracture planes dominated flow. Several reasons were given by various studies to explain this correlation for brittle rocks. First, the permeability increase in critically-stressed faults was due to brecciation and damage formation (Zoback, 2007). Second, dilatancy of sheared fracture planes from pore-volume expansion of microcracks would improve both porosity and permeability along the plane (Barton et al., 1995). Third, majority of geologic process such as precipitation, cementation, pressure solution formation, and mineral alteration led to fracture closure. Hence, slip would be needed to keep fractures open (Zoback, 2007; Hickman et al., 1997).

4.6.3 Fracture Density

McLean and McNamara (2011), in their investigation of data from the Wairakei Geothermal Field, concluded that there was no correlation observed for fracture density and permeable zone depths. However, the number of interpreted fractures was highly dependent on the image quality. The same problem was encountered for the data of well 27-15 of the Desert Peak Geothermal Field as shown in Figure 4.9 (Devatzes and Hickman, 2009). No direct correspondence between fracture density and permeable zones locations was observed. Thus, this lack of correlation implied that fracture density was not an effective indicator of permeable zones because it was extremely difficult to obtain good quality image logs in highly fractured reservoirs. Another issue was the overlapping of fractures which led to two interpretations. First, a large fracture aperture reading could be made when overlapping fractures have consistent orientations. Second, the whole fracture set could be discarded in confidence filtering of the data because the aggregate set would not exhibit the typical sinusoidal shape that was expected. Thus, a high aperture fracture plane could also be interpreted as a high density cluster of fractures with smaller apertures. Therefore, both high density and high aperture values could be used to identify permeable zones. Other possible sources of errors were data binning inaccuracies and tool measurement uncertainties.

4.6.4 Lithology

Glynn-Morris et al. (2011) investigated the characteristics of feed zones of wells in the Wairakei and Tauhara Geothermal Fields in New Zealand. They sought to evaluate whether the permeability was derived from lithology or structures. Feedzone locations were identified from PTS logs and completions tests. The characteristic signature of primary permeability from

lithology was a diffuse change in temperature with depth. In contrast, structurally based secondary permeability demonstrated sharp variations in PTS logs. Other measured properties from drilled cores included the following: lithology, rock-quality designation (RQD), core recovery factor, loss circulation zones, porosity, smectite presence, rock strength, and core photos. It was concluded that secondary permeability from structures becomes more important as the feed zone depth increases (Glynn-Morris et al., 2011; McLean and McNamara, 2011).

Permeable zones for well 27-15 in the Desert Peak Geothermal Field exhibited some correlation among temperature anomaly locations, stratigraphic boundaries, and mineral content (Devatzes and Hickman, 2009). One significant feed zone at 4720 ft MD was found just above the boundary between a shale and diorite region. Aside from this, increased illite-chlorite and quartz alteration were observed at this section. Data from the Soultz Geothermal Field study found that there was high potassium content due to granite alteration in high permeability regions (Sausse et al., 2008). This was claimed to be due to the dissolution of minerals as the fluid flows through the rock matrix thereby increasing the permeability and porosity even further. These altered granite zones represented high conductivity but channelized flow paths as seen in the depth where well GPK3 intersected the fault zone. Lower degrees of alteration, however, resulted to a higher number of low conductivity paths which resulted to poor well performance such as in the case of GPK4.

Massart et al. (2010) describes the fault geometry encountered in Soultz. Figure 4.20 shows the lithofacies and equivalent porosity of the different zones within a major fault that intersects all three wells (GPK1, GPK2, and GPK3). Three main zones are present within this fault. First, there is a fault core in the middle containing quartz which has the lowest porosity. Second, there are cataclased and brecciated granite zones due to shearing of the fault. Third, hydrothermally altered granite zones have high porosity and serve as main conduits for flow equivalent to 75% of the total. The decreasing porosity with distance of the outermost altered zone is consistent with the inverse fracture density scaling with distance finding of Johri et al. (2012). Furthermore, owing to the symmetry and consistency of the rock properties within each zone, these could be represented by a parallel network of porous channels satisfying tracer and temperature analytical equations derived.

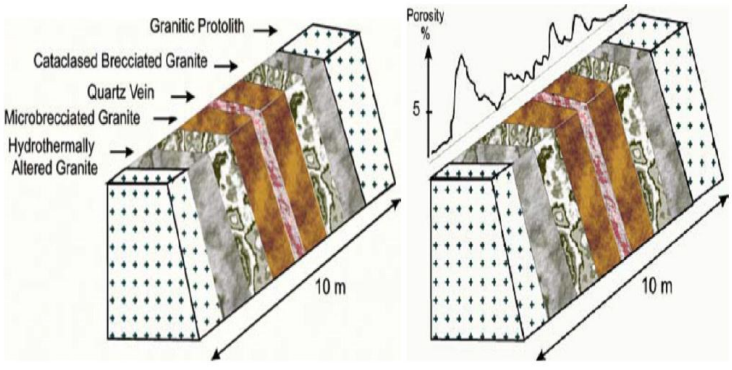

Figure 4.20. Zonation and porosity schematic of a hydrothermally altered fault zone at Soultz (from Massart et al., 2010).

On the other hand, steam production at The Geysers geothermal field was attributed to a network of fractures within a wide shear zone bounded by the right lateral Maacama and Collayomi Fault zones (Sammis et al., 1991). Steam feed zones were observed to occur in a few major fractures hosted in a relatively impermeable greywacke rock. Because steam feed zones were typically observed at shallow depths, this result contradicted the observations of the previous study discussed where shallow feed zones were attributed to lithology and not structures.

4.7 FUTURE WORK

The relationship between scaling properties and heat and mass transport should be investigated further. Analytical models for tracer and heat transport incorporating scaling correlations of aperture and length could be derived. Uncertainty analysis on scaling parameters and borehole imaging data for analytical models should be explored.

The long-term goal is to generate fracture networks using scaling properties and use this in reservoir simulation.

5. REFERENCES

Alaskar, M., Ames, M., Horne, R.N., Li, K., Connor, S. and Cui, Y.: "In-situ Multifuction Nanosensors for Fractured Reservoir Characterization," Geothermal Resources Council Annual Meeting, Sacramento, USA, vol. 34 (2010).

Alaskar, M., Ames, M., Liu, C., Connor, C., Horne, R.N., Li, K. and Cui, Y.: "Smart Nanosensors for In-situ Temperature Measurement in Fractured Geothermal Reservoir," Transactions, Annual Meeting of the Geothermal Resources Council, San Diego, California, Vol. 35, 2011.

Albertoni, A., and Lake, L.: SPE 75225: Inferring Interwell Connectivity From Well-Rate Fluctuations in Waterfloods. *SPE/DOE Improved Oil Recovery Symposium*. Society of Petroleum Engineers, (2002).

Alkafeef, S.F., Gochin, R.J., and Smith, A.L. (1991), Measurement of the electrokinetic potential at reservoir rock surfaces avoiding the effect of surface conductivity, *Particles and Surf.*, **159**, 263–270.

Alshehri, A., (2009). Low Tension Methods for Fractured Resources. MS thesis, Stanford University.

Archie, G.E., The Electrical Resistivity Log as an Aid in Determining some Reservoir Characteristics, *Transaction of the American Institute of Mining, Metallurgical and Petroleum Engineers*, **146**, (1942), 54-62.

Auset M, Keller AA. Pore-scale processes that control dispersion of bioparticles in saturated porous media. *Water Resour. Res.* 2004; **40**(3): W03503. doi:10.1029/2003WR002800.

Babadagli, T.: "Evaluation of outcrop fracture patterns of geothermal reservoirs in southwestern Turkey," *Proceedings,* World Geothermal Congress. 2000.

Bales, R. C., C. P. Gerba, G. H. Grondin, and S. L. Jensen (1989), Bacteriophage transport in sandy soil and fractured tuff, *Appl. Environ. Microbiol*., **55**, 2061– 2067.

Barelli, A., Cappetti, G., and Stefani, G.: Exploitation Strategy at Laderello Valle Secolo. *World Geothermal Congress* International Geothermal Association, (1995).

Barton, C.A., Hickman, S., Morin, R., Zoback, M.D., Benoit, D.: "Reservoir-scale fracture permeability in the Dixie Valley, Nevada, geothermal field," *Proceedings,* 23th workshop on Geothermal Reservoir Engineering, Stanford University. 1998.

Barton, C.A., Moos, D., and Tezuka, K.: "Geomechanical wellbore imaging: implications for reservoir fracture permeability," *AAPG Bulletin,* v. 93, no. 11. 2009, 1551-1569.

Barton, C.A. and Zoback, M.D.: "Self-similar distribution and properties of macroscopic fractures at depth in crystalline rock in the Cajon Pass scientific drill hole," *Journal of Geophysical Research,* v.97, no. B4, 1992. 5181-5200.

Barton, C.A., Zoback, M.D., and Moos, D.: "Fluid flow along potentially active faults in crystalline rocks," *Geology,* v.23. 1995, 683-686.

Baumann T, Werth CJ. Visualization and modeling of polystyrol particle transport in a silicon micromodel. *Vadose Zone J*., 2004; 3:434–43.

Bayon, F.E.B. and Ogena, M.S.: "Handling the problem of rapid reinjection returns in Palinpinon-I and Tongonan, Philippines," *Proceedings,* World Geothermal Congress. 2005.

Beal, J.J., Adams, M.C. and Hrtz, P.N., R-13 Tracing of Injection in The Geysers, Geothermal Resources Council, 18, (1994), 151-159.

Bear, J.: *Dynamics of fluids in porous media,* Dover, (1972).

Bennett, K., and Horne, R. N.: Power Generation Potential from Coproduced Fluids in the Los Angeles Basin, *Geothermal Resources Council*, San Diego, (2011).

Bergendahl, J., Grasso, D., 1999. Prediction of particle detachment in a model porous media: thermodynamics. *AIChE J*. **45** (3), 475–484.

Bergendahl, J., Grasso, D., 2000. Prediction of particle detachment in a model porous media: hydrodynamics. *Chem. Eng. Sci.* **55**, 1523–1532.

Bodvarsson, G.: "Thermal problems in the siting of reinjection wells," *Geothermics,* v. 1, no. 1. 1972, 63-66.

Bodvarsson, G., and Pruess, K.: Thermal effects of reinjection in geothermal reservoirs with major vertical fractures. *Journal of Petroleum Technology*, *36*(9), Society of Petroleum Engineers (1984).

Bogush, G. H., Tracy, M. A., and Zukoski, C. F., IV: "Preparation of Monodisperse Silica Particles: Control of Size and Mass Fraction," *Non-Cryst. Solids* **104** (1988) 95.

Bradford, S. A., J. Simu°nek, M. Bettahar, M. Th. van Genuchten, and S. R. Yates (2006), Significance of straining in particle deposition: Evidence and implications, *Water Resour. Res*., **42**, W12S15, doi:10.1029/2005 WR004791.

Bradford, S. A., S. Torkzaban, and S. L. Walker (2007), Coupling of physical and chemical mechanisms of particle straining in saturated porous media, *Water Resour. Res.*, **41**, 3012–3024.

Bradford, S.A., Yates, S.R., Bettahar, M., Simunek, J., 2002. Physical factors affecting the transport and fate of particles in saturated porous media. *Water Resour. Res*. **38**, 1327 (12).

Buckley, J.S. (1991): "Multiphase Displacements in Micromodels," *Interfacial Phenomena in Petroleum Recovery*, Morrow, N.R. (ed.), Marcel Dekker Inc., New York, NY, 157-189.

Bullivant, D.P. and O'Sullivan, M.J.: "Some simple models of tracer tests," *Proceedings,* 7th New Zealand Geothermal Workshop. 1985.

Cardoso, M. A., Durlofsky, L. J., and Sarma, P.: Development and application of reduced-order modeling procedures for subsurface flow simulation, *International Journal for Numerical Methods in Engineering*, *77*(9), (2009).

Champ, D.R., Schroeter, J., 1988. Bacterial transport in fractured rock—a field-scale tracer test at the Chalk River Nuclear Laboratories. *Water Sci. Technol*. **20**, 81–87.

Chen, H., Li, Z., Wu, Z. and Zhang, Z.: "A novel route to prepare and characterize Sn-Bi nanoparticles," *Journal of Alloys and Compounds*. 2005, **394**, 282-285.

Churcher, P.L., French, P.R., Shaw, J.C., and Schramm, L.L., "Rock Properties of Berea Sandstone, Baker Dolomite, and Indiana Limestone." Published in Proceedings from the SPE International Symposium on Oilfield Chemistry, Anaheim, California. SPE Paper No. 21044, (1991).

Chrysikopoulos, C. V. (1993), Artificial Tracers for Geothermal Reservoir Studies, *Environmental Geology*, 22(1), 60-70.

Co, C.K.D. and Horne, R.N.: "Characterization of Geothermal Interwell Connectivity Using Thermal and Tracer Data," *GRC Transactions*. 2011, 1411-1416.

Connor, Steve. <stconnor1@gmail.com> (2010, March 11). [Personal email].

Crain, E.R.: Crain's Petrophysical Handbook. Web 17 November 2010. www.spec2000.net

Cumbie, D. H., and L. D. McKay. "Influence of Diameter on Particle Transport in a Fractured Shale Saprolite." *Journal of Contaminant Hydrology* **37** (1998): 139-57.

Derjaguin, B.V., Landau, L.D., 1941. Theory of the stability of strongly charged lyophobic sols and of the adhesion of strongly charged particles in solutions of electrolytes. *Acta Physicochim. USSR* **14**, 733–762.

Devatzes, N.C. and Hickman, S.H.: "Fractures, stress, and fluid flow prior to stimulation of well 27-15, Desert Peak, Nevada, EGS project," *Proceedings*, 34th workshop on Geothermal Reservoir Engineering, Stanford University. 2009.

Devatzes, N.C. and Hickman, S.H.: "In-situ stress and fracture characterization for planning of an EGS stimulation in the Desert Peak Geothermal Field, Nevada," *Proceedings*, 35th workshop on Geothermal Reservoir Engineering, Stanford University. 2010.

Dey, A. and Morrison, H.F.: Resistivity Modeling for Arbitrarily Shaped Two-Dimensional Structures, Geophysical Prospecting 27, I06-I36, University of California, Berkeley, CA (1979).

DHI-WASY.: *FEFLOW 6: User Manual*, Berlin, (2010).

Dinh, A. V.: *Interwell Connectivity Tests in Waterflood Systems*. University of Oklahoma, (2009).

Dong, H., T. C. Onstott, C.-H. Ko, A. D. Hollingsworth, D. G. Brown, and B. J. Mailloux (2002), Theoretical prediction of collision efficiency between adhesion-deficient bacteria and sediment grain surface, *Particle Surf. B: Biointerfaces*, **24**, 229–245.

Echeverria Ciaurri, D., Isebor, O. J., and Durlofsky, L. J.: Application of derivative-free methodologies to generally constrained oil production optimisation problems.

International Journal of Mathematical Modelling and Numerical Optimisation, *2*(2), Inderscience, (2011).

Elimelech, M., J. Gregory, X. Jia, and R. A. Williams (1995), in *Particle Deposition & Aggregation Measurement, Modeling and Simulation*, Butterworth-Heinemann, Woburn, MA.

Fukuda, D., Akatsuka, T., and Sarudate, M: "Characterization of inter-well connectivity using alcohol tracer and steam geochemistry in the Matsukawa vapor-dominated geothermal field, Northeast Japan," *GRC Transactions*. 2006, 797-801.

Ganefianto, N., Stimac, J., Azwar, L. S., Pasikki, R., Parini, M., Shidartha, E., Joeristanto, A., et al.: Optimizing Production at Salak Geothermal Field, Indonesia, Through Injection Management. *World Geothermal Congress*, (2010).

Garg, S.K., Pritchett, J.W., Wannamaker, P.E. and Combs, J., Characterization of Geothermal Reservoirs with Electrical Surveys: Beowawe geothermal field, *Geothermics*, **36**, (2007), 487-517.

Gentier, Sylvie, Xavier Rachez, Tien Dung Tran Ngoc, Mariane Peter-Borie, and Christine Souque.: "3D Flow Modelling of the Medium-Term Circulation Test Performed in the Deep Geothermal Site of Soultz-Sous-forets (France)." Proc. of World Geothermal Congress 2010, Bali, Indonesia.

Glynn-Morris, T., McLean, K., and Brockbank, K.: "Characterizing feed zones in geothermal fields: integrated learnings from completion testing, image logs and continuous core," *Proceedings*, New Zealand Geothermal Workshop. 2011.

Grabbe, A.; Horn, R. G. *J. Particle Interface Sci.*, 1993, **157**, 375.

Gregory, J., 1981. Approximate expression for retarded van der Waals interaction. *J. Particle Interface Sci.* **83**, 138–145.

Gringarten, A.C. and Sauty, J. P.: "A theoretical study of heat extraction from aquifers with uniform regional flow," *Journal of Geophysical Research*. 1975, 4956-4952.

Gringarten, A.C., Witherspoon, P.A., and Ohnishi, Y.: "Theory of heat extraction from fractured hot dry rock," *Journal of Geophysical Research*. 1975, 1120-1124.

Happel, J. AIChE J. 1958, 4, 197-201.

Harter T, Wagner S, Atwill ER. Bioparticle transport and filtration of Cryptosporidium parvum in sandy soils and aquifer sediments. *Environ Sci Technol* 2000; **34**(1): 62–70.

Harvey, R. W., N. E. Kinner, D. MacDonald, D. W. Metge, and A. Bunn (1993), Role of physical heterogeneity in the interpretation of small-scale laboratory and field observations of bacteria, microbial-sized microsphere, and bromide transport through aquifer sediments, *Water Resour. Res.*, **29**, 2713– 2721.

Hickman, S.H., Barton, C.A., Zoback, M.D., Morrin, R., Sass, J., and Benoit, R.: "In-situ stress and fracture permeability along the Stillwater fault zone, Dixie Valley, Nevada," *Int. J. Rock Mech. & Min. Sci.*, 34:3-4, Paper No. 126. 1997.

Hogg, R., Healy, T.W., Fuerstenau, D.W., 1966. Mutual coagulation of particle dispersions. *Trans. Faraday Soc*. **62**, 1638–1651.

Holland, J.H.: Adaptation in Natural and Artificial Systems, *Ann Arbor*, University of Michigan Press, **54**, (1975).

Hornbrook J., (1991). Visualization of Foam/Oil Interactions in a New, High Resolution Sandstone Replica Micromodel. MS thesis, Stanford University

Horne, R.N.. Effects of Water Injection into Fractured Geothermal Reservoirs: a Summary of Experience Worldwide, Geothermal Resources Council, Davis, CA, 12, (1982), 47–63.

Horne, R.N.: "Reservoir Engineering of Reinjection," Course Notes. Stanford University, 1996.

Inwood, S., (2008). High-Resolution Microvisual Study of High Mobility Ratio, Immiscible Displacements. MS thesis, Stanford University

Ishibashi, T., Watanabe, N., Hirano, N., Okamoto, A., and Tsuchiya, N.: "Experimental and numerical evaluation of channeling flow in fractured type of geothermal reservoir," *Proceedings*, 37th workshop on Geothermal Reservoir Engineering, Stanford University. 2012.

Israelachvili, J., *Intermolecular and Surface Forces*. 2nd ed.; Academic Press: London, 1992; p 480.

Jansen, J.: Adjoint-based optimization of multi-phase flow through porous media - A review. *Computers and Fluids*, *46*(1), 40–51, Elsevier, (2011).

Johnson, P. R., and M. Elimelech (1995), Dynamics of particle deposition in porous media: Blocking based on random sequential adsorption, *Langmuir*, **11**, 801–812.

Johri, M., Zoback, M.D., and Hennings, P.: "Observationsof fault damage zones at reservoir depths," *Proceedings*, 45th US Rock Mechanics / Geomechanics Symposium, American Rock Mechanics Association. 2012.

Jourde, H., Flodin, E.A., Aydin, A., Durlofsky, L.J., Wen, X.H.: "Computing permeability of fault zones in eolian sandstone from outcrop measurements," *American Association of Petroleum Geologists Bulletin*. 2002.

Juliusson, E.: Characterization of Fractured Geothermal Reservoirs based on Production Data, *Ph.D. Thesis*, Stanford University, (2012).

Juliusson, E, and Horne, R.N.: Fracture Characterization using Production and Injection Data, *DOE Quarterly Report (2009 January to March), Contract DE-FG36-08GO18182*, (2009), 1-17.

Juliusson, E, and Horne, R.N.: Study and Simulation of Tracer and Thermal Transport in Fractured Reservoirs, *Proceedings*, 35th Workshop on Geothermal Reservoir Engineering, Stanford University, Stanford, CA (2010).

Juliusson, E., and Horne, R.N.: "Analyzing Tracer Tests During Variable Flow Rate Injection and Production," Proc. of Thirty-Sixth Workshop on Geothermal Reservoir Engineering, Stanford University, Stanford, CA. 2011.

Juliusson, E., and Horne, R. N.: Optimization of Reinjection Scheduling in Fractured Reservoirs based on Tracer Tests. *Geothermal Resources Council*, San Diego, (2011).

Juliusson, E., Horne, R. N., Sweeney, J., Hart, M., Rich, J., and Sandler, J.: Optimal Extraction of Geothermal Resources, *Geothermal Resources Council*. San Diego, (2011).

Kanj, M., Funk, J., and Al-Yousif, Z.: "Nanofluid Coreflood Experiments in the Arab-D," SPE paper 126161, presented at the 2009 SPE Saudi Arabia Technical Symposium and Exhibition held in Saudi Arabia, Alkhobar, May 09-11.

Karimi-Fard, M., Durlofsky, L.J. and Aziz, K.: An Efficient Discrete Fracture Model Applicable for General Purpose Reservoir Simulators, SPE 79699, SPE Reservoir Simulation Symposium, Houston, TX (2003).

Keller A. A., Auset M. A review of visualization techniques of biocolloid transport processes at the pore scale under saturated and unsaturated conditions. Advanced *Water Resour. Res*., 2006; **30**, 1392-1407, doi:10.1016/j.advwatres.2006.05.013.

Keller, A. A., S. Sirivithayapakorn, and C. Chrysikopoulos (2004), Early breakthrough of particles and bacteriophage MS2 in a water-saturated sand column, *Water Resour. Res.*, **40**, W08304, doi:10.1029/2003WR002676.

Kennelly, AE. The equivalence of triangles and three-pointed stars in conducting networks, *Electrical World and Engineer*, **34**, (1899), 413-414.

Kim, D., Jeong, S. and Moon, J.: "Synthesis of sliver nanoparticles using the polyol process and the influence of precursor injection," *Nanotechnology* **17** (2006), 4019-4024.

Kocabas, I.: Geothermal reservoir characterization via thermal injection backflow and interwell tracer testing. *Geothermics*, *34*(1), (2005).

Kreft, A. and Zuber, A..: "On the physical meaning of the dispersion equation and its solutions for different initial and boundary conditions," *Chemical Engineering Science*. 1978, **33**(11), 1471–1480.

Kretzschmar, R., Barmettler, K., Grolimun, D., Yan, Y.D., Borkovec, M., Sticher, H., 1997. Experimental determination of particle deposition rates and collision efficiencies in natural porous media. *Water Resour. Res*. **33** (5), 1129–1137.

Krige, D.G., A Statistical Approach to some Basic Mine Valuation Problems on the Witwatersrand, *Journal of the Chemical, Metallurgical and Mining Society of South Africa*, **52 (6)**, (1951), 119-139.

Lauwerier, H.A.: "The Transport of Heat in an Oil Layer Caused by the Injection of Hot Fluid," *Applied. Scientific Research*, **5**(2-3). 1955, 145-150.

Lee, K. H.: Investigating Statistical Modeling Approaches for Reservoir Characterization in Waterfloods from Rates Fluctuations, *Ph.D. Thesis*, University of Southern California, (2010).

Liang, X., Lake, L., Edgar, T., Al-Yousef, A., Sayarpour, M., and Weber, D.: SPE 107713: Optimization of Oil Production Based on a Capacitance Model of Production and Injection Rates, *Proceedings of Hydrocarbon Economics and Evaluation Symposium*, Society of Petroleum Engineers, (2007).

Lovekin, J., and Horne, R. N.: Optimization of injection scheduling in geothermal fields. *DOE Research and Development for the Geothermal Marketplace, Proceedings of the Geothermal Program Review VII*, (1989).

Lu, Yu, Yin, Yadong, Mayers, Brian T., and Xia, Younan: "Modifying the Surface Properties of Superparamagnetic Iron Oxide Nanoparticles through a Sol-Gel Approach," *Nano Letters*. 2002, **2**, 182-186.

Main, I. G., Meredith, P. G., Sammonds, P. R., and Jones, C.: Influence of Fractal Flaw Distributions on Rock Deformation in the Brittle Field, in Deformation Mechanisms, Rheology and Tectonics, *Geol. Soc. Spec. Publ. London*, **54**, (1990), 81-96.

Marrett, R., Ortega, O.J., Kelsey, C.M.: "Extent of power-law scaling for natural fractures in rock," *Geology*. 1999. 799-802.

Massart, B., Paillet, M., Henrion, V., Sausse, J., Dezayes, C., Genter, A., Bisset, A.: "Fracture characterization and stochastic modeling of the granitic basement in the HDR Soultz Project (France)," *Proceedings*, World Geothermal Congress. 2010.

Matsunaga, I., Yanagisawa, N., Sugita, H., Tao, H.: "Reservoir monitoring by tracer testing during a long term circulation test at the Hijiori HDR site," *Proceedings*, Twenty-Seventh Workshop on Geothermal Reservoir Engineering, Stanford University. 2002.

Matsunaga, I., Yanagisawa, N., Sugita, H., Tao, H.: "Tracer tests for evaluation of flow in a multi-well and dual fracture system at the Hijiori HDR test site," *Proceedings*, World Geothermal Congress. 2005.

Matthess, G., and A. Pekdeger (1985), Survival and transport of pathogenic bacteria and viruses in ground water, in *Ground Water Quality*, edited by C. H. Ward, W. Giger, and P. McCarty, pp. 472–482, John Wiley, Hoboken, N. J.

Maturgo, O.O., Sanchez, D. R., and Barroca, G.B.: "Tracer test using naphthalene disulfonates in Southern Negros Geothermal Production Field, Philippines," *Proceedings*, World Geothermal Congress. 2010.

McCabe, W. J., Barry, B. J., and Manning, M. R.: Radioactive tracers in geothermal underground water flow studies, *Geothermics*, (1983).

McDowell-Boyer, L. M., J. R. Hunt, and N. Sitar (1986), Particle-transport through porous media, *Water Resour. Res*., **22**, 1901– 1921.

McLean, K. and McNamara, D.: "Fractures interpreted from acoustic formation imaging technology: correlation to permeability," *Proceedings,* 36th workshop on Geothermal Reservoir Engineering, Stanford University. 2011.

Mufti, I.R.: Finite-Difference Resistivity Modeling for Arbitrarily Shaped Two-Dimensional Structures, *Geophysics*, **41**, (1976), 62-78.

Muskat, M.: Potential Distributions in Large Cylindrical Disks with Partially Penetrating Electrodes, *Physics*, **2**, (1932), 329-364.

Olson, J.E.: Sublinear scaling of fracture aperture versus length: An exception or the rule?, Journal of Geophysical Research, **108**, (2003).

Olson, J.E. and Schultz, R.A.: "Comment on "A note on the scaling relations for opening mode fractures in rock" by C.H. Scholz," *Journal of Structural Geology*. 2011, 1523-1524.

Ozaki, M., Kratohvil, S., Matijevic, E. (1984), *J. Colloid Interface Sci*., **102**, 146-151.

Paul, P., Zoback, M.D., and Hennings, P.: "Fluid flow in a fracture reservoir using a geomechanically constrained fault-zone-damage model for reservoir simulation," *Proceedings,* 2007 SPE Annual Technical Conference and Exhibition.

Paul, P., Zoback, M.D., and Hennings, P.: "A method to implement permeability anisotropy associated with fault damage zones in reservoir simulation," *SPE Reservoir Evaluation and Engineering*. 2011.

Place, J., Garzic, E. L. E., Geraud, Y., Diraison, M., and Sausse, J.: Characterization of the Structural Control on Fluid Flow Paths in Fractured Granites, *Thirty-Sixth Workshop on Geothermal Reservoir Engineering*, Stanford, (2011).

Pollard, D.D. and Segall, P.: "Theoretical displacement and stresses near fractures in rock: with applications to faults, joints, veins, dikes, and solution surfaces. In B.K. Atkinson, ed.," *Fracture Mechanics of Rock,* Academic Press Inc. 1987, 277-349.

Poulton, S.W., Raiswell, R., 2005. Chemical and physical characteristics of iron oxides in riverine and glacial meltwater sediments. *Chem. Geol*. **218**, 203–221.

Pritchett, J.W.: Finding Hidden Geothermal Resources in the Basin and Range Using Electrical Survey Techniques. A Computational Feasibility Study (2004).

Prieve, D.C., and E. Ruckenstein, Rates of deposition of brownian particles calculated by lumping interaction forces into a boundary condition. *J. Particle Interface Sci*., 1976. **57**(3): p. 547–550.

Pruess, K. and Bodvarsson, G. S.: "Thermal effects of reinjection in geothermal reservoirs with major vertical fractures," *Journal of Petroleum Technology*. 1984, 1567-1578.

Rajagopalan, R., and C. Tien (1976), Trajectory analysis of deep-bed filtration with the Sphere-in-Cell porous-media model, *AIChE J.*, **22**, 523–533.

Rajagopalan, R., C. Tien, R. Pfeffer, and G. Tardos (1982), Letter to the editor, *AIChE J.*, **28**, 871–872.

Rangel-Germán, E., (2002). Water Infiltration in Fractured Porous Media: In-situ Imaging, Analytical Model, and Numerical Study. PhD thesis, Stanford University

Redman, J.A., Grant, S.B., Olson, T.M., Estes, M.K., 2001. Pathogen filtration, heterogeneity, and the potable reuse of wastewater. *Environ. Sci. Technol.* **35** (9), 1798–1805.

Reimus, P.W., 1995. The Use Synthetic Particles in Tracer Transport Experiments in Saturated Rock Fractures. LA-13004-T, Los Alamos National Laboratory, Los Alamos, NM.

Reimus, P. W., Watson, T., Vermeul, V., Newell, D., and Williams, M.: Laboratory Testing and Modeling to Evaluate Perfluorocarbon Compounds as Tracers in Geothermal Systems, *Thirty-Sixth Workshop on Geothermal Reservoir Engineering*, Stanford, (2011).

Renshaw, C.E. and Park, J.C.: "Effect of mechanical interactions on the scaling of fracture length and aperture," *Nature*. 1997, 482-484.

Rivera, J.R., Ramirez, J.S., and Rodriguez, F.G.: "Parallel fractures model for tracer flow through geothermal reservoirs – preliminary results," *Proceedings*, 12th workshop on Geothermal Reservoir Engineering, Stanford University. 1987.

Russel, W. B., D. A. Saville, and W. R. Schowalter (1989), *Particleal Dispersion*, Cambridge Univ. Press, New York.

Ryan, J. N., and M. Elimelech (1996), Particle mobilization and transport in groundwater, *Particle Surf. A: Physicochem. Eng. Aspects*, **107**, 1–56.

Sagar, N.S. and Castanier, L.M. (1997): "Oil-Foam Interactions in a Micromodel," SUPRI TR110 Report, Stanford University.

Sakthivadivel, R., Clogging of a granular porous medium by sediment, Rep. HEL 15-7, 106 pp., Hydraul. Eng. Lab., Univ. of Calif., Berkeley, 1969.

Sakthivadivel, R., Theory and mechanism of filtration of non-particleal fines through a porous medium, Rep. HEL 15-5, 110 pp., Hydraul. Eng. Lab., Univ. of Calif., Berkeley, 1966.

Saleh, S.M., Muller, R., Mader, H.S., Duerkop, A., Wolfbeis, O.S.: "Novel multicolor fluorescently labeled silica nanoparticles for interface fluorescence resonance energy transfer to and from labeled avidin," *Anal Bioanal Chem* (2010) **398**:1615-1623.

Sammis, C.G., An, L.J., Ershaghi, I.: "Fracture patterns in greywacke outcrops at the Geysers geothermal field," *Proceedings,* 16th workshop on Geothermal Reservoir Engineering, Stanford University. 1991.

Sammis, C.G., An, L.J., Ershaghi, I.: "Determining the 3-D fracture structure in the Geysers geothermal reservoir*," Proceedings,* 16th workshop on Geothermal Reservoir Engineering, Stanford University. 1992.

Sarma, P., Durlofsky, L., Aziz, K., and Chen, W.: Efficient real-time reservoir management using adjoint-based optimal control and model updating. *Computational Geosciences*, *10*(1), (2006).

Sausse, J., Dezayes, C., Genter, A., and Bisset, A.: "Characterization of fracture connectivity and fluid flow pathways derived from geological interpretation and 3D modeling of the deep seated EGS reservoir of Soultz (France)," *Proceedings*, 33rd workshop on Geothermal Reservoir Engineering, Stanford University. 2008.

Sayarpour, M., Zuluaga, E., Lake, L., and Kabir, C. S.: SPE 110081: The Use of Capacitance-Resistive Models for Rapid Estimation of Waterflood Performance and Optimization. *SPE Annual Technical Conference and Exhibition*. Society of Petroleum Engineers, (2006).

Scholz, C.H.: "A note on the scaling relations for opening mode fractures in rock," *Journal of Structural Geology*. 2010, 1485-1487.

Shaw, H. R., Gartner, A. E.: On the graphical interpretation of paleoseismic data: U.S., Geological Survey Open-File Report, (1986), 86-394.

Shaw, J.C., Churcher, P.L. and Hawkins, B.F., "The effects of firing on Berea sandstone." Published in Proceedings from the SPE International Symposium on Oilfield Chemistry, Houston, Texas. SPE Paper No. 18463, p. 63-74 (1989).

Shewchuk J.R.: Triangle: Engineering a 2D Quality ;Mesh Generator and Delaunay Triangulator, *Applied Computational Geometry: Towards Geometric Engineering,* **1148**, (1996), 203-222.

Shook, G. M.: Predicting thermal breakthrough in heterogeneous media from tracer tests, *Geothermics*, *30*(6), (2001).

Shook, G. M.: A simple, fast method of estimating fractured reservoir geometry from tracer tests. *Geothermal Resources Council*, (2003).

Shook, G. M. Estimating Fracture Surface Areas from Tracer Tests : Mathematical Formulation. *Geothermal Resources Council*, (2004).

Singha, K. and Gorelick, S.M. Saline Tracer Visualized with Three-dimensional Electrical Resistivity Tomography: Field-scale Spatial Moment Analysis. *Water Resources Research*, **41,** (2005), W05023.

Sirivithayapakorn, S., and A. A. Keller (2003), Transport of particles in saturated porous media: A pore-scale observation of the size exclusion effect and particle acceleration, *Water Resour. Res*., **39**(4), 1109, doi:10.1029/2002WR001583.

Slater, L., Binley, A.M., Daily, W. and Johnson, R. Cross-hole Electrical Imaging of a Controlled Saline Tracer Injection. *Journal of Applied Geophysics*, **44**, (2000), 85-102.

Spencer, R.L. and Ware, M.: Computational Physics 430, Partial Differential Equations, Department of Physics and Astronomy, Brigham Young University (2009).

Sun, Yugang, Yin, Yadong, Mayers, Brian T., Herricks, Thurston and Xia, Younan: "Uniform Silver Nanowires Synthesis by Reducing AgNO3 with Ethylene Glycol in the Presence of Seeds and Poly (Vinyl Pyrrolidone)," American Chemical Society 2002.

Syndansk, R.D., "Discussion of the effect of temperature and confining pressure on single-phase flow in consolidated rocks." *JPT*, August, p. 1329-1330 (1980).

Tateno, M., Watanabe, K., Nakatsuka, K., and Takahashi, H.: "Fractal Characterization of the Fracture Distribution and the Permeability in Geothermal Reservoirs," *Proceedings,* World Geothermal Congress. 1995.

Tenma, N., Yamaguchi, T., and Zyvoloski, G.: Variation of the characteristics of the shallow reservoir at the Hijiori test site between 90-days circulation test and long-term circulation test using FEHM code." *Proceedings,* World Geothermal Congress. 2005.

Tester, J., Anderson, B., Batchelor, A., Blackwell, D., DiPippo, R., Drake, E., Garnish, J., et al.: *The future of geothermal energy: Impact of Enhanced Geothermal Systems on the United States in the 21st Century*, MIT, (2006).

Tipping, E., 1981. The adsorption of aquatic humic substances by iron oxides. *Geochim. Cosmochim. Acta* **45**, 191–199.

Tipping, E., Cooke, D., 1982. The effects of adsorbed humic substances on the surface charge of goethite (a-FeOOH) in freshwaters. *Geochim. Cosmochim. Acta* **46**, 75– 80.

Tufenkji, N., and M. Elimelech (2004), Correlation equation for predicting single-collector efficiency in physiochemical filtration in saturated porous media, *Environ. Sci. Technol.*, **38**, 529–536.

Ucok, H., Ershaghi, I. and Olhoeft, G.R.: Electrical Resistivity of Geothermal Brines, *Journal of Petroleum Technology*, **32**, (1980), 717-727.

Verwey, E. J. W., and J. T. G. Overbeek (1948), *Theory of Stability of Lyophobic Particles*, Elsevier, New York.

Vilks, P., Bachinski, D.B., 1996. Particle and suspended particle migration experiments in a granite fracture. *Journal of Contaminant Hydrology* **21**, 269–279.

Vilks, P., Frost, L.H., Bachinski, D.B., 1997. Field scale particle migration experiments in a granite fracture. *Journal of Contaminant Hydrology* **26**, 203–214.

Voskov, D.: Description of the Thermal GPRS, Technical Report, Department of Energy Resources Engineering, Stanford University, Stanford, CA (2006).

Wang, H., Brandl, D., Le, F.i, Nordlander, P. and Halas, N., (2006), "Nanorice: A Hybrid Plasmonic Nanostructure," *Nano Letters*, **6** (4), 827-32.

Watanabe, K., Takahashi, H.: Fractal Geometry Characterization of Geothermal Reservoir Fracture Networks. *Journal of Geophysical Research*, **100**, (1995), 521-528.

Williams, M. D., Newell, D., Vermeul, V., Watson, T., and Reimus, P. W.: *Development of Models to Simulate Tracer Behavior in Enhanced Geothermal Systems Status Report*. Richland, Washington, (2010).

Willis, M. S., and I. Tosun, A rigorous cake filtration theory, *Chem. Eng. Sci*., **35**, 2427–2438, 1980.

Wu, E.C., Park, J.H., Park, J., Segal, E., Cunin, F., and Sailor, M.J.: Oxidation-triggered release of fluorescenct molecules or drugs form mesoporous Si Microparticles," *ACS Nano* (2008), Vol. **2** No. 11: 2401-2409.

Wu, X., Pope, G., Shook, G. M., and Srinivasan, S.: Prediction of enthalpy production from fractured geothermal reservoirs using partitioning tracers, *International Journal of Heat and Mass Transfer, 51*(5-6), (2008).

Yahara, T., and Tokita, H.: Sustainability of the Hatchobaru geothermal field, Japan, *Geothermics, 39*(4), CNR-Istituto di Geoscienze e Georisorse, (2010).

Yao, K., M. T. Habibian, and C. R. O'Melia (1971), Water and wastewater filtration: Concepts and applications, *Environ. Sci. Technol*., **5**, 1105–1112.

Yousef, A., Gentil, P., Jensen, J., and Lake, L.: SPE 95322: A capacitance model to infer interwell connectivity from production and injection rate fluctuations, *SPE Reservoir Evaluation and Engineering*, (2005).

Zoback, M.D.: "Reservoir Geomechanics," Cambridge: Cambridge University Press, 2007.